### Ph.D. Thesis

## Novel Switchable and DC Bias Controllable High-Quality Factor High-Overtone Bulk Acoustic Resonators (HBAR)

A thesis submitted for the degree of

### **DOCTOR OF PHILOSOPHY**

Ιn

**Electronics Science** 

By

### KONGBRAILATPAM SANDEEP SHARMA

**Reg.No.** 14PHPE04



**Under the supervision of** 

### Prof. K. C. JAMES RAJU

Center for Advanced Studies in Electronics Science and Technology (CASEST), School of Physics

University of Hyderabad

Telangana, India

Hyderabad- 500046

January 2021

## **DECLARATION**

I, KONGBRAILATPAM SANDEEP SHARMA, hereby declare that the research work presented in this thesis entitled "Novel Switchable and DC Bias Controllable High-Quality Factor High-Overtone Bulk Acoustic Resonators (HBAR)" submitted to the University of Hyderabad in partial fulfillment for the award of Doctor of Philosophy (PH.D) in Electronics Science is an original research work carried out by me under the supervision of Prof. K. C. James Raju in Centre for Advanced Studies in Electronics Science and Technology (CASEST), School of Physics, University of Hyderabad, Telangana, India. I also declare that this work has not been submitted previously in part or in full to this University or any other university or institution for the award of any degree or diploma.

A report on plagiarism statistics from university of Hyderabad library is also enclosed.

K. Sarder Sharma Kongbrailatpam Sandeep Sharma

Reg. No: 14PHPE04

Place: Hyderabad

Date: 8 1 2021



### **CERTIFICATE**

This is to certify that the research work presented in the thesis entitled "Novel Switchable and DC Bias Controllable High-Quality Factor High-Overtone Bulk Acoustic Resonators (HBAR)" submitted by KONGBRAILATPAM SANDEEP SHARMA bearing the registration number 14PHPE04 in partial fulfillment of the requirements for the award of DOCTOR OF PHILOSOPHY (Ph. D) in ELECTRONICS SCIENCE at Center for Advanced Studies in Electronics Science and Technology (CASEST), School of Physics is a bonafide work carried out by him under my supervision and guidance.

This thesis is free from plagiarism and has not been submitted previously in part or in full to this University or any other University or institution for the award of any degree or diploma. Further, the student has the following publications before submission of the thesis for adjudication.

- Kongbrailatpam Sandeep, J. Pundareekam Goud, and K. C. James Raju, "Effects of a Coated Material Layer on High Overtone Bulk Acoustic Resonator and its Possible Applications", IEEE Transactions on Ultrasonics, Ferroelectrics, and Frequency Control, Sept-21, (2020). DOI: 10.1109/TUFFC.2020.3025618.
- 2. **Kongbrailatpam Sandeep**, J. Pundareekam Goud, and K. C. James Raju, Resonant spectrum method for characterizing Ba<sub>0.5</sub>Sr<sub>0.5</sub>TiO<sub>3</sub> based high overtone bulk acoustic wave resonators, **Applied Physics Letters 111, 012901 (2017).**

### **Conference Proceedings:**

3. **Kongbrailatpam Sandeep**, J. Pundareekam Goud, K.C. James Raju, "Switchable High Overtone Resonance in BST film with MIM structure on Sapphire Substrate", 978-1-5090-

# 1871-2016 IEEE Workshop (ISAF/ECAPD/PFM IEEE International Symposium) (2016).

Further, the student has passed the following course towards the fulfillment of course work required for Ph.D.

S. No.	Course code	Name	Credits	Pass/Fail
1	IC801	Semiconductor Devices physics and	4	Pass
		Modeling		
2	IC804	RF/Mw ICs Theory	4	Pass
3	PY821	Research Methodology	4	Pass

**Supervisor** 

Prof. K. C. James Raju

Head, CASEST, School of Physics,

University of Hyderabad

Place: Hyderabad

Date: 8.1.2021

Head, CASEST

(Centre for Advanced Studies in Electronics Science & Technology) School of Physics

University of Hyderabad.

Dean, School of Physics,

University of Hyderabad.

Place: Hyderabad

Date: DEAN

School of Physics

University of Hyderabad HYDERABAD - 500 046.

### **Abstract**

The primary motivation of this thesis is to study a novel microwave acoustic resonator, the high-overtone bulk acoustic wave resonator (HBAR), based on ferroelectric Ba<sub>0.5</sub>Sr<sub>0.5</sub>TiO<sub>3</sub> (BST) thin films which is in the paraelectric phase at room temperature.

Traditional HBARs based on piezoelectric transduction mechanism are often chosen for a wide variety of applications such as sensing, microwave sources, quantum acoustodynamics (QAD) and acoustic spectroscopy. The novel HBARs presented in this thesis utilize electrostriction mechanism which in turn induces piezoelectric effect in the thin ferroelectric BST film under an applied external DC field. This gives the HBARs an added advantage of having the capability of switching from a simple capacitor to a resonator. Even though the individual tuning of each resonant mode is insignificant when compared to other tunable film bulk acoustic wave resonators (FBAR) and solidly mounted resonators (SMR) based on ferroelectric thin films because of the heavy mass loading the HBARs suffer from its thick substrate, important parameters of the resonators like the coupling coefficient  $(k_t^2)$  and the quality factor (Q) of the HBAR are affected by the applied DC field, making the parameters controllable or dependent on the external force i.e., DC field.

The thesis introduces the HBAR technology by laying down a state-of-the-art literature review. The experimental methodologies and techniques used in designing, fabrication and characterization of the HBAR is discussed in detail. Modeling using 1-D numerical simulation, 2-D FEM and 2-D axisymmetric FEM are performed and correlated with experimental results. HBARs are fabricated with various substrates (YAG, sapphire, silicon and fused silica). Using HBARs made on YAG and sapphire substrates, the acoustic velocity, the mass density, the elastic constant and the coupling coefficient of the BST thin film are extracted from its spectral

data. The DC field dependent nature of the  $k_t^2$  and the Q factor of both the HBARs are established. Furthermore, the relationship between the relative tunability of the thin film used and the  $k_t^2$  of the thin film BST is confirmed.

In order to understand the effect of the introduction of a new material layer in the HBAR, SU-8 of varying thicknesses are coated and the variation in the distributions of the spacing of parallel resonance frequencies (SPRF), the effective coupling coefficients ( $k_{eff}^2$ ) and the Q factor before and after coating are studied. From this analysis, the acoustic velocity and the material Q factor of the SU-8 layer coated are extracted. The effect of the electrodes (materials and geometry) on the various parameters of the HBAR is also discussed. HBAR exhibiting coupling coefficient as high as 7.8 % and Q factor as high as 35,700 at 1.57 GHz is reported in this thesis. Such switchable and DC field controllable high Q factor resonators working in the microwave frequency range show immense potential in giving more flexibility and functionalities in applications such as sensors, QAD systems, spectroscopy, oscillators, atomic clocks etc.

## <u>ष्ट्राणीकर उसे उजारेणीयस्या</u>

For my loving parents

### **ACKNOWLEDGMENT**

I have good reasons to be indebted to a large number of people, and I take this occasion to thank them publicly, for both their assistance and support during the performance and working of this thesis, and also for their help extended during many prior years leading up to it.

Firstly, I am greatly honored to express my deepest gratitude to my supervisor, Prof. K.C James Raju for giving me the opportunity to join his research group. I would like to specially thank him for his guidance, valuable scientific discussions, inspiring attitude and support throughout the research work. His constant encouragement, freedom to work with anything and at any time made my life much easier and it helped me a lot.

I am grateful to my doctoral committee members, **Prof. S. L. Sabat** and **Prof. G. Rajaram** for the discussions, the suggestions, the encouragement and the support throughout my Ph.D. I thank the present and former Heads, CASEST for the support and facilities provided.

I thank **Prof. G. Rajaram** for allowing me to use the facilities in his lab to carry out my research work and for his encouragement and help in gaining practical knowledge through numerous troubleshooting techniques.

I am heartily thankful to the present **Dean Prof. Ashok Chatarji** and former Deans, **Prof. Seshu Bai**, **Prof. Bindu A Bamba**, **Prof. Rajender Singh**, **Prof. S. Chaturvedi** and **Prof. S. P. Tiwari** for providing me with the necessary facilities in School of Physics.

I am grateful to **Prof. M. Ghanashyam Krishna** and **Prof. S.V.S Nageshwar Rao**, coordinators of Center for Nanotechnology (CFN), University of Hyderabad (UoH) for allowing me to access clean room facility, and Prof. Seshu Bai, coordinator of UGC-NRC for allowing me to use the required characterization facilities.

I acknowledge the financial support by UGC, India.

I thank Dr. Sandeep Chaturvedi, GAETEC for his valuable suggestions on the work dealing with high frequency measurement.

I am thankful and lucky to have a friend like J **Pundareekam Goud** who is also my lab mate. His calmness, sincerity and dedication to work is second to none and something to be aspired by everyone. He has taught me to persevere and be patient in the face of difficulties.

I am very grateful to my seniors and group mates, Dr. S. Ramakanth, Dr. Ajeet Kumar, Mr., Mr. Andrew Joseph, Dr. MS Alkathy, Dr. T. Anil, Dr. S. Bashaiah, Dr. S. V. N. Reddy,

Dr P. Akshara, Akhil Raman, Sampath, Rahul Gayam, Vishnu, Srikanth, Shivikram, Surjithnath, Rakesh, Sravan, Gnanashekar, Sravani, Shivakumar, Nikhil and Nimala Arun for their moral support and useful discussions during my Ph.D.

I would like to thank (late) **Dr. Kiran K Bokinala** for all the invaluable times we spent together and lifting my academic spirits.

I would like to thank Shravan Kudikala, Laishram Ayangleima and Dr. Kiran Kumar Anumandla for helping me with the coding of my programs used in the research. I would like to thank Dr. SLD Varma for providing constant guidance and support. I would also like to thank **M. Shravani** for her motivating spirit and helping me in various works done inside the clean room (CFN).

I thank all the technicians and non-teaching staff in CFN specially **Mrs. B. Sandya** (former staff), **G Prashanth**, **V Rajendra Prasad**, Mrs. Grace, Mr. Pankaj and Srikanth.

My sincere thanks to the School of Physics office staff, Mr. Abraham, Mr. Sudharshan, Mrs. Deepika, Mr. Ravi Babu, Mrs. Sailaja, Mrs. Vijaya Lakshmi, Mr. Shekar, Mr. K. Srinivas, Mr. Prasad, Mr Suresh Babu, Mr Mukunda Reddy, Narsimha Rao, Somla, Santhosh and Krishna. I thank Ms. Sunitha (FESEM) and Mr. Naresh (GIXRD), NRC staff.

I thank M&W maintenance staff Mr. T. Rajiv and Mr. Tyagaraju for their support related to cleanroom and other technical works.

I am thankful to my M. TECH IC. Technology mates specially Dr. GDV. Santosh and Dr. Satish Bonam.

I want to express my gratitude to **Akoijam Malemnganbi** (Research Scholar, CALTS, UoH) for editing and proof reading my thesis and the published journal articles. Her prompt, skillful editing and attention to little details has helped in improving clarity in the thesis. I would also like to thank her for being supportive throughout my *ups and down* of my Ph.D. journey.

I am forever indebted to my friends Merenmeso Pongen, Aso Aier, Zulu Jamir, Shinaj PS, Laishram Samyokpha, Priyanka Laishram, Yingmei Konyak, and Thangjam Sumanta for holding me up during difficult times.

I would like to thank my friends whom I have met in campus, Dr. Thongam Bipin, Alezo James, Majaw Donbok, Dr. Mayengbam Lalit, Goutham Uyalla, Moirangthem Suresh, Dr. Newme Atungbao, Laishram Banty, Thungdemo N Yanthan, Bikash Borah, (late) Prasantha, San, and Komuni.

I would like to thank my childhood friends, Soibam Naotonba, Khumanthem Amit, Rk. Satish, Rk. Gyandeep, Rodi Khumukcham, Chongtham Sunni, Atom Rajiv, Langpoklakpam Kula and Lambalmayum Kishorjit Meetei for rejuvenating my mind whenever we talk or meet.

I am grateful to my mother Leihaothabam Tilotama and my father Konbrailatpam Sharatchandra for their unconditional love and indomitable energy in supporting not only my career but also looking after my health and well-being every single day. I am filled with love for my brothers, Kongbrailatpam Nanaocha, Kongbrailatpam Jackey and Kongbrailatpam Ricky for their warmth and excitement we shared since childhood and for their constant reminders to push myself in becoming who I am today. I would like to thank my two sisters-in-law, Ajeeta Slong and Anoubam Diana for their support and understanding. I would to thank my lovely niece Kongbrailatpam Laija for relaxing my mind with her laughter.

Above all, it is the endless sacrifice, support and motivation from my family and friends which has brought me to the position where I am.

My apologies to the people who are not covered in this note but helped throughout my career.

## **CONTENTS**

CHA	PTER 1	. INTRODUCTION		
1.1	Introdu	ction	1	
1.2	Ultraso	Ultrasonics		
	1.2.1	Introduction	2	
	12.2	Acoustic waves	4	
1.3	Bulk a	Bulk acoustic wave (BAW) resonator		
	1.3.1	Film bulk acoustic wave resonator (FBAR)	11	
	1.3.2	High overtone bulk acoustic resonator (HBAR)	15	
1.4	Applications of High overtone bulk acoustic resonator (HBAR)			
	1.4.1	Microwave sources	23	
	1.4.2	Quantum acoustics	27	
	1.4.3	Sensors	30	
	1.4.4	Material Characterization	30	
1.5	Choice	Choice of transducer materials for BAW		
	1.5.1	Ferroelectric films as transducer materials	38	
		1.5.1.1 Field -Induced strain	39	
		1.5.1.2 Barium strontium titanate (BST)	40	
1.6	Motiva	ation and Goals of the thesis	49	
1.7	Thesis	outline	51	
CHA	PTER 2	. Experimental Methods		
2.1	Introdu	action	53	
2.2	Target	preparation of Barium strontium titanate	53	
2.3	Thin fi	lm preparation techniques	56	
	2.3.1	Pulsed laser deposition (PLD)	56	
	2.3.2	RF magnetron sputtering	61	
2.4	Device	e fabrication	64	
2.5	Struct	Structural and microstructural characterization techniques		
	2.5.1	X-Ray Diffraction (XRD)	67	
	2.5.2	Scanning electron microscope (SEM)	68	
2.6	High frequency characterization			
	2.6.1	Vector Network Analyzer	69	
	2.6.2	On-wafer probing set-up	72	



	2.6.3	Calibration	73
	2.6.4	De-embedding procedures	78
2.7	Softw	vare used	81
-	oter 3: N nators (H	Modelling of BST based High Overtone Bulk Acoustic Wave HBAR)	
3.1	Introdu	action	83
3.2	Field in	nduced piezoelectricity mechanism in BST	84
	3.2.1	Field dependence of material properties in ferroelectrics	85
	3.2.2	The relation between relative tunability and the electromechanical coupling coefficient	91
3.3	•	of frequency spectra of high overtone bulk acoustic resonator	93
	3.3.1	Resonant spectrum method (RSM)	93
		3.3.1.1 The impedance of a composite resonator (HBAR)	93
		3.3.1.2 SPRF and $k_{eff}^2$	99
		3.3.1.3 The first normal region $\Delta f_N$ and coupling coefficient $k_t^2$ .	101
		3.3.1.4 The first transition region $\Delta f_T$ and coupling coefficient $k_t^2$	103
	3.3.2	The impedance of HBAR with a coated material	104
3.4	Summa	ry and conclusions	109
_	•	Characterization of BST based High Overtone Bulk Acoustic tors (HBAR)	
4.1	Introdu	ction	110
4.2	Sample	preparation and experimental set-up	111
4.3	Switcha	able HBAR base on ferroelectric thin film BST	116
4.4		al property extraction of BST using resonant spectrum method	121
(RSN	4.4.1	HBAR on sapphire substrate	122
	4.4.2	HBAR on YAG substrate.	125
4.5	Effects	of DC bias on BST based HBAR	128
	4.5.1	HBAR on sapphire substrate	130
	4.5.2	HBAR on YAG substrate	133
	4.5.3	Relationship between the relative tunability and the coupling coefficient	136
4.6	Summa	ary and conclusions.	138

## Chapter 5: Effects of a coated material layer on HBAR and its possible applications



5.1	Introdu	action	140	
5.2	Experi	mental setup and measurement results	141	
	5.2.1	Experimental setup	141	
	5.2.2	Experimental results	143	
	5.2.3	Effects of coating on SPRF, $k_{eff}^2$ and Q factor of HBAR	146	
5.3	Simula	tion to extract th acoustic properties of SU-8	152	
	5.3.1	Numerical simulation	153	
	5.3.2	Finite element method (FEM) simulation	159	
5.4	Summ	ary and conclusion	162	
		Effect of electrode on the parameters of High Overtone Bulk onators (HBAR)		
6.1	Introdu	ction	164	
6.2	The ele	ectrode material	165	
	6.2.1	Effect of the electrode material on SPRF of HBAR	166	
	6.2.2	Effect of the electrode materials on $k_{eff}^2$ of HBAR	168	
	6.2.3	Effect of the electrode materials on Q factor of HBAR	169	
6.3	Effect	of the electrode shape and area	170	
	6.3.1	Circular electrodes	172	
	6.3.2	Apodized electrodes	176	
	6.3.3	Square electrodes	179	
6.4	Summ	ary and conclusion	184	
CHA	APTER 7	: Conclusions and Future Work		
7.1	Conclu	ısions	186	
7.2	Potent	ial for future work	188	
REF	ERENC	ES	197	
List	of Figure	es	201	
List	of Tables	S	207	
Abb	reviation	s	208	
List	List of Publications			
Appendix				
Originality report				



## **CHAPTER 1: INTRODUCTION**

#### 1.1 Introduction

Microwave resonators are one of the vital elements for designing various components in RF systems like filters, oscillators etc. for applications in communication devices. Resonators, particularly RF MEMS based ones are widely used for sensing applications like pressure sensors, gravimetric sensors, explosive trace detection and biosensors. Amongst the RF MEMS based resonators, surface acoustic wave (SAW) and bulk acoustic wave (BAW) based resonators have proven themselves to be one of the most prominent front runners, and still garner interest from both research and development (R & D) as well as commercial markets. The evolution and success of acoustic wave devices, needless to say, have stemmed from various technological advancements in both material science and microelectronics. At present, there is still an ever-growing necessity to give focus on exploiting numerous functionalities these devices have to offer, one such example is the use of ferroelectric thin film instead of the conventionally used piezoelectric ones for designing BAW devices. Such devices are switchable and tunable, which makes it a preferred technology to be used for new communication systems and helps in scaling down the end products.

In this thesis, the devices discussed are a type of composite BAW resonators called high overtone bulk acoustic resonators (HBARs), also called as an overmoded resonator. Compared to other BAW devices like FBARs and SMRs based on ferroelectric thin film, there is a lacklustre research on ferroelectric based HBARs. The first intent of the thesis is to achieve a switchable HBAR and study its characteristics which are dependent on an external electric field (DC bias). The characterization of the HBAR can also yield important

material parameters like acoustic wave velocity, coupling coefficient and elastic constant of the thin film used as the transducer of the HBAR. The knowledge of material property is very important in designing other BAW devices.

The second scheme of the thesis is to consider HBAR as a tool to analyse and extract the effects and properties, respectively of a polymer coated onto the resonator. The characterization of polymer or polymer composites are important when it comes to designing acoustic matching layers for applications in BioMEMS.

With further studies, the switchable and high Q factor response in the GHz range exhibited by ferroelectric thin film-based HBARs can be used in designing switchable narrow band filters and has the potential for application in microwave sources, sensing and quantum acoustodynamics (QAD).

#### 1.2 Ultrasonics

### 1.2.1 Introduction

Definitions of sound, acoustics and ultrasonics as per ANSI/ASA S1.1 & S3.20 Standard acoustical & Bioacoustical Terminology database [1]:

**Sound**: - "(a) Oscillation in pressure, stress, particle displacement, particle velocity, etc., propagated in a medium with internal forces (e.g., elastic or viscous), or the superposition of such propagated oscillation. (b) Auditory sensation evoked by the oscillation described in (a)."

**Acoustics**: - "(a) Science of sound, including its production, transmission, and effects, including biological and psychological effects. (b) those quantities that, together, determine its character with respect to auditory effects."

**Ultrasonics**: - "Technology of sound at frequencies greater than 20 kHz."

As implied by the definition of acoustics, a variety of applications in both research and industry, utilize the information gathered from studying the effects generated by a medium through which sound is transmitted. Lindsay's Wheel of Acoustics, shown in Fig.1.1, represents the realms of acoustics associated with earth science, engineering, arts and life sciences [2]. Acoustics can be categorized into the following depending on their applications: atmospheric acoustics, architectural acoustics, aeroacoustics, environmental acoustics, nonlinear acoustics, noise acoustics, musical acoustics, underwater acoustics and ultrasonics [3].

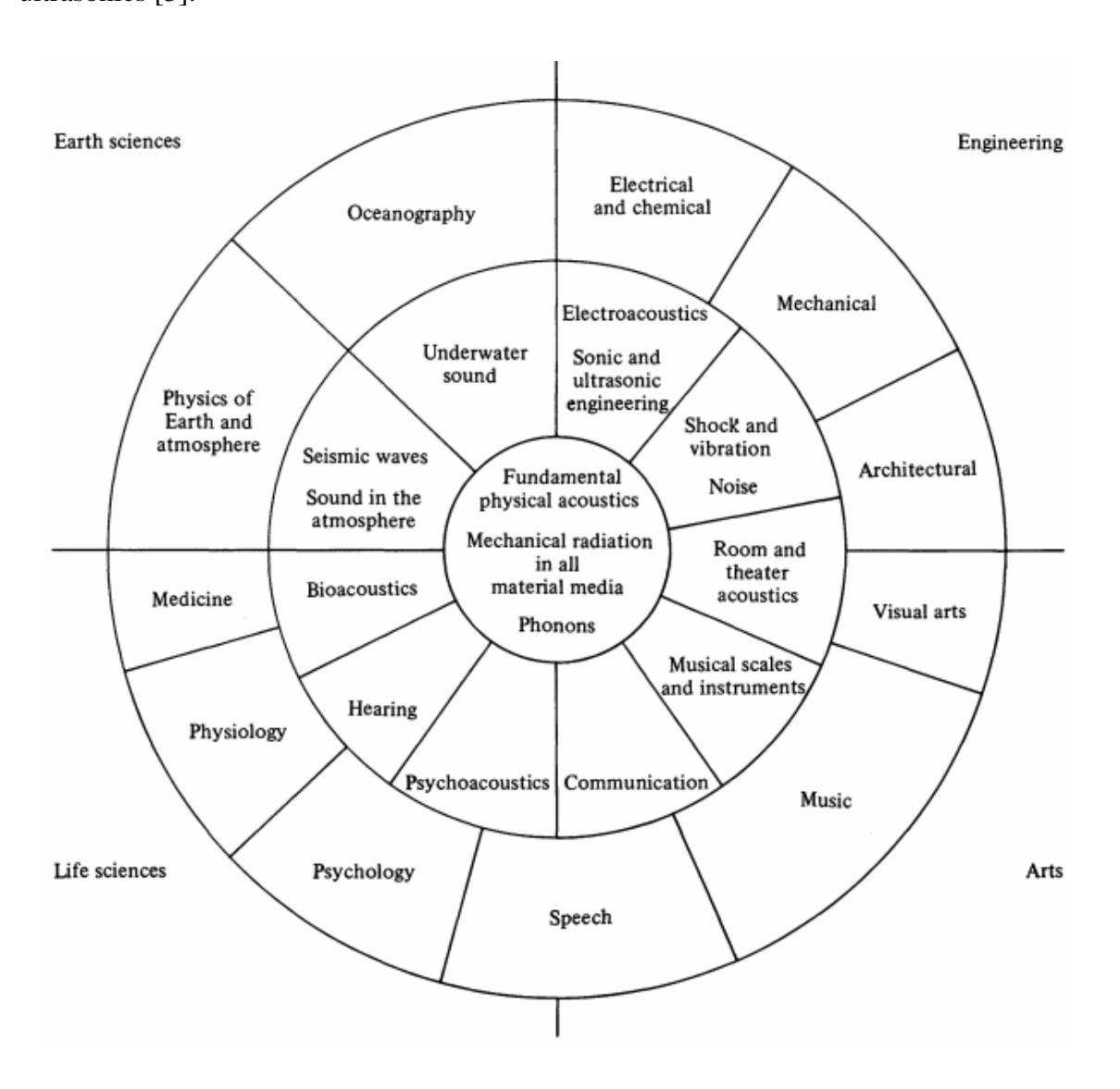


Figure 1.1. Lindsay's Wheel of Acoustics [2].

The audible spectrum of frequency of an average person is from 20 Hz to 20 kHz. The acoustic spectrum, however, extends from below the audible range of frequency of humans to as high as above 1 THz. Ultrasonics can also be defined as a branch of acoustics which explores the effects of propagation, transmission through matter and its applications at frequencies above the audible range of humans. Ultrasonics encompasses the fundamental science of energy-matter interaction, generation and detection, and other ever-increasing varying range of applications in just about every engineering fields, sciences and medicine [4].

The core of all ultrasonic works lies in some form of ultrasonic transducer which are achieved from various range of phenomenon and methods such as piezoelectric effect, electrostriction, lasers, mechanical electromagnetic coupling etc. Ultrasonics can operate from as low as cryogenic temperatures to above 1500°C. Application of ultrasonics includes material characterization, non-destructive testing (NDE), medical diagnostics, underwater acoustics (SONAR), sonochemistry and physical acoustics [5-10]. The historical aspects of the evolution of acoustics and ultrasonics are well documented in the literatures of [5,11-15].

#### 1.2.2 Acoustic waves

Acoustic waves, also called as ultrasonic waves or elastic waves, are stress waves and hence are supported only within a mass medium. Unlike electromagnetic waves, they cannot be transmitted through vacuum. Acoustic waves entail mechanical deformations or disturbances in an elastic medium (materials) and its associated internal forces (stress) as it propagates in space and time. Energy transmission takes place from the excitation source through the medium as oscillation or vibration, i.e., energy transfer happens from one "mass" or element of the medium (material) to another through direct and strong contact

between the elements [4,16]. a) Sound heard at the end of a metal pipe by a listener (staying close to pipe) when the pipe is tapped/struck at the other end and b) the audible resonance which occurs for hundreds of cycles when a bell is struck, are good evidences for low-loss acoustic waves propagation at audible frequency. In case of *microwave acoustics*, the propagation and resonances of the acoustic waves are at a much higher frequency, well above 10 GHz [17].

Acoustic waves are similar to electromagnetic waves as it follows the general wave equation. The velocity of the waves, while travelling in a medium, depend on the properties of the medium. Similar to light, acoustic waves experience reflection from surfaces, refraction occurs when they are passing from one medium to another which affects the velocity of sound, and they are diffracted at edges or about an obstacle. Scattering of energy takes place from rough surfaces or particles similar to the scattering of light by dust particle or surfaces. In many ways acoustic waves can be considered as analogous to electromagnetic waves [18].

It is important to note that when acoustic waves propagate through a medium, even though the energy introduced by the disturbance travels by transferring energy from one element to the next element, the elements of the medium does not move simultaneously until the energy is dissipated. The reasons behind this are a) it follows Newton's laws of motion, i.e., the medium experiences inertia and accelerates only in correspondence to the applied force and b) it is elastic in nature and deformation occurs due to stress, and hence the disturbance propagates at the velocity of sound through the medium. The propagation of acoustic waves depends upon various factors like density, elastic properties of the medium and the type of the wave. Since acoustic waves are stress waves, the velocity of sound also depends on the vibrational mode it is associated with. Only compressional or longitudinal waves can be propagated in gases. Surface waves and longitudinal waves occur in most

liquids. Solids, on the other hand, are capable of transmitting various acoustic wave modes [4].

The main focus of this thesis is on acoustic waves propagating in solids (bulk waves) and it can be categorized into two types i.e., longitudinal wave in which the particle displacement is parallel to the direction of wave propagation and shear/ transverse wave in which the particle displacement is normal to the direction of wave propagation. The schematics of longitudinal and shear waves are illustrated in Fig. 1.2 [17]. The velocity of longitudinal wave is generally in the range 5000 m/s to 10,000 m/s. The velocity of shear waves is lower than longitudinal waves, and are in the range 3000 m/s to 6000 m/s. Fig. 1.3 and 1.4 show the longitudinal wave velocity vs density and transverse wave velocity vs density respectively for various solid materials. The excitation of longitudinal and shear vibrational modes of bulk acoustic wave (BAW) using thickness and lateral electric fields is shown in Fig. 1.5.

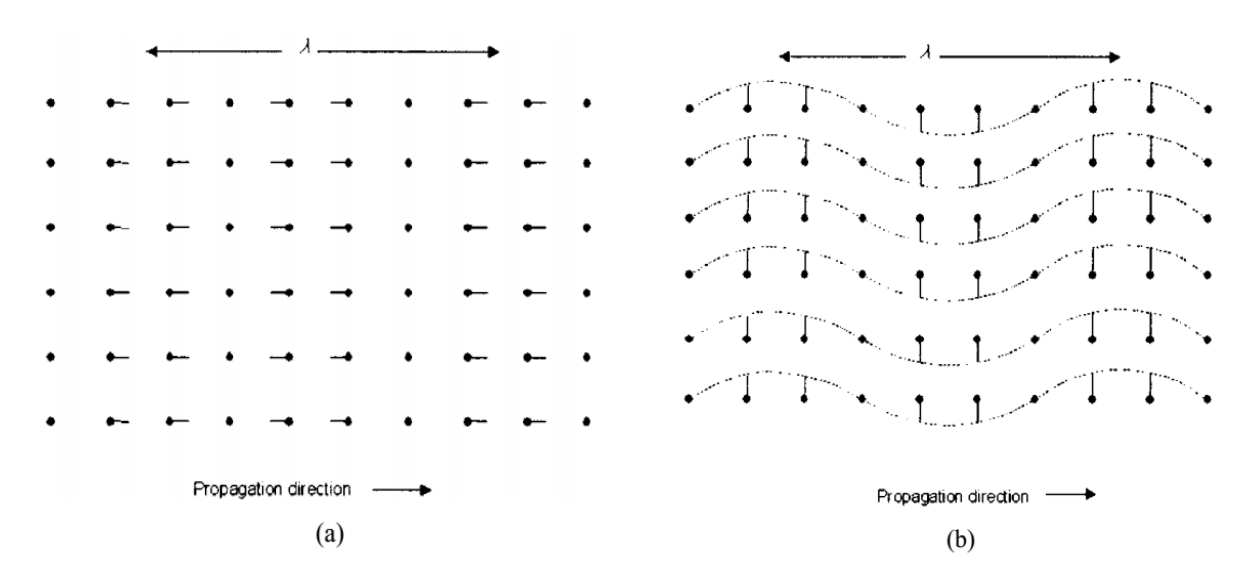


Figure 1.2 Schematic of an acoustic (a) longitudinal wave b) shear wave, in infinite solid material. The dots represent particles at rest, lines indicate instantaneous positions of particles where acoustic wave is present (displacements exaggerated);  $\lambda$  is the acoustic wavelength [17].

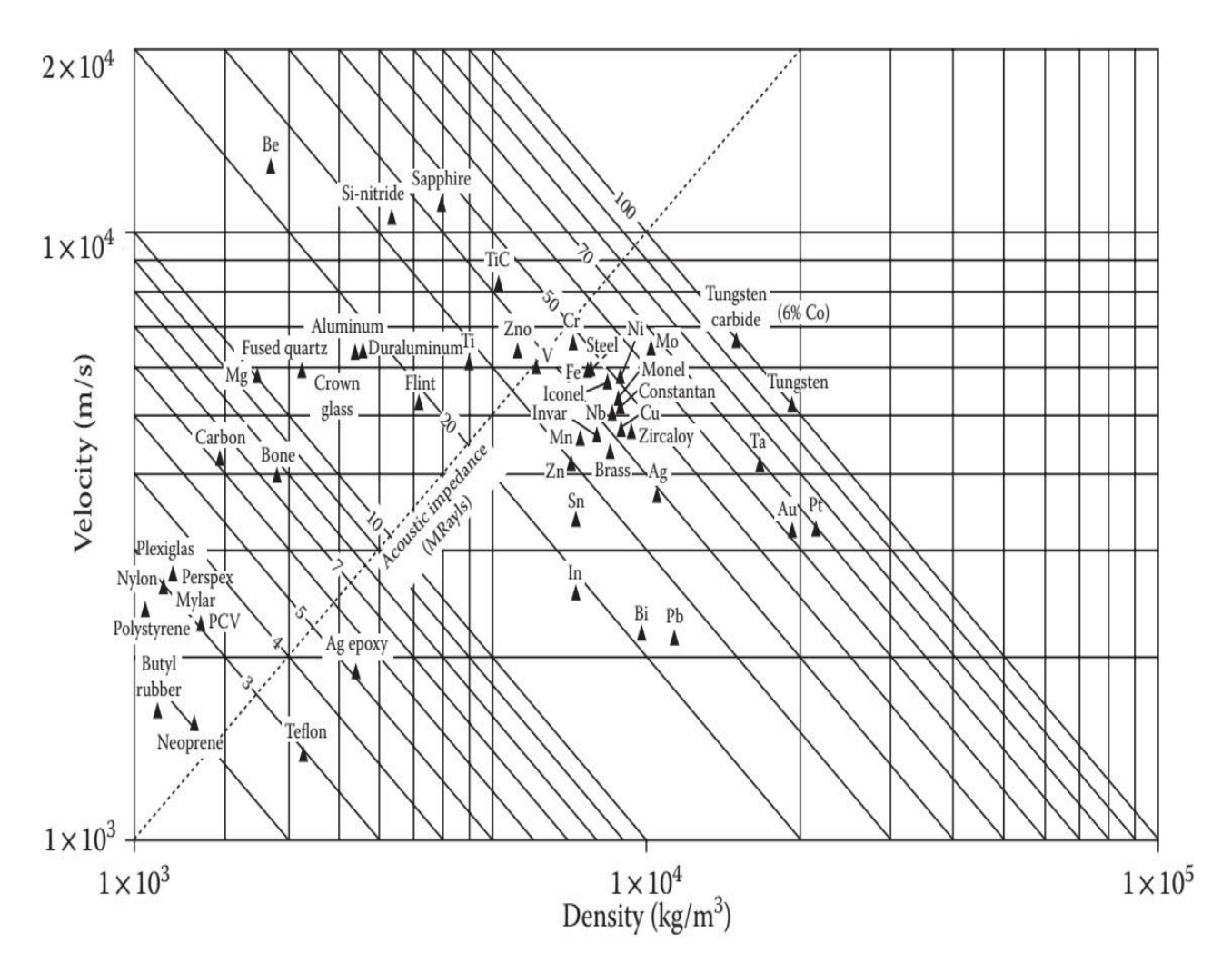


Figure 1.3 Longitudinal velocity of sound in various solid materials [19].

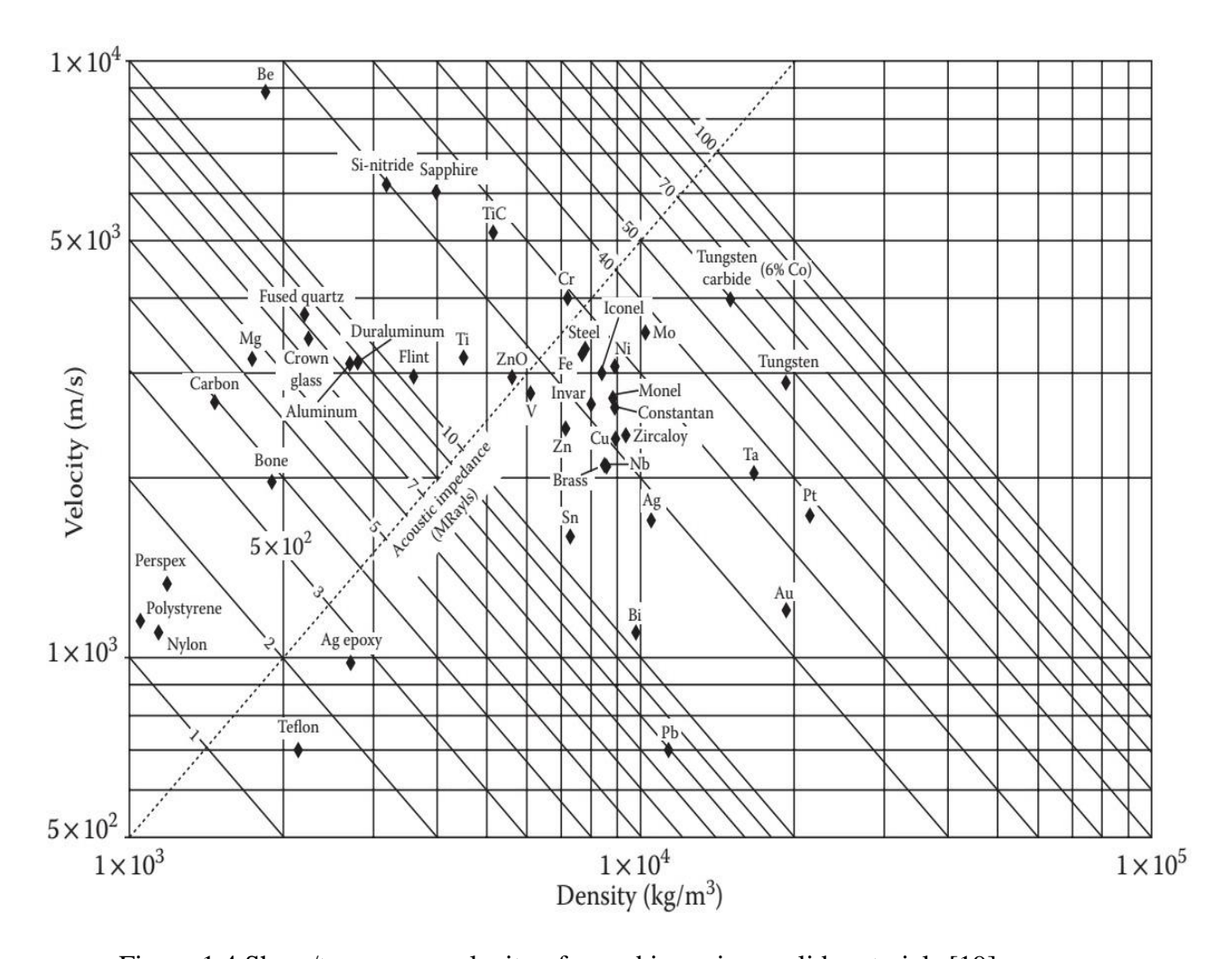


Figure 1.4 Shear/transverse velocity of sound in various solid materials [19].

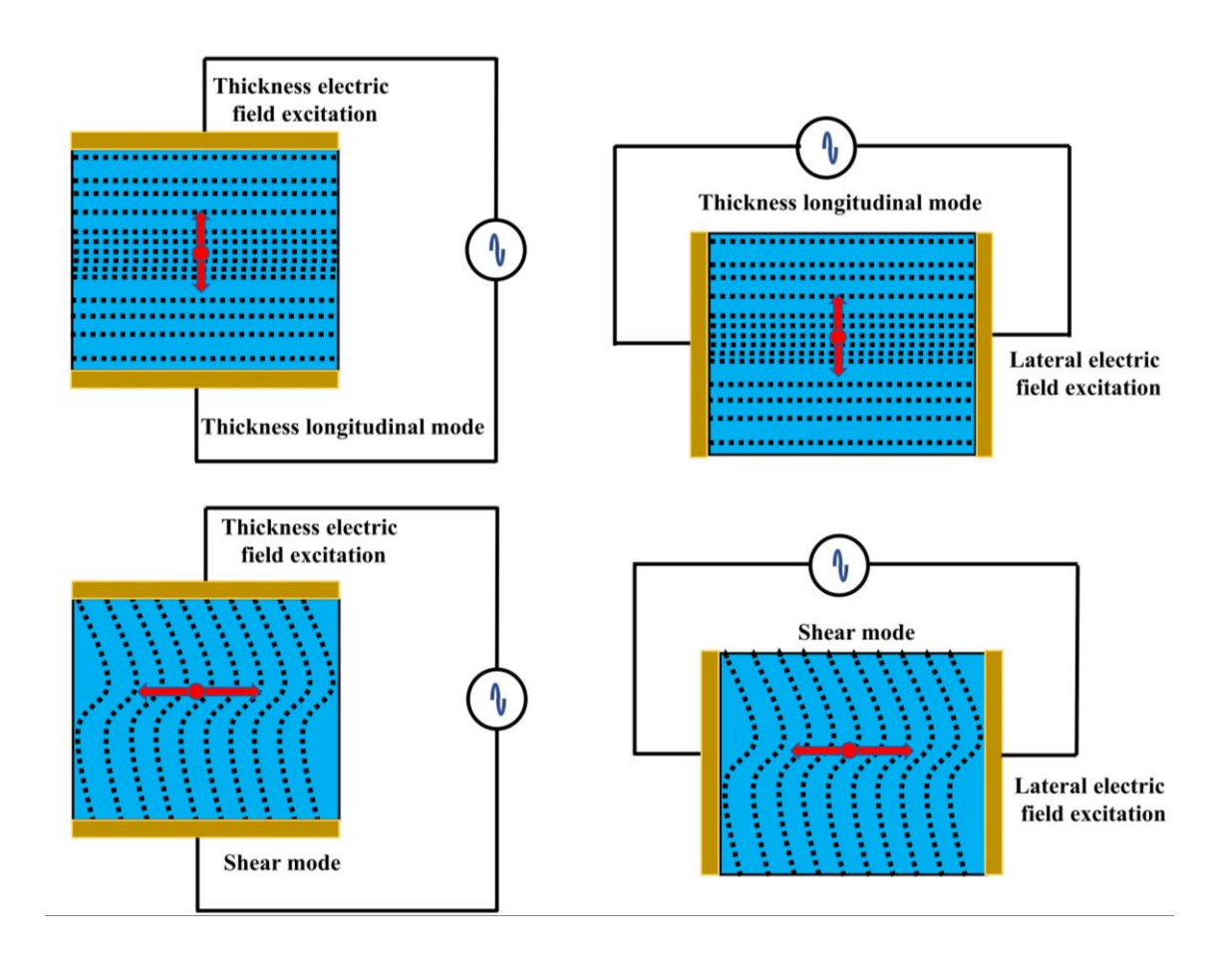


Figure 1.5. Excitations of thickness longitudinal and shear modes in piezoelectric thin film.

Arrows indicate the direction of propagation of the particle (oscillations) [20].

### 1.3 Bulk acoustic wave (BAW) resonator

Conventional microwave resonators like LC resonators, transmission line resonators, ceramic resonators are all used in various applications such as filters, oscillators, amplifiers etc. Such devices are all dependent on developing their component microwave resonators, which are excited by electromagnetic waves. The expanding communication applications has pushed designers to scale down the size of high-performance devices in order to achieve integration of various active and passive components into a single chip (like SoCs). But, one big challenge is that, at the RF/microwave frequencies, the electromagnetic (EM) wave-based resonators are much larger than the other components to be integrated with it. This is basically due to the fact that the device size is directly related to the wavelength of

the EM wave at the operating frequency, which is again a function of the propagation velocity of the EM wave.

Acoustic resonators are a type of microelectromechanical systems (MEMS) where acoustic wave can be propagated, leading to mechanical vibration at a resonant frequency in the system which depends on the dimensions and elastic/mechanical properties of the system. It can also be treated as an acoustic cavity which traps energy (of the mechanical wave) in the medium. Acoustic resonators have become a key component in overcoming the challenges a microwave resonator (EM wave based) face. This is due to the fact that the wave velocity or the propagation velocity of acoustic waves are four to five orders of magnitude lower than that of EM waves, and hence the resulting wavelength and the size of the device utilizing acoustic wave is smaller by four to five times order of magnitude compared to the ones utilizing EM waves. BAW resonators are usually made on silicon substrates and are therefore compatible with the standard IC technology, and due to these factors, their wireless communication applications have grown exponentially [16,21].

The most important aspect of acoustic resonators or devices is the acoustoelectric transduction. The transducer's basic function is to convert electrical energy to acoustic energy/mechanical energy, and vice versa. Examples of such transducers in the lower frequency range are microphones and loudspeakers. For applications in the microwave frequency range, piezoelectric transducers and more recently ferroelectric transducers are used for both generating and detecting the acoustic waves [17]. Newell [22] in 1965 reported the first BAW resonator which was based on a sandwiched configuration of deposited piezoelectric layer between a bottom and a top electrode.

The main focus of discussion in this thesis is thin film BAW resonators which operate at microwave frequencies. The bulk acoustic resonators can be broadly classified as film bulk acoustic resonator (FBAR) and high overtone bulk acoustic resonator (HBAR).

### 1.3.1 Film bulk acoustic wave resonator (FBAR)

Grudkowski et al. [23] in 1980 and Lakin et al. [24] in 1981 reported their works on high Q FBAR by integration of thin film ZnO on silicon, by realizing a membrane/ diaphragm for reflecting acoustic wave at air interface. Nakamura et al. [25] in 1981 further studied the effect of temperature on ZnO/SiO<sub>2</sub> diaphragm composite resonator (FBAR). In 1982, Lakin et al. [26], published an enthralling paper which not only brought out the prospects of thin film BAW resonators and filters but also put forward the use of AlN as the piezoelectric material of choice. The enthusiasm in research of thin film BAW thrived in the 80's and up until early 90's but died down due to lack of market interest along with the challenges in fabrication of such devices. However, in the early 2000's FBAR became the forerunner for application in mobile communication devices. It was also supported by the advancement in microfabrication techniques [27].

The advancement of microfabrication techniques has led to the development of diverse MEMS devices which are employed in various commercial and military applications. Amongst the MEMS devices, FBAR has also found applications in widespread areas such as a) communication systems- RF filters and duplexers [28,29] and b) sensors for physical (temperature [30], humidity [31], UV light [32] and pressure [33-34]) and chemical (explosives [35], toxic ions [36] and organic gas [37]) and biological (proteins and antigens [38-41]) [42,43]. FBAR sensors are extremely sensitive since they operate at a high resonant frequency (in 1-3 GHz range, or above) and high Q factor. Mass as low as  $10^{-15}$  g can be detected using gravimetric FBAR sensors [39,44].

FBARs can be subcategorised based on the device's architecture as back-etched membrane, membrane over air gap (using sacrificial layer) and solidly mounted resonator (Bragg reflector based) [45]. The back-etched and the sacrificial layer membrane-based versions are generally referred to as FBAR or TFBAR and the solidly mounted resonator as SMR. The configurations of these three BAW types are shown in Fig. 1.6. The thin film used for transduction can be either piezoelectric (PE) or ferroelectric (FE), the configuration stays the same; the choice of material is discussed later in this chapter.

As seen from Fig. 1.6, it is clear that all the configurations have two things in common:

- 1) The PE/FE thin film is sandwiched between electrodes and the thin film is acoustically isolated from the substrate using membrane/Bragg reflector to contain the acoustic energy inside the transducer to get high Q factor and supress spurious modes.
- 2) Such kind of thin film BAW is made on silicon wafer which is a high acoustic loss material (low material Q). Thus, a high contrast acoustic impedance is required to be maintained at the boundary between the transducer and the substrate.

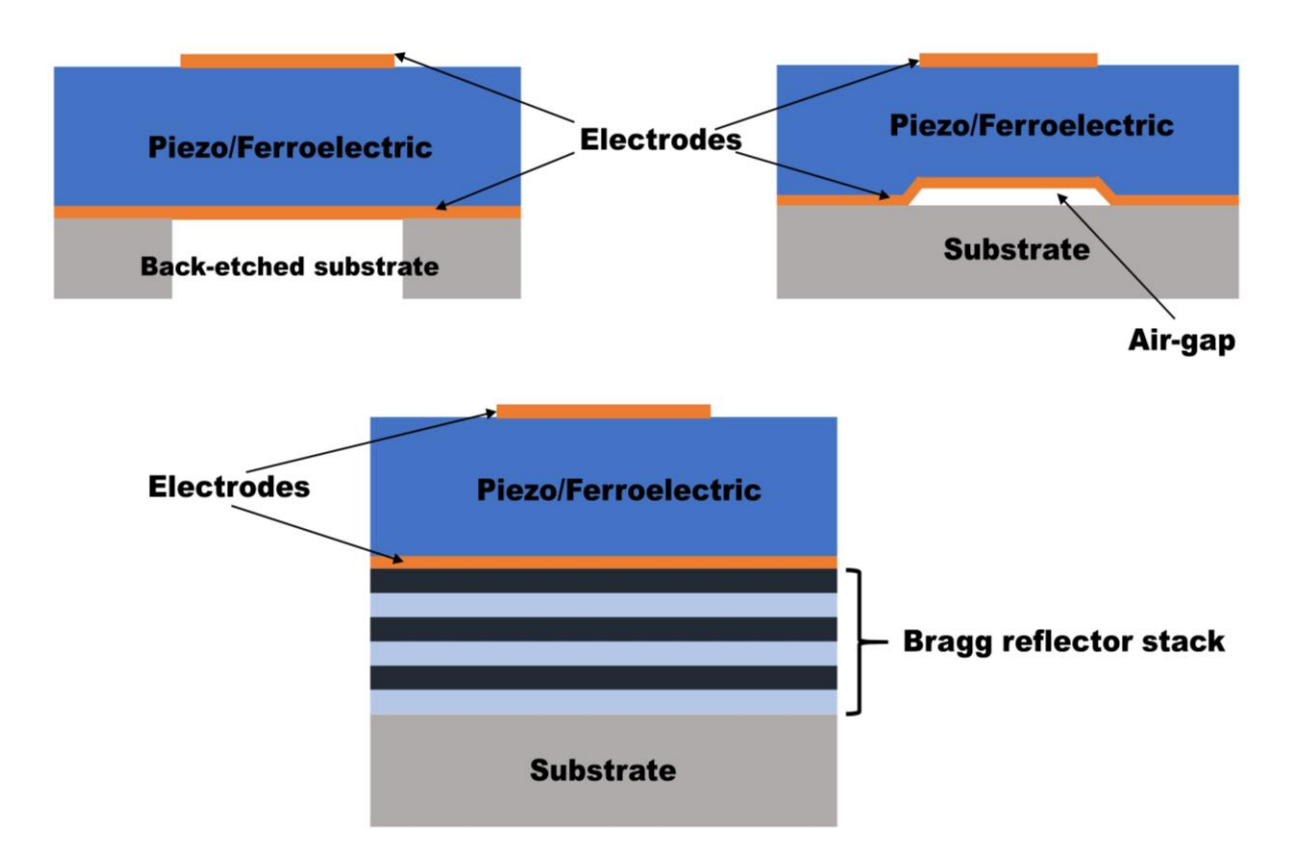
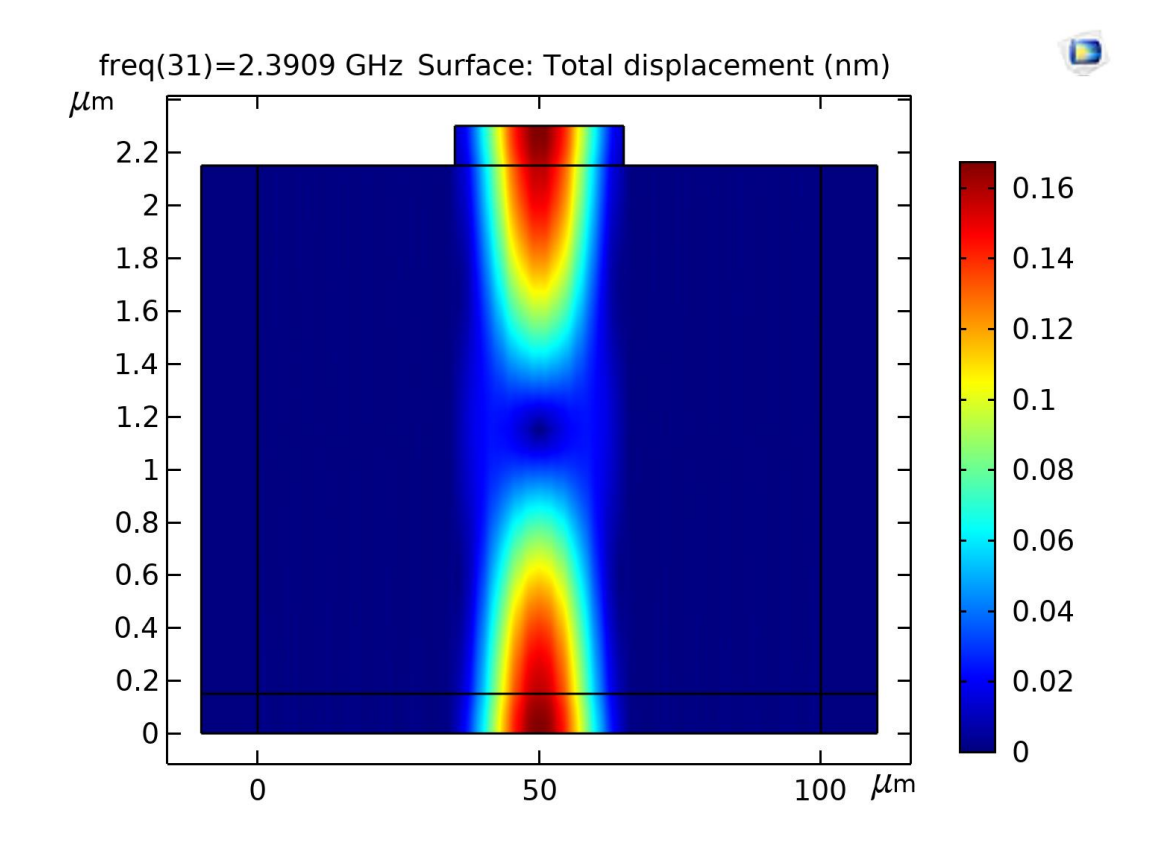


Figure 1.6. Configurations of thin film BAW.

In the thin film BAW like FBAR and SMR, when RF signal is applied across the electrodes, resonant standing waves are produced at such frequencies where the thickness of the film equals half of the corresponding wavelength which depend on the thickness and acoustic properties of the thin film PE/FE. Fig. 1.7 shows the thickness extension mode in FBAR and SMR simulated using COMSOL Multiphysics®; with the acoustic wave velocity of AlN around 10400 m/s [46] and thickness of the film 2 μm. The resonance exhibited is at approx. 2.4 GHz. SiO<sub>2</sub> and Si<sub>3</sub>N<sub>4</sub> are the materials of choice for realizing the suspended membrane in both back-etched and air-gap membrane type FBARs [27,47]. These devices require bulk micromachining by deep reactive ion etch (DRIE) in case of the back-etch membrane structure [48] and wet and dry etching of sacrificial layer. Both the configurations suffer from residual stresses in the membrane and PE/FE layer and requires lengthy etching processes.



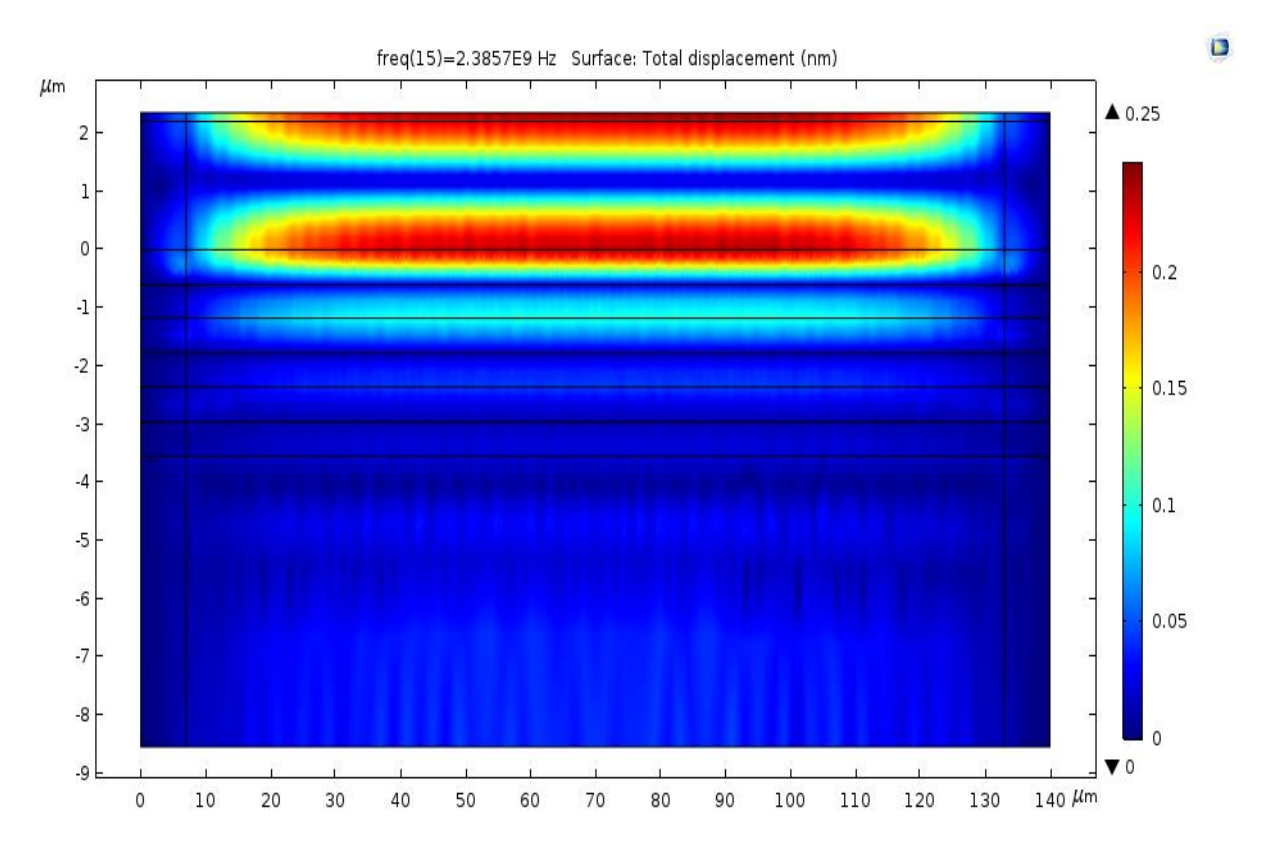


Figure 1.7. 2D simulation showing the total displacement (thickness extensional mode) in FBAR (top) and SMR (bottom).

The SMR takes a different approach by achieving the acoustic isolation using a Bragg reflector mirror stacks. The acoustic mirror is realized by fabricating (depositing) alternating layers of high and low acoustic impedance quarter wavelength thick films. At every boundary between the high and low layers, acoustic waves are reflected which finally adds up to the correct phase because of the quarter wavelength thickness of the layers. The end result is an acoustically isolated BAW resonator. Although robust, this configuration of thin BAW resonator needs long deposition time for each layer and controlling the thickness precisely down to a few nanometers is quite complex. Another major drawback of SMR is that the deposition of these layers generally requires high temperature which makes it incompatible for integration into CMOS technology [45].

### 1.3.2 High overtone bulk acoustic resonator (HBAR)

Piezoelectric composite resonators are important tools for characterizing the properties of materials. L. Quimby of Columbia University published in 1925 the use of a quartz based composite resonator to determine the coefficient of viscosity and acoustic velocity of aluminium, copper and glass [49]. But, the first composite resonator which was designed for the sole purpose to exhibit frequency-temperature stability at high frequency (250-300 MHz) exhibiting electrical Q's above 5000 was reported in 1967 by T.R. Sliker and D.A. Roberts. They realized the device by using Cadmium sulfide (4 μm and 8 μm thickness samples) as the piezoelectric film on a quartz wafer [50]. D.J. Page from Westinghouse Research Labs in 1968 demonstrated the viability of using silicon for generating acoustic resonance (above 400 MHz) as a follow up to the work done by T.R. Sliker et.al. This work gave direction towards the possibility of using acoustic waves in integrated circuits [51]. It is worth noting that the FBAR technology developed much later after HBAR due to the premature microfabrication technology at that time.

For coherent communication systems, electronic warfare systems and certain radars to function ideally, a stable reference source is of prime importance. The accelerating growth in devices operating in the microwave frequencies with a further push going towards the millimetre-wave range has led to the development of new and distinctive frequency sources. Due to the disadvantages, the traditional BAW crystals suffer such as low frequency output, the need for resonators operating at higher frequency with higher Q and temperature stability became evident. Surface acoustic wave (SAW) and BAW based on thin films were considered [52]. To design an oscillator which could match the phase noise characteristics of a VHF quartz oscillator, R.A. Moore et.al. incepted the idea of using low acoustic loss substrate, i.e., high Q material instead of silicon or quartz in the composite resonator configuration. The group reported BAW composite resonators made on sapphire, ruby, spinel, YAG and diamond which exhibited Q factor above 15,000 operating in the frequency range of 1-10 GHz [53]. During the 1980's, The Westinghouse Defence and Electronics Centre, Baltimore designed various microwave sources and HBARs for frequencies up to 10 GHz and have achieved HBARs which exhibited Q's above 60,000 at 1.5 GHz [54-57]. Lakin et.al. in 1993 reported an HBAR which exhibited Q factor of around 67,000 at 1.6 GHz [58].

The Q factor of most resonators decreases as the frequency of operation increases, so the product of frequency and Q factor (FQ product) is taken as a basis of comparison for resonators. Fig. 1.8 shows the FQ product charts for various resonators. Among the competing technologies for application in microwave stabilized source, the HBAR exhibits the highest FQ product and offers multiple resonant frequencies/modes for a single device.

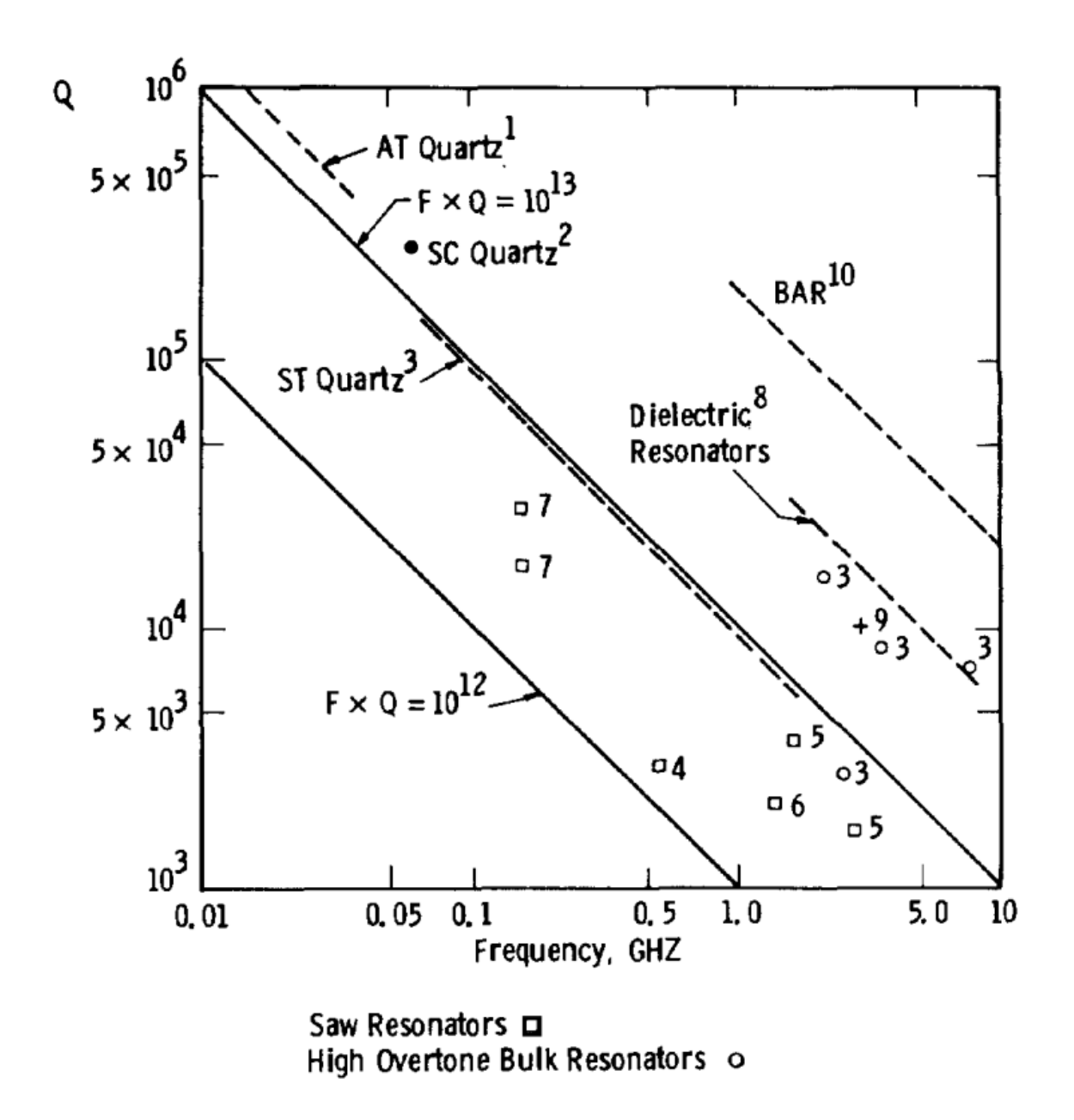


Figure 1.8. Q values of various resonators in the frequency range of 10 MHz to 10 GHz [57].

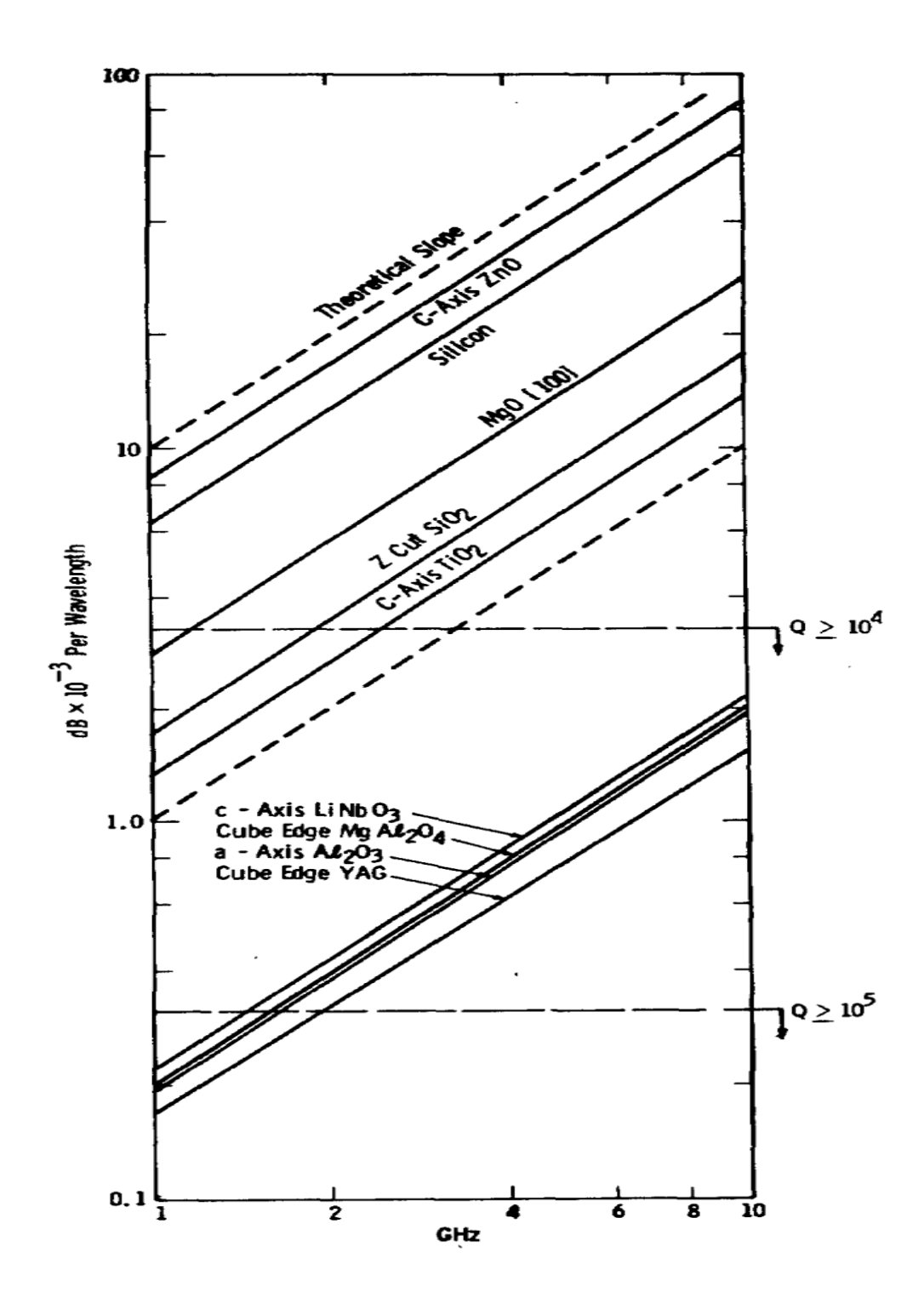


Figure 1.9. Q and attenuation of different material [57].

Therefore, HBAR provides the lowest phase noise in direct frequency stabilization, and all this with minimal hardware requirement making it possibly the cheapest among all the other competing technology [57]. The choice of materials available for use in HBAR as a substrate with its Q value and attenuation as a function of frequency are shown in Fig. 1.9.

### **Device Configuration**

As discussed before, when RF signal is excited across the electrodes, standing waves are created which translates as resonances in BAW resonators. For these plane waves, the reflectance (R) and transmittance (T) at the boundary between transducer (PE/FE) and substrate is given by:

$$R = \frac{(Z_2 - Z_1)}{(Z_2 + Z_1)} \tag{1.1}$$

$$T = \frac{2Z_2}{(Z_2 + Z_1)} \tag{1.2}$$

where  $Z_I$  and  $Z_2$  are the acoustic impedances of the PE/FE thin film and substrate, respectively. For FBARs and SMRs, the ideal case is to have R=1 and T=0 which is satisfied if only  $Z_I >> Z_2$  and hence all the acoustic waves are trapped in the PE/FE layer. To achieve the condition of  $Z_I >> Z_2$ , membrane suspended over air or Bragg reflectors are used; more recently a low acoustic impedance polymer layer was used as a substrate [45]. This results in FBARs and SMRs exhibiting high coupling coefficients, which is a crucial parameter in filter design. The Q factor of such resonators are, however, limited by the low material Q of PE/FE layer (<5000).

In order to achieve high Q factor resonator, as demonstrated by researches done in Westinghouse [53-57], instead of confining the acoustic energy inside the PE layer, the thin film PE transducer is used to generate the acoustic energy and it is trapped inside a very high Q substrate (low acoustic loss) with relatively higher thickness as compared to

thickness of the PE layer. So, in contrast to FBARs and SMRs, the HBAR is deliberately designed for acoustic energy to be transmitted and stored inside the substrate rather than in

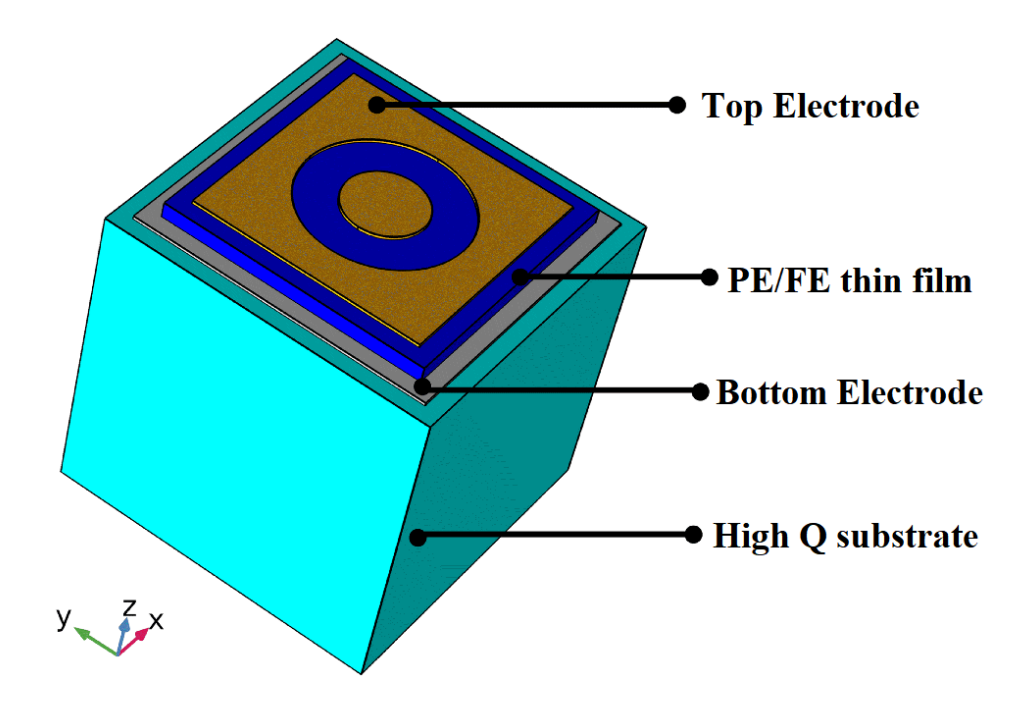


Figure 1.10. Schematic of HBAR; not to scale (practically the thickness of substrates is hundreds of microns and that of PE/FE just few microns).

the active PE/FE layer. Fig. 1.10 shows the basic schematic of an HBAR. The device can be considered as analogous to an FBAR mounted onto a low acoustic loss substrate acting as an acoustic resonant cavity. Structurally, the HBAR is similar to microwave delay lines in contrast to other acoustic resonators. HBAR is an acoustic device which parallels to the operation of an optical Fabry-Perot interferometer. The HBAR consists of two conjoined cavities, the transducer and the acoustic cavity, i.e., the substrate. The primary function of the transducer is to couple the energy produced by means of piezoelectricity (in PE thin films) or induced piezoelectricity from electrostriction (in FE thin films) into the low loss substrate. The transducer occupies a very small volume compared to the substrate in such resonator and hence, the Q factor of the device can ideally be the material Q of the substrate.

The acoustic modes are defined by the electrodes which couple to electric field by either piezoelectric effect (PE thin films) or induced piezoelectric effect (FE thin films). Upon excitation of the transducer by application of RF signal, longitudinal or thickness extension modes are created which travel through the whole resonator structure. The two interfaces of the substrate are polished to form parallel and reflecting surfaces for trapping the acoustic wave (energy) in it. Due to the configuration of the electrodes, the HBAR exhibits the thickness extension mode where expansion and contraction occur in the vertical direction, this in turn generates standing waves. The thickness expansion mode of an HBAR is shown in Fig. 1.11. HBAR exhibits a concentrated spectrum of resonances (multiple resonances). The PE/FE layer modulates the amplitudes of the overall frequency spectrum and hence strongly excited modes/resonances tend to occur where an acoustic half wavelength is equal to the thickness of the PE/FE thin film i.e.,  $f = v_p/2t_p$ , where  $v_p$  and  $t_p$  are the acoustic wave velocity and thickness of the PE/FE thin film, respectively. Therefore, the centre frequency of the resonant peaks/modes is a function of the PE/FE thin film. The resonator exhibits overtone resonances which occur at spans corresponding to all frequencies for which the parallel surface separation of the substrate is an integral multiple of the acoustic half wavelength. This overtone response is because of the standing acoustic wave propagating in the high Q substrate as reflections occur at the impedance mismatched boundary of solid-air of the resonator. Fig. 1.12. shows the frequency response of an HBAR made with BST thin film as the active transducer layer and sapphire as a substrate. The frequency spacing of adjacent modes depends on the thickness of the substrate and its acoustic velocity i.e.,  $f_{\scriptscriptstyle S}=v_{\scriptscriptstyle S}/2t_{\scriptscriptstyle S}$  , where  $v_{\scriptscriptstyle S}$  and  $t_{\scriptscriptstyle S}$  are the acoustic wave velocity and thickness of the substrate, respectively. Typical substrate thickness is around a few hundreds of microns and hence  $f_s$  is around a few tens of MHz. And since the thickness of

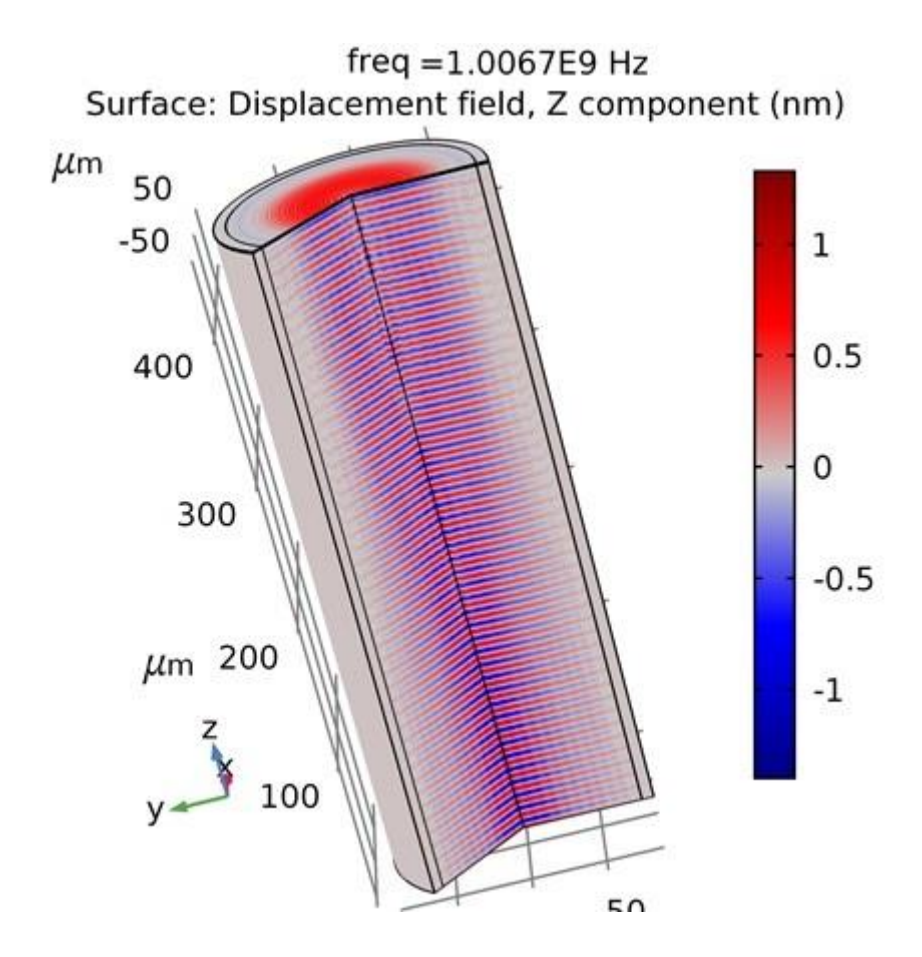


Figure 1.11. Thickness extensional mode of HBAR.

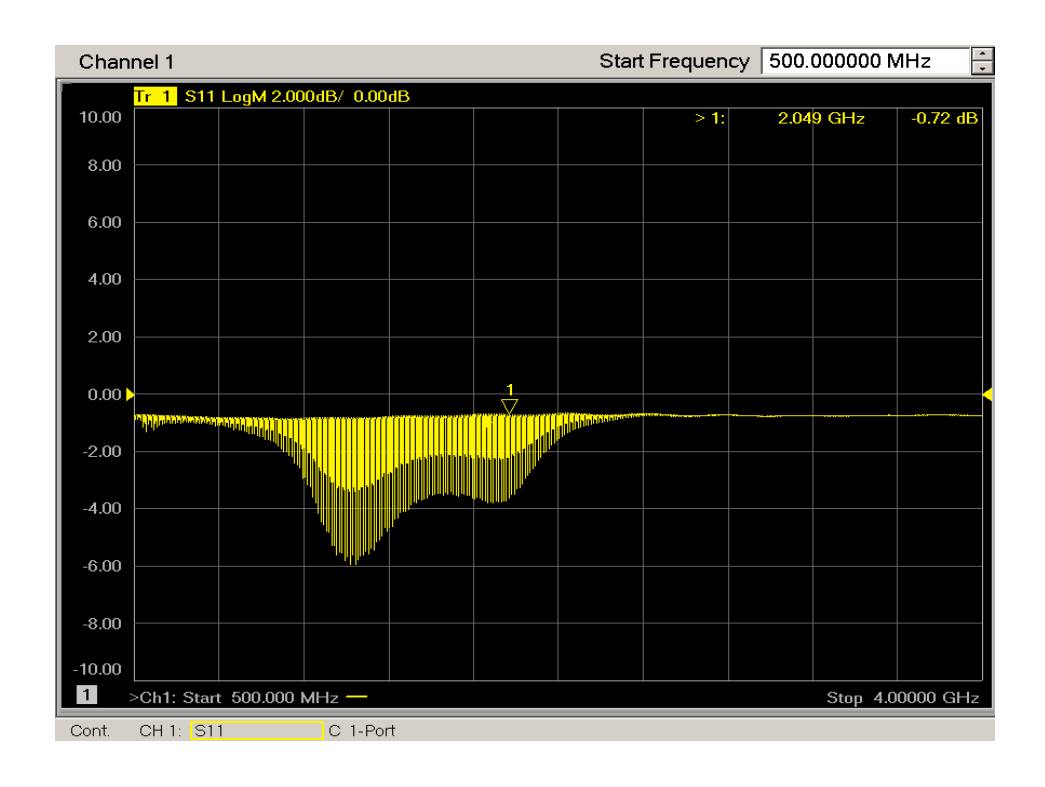


Figure 1.12. Frequency response of HBAR in measured  $S_{11}$  of the device.

PE/FE thin film is chosen to be generally around a micron, HBARs typically operates in the GHz frequency range [57,59-61].

The key advantages of HBAR due to its device configuration are:

- 1. High-order overtones can be coupled i.e., several hundreds of overtones can be utilized.
- 2. The option to choose high Q non-piezoelectric substrates.
- 3. Robustness of the device design.

Using high order overtones, the resonators can operate at microwave frequencies providing high Q factor equally (approx.) spaced modes in the operating band. The robustness in the design has made it possible to suppress almost two orders of magnitude in the device sensitivity. HBAR gives better physical rigidity and is less sensitive to vibration when compared to even high Q VHF quartz resonators [53].

### 1.4 Applications of high overtone bulk acoustic resonator (HBAR)

This section discusses various areas of applications where HBAR is employed. The applications are classified broadly as a) microwave sources b) material characterization c) sensor and d) quantum acoustics.

### 1.4.1 Microwave sources

HBAR fabricated on sapphire, spinel, silicon, LiTaO<sub>3</sub>, LiNbO<sub>3</sub> and ruby as substrates with ZnO and AlN as the transducers working in the frequency range of 1 to 10 GHz have been used as a frequency stabilization medium for applications in microwave sources (phase noise floor -135 to -165 dBc/Hz) and have been reported by groups from Westinghouse [52-57]. M.M. Driscoll et.al. reported an HBAR (with YAG as substrate and ZnO as transducer) which exhibited a Q of 80,000 at 640 MHz that was used as an element for frequency control in very low phase noise oscillators. The white noise floor level of the

oscillator output signal when driven at 16 dBm was -175 dBc/Hz [62]. Eva S. Ferre-Pikal et.al. reported in 2001 the use of an HBAR (at 2 GHz, Q-20,000 made on sapphire substrate with AlN as the transducer) in an oscillator which exhibited a phase modulation (PM) noise ranging from -39 to -47 dBc/Hz. This PM noise of the oscillator is approx. 30dB lower to commercially available VCO working in the same frequency range. The disadvantage with the HBAR based oscillator is the difficulty in selecting the closely packed resonant modes [63].

In 2009, Hongyu Yu et.al. reported the implementation of HBAR for designing and realizing two oscillators operating at 1.2 GHz (Colpitts oscillator) and 3.6 GHz (Pierce oscillator); circuit schematic of both the oscillators are shown in Fig.1.13. The Colpitts oscillator uses a 1.2 GHz HBAR with Q value of around 25,200. This oscillator consumes only 8 mW of DC power and the phase noise reported was -73 dBc/Hz at 300 Hz offset. The Pierce oscillator utilizes an HBAR operating at 3.6 GHz with Q of 19000. The power consumption of the oscillator was 3.2 mW and the reported phase noise is -67 dBc/Hz at

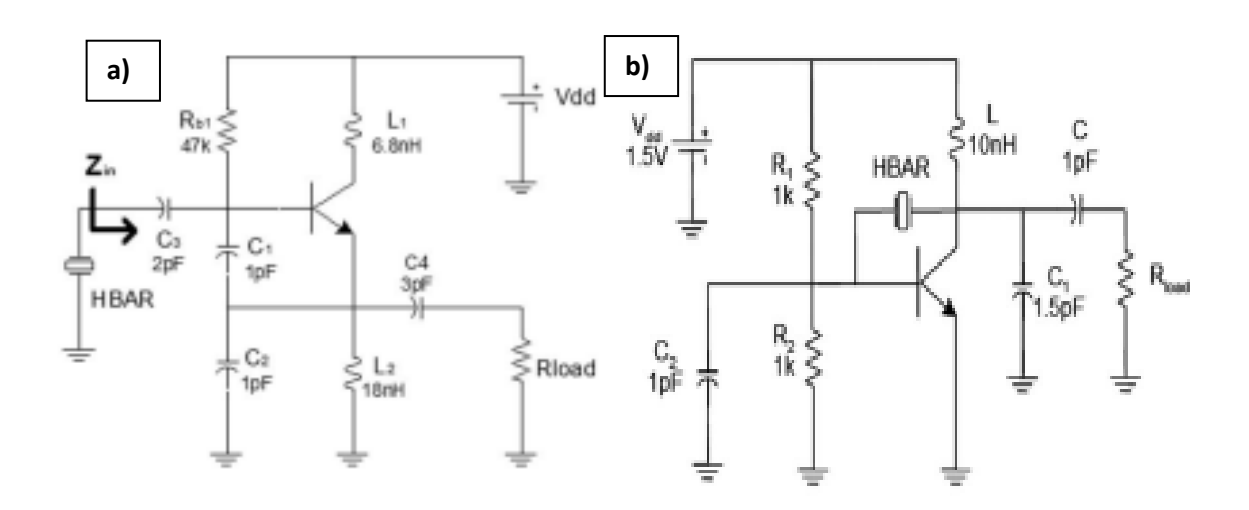


Figure 1.13. Schematic of HBAR implemented in a) 1.2 GHz Colpitts oscillator and b) 3.6 GHz Pierce oscillator [64].

300 Hz offset. The reported Allan deviation (free running) of the Pierce oscillator is 1.5 x 10<sup>-9</sup> at 1 second of integration time. From the measurement results and the fact that the size of the oscillator is small with lower power consumption, HBAR (instead of ceramic coaxial resonators or FBARs) can be used for integration in chip-scale atomic clocks (CSACs) [64]. Thomas Daugey et.al. presented in 2015 the strategy to design an oscillator (4.6 GHz) by using HBAR (2.3 GHz) for integration as a local oscillator for applications in coherent population trapping (CPT) of Cs vapor cell atomic clock [65]. In 2018, Mustafa Mert et. al., by taking advantage of recent advancements in spintronics which allows realization of CMOS compatible nanoscale tunable spin torque nano oscillators (STNO) operating in the GHz range, proposed a magneto acoustic spin Hall (MASH) oscillator wherein a three terminal magnetic tunnel junction (MTJ) and an HBAR are integrated on the same CMOS circuitry. In current and magnetic field feedback type of MASH oscillators, the voltage oscillations in the MTJ due to spin-orbit torque (SOT) are shaped by the response of the HBAR. Due to the availability of multiple resonant modes, the HBAR can be considered as having multiple bandpass filters which is used for reducing the linewidth of the STNO in open loop configuration. In case of strain feedback MASH oscillator, the HBAR serves as a stress generator. Fig.1.14 shows the MASH oscillator having a strain, current and magnetic field feedback line. The 3-port MTJ and 1-port (strain feedback type) or 2-port (current and magnetic field feedback type) HBAR are fabricated on opposite sides for strain feedback and on the same silicon substrate and is strain-coupled using magnetostriction effect for current and magnetic field feedback [66].

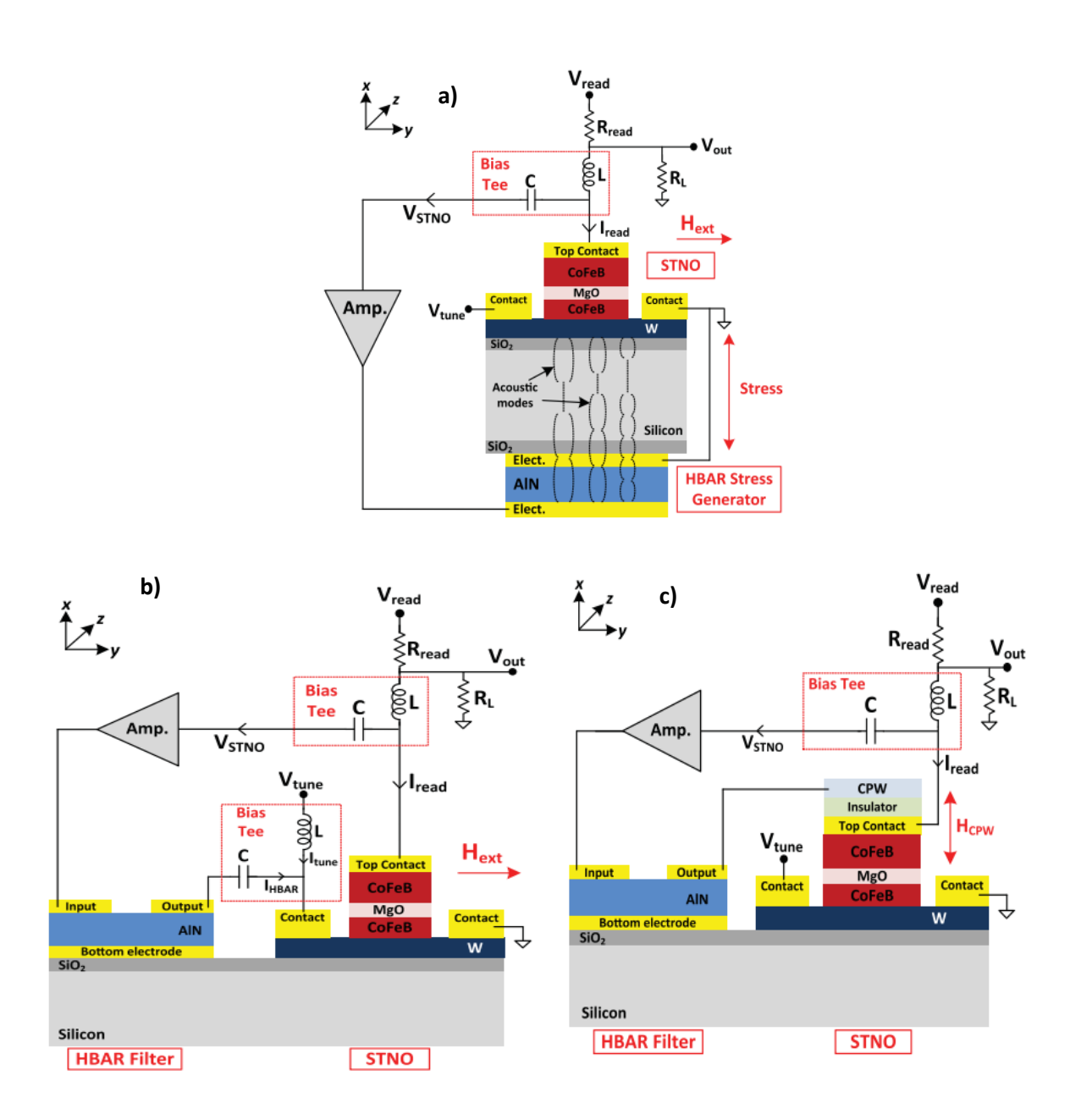


Figure 1.14. MASH oscillators with a) strain b) current and c) magnetic field feedback [66].

## 1.4.2 Quantum acoustics

A very interesting area of application where HBAR has emerged to hold huge potential is in quantum acoustodynamics (QAD). Quantum technologies primarily depend on the efficient interlinkage of a quantum state with either a probe or pump signal for applications in computing and sensing. For studying the fundamental physics, trapped ions or atoms which can exhibit quantum states are of primary focus but practical applications of the technology require other methods which are scalable. Hence, for practical applications, comprehensive work has been dedicated to cavity quantum electrodynamics (QED) which uses the coupling of qubits and microwave (or optical) photons confined in a resonant cavity [67]. To achieve strong coupling between photon and qubit which makes the decoherence lower, the qubit and the cavity should exhibit extremely low dissipation which are possible by using a high Q factor photonic cavity (e.g., Fabry-Perot cavity) for the case of optical photons and a super conducting transmission line-based cavity resonator in case of microwave photons.

Cavity quantum acoustodynamics (QAD or QA) has the same approach as that of photonic cavities but utilizes the coupling between qubits and phonons instead of photons. This approach gives a crucial advantage of enabling the quantum states or information to be retained for a significantly longer duration (due to phonons having slower wave velocity than photons by a factor of around 10<sup>5</sup>) under the condition that the cavity exhibits high Q. The implementation of micron sized acoustic transducer as a source of phonons and cavities has made the possibility of chip-scale fabrication and electrical control systems which has reduced the footprint, power consumption and complexity when compared with macroscale phonon sources like optomechanically transduced quartz resonators [68]. The use of SAW, BAW and flexural beam as phonon sources in QAD have been reported in [59,69-73].

The first use of HBAR for application in quantum spin control was reported by E.R. MacQuarrie et.al. in 2013 at Cornell University [73]. Their group achieved the direct coupling between phonons and diamond nitrogen-vacancy (NV) spins by utilizing the driving spin transitions with mechanically transduced harmonic strains (at room temperature). The device is composed of two sections a) a loop antenna for generating GHz frequency range magnetic fields for acting as magnetic control and b) an HBAR which generates multiple modes (stress standing waves inside a diamond substrate) in GHz frequency range. The ability to manipulate spin-phonon interaction finds applications in NV-based metrology. A schematic of the device is shown in Fig. 1.15. The same group reported the use of HBAR to drive the Rabi oscillations of a NV centre spin unit mechanically [74,75]. Ywien Chu et.al from Yale University reported in 2017 the use of HBAR in a three-dimensional (3D) transmon architecture for achieving strong coupling between a superconducting qubit and the phonon modes (generated by HBAR) to a cooperativity value of 260 which is comparable to that achieved by QED devices [71]. Instead of using 3D transmon architecture as reported in [75], Mikael Kervinen et.al. from Aalto University utilizes an HBAR made on GaN/Si wafer [59]. GaN being a widebandgap-semiconductor was chosen as the transducer material because of the potential it holds for applications in optoelectronics and high-power and high-speed electronics. They were able to fabricate and characterize the device as a simple on-chip design. Fig. 1.16 shows the schematic of the device realized in [59]. Vikrant J. Gokhale et.al. from the US Naval Research Laboratory reported in 2020 the use of an epitaxial-HBAR for QAD. Using molecular beam epitaxy (MBE), the bottom electrode, i.e., Niobium nitride (NbN) and the transducer material GaN are realized on a SiC substrate [76]. The reported FQ (frequency and Q factor) product is  $1.36 \times 10^{17}$  Hz and the lifetimes of phonons are  $500 \mu s$ .

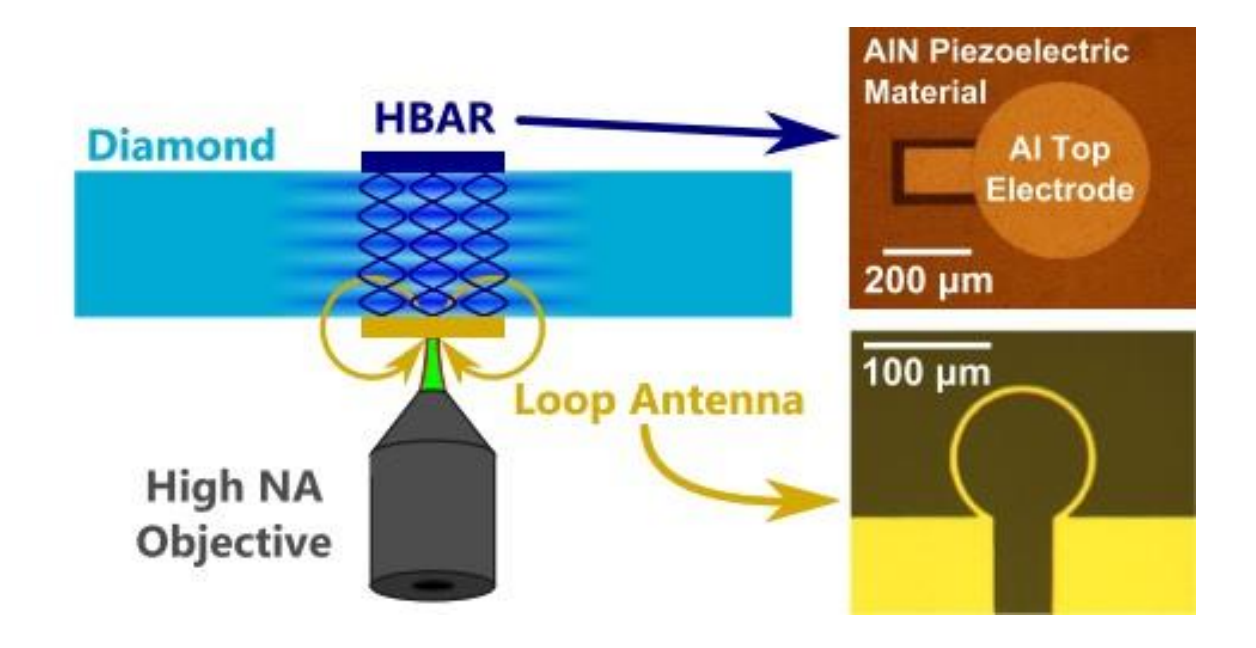


Figure 1.15. Device schematic to achieve direct coupling of phonons and diamond NV centre spins [73] ;(NA – Numerical aperture).

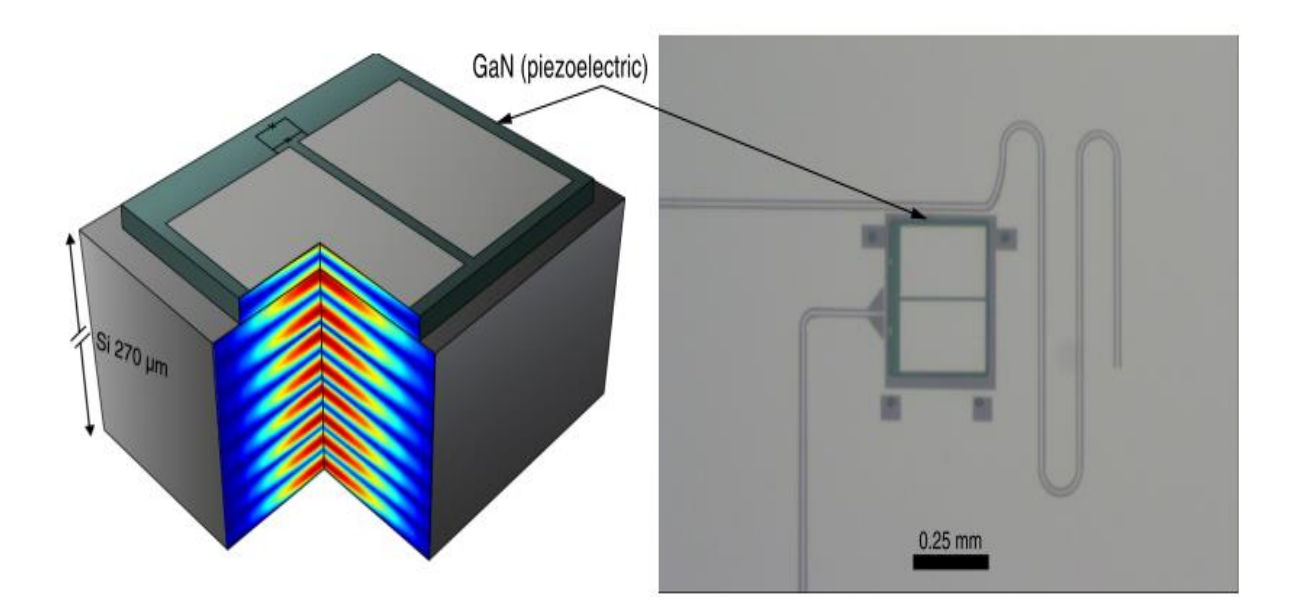


Figure 1.16. Schematic of on-chip realization of HBAR, a split Josephson junction transmon qubit and microwave CPW cavity [59].

### 1.4.3 Sensors

The use of HBAR as mass sensors in liquids has been reported by Hao Zhang et. al. [77], where mass sensitivity of the HBAR is 9.3 cm<sup>2</sup>/g. The minimum detectable mass (liquid) for the HBAR is derived as 11.9 ng/cm<sup>2</sup> from the mass sensitivity and noise floor. The HBAR has the edge over single-crystal QCM since the size of HBAR is significantly smaller.

## 1.4.4 Material characterization

The heart of devices discussed in the previous sections like SAW, FBAR, SMR etc. is the transducer but in HBAR it is both the transducer and the substrate. New requirements for acoustic devices for applications in communication systems, sensing, or quantum systems demand specific functionality which only new multifunctional materials can deliver [76,78-80]. Characterization of these new multifunctional materials are a must to get optimal result for applications in MEMS or in QAD technology. Piezoelectric thin films (AIN, ZnO etc.) have been studied for a long time due to its excellent coupling coefficient with reasonably good Q factor. They are extensively used in designing RF MEMS particularly FBAR, SMR etc. which in turn are employed as components in filters and oscillators. Due to the demand for more information exchange by mobile devices, to make the architecture more compact, functional materials, i.e., ferroelectric thin films like Barium Strontium Titanate (BST), Strontium Titanate (STO) etc. were introduced which take advantage of the induced piezoelectricity (due to strong electrostriction) from which tunable and switchable FBAR and SMR can be made [81].

The methods used for characterizing the mechanical properties of piezoelectric thin films have been classified as a) direct measurement and b) indirect measurement. Direct measurement methods directly probe the stress produced (mechanical wave) upon

application of electric field or charge accumulated under applied load, the information from which the piezoelectric coefficient can be calculated. Some examples of direct measurement techniques are normal load method, periodic compressional force, cantilever method, Pneumatic pressure rig, optical interferometry etc [82].

Indirect measurements are based on studying the resonance response of usually a device with PE/FE thin films bounded by top and bottom electrodes made on a thick substrate. Such techniques are used for characterizing the elastic properties of a PE/FE thin film. Characterization of PE/FE thin film by employing SAW or BAW devices is a good example of indirect method [82]. Composite resonators (HBAR configuration) have extensively been used for characterizing piezoelectric and ferroelectric thin films. Indirect methods like the *Resonant Spectrum Method* (RSM) takes advantage of the spectral information of an HBAR to extract the mechanical properties of thin film PE/FE [83,84]. The various work reported by different groups in characterization of materials (material under test (MUT)) by using the composite resonator or HBAR configuration is given in Table 1.1.

Table 1.1. Literature review of material characterization using composite resonator/HBAR.

		1677	Acoustic		Year
S.no.	Brief description	MUT	properties	Application	&
		Characterized	Characterized		Reference
1	$SiO_2$ thin film was sputter deposited on the backside of the HBAR (ZnO/Sapphire) for matching acoustic impedance of solid/liquid interface.	${ m SiO_2}$	Transmission loss in HBAR after deposition of SiO <sub>2</sub>	SiO <sub>2</sub> acts as acoustic antireflective coating for acoustic microscopy	1980 [85]
2	Uses pulse mode measurement technique where reflection loss in the composite resonator (considered as an acoustic transmission line).	Quartz film, borosilicate glass films, $As_2S_3$ and $As_2Se_3$	Acoustic impedance, mass density, elastic constant and acoustic velocity	Acoustic Spectroscopy	1982 [86]
3	Uses the echo pulse method in the frequency domain instead of time for a composite resonator having configuration of ZnO/YAG/MUT.	Langmuir- Blodgette films	Acoustic wave attenuation and acoustic velocity	Acoustic  Spectroscopy	1994[ 87]
4	Employ the Butterworth  Van Dyke (BVD) model  for characterization of a  single mask HBAR.	AlN	Electromechani  cal coupling  coefficient $(k_t^2)$	Acoustic  Spectroscopy	1998 [88]
5	Introduced the theoretical methodology for using	Simulated material	Density and acoustic velocity	Acoustic Spectroscopy	1998 [89]

	the modal frequency		of both	for PE films	
	spacing (MFS), i.e., the		piezoelectric	applied as	
	spacing between adjacent		thin film and	actuators, filters	
	resonant modes.		substrate	and sensors	
6	Utilizes the resonant	Simulated	Density,	Acoustic	1998 [90]
	spectra of the HBAR to	material	acoustic velocity	Spectroscopy	
	establish a theoretical		and $k_t^2$		
	method for				
	characterization of PE				
	thin films				
7	Experimentally	ZnO	Density, elastic	Acoustic	1999 [91]
	demonstrated the use of a		constant,	spectroscopy	
	HBAR (ZnO/Fused		acoustic velocity		
	quartz) for		and $k_t^2$		
	characterization of ZnO				
	thin film using the				
	frequency spectra.				
8	Numerical simulation of a	Simulated PZT	$k_t^2$	Acoustic	1999 [92]
	PZT film/ stainless steel			spectroscopy	
	HBAR from which the $k_t^2$				
	is determined from the				
	distribution of effective				
	coupling coefficient				
	$(k_{eff}^2)$				
9	Evaluation of thin film	SiO <sub>2</sub> , TiO <sub>2</sub> , Al <sub>2</sub> O <sub>3</sub>	Density, elastic	Acoustic	2000[93]
	deposited on a	and ZnO	constant and	spectroscopy	
	piezoelectric transducer		acoustic velocity		
	(Z-cut LiTaO <sub>3</sub> ).				

10	Numerical simulation of	Simulated	$k_t^2$	Acoustic	2000[94]
	HBAR for PE thin film	material		spectroscopy	
	characterization with				
	consideration for the				
	effects of electrodes in				
	the configuration.				
11	A deviation from [92] by	Simulated	$k_t^2$	Acoustic	2001 [95]
	which instead of using the	material		spectroscopy	
	modal distribution of all				
	the resonant modes, two				
	special modes were				
	selected. The thickness of				
	the transducer film				
	doesn't play a significant				
	role and hence useful				
	when determining the				
	thin film thickness is				
	difficult.				
12	Resonant Spectrum	ZnO	Density, elastic	The material	2003 [83]
	Method (RSM) which is		constant,	data can be used	
	based on the distribution		acoustic velocity	for filter or	
	of spacing of parallel		and $k_t^2$	sensor design	
	resonance frequencies				
	(SPRF) and the effective				
	coupling coefficient				
	$(k_{eff}^2)$ to determine				
	experimentally the elastic				
	properties of ZnO thin				
	film				
	film				

13	Numerical simulation of	ZnO, AlN, SPZT	Density, elastic	Acoustic	2005 [96]
	HBAR models. The	(simulated	constant,	spectroscopy,	
	effects of electrode on the	material)	acoustic velocity	RSM	
	resonance spectra are		and $k_t^2$		
	studied.				
14	Studied the acoustic	Sapphire, quartz,	Temperature	Acoustic	2006 [97]
	absorption variation with	fused silica and	coefficients of	spectroscopy	
	temperature for various	silicon	both frequency		
	substrates used in HBAR		and acoustic		
			velocity		
15	Characterization of	SU-8, SU-8 based	Attenuation and	BioMEMS	2009 [98]
	acoustic properties in	nanocomposites	acoustic velocity		
	time domain as matching	and SiO <sub>2</sub>			
	layer for lab-on-chip				
	applications.				
16	A Novel technique for	AIN	$k_t^2$	Acoustic	2012 [99]
	extracting the $k_t^2$ from the			spectroscopy	
	input impedance of the				
	HBAR.				
17	A theoretical method of	Simulated	SPRF and	Non-destructive	2012 [100]
	using the variation in	material	thickness	evaluation	
	SPRF of an HBAR as a			(NDE)	
	means to probe thickness				
	variation of the substrate				
	(elastic plate).				
18	Experimental study of	ZnO, Fused silica	SPRF and	Acoustic	2015 [101]
	effects of electrodes and	and sapphire	$k_t^2$	spectroscopy	
	substrates on the				
	parameters of HBAR.				
<u> </u>	<u> </u>				

19	RSM is used to study the	BST	Density, elastic	Acoustic	2017 [84] *
	acoustic properties of		constant,	spectroscopy,	
	paraelectric-state		acoustic velocity	RSM	
	ferroelectric thin film.		and $k_t^2$		
	The dependence of				
	$k_t^2$ on the DC bias voltage				
	is also reported.				
20	The use of XRD to	AlN and ScAlN	$k_t^2$	Material	2019 [102]
	estimate the $k_t^2$ of thin			characterization	
	films using its lattice				
	strain information				
	obtained under an applied				
	electric field.				
21	A new method by using	AlN and ScAlN	Material Q	Acoustic	2019 [103]
	the FWHM of the			spectroscopy	
	impedance (real) is				
	introduced to evaluate the				
	mechanical Q of the PE				
	thin film. The Q is				
	extracted by analysing the				
	material Q of the				
	substrate and Q factor				
	exhibited by the HBAR.				
22	Investigates the effects on	SU-8	Material Q	Acoustic	2020 [104] *
	the parameters of HBAR			spectroscopy,	
	when a polymer layer			RSM	
	with low material Q is				
	introduced. A novel				
	method to extract the				
	material Q of SU-8 or				
	<u> </u>				

other polymer composites		
achieved by analysis		
using experimental,		
numerical simulation and		
FEM simulation.		

<sup>\*</sup> Work reported in this thesis

## 1.5 Choice of transducer materials for BAW

As discussed in Sec.1.4, HBAR occupies a prominent place in the present demanding and expanding areas of applications like quantum acoustodynamics (QAD) and microwave sources. HBAR, due to its attributes such as exhibiting high Q factor, is the perfect candidate for generating multiple high Q equally spaced modes which is the primary requisite for designing QAD and some of the microwave sources. Further advancement of QAD and microwave sources requires materials with multifunctionalities. The use of HBAR as a means of acoustic spectroscopy is another interesting area which has pushed HBAR designers to further make optimization using new materials and techniques to achieve extremely high Q and which works at a much higher frequency. Paraelectric thin film BST based HBAR has the advantage of possessing multiple modes exhibiting high Q factor of which the spacing between two modes and the Q factor can be controlled by the thickness and material Q of the substrate and has the capability for getting switched on and off controlled by a DC field. The acoustic velocity and thickness of the thin film BST decides the frequency regime of the resonator and makes the Q factor to be controlled by a DC field. Using substrate which possesses extremely high material Q like diamond would be an interesting choice for the BST based HBAR for future study. The Q factor achieved by HBAR using conventional piezoelectric thin film (ZnO or AlN) as transducer is fixed,

but by using ferroelectric thin films it is possible to change the Q factor of the resonator by increasing the DC bias voltage applied.

# 1.5.1 Ferroelectric thin films as transducer materials

The demand for smart devices has led to the development of smart materials which links various cause-effect relations to give multifunctionality and adaptability to the devices being developed. Fig.1.17 shows an important chart [105] of the various relations between the input (i.e., electric and magnetic field, stress etc.) and output (i.e., charge/current, magnetization, strain etc.) in a material. The off-diagonal couplings in the chart shown in Fig. 1.17 is interesting to study because it covers areas like sensing and actuation of signals. Ferroelectric materials fall under the class of materials exhibiting numerous effects.

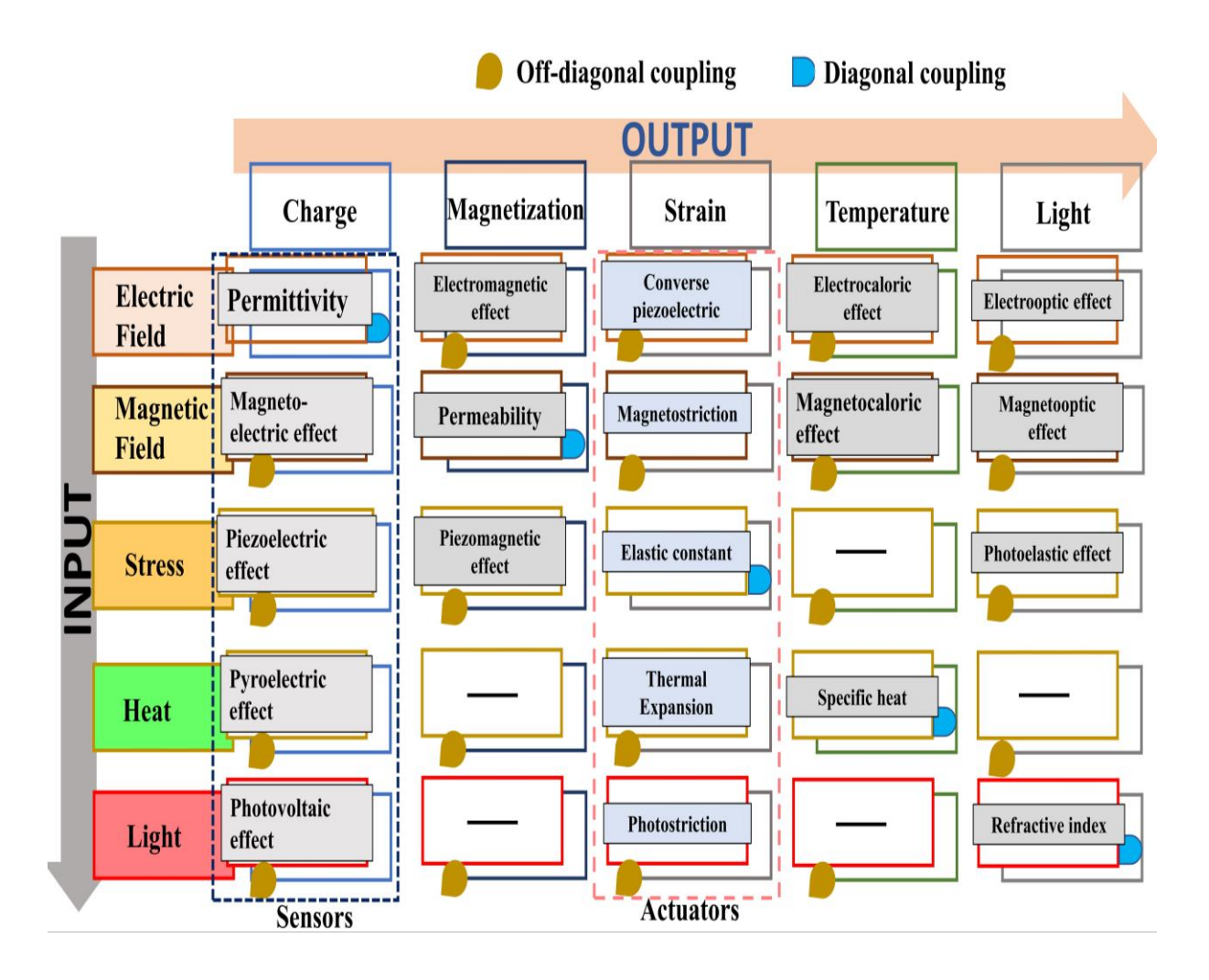


Figure 1.17. Relation between input and output in a material system [105].

## 1.5.1.1 Field-Induced Strain

In ceramics, even though they are mechanically hard, they do undergo deformations i.e., strains are produced due to change in parameters like temperature and stress (called thermal expansion for the case of application of heat and elastic deformations because of stress). Such deformations can also be excited by means of applying an external electric field to the material and is called the electric field-induced strain. This property of ceramic materials is called *electrostriction*. It is similar to converse piezoelectric effect, however, in case of electrostriction, the proportionality of electromecahnical coupling to the applied field is secondary rather than being primary as in the case of converse piezoelectric effect. To understand the mechanism of electric field-induced strain hence forth called as induced piezoelectricity, a simple ionic crystal is considered. Fig.1.18 shows the 1-D spring model of the crystal lattice showing two cases, i.e., the non-centrosymmetric (a) and centrosymmetric (b). The springs in Fig.1.18a which joins the ions are different depending

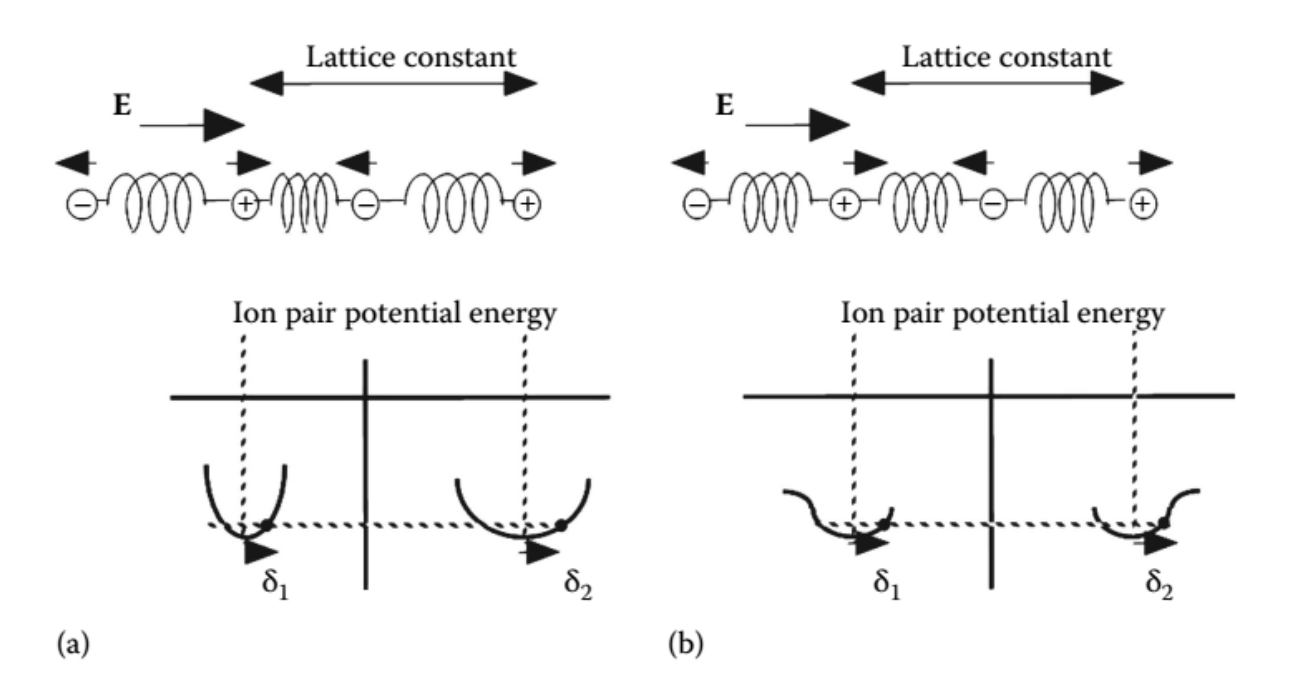


Figure 1.18. 1-D rigid-ion spring models of a) piezoelectric and b) field induced strain [105].

on the ionic distances; hence both hard and soft springs exist alternately in such crystal lattice. The spring in Fig.1.18b joining the ions are the same. An applied electric field in the non-centrosymmetric case (Fig.1.18a) excites the movement of cations in the direction of the field applied and the anions in the counter direction which changes the relative interionic distance. Along the direction of the electric field, expansions and contractions of the softer spring are more than that of the hard springs which causes the strain (=x is a change with respect to one-unit length) to compensate the applied external electric field E. This phenomenon is called the converse piezoelectric effect and can be formulated as x =dE, where the piezoelectric constant (d) is the proportionality constant. But for centrosymmetric system (Fig.1.18b), the expansions and contractions of the spring is almost the same and the distance between the two cations stay the same, and hence no strain is generated. The springs in this case have anharmonicity making it easier to extend than to contract. This minute differences in net displacement can cause changes in lattice parameters which generates strains that are not influenced by the direction of the electric field applied which makes the strain an even function of the field. This phenomenon is called as the electrostrictive effect and is formulated as  $x = ME^2$ , where M is the proportionality constant known as electrostrictive constant.

# **1.5.1.2** Barium strontium titanate (BST)

"Regular dielectrics" whose permittivity is around few tens or lower have two distinct characteristics of being weakly dependent on temperature and having weak dielectric non linearity which is important for getting tunability of the permittivity. However, ferroelectrics exhibits exceptionally high permittivity which has a strong temperature dependence and a considerable dielectric nonlinearity. Ferroelectrics are therefore a sought-after material for designing agile components. Dielectric polarization in ferroelectrics due to an applied external source (electric field, stress or temperature changes) makes it suitable

# **FERROELECTRICS**

# MULTIFUNCTIONALITIES PROPERTIES

- Ferroelectric in polar phase Switching of spontaneous polarization
- Antiferroelectric materials Antiparallel dipoles moments
- Ferroelastic materials Stable and switchable spontaneous deformation
- Piezoelectric materials-Polarization is a linear function of stress
- Electrostriction phenomenon-Variation of strain as a quadratic function of electric field
- Multiferroic materials- Having combined properties of both ferroelectric and ferromagnetic

#### **APPLICATIONS**

- Acoustic wave devices SAW, FBAR, tunable FBAR, filers/ tunable filters, Switchable HBAR
- Passive components High density capacitors, low impedance transmission line and dielectric spacer (MEMS switches)
- Lumped components resistors, inductors and distributed varactors
- Tunable microwave systems-Tunable delay line, phase shifters, matching networks, VCOs, power amplifier etc.

Figure 1.19. The multifunctionality of ferroelectric materials [106].

for various applications. The multifunctionality of properties displayed by ferroelectrics and corresponding applications are illustrated in Fig.1.19 [106].

Among the ferroelectric materials, BST is a very good example for materials which exhibit multifunctionality due to its typical behaviour of having high dielectric constant ( $\varepsilon_r$ > 100) and having significant nonlinearity. The Curie temperature ( $T_c$ ) of BST decides whether it is in the ferroelectric phase or the paraelectric phase. Fig.1.20 shows the dependence of BST on temperature. Ba<sub>x</sub>Sr<sub>1-x</sub>TiO<sub>3</sub> (BST) is a solid solution of barium titanate (BTO) and strontium titanate (STO); x specifies the mole fraction of Ba.  $T_c$  of bulk BST can simply be engineered by changing the concentration of Sr in the compound. The  $T_c$  of BTO is 130°C and thus stays in the ferroelectric phase at room temperature on the other hand STO is an incipient ferroelectric material with  $T_c$  as low as absolute zero thereby staying at

paraelectric phase in room temperature. The significance of STO is that it inherently exhibits high permittivity and hence, in BST the permittivity remains high even with the change of the ratio of Ba to Sr while the  $T_c$  decreases (3.8°C per molar percent Sr) linearly with increasing amount of Sr. The temperature dependent nature of permittivity in BST with various concentrations is shown in Fig. 1.21.[20,106-108]

BST which is a complex metal oxide ferroelectric has the perovskite unit-cell structure categorized under  $ABO_3$  compounds (A – alkaline earth or larger lanthanide and B – transition metal or smaller lanthanide). In BST, the Ba and Sr occupy the A site and Ti occupy the B site. As seen from Fig.1.21, the permittivity of BST near the transition temperature undergoes a sharp increase represented by the Curie-Weiss law. Above the phase transition temperature (paraelectric phase), the crystal has a cubic structure and below the phase transition temperature (ferroelectric (polar) phase) it is non-cubic. The crystal structures of BST at both paraelectric and ferroelectric phases are shown in Fig.1.22. In the crystal structure of BST, the Ti atom at the centre is inside an octahedral cage made by the oxygen ions which is relatively bigger than Ti atoms [106-108].

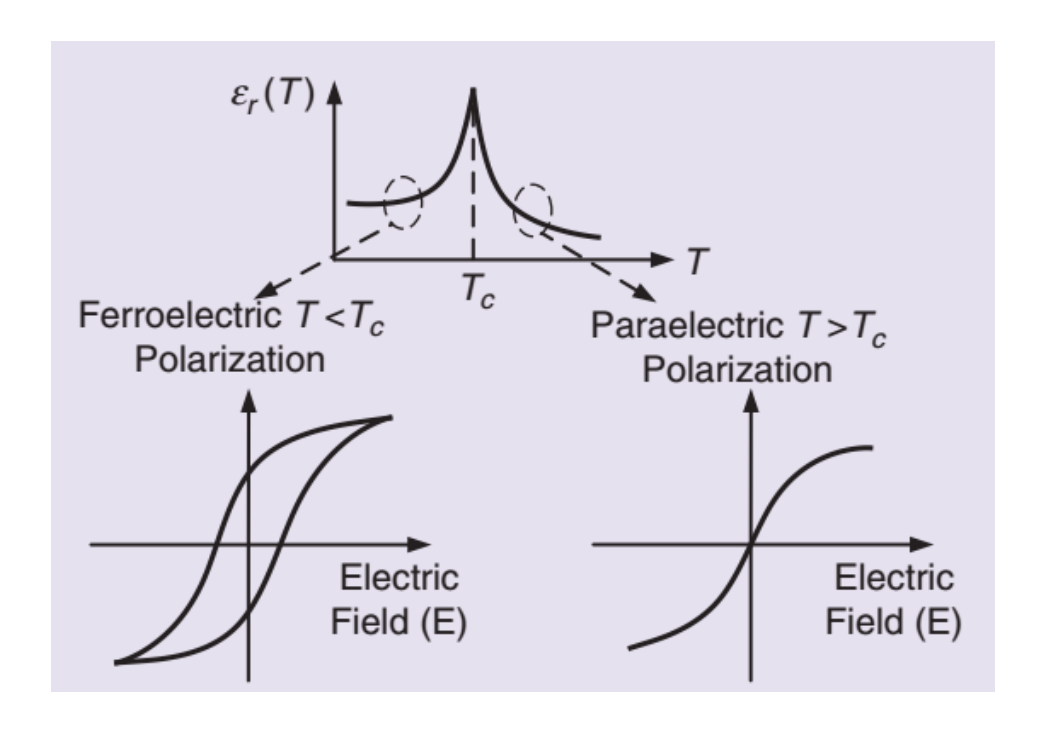


Figure 1.20. BST is in ferro or paraelectric phase depending on the temperature relative to  $T_c$  [107].

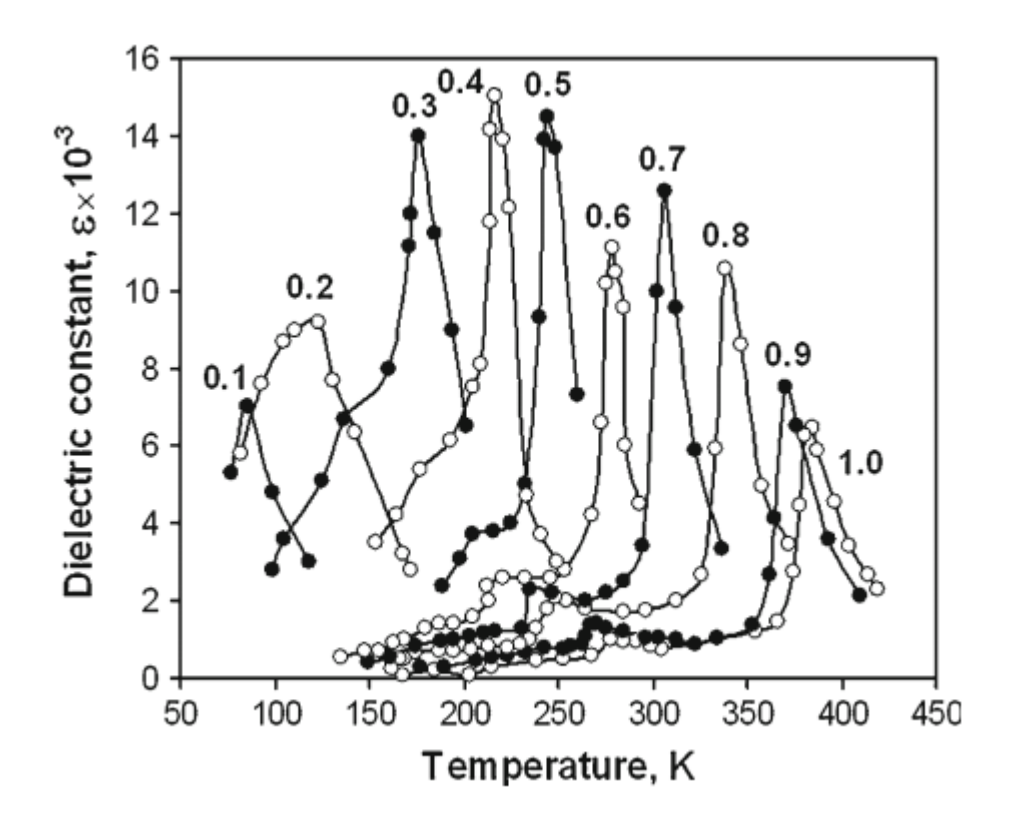


Figure 1.21. Permittivity vs temperature for different concentrations of BST; Ba conc.is given as a number [20].

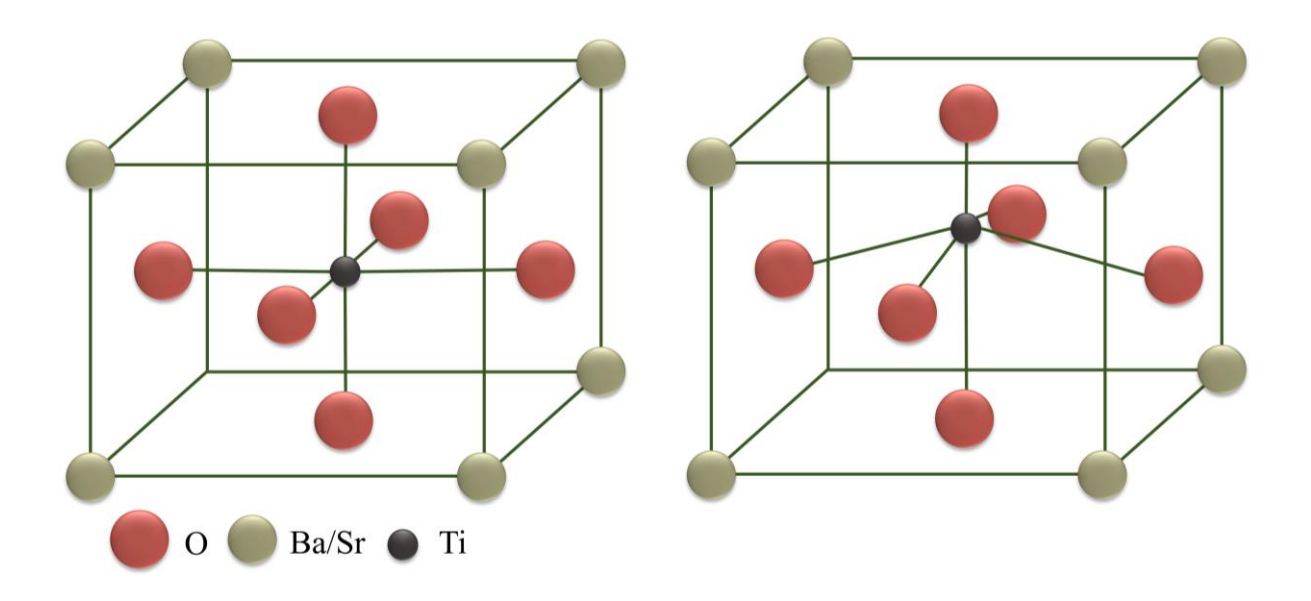


Figure 1.22. Unit cell of BST in paraelectric phase (left) and ferroelectric phase (right).

# The paraelectric phase of thin film ferroelectric BST

BST in its paraelectric phase takes advantage of the displaceability of the Ti ion by application of a quasi-static electric field inducing a large dipole moment or polarization, making BST possess a high dielectric permittivity which at low temperature is enhanced due to the long-range ordering effects. The polarization starts to saturate at high fields thereby reducing the effective dielectric permittivity. Dielectric permittivity as high as 20,000 can be achieved with BST material. In its bulk state, i.e., single crystals or ceramic powder, it shows strong temperature dependence of the dielectric permittivity exhibiting a sharp peak at its  $T_c$ . But in its thin film state, the permittivity has lesser temperature dependence. The dielectric permittivity of both bulk and thin film samples as a function of temperature for Ba<sub>0.7</sub>Sr<sub>0.3</sub>TiO<sub>3</sub> is shown in Fig.1.23 [109].

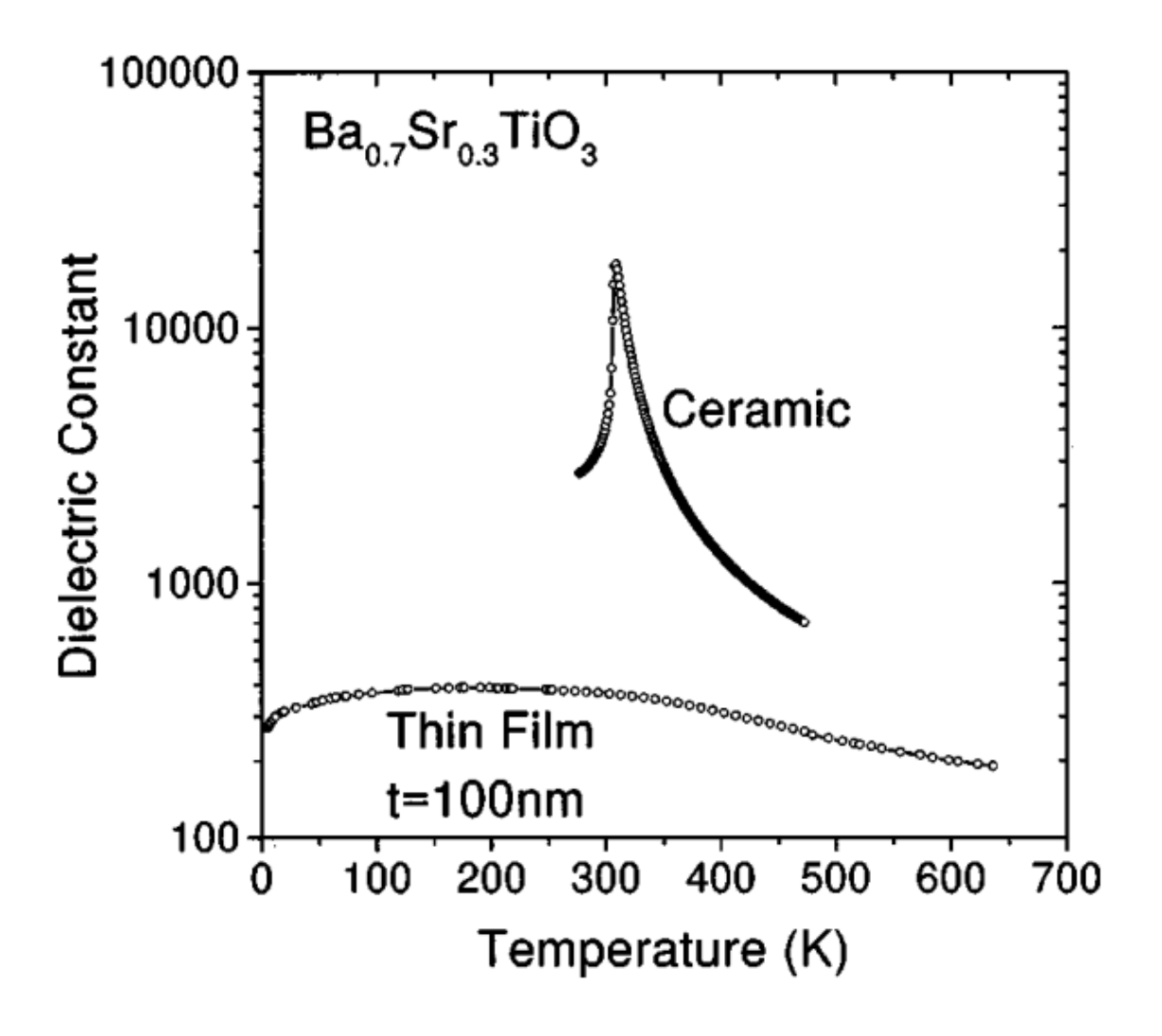


Figure 1.23. Dielectric constant as a function of temperature for Ba<sub>0.7</sub>Sr<sub>0.3</sub>TiO<sub>3</sub> [109].

As seen in the above Fig.1.23, the dielectric constant of thin film is much lower than that of its bulk counterpart. The three causes for this reduction of permittivity in thin films are a) fine grains b) interfacial capacitance and c) residual stress [109].

- a) Fine grains The permittivity of bulk ferroelectric materials is affected by the grain size but for thin films, the grain size is less significant since the grains are columnar wherein all the grain boundaries and grains are in parallel. The effect of fine grains is less understood for BST thin films.
- b) Interfacial capacitance –A "dead" layer is present which is of few lattice constant thickness due to suppression of the ionic contribution to the dielectric response around

- the two film-electrode interfaces. Due to this, when a voltage is applied across the capacitor structure, the voltage drops across the interfaces and the bulk of the film.
- c) Residual stress For paraelectric phase, high dielectric constant thin films which are grown on substrates, the tensile residual stress and the permittivity of the unstressed film are high and hence, the relation between stress and change of permittivity is significant.

Most applications which include microwave devices like resonators, filters, oscillators etc., use in both consumer electronics and research, are made to function at room temperature. As discussed earlier, BST thin films can be operated at room temperature in their paraelectric phase. This gives BST thin films the property of having a very high tunability and low dielectric loss in the microwave frequency range. It is interesting to note that BST can also be piezoelectric in its polar phase but due to domain wall motion which causes mechanical damping, dielectric losses are high at microwave frequencies. The factors in BST thin films contributing to the dielectric loss is shown in Fig.1.24 [108,110].

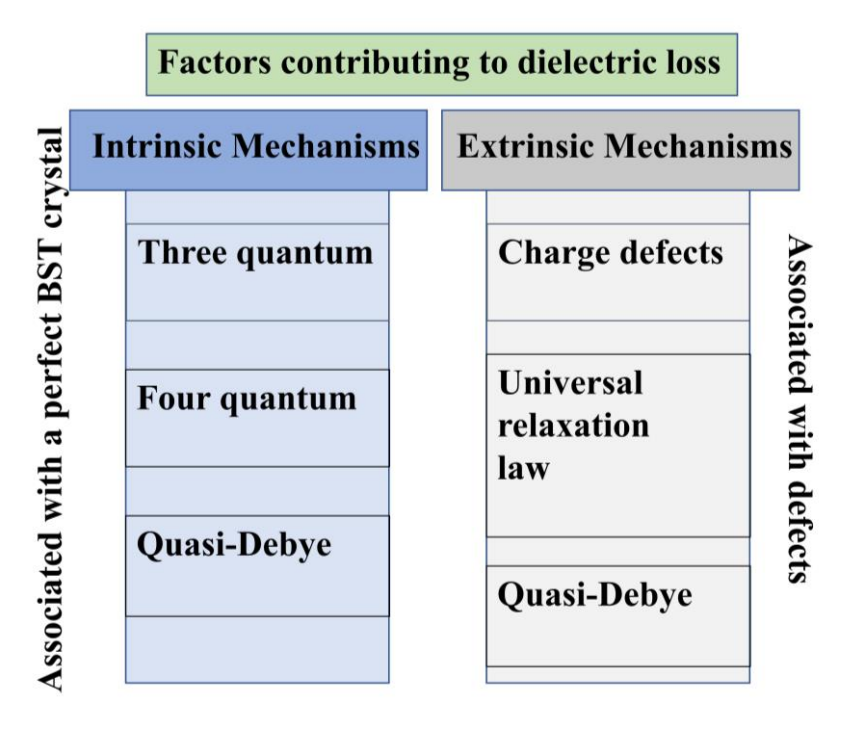


Figure 1.24. Mechanisms contributing to dielectric loss in BST [110].

In conventional PE thin films like ZnO and AlN, the electric and the acoustic fields have a linear relationship (small signal domain) while in ferroelectrics like BST thin films in its paraelectric phase (centrosymmetric structure), the induced strain (u) and polarization (P) are related by the electrostriction coefficient as [107]

$$u = QP^2 \tag{1.3}$$

The electric polarization due to the applied electric field E is expressed as

$$P = P_S + \chi E \tag{1.4}$$

where, Q is the electrostriction coefficient,  $P_S$  is the spontaneous polarization and  $\chi$  is the susceptibility of material. Putting (1.4) in (1.3) gives

$$u = QP_S^2 + (2QP_S\chi + Q\chi^2 E)E$$
 (1.5)

From equation (1.5) it is clear that in BST film on paraelectric phase, since there is no spontaneous polarization, the first term becomes zero. The two terms  $2QP_S\chi$  and  $Q\chi^2E$  are the effective piezoelectric coefficient of BST. The term  $2QP_S\chi$  is constant while the term  $Q\chi^2E$  is an electric field dependent term. This is why electrostriction can be called as induced piezoelectricity [107]. The transduction of electrical to acoustic energy and vice versa happens in BST (paraelectric phase) because of the strong electrostriction in BST which facilitates the electric field induced piezoelectricity. This unique property of BST is the reason why it has been chosen for applications in designing switchable and tunable acoustic wave devices. The frequency tunability as well as its DC bias dependence nature are discussed in details in Chapter 3. The various techniques available for growing BST thin films with their respective pros and cons are given in Fig.1.25 [108].

<b>Growth Technique</b>	Advantages	Limitations	
<ul><li>Solution</li><li>Sol-Gel and</li><li>Chemical</li><li>solution deposition</li></ul>	<ul><li>Inexpensive</li><li>Rapid turnaround and sampling</li></ul>	<ul> <li>Phase control</li> <li>Composition control</li> <li>Morphology</li> <li>Reproducibility</li> <li>Scalability</li> </ul>	
(CSD)  Energetic  • Sputtering	<ul><li> Uniformity</li><li> Scalability</li><li> Low thermal budget</li></ul>	<ul><li>Point defect conc.</li><li>Composition control</li><li>High residual stress</li></ul>	
<ul> <li>Pulsed Laser Deposition (PLD)</li> </ul>	<ul> <li>Rapid sampling</li> <li>Quick production of new materials</li> </ul>	<ul> <li>Poor conformality</li> <li>Morphology</li> <li>High residual stress</li> <li>Scalability</li> <li>Uniformity</li> </ul>	
Vapour MOCVD	<ul><li> Uniformity</li><li> Scalability</li><li> Morphology</li><li> Low thermal budget</li></ul>	<ul><li>Expensive</li><li>Precursor availability</li><li>Precursor stability</li></ul>	

Figure 1.25 Various techniques available for BST thin film deposition/growth [108].

## 1.6 Motivation and Goal of the Thesis

From the detailed literature review and accomplishments of the high overtone bulk acoustic resonator (HBAR), the application or the targeted applications using HBAR are diverse like microwave source, quantum acoustodynamics (QAD), acoustic spectroscopy, sensing etc. The focus for transducer materials in such applications have been mainly on piezoelectric thin film. The use of ferroelectric thin films in tunable FBARs and SMRs have been studied well for their application in communication systems. The use of ferroelectric thin film instead of piezoelectric ones in HBAR makes the characteristics of the resonator inherently dependent on an external DC electric field which can control important parameters such as the Q factor and the coupling coefficient. Using such HBARs for the applications mentioned above (i.e., QAD, microwave sources etc.), shows great potential for further improving the various functionality of the devices. Some aspects which need to be stressed with regards to HBAR based on ferroelectric (paraelectric) thin films when it comes to applications such as in microwave sources, QAD, acoustic spectroscopy and sensing are:

- 1. BST thin films are well-studied materials and the use of BST in tunable microwave devices is reported vastly. The use of FE thin films like BST in its paraelectric phase for transduction in HBAR is an area of research which lacks attention. The electric field dependent nature of the effective coupling coefficient and Q-factor for a resonator which has multiple resonant modes across a broad frequency spectrum holds immense potentials.
- 2. The electrodes, the FE thin film and the substrate where the acoustic wave travels affect the characteristics of the resonator. Numerical simulations which are in 1-D can be used to fit with the experimental data, but in addition to this, 3-D simulations are necessary to predict the different variations in designs and choice of materials. The addition of

any extra layer on the resonator changes the response and this drastic effect which happens due to the change in acoustic boundaries in the system needs to be studied both by simulation and experiments. The capability to characterize a newly synthesized material quickly and accurately using HBAR with the multimode nature of the resonator still needs more study to improve.

3. Oscillators, Atomic clock, sensors and QAD systems require high Q resonators which operate in the GHz frequency range. The requirement for this is fulfilled by HBAR with an added advantage of being compact in size and having ease of integration for on-chip applications. Ideally for an HBAR, the achievable Q factor is near the material Q of the substrate. Higher the Q of the substrate and efficiency of the transducer, higher the Q factor of the resonator. The Q factor of the resonator is affected by various aspects which include the choice of the materials, electrode design, lateral loss etc. For conventional PE thin film based high Q HBAR, the Q is not significantly dependent on the external DC bias voltage, but by using BST instead of ZnO or AlN, the Q can be varied using a DC bias voltage. This added advantage of controlling Q could provide an extra edge for achieving more efficient oscillators, QAD systems etc.

In the light of the above discussion, the work reported in this thesis is concentrated on theoretical (simulation based) and experimental study of the high overtone bulk acoustic wave resonator (HBAR) which uses induced piezoelectricity through electrostriction of a ferroelectric film in its paraelectric phase. Importance is given in using the HBAR primarily for characterizing the BST thin film grown using PLD technique. The acoustic properties of BST are first extracted using the composite resonator technique (RSM). The frequency spectra of the HBAR are exhaustively used for studying the effects of both DC bias and adding a polymer layer in the configuration. The goals set for the thesis are condensed as follows:

- 1. To understand the intricate working of the HBAR which uses electrostriction as a transducing force. The use of 1-D numerical models and 3-D model using FEM are useful means to get maximum knowledge of the device. Most important of all, to fabricate numerous HBARs and characterize them in order to study and analyse the experimental results to derive the field dependent nature of the resonator.
- 2. To use the HBAR for extracting the acoustic properties of the thin film used as the transducer (BST for this work). For this, the resonant spectrum is to be analysed and parameters like effective coupling coefficient and spacing of parallel resonance frequency (SPRF) for the multiple modes are investigated.
- 3. To study how the response of the HBAR changes when a new medium is introduced in the acoustic path. The properties of the materials will be investigated by the variation it introduces in the frequency spectra of the HBAR. The use of FEM bundles like COMSOL® could give a clearer picture as to how the wave changes in an added layer.
- 4. To study the effects of substrates and electrode materials, the thickness of the substrates and the dimensions of the electrode on various parameters of the HBAR.

## 1.7 Thesis Outline

Chapter 1 introduces the BAW technology with a brief history of ultrasonics. The chapter delves more specifically on various aspects of HBAR like design and applications. The motivation and the goals of the thesis are laid out in this chapter.

Chapter 2 deals with the methodology and techniques used in preparation, fabrication or characterization of the HBAR. The techniques of depositing BST using PLD and electrodes (i.e., Pt and Au) using RF magnetron sputtering are explained. The steps of the device's fabrication process are discussed and the characterizations which were performed are

briefly discussed. The high frequency measurements using on-wafer probing technique are discussed elaborately.

Chapter 3 discusses in detail the mechanisms behind the induced piezoelectricity in BST thin film under application of DC bias field. The relationship between the coupling coefficient and the relative tunability of the thin film is also discussed. The frequency spectra of a numerically simulated HBAR model are used to derive formulae which will be used for later material property extraction. Important parameters of HBAR like effective coupling coefficient and SPRF are discussed in detail.

Chapter 4 explains the experimental studies of the HBARs fabricated on various substrate materials with BST thin film that are all switchable with DC bias field. Using the RSM technique given in Chapter 3, the acoustic properties of BST thin films are extracted. Most important of all, the field dependent nature of the Q factor and the coupling coefficient of the HBAR are analysed.

Chapter 5 discusses in detail the effects of adding a medium in the HBAR's acoustic pathway. SU-8 layer is coated on the backside of the HBAR and the effect it has on the parameters of the resonator, i.e., the SPRF, the  $k_{eff}^2$  and the Quality factor are studied. The acoustic property of the coated material is derived using modelling (1D and 3D models) and experimental results.

In Chapter 6, the effect of the electrode material, its area and geometry, on the various parameters of HBAR like the SPRF,  $k_{eff}^2$  and Q factor are studied. 2D FEM simulation are carried out to better understand the effect of electrodes.

And lastly Chapter 7 gives a quick summary and the conclusion of the thesis. The chapter also includes the scope for future work in this area.

# Chapter 2: Experimental Methods

## 2.1 INTRODUCTION

This chapter lays the foundation for all techniques and methods used in preparing, fabricating or characterizing materials or devices to be applied in the latter chapters. This chapter gives the fundamental background or the set of techniques that are followed during this research work (thesis). Bulk and thin film preparation techniques are introduced for the Barium strontium titanate (BST) material and deposition technique used for thin film electrodes such as gold and platinum are discussed. The deposition of BST films by using pulsed laser deposition technique (PLD) and the optimized condition for getting high quality thin films are discussed in detail. As for the case of device fabrication, a step-by-step preparation technique is discussed. Apart from this, the characterization tools for structural and microstructural properties such as X-Ray diffraction and Scanning Electron Microscope (SEM) are introduced to some extent. Finally, the most important component of the thesis i.e., the high frequency measurement, is elaborated and its sub components are carefully discussed.

# 2.2 TARGET PREPARATION OF BARUIM STRONTIUM TITANATE (BST)

By using a standard solid-state reaction technique, the stoichiometric BST target is made which involves milling of materials at optimized conditions and then calcinating at the reaction temperature in a furnace. Manufacturing a high-quality target with necessary optimization is one of the keys to producing high quality thin films. From the optimized target, with the help of laser ablation process, the thin film produced should be reproducible [111,112].

High purity reagents such as Barium carbonate (BaCO<sub>3</sub>), Strontium carbonate (SrCO<sub>3</sub>) and Titanium dioxide (TiO<sub>3</sub>) are procured from Sigma-Aldrich (purity 99.99%, USA) which is used for the Ba<sub>0.5</sub>Sr<sub>0.5</sub>TiO<sub>3</sub> (BST) ceramic target preparation. The chemical reaction for getting Ba<sub>0.5</sub>Sr<sub>0.5</sub>TiO<sub>3</sub> (BST) is as follows

$$0.5$$
BaCO<sub>3</sub>+ $0.5$ SrCO<sub>3</sub>+TiO<sub>2</sub>  $\longrightarrow$  Ba<sub>0.5</sub>Sr<sub>0.5</sub>TiO<sub>3</sub>+CO<sub>2</sub>

The steps involved in getting the end product, i.e., the BST target is as follows. First of all, the reagent powders are mixed by using ball milling technique for 2 Hours. After the reagents are properly mixed, it is calcined in a microwave sintering system at a temperature of 1000°C by providing a dwell time of 30 minutes, and the heating rate is maintained at a rate of 25°C/min. In order to reduce the particle size, thereby, to increase the density of the sintered target, the calcined powder is again subjugated to ball milling for another 6 hours. 1% Poly Vinyl Alcohol (PVA) is added to the ground powder as a binder and made into 25 mm diameter and 3 mm thick pellets by using a uniaxial press of applied pressure 2 MPa. The pellets are then heated up to 500°C with a heating rate of 2°C/min for evaporation of the PVA binder. By using a conventional furnace, the prepared pellets were sintered at an optimized temperature of 1400°C for 2 hours with a heating rate of 5°C/min. And finally, the surfaces of the sintered BST targets were polished to avoid surface contamination [111,112]. Microwave heating was used for the calcination for fast heating which can yield powder with higher sinterability. In case of the microwave furnace, the heating is generated within the sample initially and spreads to the entire volume [113].

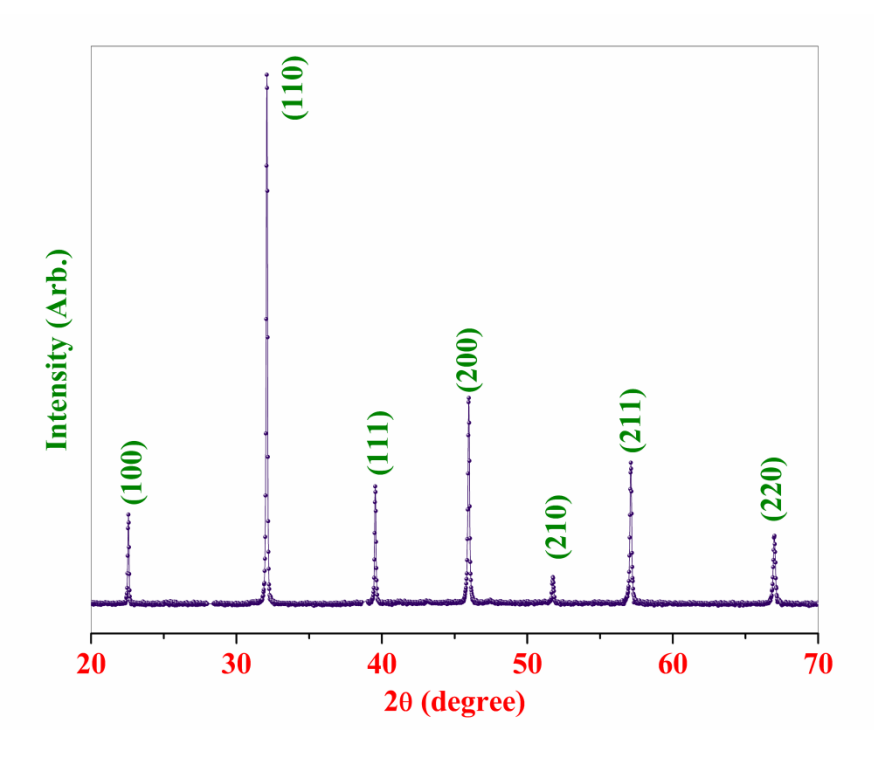


Fig.2.1 X-ray diffraction pattern of Ba<sub>0.5</sub>Sr<sub>0.5</sub>TiO<sub>3</sub> target.

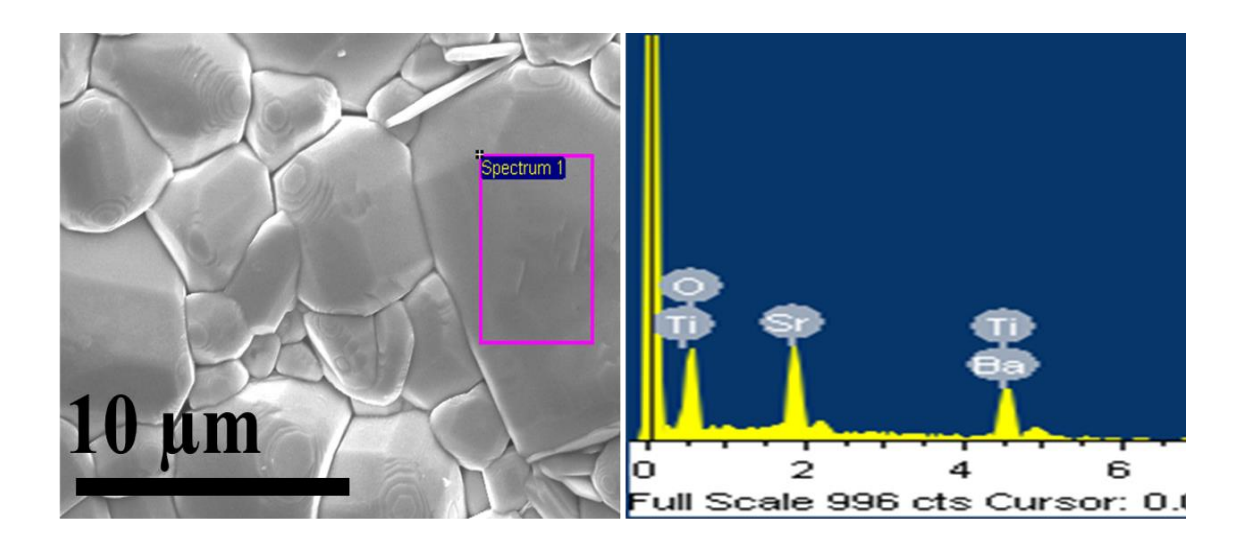


Figure.2.2 FESEM and EDAX of Ba<sub>0.5</sub>Sr<sub>0.5</sub>TiO<sub>3</sub> target.

The X-ray diffraction shown in Fig. 2.1 confirms the formation of polycrystalline Ba<sub>0.5</sub>Sr<sub>0.5</sub>TiO<sub>3</sub> (BST). To confirm the presence of constituent elements of the compound, EDAX of the BST target was done and is shown in Fig. 2.2 which shows that Ba, Sr, Ti

and O are present without any impurity within the detectability limit. The atomic percentages present are given in Table 2.1. EDAX also gives the ratio of the elements as Ti/Sr=1.76 and Ti/Ba= 1.64 confirming the stoichiometric ratio of the elements within the target disc prepared.

Table 2.1 Atomic percentages of elements in the BST target

Elements	Atomic
	percentage (%)
Barium (Ba)	12.6
Strontium (Sr)	11.7
Titanium (Ti)	20.7
Oxygen (O)	55.0

# 2.3 THIN FILM PREPARATION TECHNIQUES

This section gives a detailed explanation of the two Physical Vapor Deposition (PVD) technique used in this study 1) The pulsed laser deposition for realizing thin BST films and 2) The RF magnetron sputtering deposition for metallization, i.e., top and bottom electrode of devices to be fabricated.

# 2.3.1 PULSED LASER DEPOSITION (PLD)

PLD is a physical vapour deposition technique used for achieving thin films of various types of materials [114-117]. The primary mechanism of the PLD is to transfer the photonic energy from a laser source to a target material to be deposited. Typical lasers used for this purpose are excimer lasers and Nd:YAG solid state lasers which provides a wavelength of about 200 to 400 nm with a pulse duration of around 5 to 20 ns. Due to the intense laser

pulse, a small volume of target material from the surface are heated and evaporate. Since the substrate to be coated is placed on the opposite side, the evaporated material condenses on it forming a thin film. So, in essence, during this process the stoichiometry of the target is transferred directly to the thin film formed in the substrate and gives an edge over other techniques which suffer from lack of stoichiometry control.

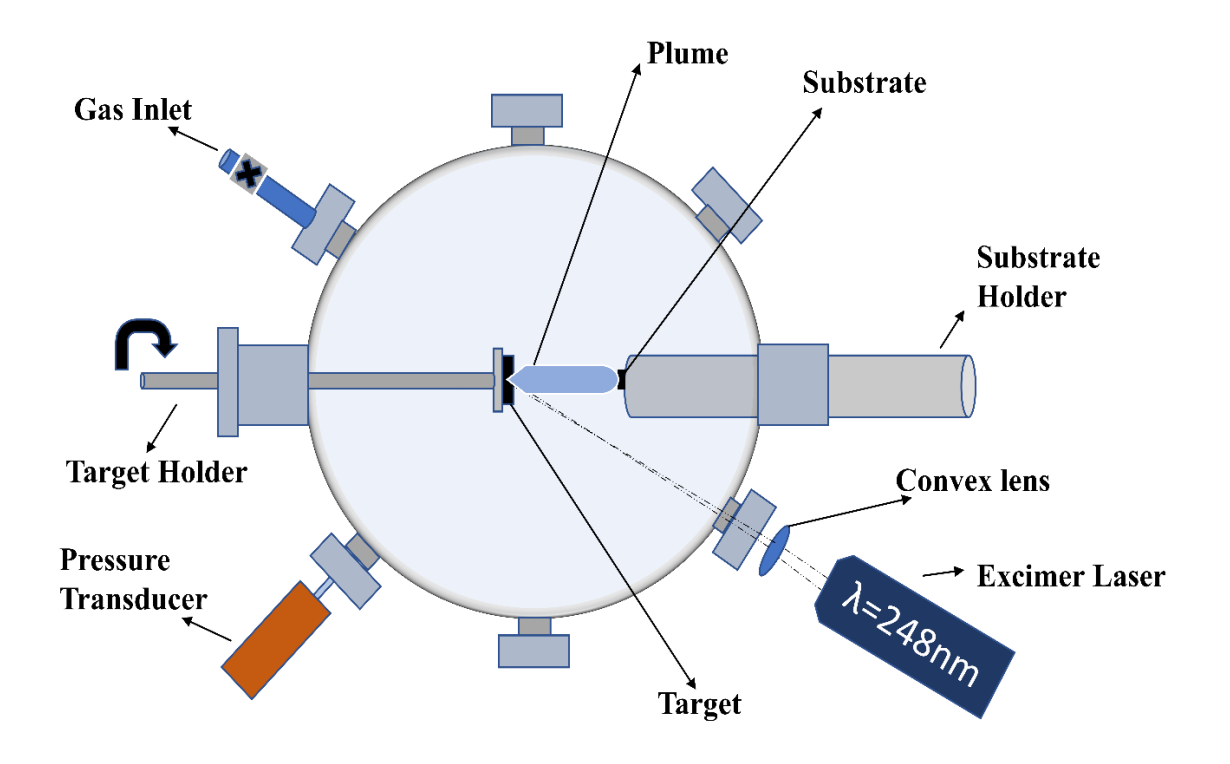


Figure. 2.3 Schematic drawing of a Pulse Laser Deposition (PLD) system.

A schematic diagram of a PLD system is shown in Fig. 2.3 above. As seen in the schematic, the deposition chamber and the laser are isolated from each other giving more flexibility to the system because by using lenses and mirrors the laser can be easily directed inside the chamber. To avoid scattering of the plume and deposition of residual particles of the sample to be deposited, the chamber is kept under vacuum. In most of the PLD systems, a multitarget carousal is equipped giving an advantage to deposit heterostructures or if a load lock system is present, it even gives the flexibility to deposit different samples with different material without breaking the chamber vacuum [118].



Figure.2.4. PLD used in this work.

# Pulsed laser deposition of barium strontium titanate thin films

For the research work presented in this thesis, Barium strontium titanate (BST) thin films are deposited using the PLD set up shown in Fig. 2.4. The laser source used for the deposition is a 20 ns pulse width KrF Excimer laser with wavelength 248 nm (Coherent-Compex Pro 102 F) which has a repetition rate of 5 Hz and the fluence or energy density of 2 J/cm² is maintained at exit. The thin film deposition takes place inside the spherical chamber (Excel Instruments®, India). The chamber is maintained at a base pressure of 5 x  $10^{-6}$  mbar using the Turbo and backing pumps. During the deposition a distance of 5 cm gap is kept between the target and the substrate and the optimized working pressure during the deposition is 8 x $10^{-3}$  mbar with a high purity O<sub>2</sub> gas being used as the background ambient gas and the temperature inside the chamber is maintained at 700°C throughout the deposition. During the deposition, the target is rotated with a specific speed of 10 rpm and

an oscillation frequency of 5 Hz. In the final step of the deposition, in-situ annealing is done for 30 mins in the presence of oxygen inside the chamber.

Since the device fabricated in this thesis, i.e., HBAR is basically a Metal-Insulator-Metal (MIM) structure, the bottom electrode is first coated using RF magnetron sputtering (which will be discussed in the next section). For BST deposition, Platinum coated substrate (Double side polished-Silicon, Sapphire, Fused Silica or YAG) are used. Once the deposition is over, the same oxygen partial (pO<sub>2</sub>) pressure is maintained and gradually brought back to room temperature. Fig. 2.5 and Fig. 2.6 shows the XRD pattern and FESEM image of the deposited BST on the platinum coated sapphire substrate.

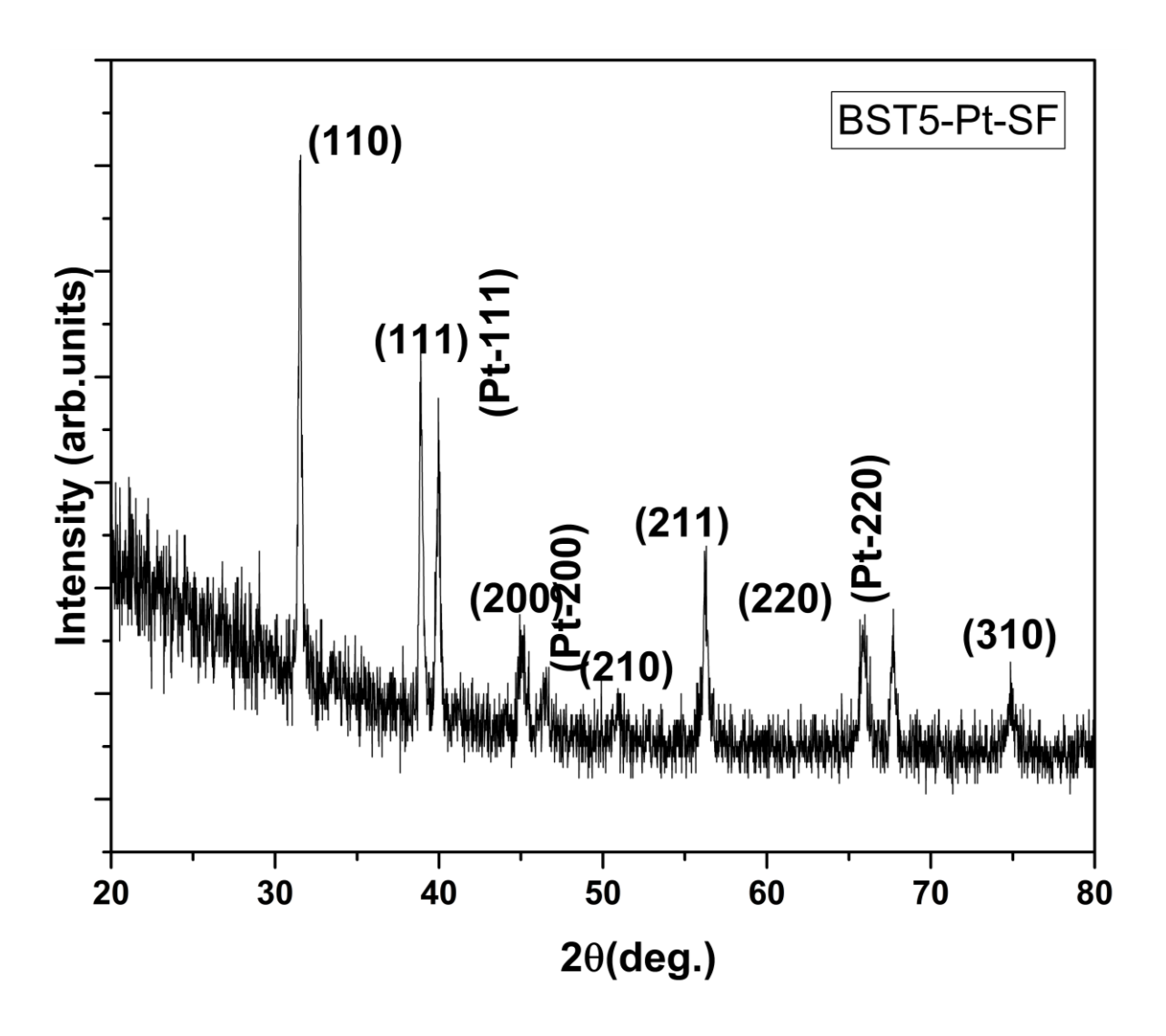


Figure. 2.5 X-Ray diffraction patterns of BST thin films on Pt coated sapphire substrate.

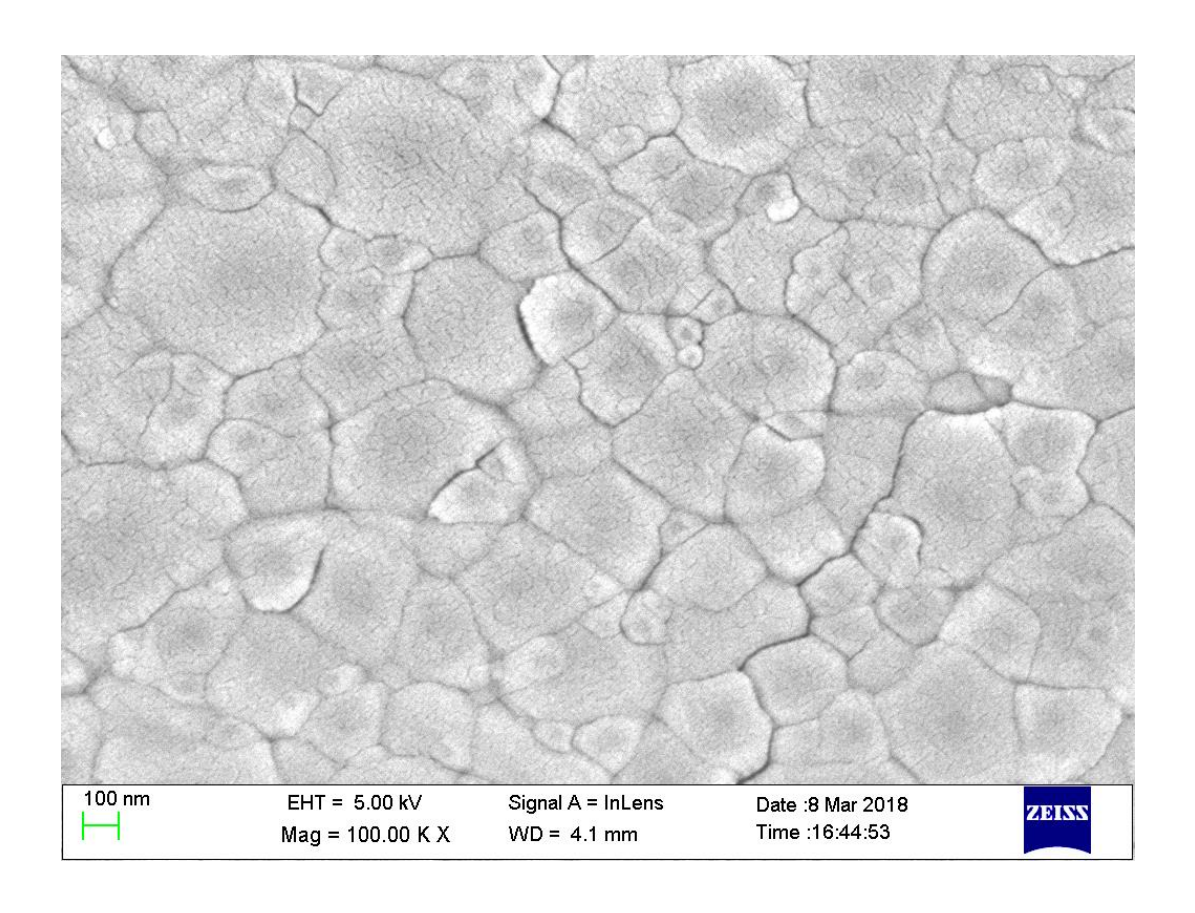


Figure.2.6. FESEM image of thin film BST on Pt coated sapphire substrate.

# 2.3.2 RF MAGNETRON SPUTTERING

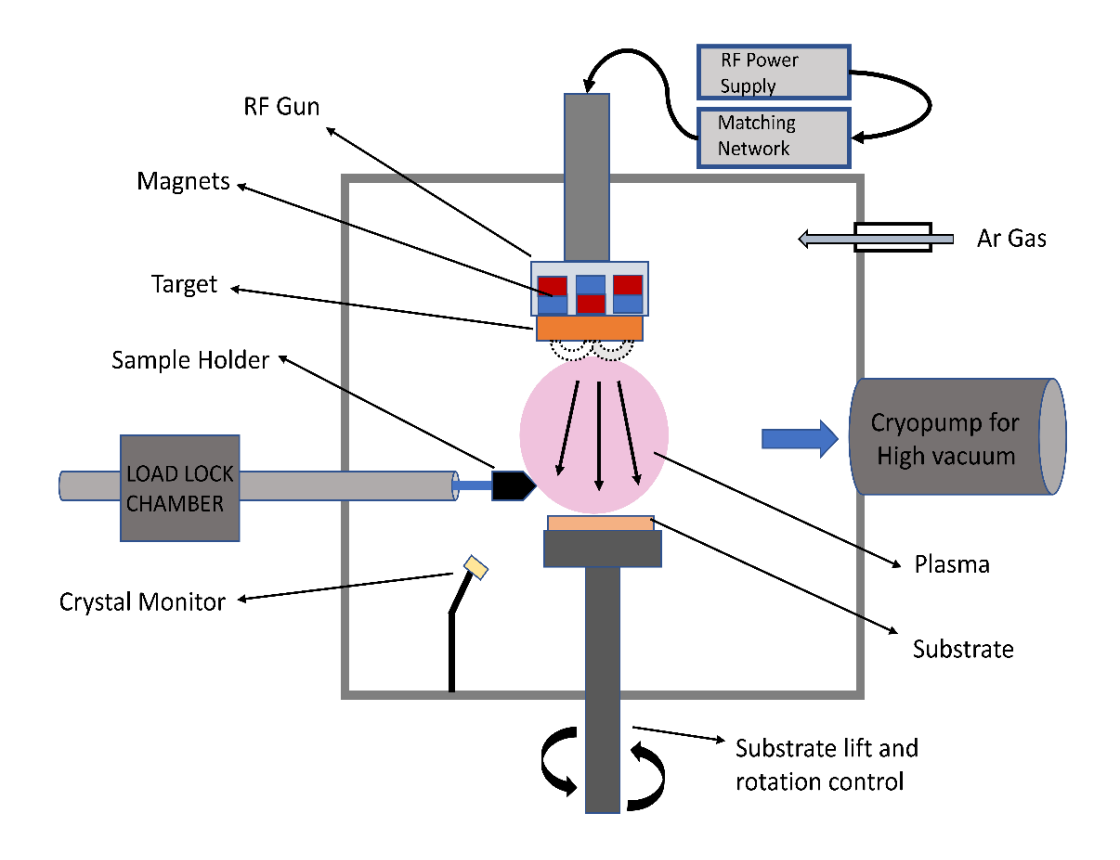


Figure.2.7. Schematic Diagram of a RF magnetron sputtering system.



Figure.2.8. The RF magnetron sputtering system used in this study.

Sputtering process for material deposition is a well sought-after physical vapor deposition (PVD) technique. It is advantageous as both metallic and non-metallic thin films can be deposited using it. As shown in figure Fig.2.7 and 2.8, the sputtering system has numerous components. The cubic shaped stainless-steel vessel acts as the chamber and provides the necessary space for accommodating all the vital parts such as the RF magnetron gun, the target holder, the various ports or opening for measuring the pressure and passing gas inside the chamber. The system installed in our clean room facility (CFN, UOH) allows for opening the chamber from the top where three different RF guns are attached. Two RF power supplies which can generate an output power of up to 100 W in the 13.56 MHz frequency band are coupled to two matching networks which give the option to manually or automatically tune the reflected power. So, the system has the capacity to sputter two different materials at the same time or alternatively with convenience.

A salient feature of this system is the load lock which facilitates for ease of transfer of samples/wafer to be deposited inside the main chamber without the need to break the chamber vacuum. The assembly is a simple manual linear movement of a steel rod/ arm after opening the slit valve (controlled by pneumatic switch) which acts as the window to the chamber. The sample placement is controlled by the movement of up-down movements of the substrate control assembly. For creation of vacuum in the system, two main types of pumps are used, a mechanical scroll pump and a Cryogenic pump. The scroll pump is used for the load lock chamber and for making the pressure in the main chamber reduced to reach medium or roughing vacuum level. The function of the cryopump is to create ultrahigh vacuum. It works on the principle of condensing the gases and storing them in a cold head kept at cryogenic temperatures by using closed loop helium gas cooling. Gases which are not condensed are absorbed by activated carbon, and the temperature within the cold head become as low as 10 K.

During sputtering, when RF power is supplied to the cathode (RF gun), the atoms from the target material are struck out due to constant bombardment to it by energized charged particles from the generated RF plasma. The gas is supplied throughout the process, i.e., Ar gas is ionized due to the high electric field between the cathode and the substrate. In the work reported in this thesis, Ar has been used as the inert gas for metallic thin film deposition of metals like Platinum and Gold. Upon achieving high potential, the gases in the chamber are ionized. These positive ions torpedo on the negatively charged target forcing it to eject atoms from its surface. The ejected atoms travel towards the substrate and are condensed forming thin film of the target material. In magnetron sputtering, the magnets put behind the cathode helps in confining the ionized particles. Since the direction of the magnetic field in cathode is arranged perpendicular to the electric field, there is an increase in the collisions by allowing the helical paths for electrons due to the crossed electric and magnetic fields. The base pressure used is maintained at  $6 \times 10^{-7}$  mbar and a working pressure of  $6.5 \times 10^{-3}$  mbar (with argon applied through the MFC) is used during deposition.

#### 2.4 DEVICE FABRICATION

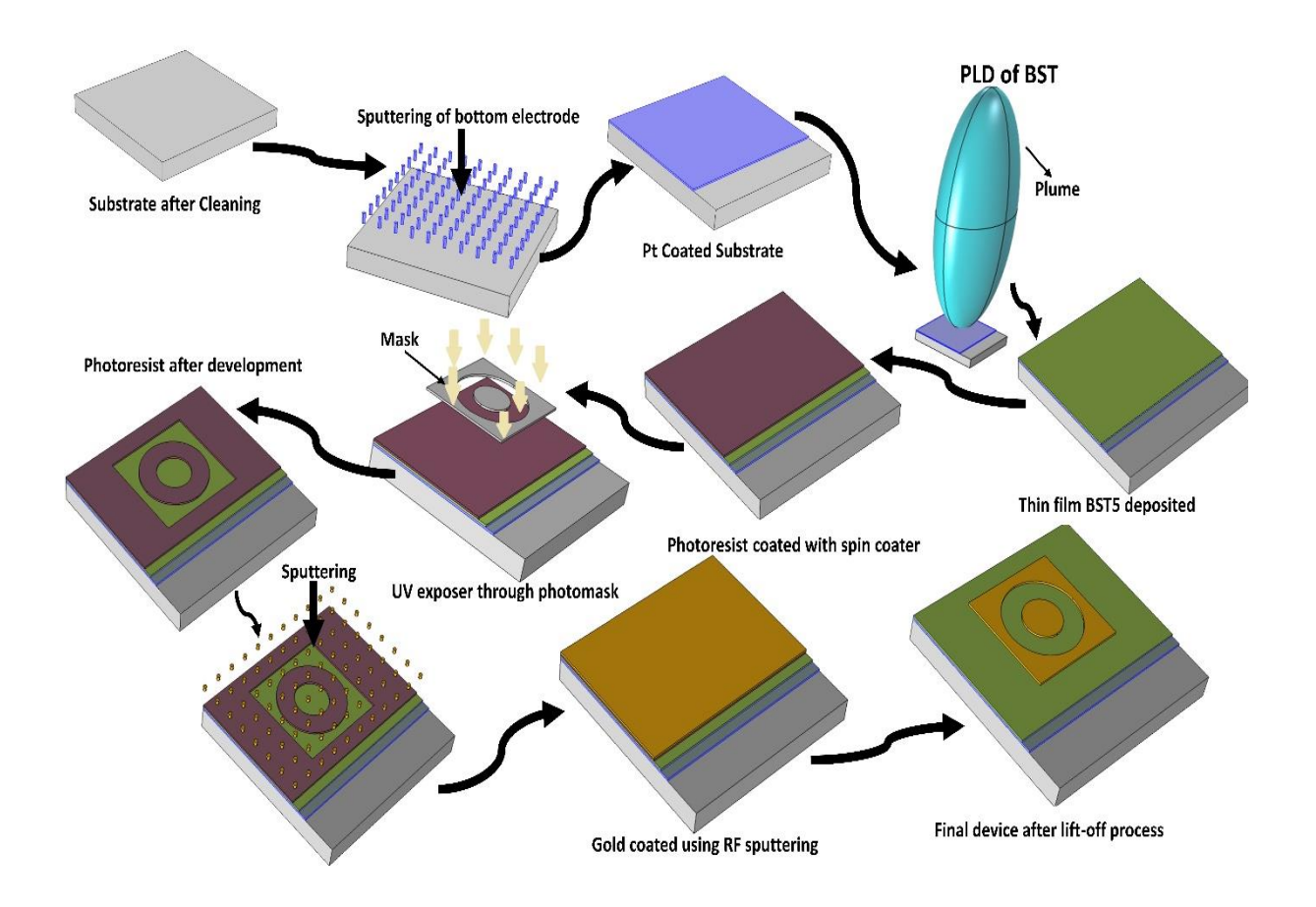


Figure.2.9. Process flow for the fabrication of High Overtone Bulk Acoustic Resonator (HBAR).

Fabrication of high overtone bulk acoustic resonator (HBAR) involves numerous processes. Fig. 2.9 shows the processes involved in fabrication of an HBAR as the end product. Some of the processes can be listed as 1) Substrate preparation and cleaning 2) bottom electrode deposition 3) BST deposition by PLD 4) Photoresist coating 5) UV-Exposure and Development 6) Deposition of top electrode and 7) Lift-off and stripping. All of the steps mentioned above except PLD are performed inside cleanroom (class 1000 cleanroom) where, the temperature, the humidity and the pressure are controlled.

**Substrate Preparation and cleaning:** For making the HBAR, various types of substrates are used. The primary criterion for the substrate selection is that it should have a high

mechanical Quality factor (low acoustic loss) and the substrate should be double side polished (Plane parallel) for facilitating the reflection of acoustic waves from the opposite ends. Hence, the preferred substrates and the ones used in this thesis are sapphire (Al<sub>2</sub>O<sub>3</sub>), Yttrium aluminium garnet (YAG), fused silica and silicon. In case of Silicon substrates, using a diamond scriber (Suss Microtech HR 100) the required dimensions are scribed and cleaved by applying tension on the scribed lines. For sapphire wafer, scribing is done with a normal diamond tip pen and cleaved by applying tension on the scribed line.

Before deposition of any layers, the surface of the substrate has to be cleaned in order to remove dirt and contaminants. The cut substrate is kept in an ultrasonic bath of acetone for 5 minutes and then kept in running de-ionized (DI) water for 1 minute. Dry nitrogen gas is used to blow away the water droplets if present in the substrate. The cleaned substrate is placed in a hotplate at 105°C for 5 minutes.

**Bottom electrode deposition:** The bottom electrodes are deposited as described in Sec. 2.3.2. Cr of around 20 nm is deposited as the adhesive layer first and Pt of thickness around 130 nm is deposited.

**BST deposition by PLD:** Thin film  $Ba_{0.5}Sr_{0.5}TiO_3$  (BST) of thickness around 1  $\mu$ m is deposited on the substrate coated with Pt as the bottom electrode. Details of the deposition is given in Sec. 2.3.1.

**Photoresist coating:** After BST deposition, for patterning the top electrode, photoresist needs to be spin coated and patterned. Fujifilm OIR 620-10M positive photoresist is used in this work. By using a spin coater and setting a two-step program, first to spread the resist and second to control the thickness, photoresist is coated on samples. The first step is set at 500 rpm for 5 s and the second step at 2500 rpm for 30 s. After coating, the sample is soft

baked by keeping at a hotplate at  $85^{\circ}$ C for 20 minutes. The thickness of the photoresist achieved is around 1  $\mu$ m.

**UV-Exposure:** In the mask aligner (Model MJB4, Karl Suss), photoresist coated sample is placed in the sample holder chuck and manually aligned with the mask. Optical lithography exposure is performed with 365 nm wavelength light at constant power of 25 mW/cm<sup>2</sup> in contact mode. The time of exposure is 5 s. Tetramethyl ammonium hydroxide (TMAH) is used as the developer solution for the photoresist and the optimized development time is 20 s.

**Top electrode deposition:** The top electrode is deposited as described in Sec. 2.3.2. Au of thickness around 150 nm is deposited.

**Lift-off and stripping:** The Lift-off process is used to get the final necessary pattern of the HBAR as shown in Fig. 2.9. In this step, the sample after top electrode deposition is dipped in acetone. By doing so, the metal deposited on to the patterned resist is stripped leaving behind the patterned top electrode.

# 2.5 Structural and microstructural characterization techniques

This section describes the characterization techniques used to investigate the crystal and microstructural properties of BST thin film used in the transducer of the HBAR.

# 2.5.1 X-Ray Diffraction (XRD)

X-ray diffraction methods are used to determine the crystal structure of different materials. In this diffraction method, chemical compounds are not identified from composition of chemical elements but rather by studying the crystalline structure. X-ray diffraction methods can also be used to study the crystallinity, phase, preferred orientation, defects, stress, strain and grain size of materials. XRD methods work on the principle of Bragg's law [121]. When X-rays of wavelength  $\lambda$  is incident on a crystal surface at angle  $\Theta$  as shown in Fig. 2.10, diffraction occurs. As seen from the figure, the ray at point P (i.e., from the second row of atoms) has travelled a distance, (SP+PQ) greater compared to the ray on top row.

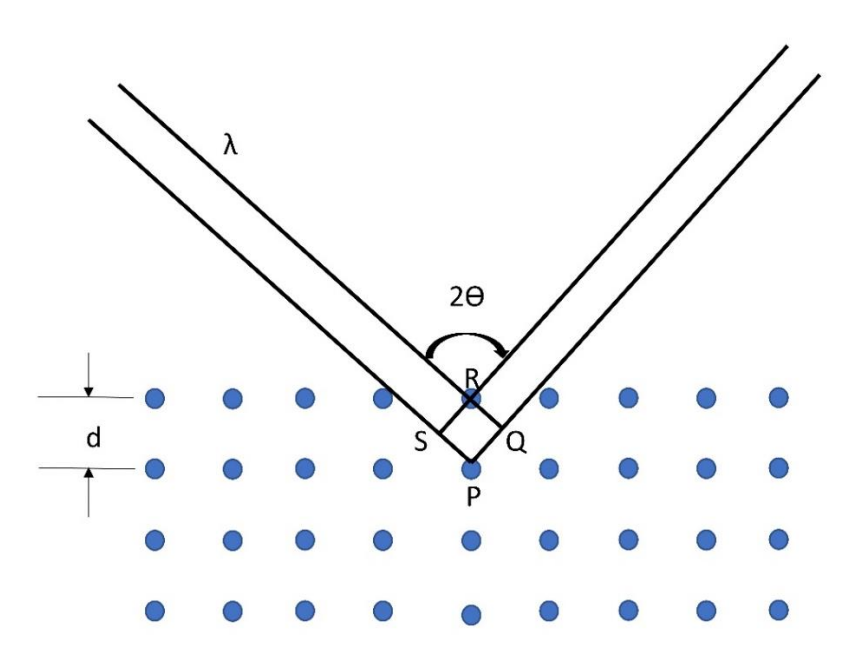


Figure 2.10. Diffraction of X-ray from atoms in a crystal.

The spacing between the parallel crystal plane is specified as d (RP) in the figure above. In order to obtain diffraction maxima, the path difference should be an integral multiple number of the wavelength. Both SP and PQ are equal  $d \sin \Theta$ , and hence, the condition for the maxima is given as

$$2d\sin\theta = n\lambda \tag{2.1}$$

The above equation (2.1) is the Bragg's law for diffraction. Therefore, by measuring  $\Theta$  and using the known wavelength  $\lambda$ , the crystal spacing d can be determined. There is a large library or database of expected diffraction patterns available. Using this database, compounds can be identified from their diffraction positions and intensities [121].

For all the BST thin films used for device fabrication, the phase and structural properties are investigated using Grazing incident X-ray diffraction (GI-XRD) mode. In grazing mode, the incident angle is very small which increases the penetration depth in the thin film rather than the substrate. In the reported work, the BST thin films are examined in GI-XRD-Bruker D8 Discover operated with a Cu-K $_{\alpha}$  radiation source of wavelength ~1.5406 Å and incident angle of 0.5°.

### 2.5.2 Scanning electron microscope (SEM)

SEM is widely used for examining microstructures. SEM enables the study of microstructures due to the high resolution and 3D appearance of the image generated. The 3D effect is created by the depth of field. The image obtained in SEM is by scanning the surface of a specimen by a focused electron beam. The electron beam is generated from an electron gun which is either thermionic or field emission type. Electromagnetic lenses are used in SEM for electron probe formation. Rectangular raster of the electron probe is obtained on the surface of the specimen using beam deflection system. The high energy electron beam upon striking the surface of the specimen produces either elastic scattering

or inelastic scattering. Backscattered electrons (BSE) are produced by elastic scattering and secondary electrons (SE) are produced by inelastic scattering. The signal electrons (SE and BSE) emitted from the specimen are absorbed using a detector and are amplified to generate the images. Formation of elemental composition contrast and topographic contrast are attributed to BSE and SE respectively.[122]

In the work reported in this thesis, an Ultra 55, Carl Zeiss microscope fitted with the Schottky FE Gun as the electron source is used for obtaining the SEM images.

# 2.6 High frequency Characterization

The high overtone bulk acoustic resonators (HBARs) or composite resonators discussed in this thesis are microelectromechanical systems which operate in the microwave frequency range. So, in order to characterize the HBARs, scattering parameters (S-parameters) are measured using Vector Network Analyzer (VNA) and RF probes. The devices can be both 1-port or 2-port devices, but one port devices are simple in fabrication and measurement. The most important parameter for studying the HBARs is the complex impedance which can be derived directly from the S<sub>11</sub> data measured. In this section, the On-wafer probing setup (Fig.2.11) and the calibration procedure are described.

#### 2.6.1 Vector Network Analyzer

Network analyzer is a widely used instrument for characterization of circuits, devices etc. It gives the ratioed amplitude and phase information as the measurement output. It provides excellent measurement accuracy by using vector-error correction. Fig.2.12 shows a simplified block diagram of a Vector Network Analyzer. As seen from the block diagram, in order to operate the VNA for measuring incident, reflected and transmitted signal, four major sections are involved, i.e., 1) Source 2) Signal separation 3) Receivers and detectors for signals and 4) Processor/Display [123].

- 1) Source: Supply stimulation for the stimulus-response test system. The frequency of source or the power level can be swept. Sources are mostly based on voltage-controlled oscillators (VCOs) or synthesized sweepers. Synthesized sources are usually integrated into most VNAs and it provides high frequency resolution and stability.
- 2) Signal separation: The hardware used for signal separation block is called the test set, and it can be an external box or be integrated within the VNA itself. The functionality of the test set can be categorised into two:
  - a) provide reference by measuring part of the incident signal. Splitters and directional couplers are used for this purpose.
  - b) separate the forward and reflected waves at input of DUT. Couplers and bridges are used for this purpose.
- 3) Receivers and detectors for signals: The two steps to detecting signal in VNA is by using Diode detectors. First the RF signal level is converted to a level proportional to DC, and second is AC detection, where the RF carrier is striped from the modulation (signal under amplitude modulation).
  - VNA uses the tuned-receiver method where a local oscillator (LO) is either locked to the RF or the intermediate frequency (IF) so that the receivers in the VNA are tuned to the input RF signal all the time.
- 4) Processor/Display: This block is the user interface, where data received from VNA, i.e., reflection and transmission data are formatted in different ways making it easier for interpretation of the measurement results.

The Vector Network Analyzer used in the setup shown in Fig.2.11 is E8361C PNA Microwave Network Analyzer (Keysight Technologies). The frequency range, the number of points, and the IF bandwidth is all defined before any calibration or measurement.

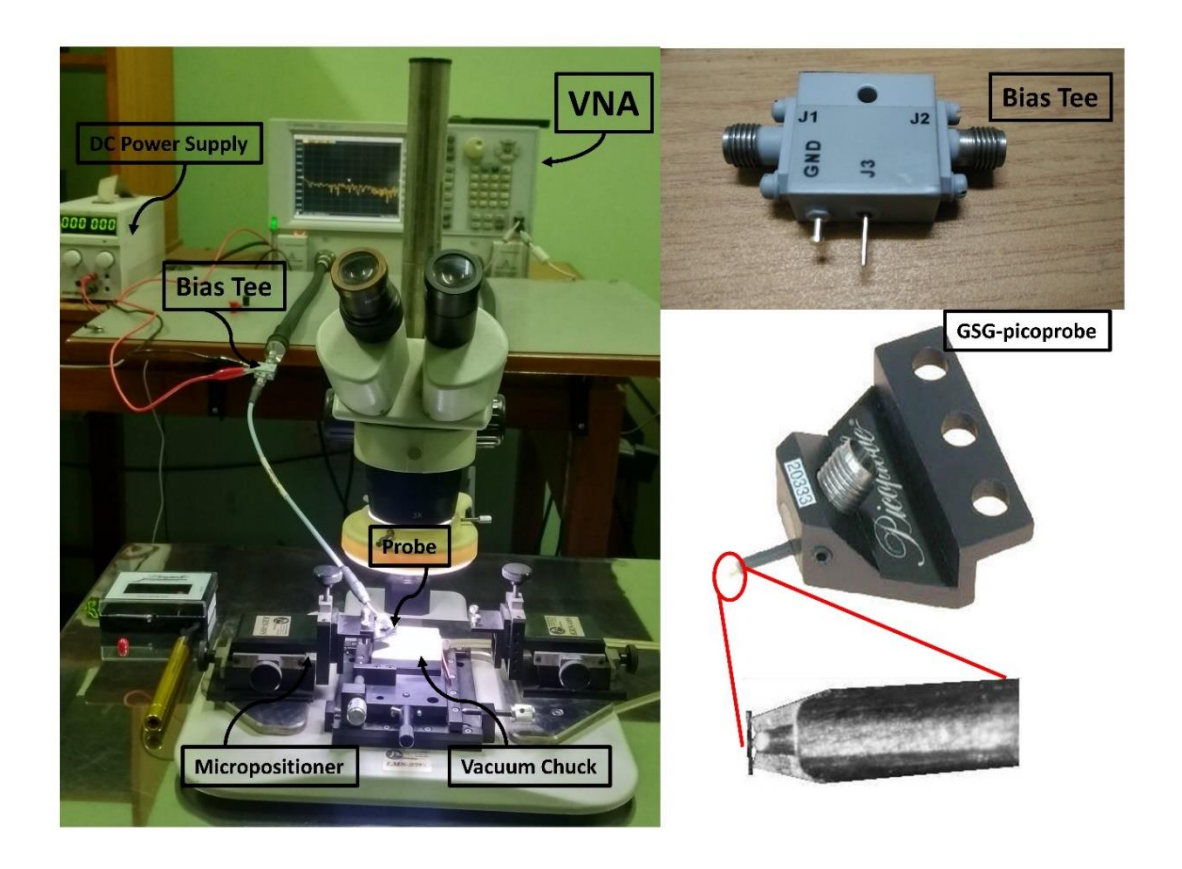


Figure 2.11. On-wafer probing setup for measuring HBAR characteristics.

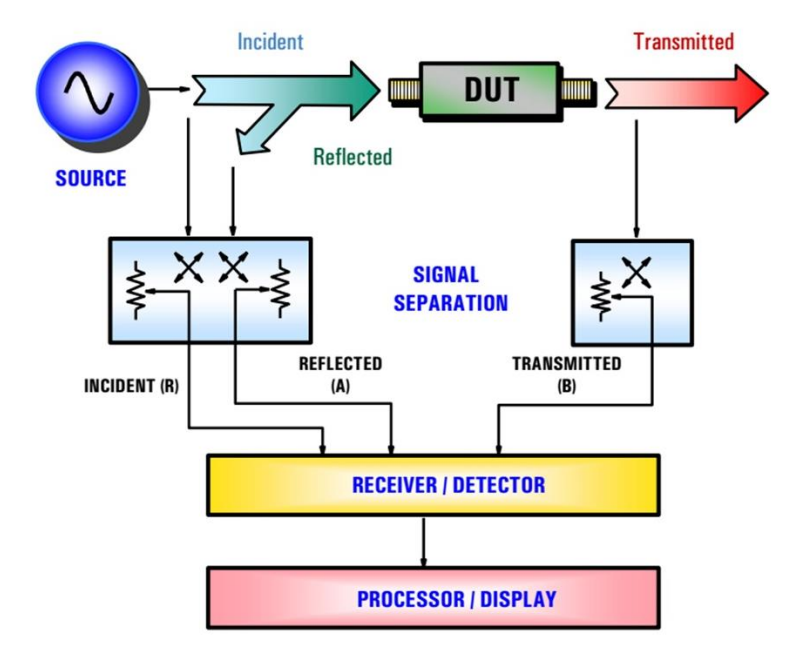


Figure 2.12. Block diagram of Vector Network Analyzer [123].

# 2.6.2 On-wafer Probing set-up

On-wafer probing technique enables testing or probing devices on wafer or devices on a single substrate. Before the emergence of coplanar probes, evaluating or testing an RF component or die required test fixture to be made which involves wire bonding into PCB. This made testing a time-consuming process and unsuitable for large scale screening. Coplanar microprobe establishes a link between the device under test (DUT) with the Vector Network Analyzer on a wafer level itself [124].

The On-wafer probing set-up consists of components such as Vector Network Analyzer, coplanar probes, probe station, and bias tee. Fig. 2.11 shows the On-wafer probing setup used in measuring the  $S_{11}$  of the HBARs discussed in this thesis. The components are discussed below:

**Coplanar Probe**: A 250 µm pitched Ground-Signal-Ground (GSG) probe (GGB Industries) (shown in Fig.2.11) is used for probing the HBARs. The GSG probe has a unique standard CS-5 substrate (GGB Industries) which is used for calibration.

**Probe station**: The DUT or in this case the HBAR is placed on a chuck which has a vacuum line running through it to secure the sample in place. The chuck has the capability to move across the sample for probing and it can also be raised or lowered w.r.t the microprobes. The probes are mounted and fixed onto a micropositioner which is firmly mounted on the probe station using a magnet present on the bottom of the micropositioner. This micropositioner enables precise movement in the x, y, and z- axis. After careful alignment of the probes, the z-axis movement allows to establish contact with the devices. The probe station used for all the probing setup is LMS -2709 (J microTechnology Inc.).

**Bias tee:** The HBARs discussed in this thesis are all switched on by giving DC bias voltage or else it is a simple capacitor. The use of needles requires pads to be included in the design

which increases complexity in fabrication. Moreover, needles have high inductance and couple to nearby probes which is undesirable [124]. This can all be avoided by using a bias tee which can give both RF and DC simultaneously to the HBARs. The bias tee used in the setup is BT-A03 (Taylor Microwave Inc, USA) and is shown in Fig.2.11.

#### 2.6.3 Calibration

It is important to calibrate the measurement setup to get accurate data from the DUT. The test setup suffers from error which can be either random or systematic. Random errors are unpredictable and occur non-uniformly during measurements. Random errors can be seen in the VNA display, emerging from the noise floor as low-level signals. Systematic error on the other hand can be identified easily but has a broad range of causes, for example, the inductance exhibited by the cables and the capacitance due to bias tee while working at high frequencies. Systematic errors are more significant than random errors and can be corrected by calibration [124].

Reference Plane: While performing measurements at higher frequencies it is very difficult to distinguish between the measurement setup and the DUT. In such cases, the concept of reference plane is introduced in order to outline where the measurement system finishes and the DUT starts. Reference plane can be classified as physical and electrical. Physical reference planes can be a simple line drawn relating the connection of two physical connectors. When connectors are not tightened properly (misalignment of physical plane), air gap can lead to measurement error. The electrical reference plane on the other hand is defined during calibration.

To calibrate is ideally to make the signal at the measurement test point/port to have zero magnitude, no shift in phase, and a characteristic impedance  $Z_o$  (50  $\Omega$ ). One method of calibration is to measure various physical elements known as standards. The magnitude and

phase response of such standards are known with precision over a range of frequency (depends on the standard used). So, before measuring the DUT, the standards are measured by which the signal (RF) path is calibrated thereby de-embedding errors in the measurement set-up [124].

Calibration methods can be broadly categorized into two types. The first is a response calibration which can only correct scalar errors. The second type is a vector calibration which is more accurate and accounts for both magnitude and phase. It can rectify certain RF behaviours like mismatch at the RF ports, tracking of frequency response in VNA and directivity errors. SOLT (short, open, load and thru), SOLR (short, open, load and reciprocal), TRL (thru, reflect and line), LRM (line, reflect and match) and LRRM (line, reflect, reflect, match) are different types of vector calibration methods.

# SOLT (short, open, load, thru) Calibration

The calibration technique used in the work reported in this thesis is SOLT. A standard CS-5 substrate (GGB Industries) along with the corresponding CalKit software (GGB Industries) loaded in the VNA are used for calibration. The standard substrate consists of numerous calibration standards such as short, open, load, and through. Since all the HBARs to be measured are 1-port devices (DUT), only short, open and load (50  $\Omega$ ) standards are used for calibration.

After defining the frequency range of interest, number of data points, and IF bandwidth in the VNA, the CalKit software for CS-5 is selected in order to start the calibration process. It is important to note that the frequency range and the IF bandwidth cannot be changed later after calibration. After calibration, narrow bands of frequencies can be selected as required within the frequency range. Fig. 2.13 shows the elements used for calibration. The three elements are probed one by one using the 250 µm pitched Ground-Signal-Ground

(GSG) probe (GGB Industries) and the calibration is saved in the VNA with a unique file name. Fig. 2.14. and Fig. 2.15 show uncalibrated and calibrated  $S_{11}$  responses in the VNA display. Fig. 2.16 shows the response of an HBAR sample measured after calibration.

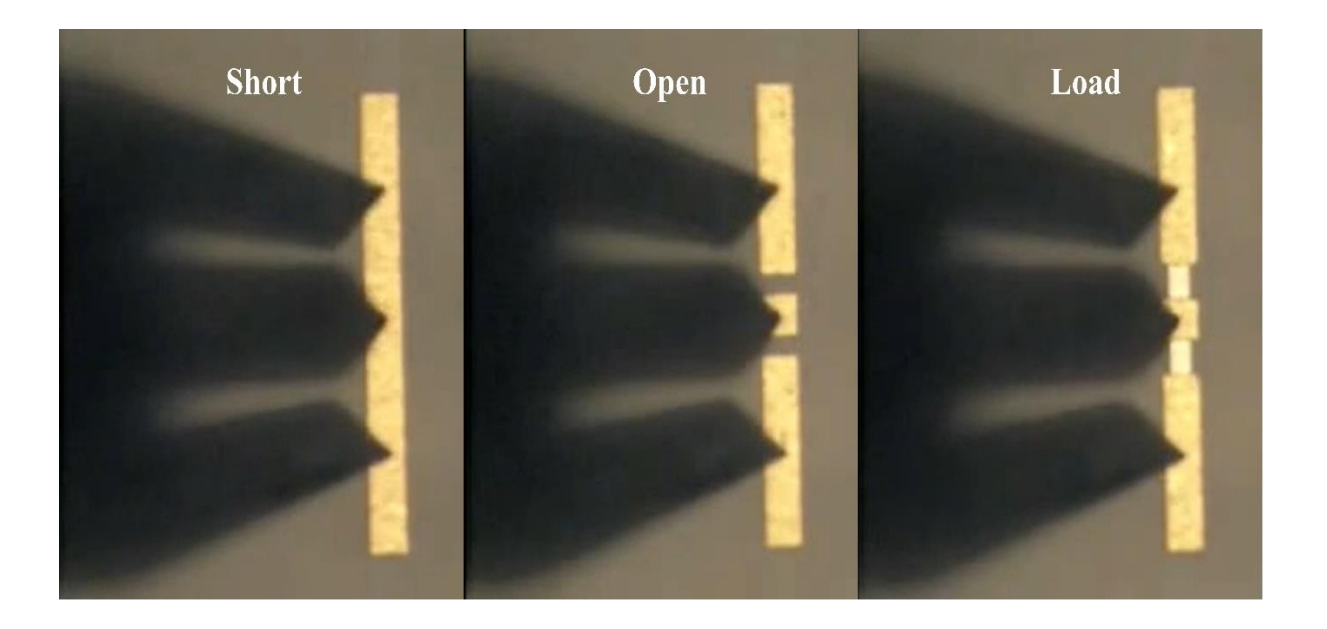


Figure.2.13. Short, Open, and 50  $\Omega$  load standards of CS-5 used for calibration.

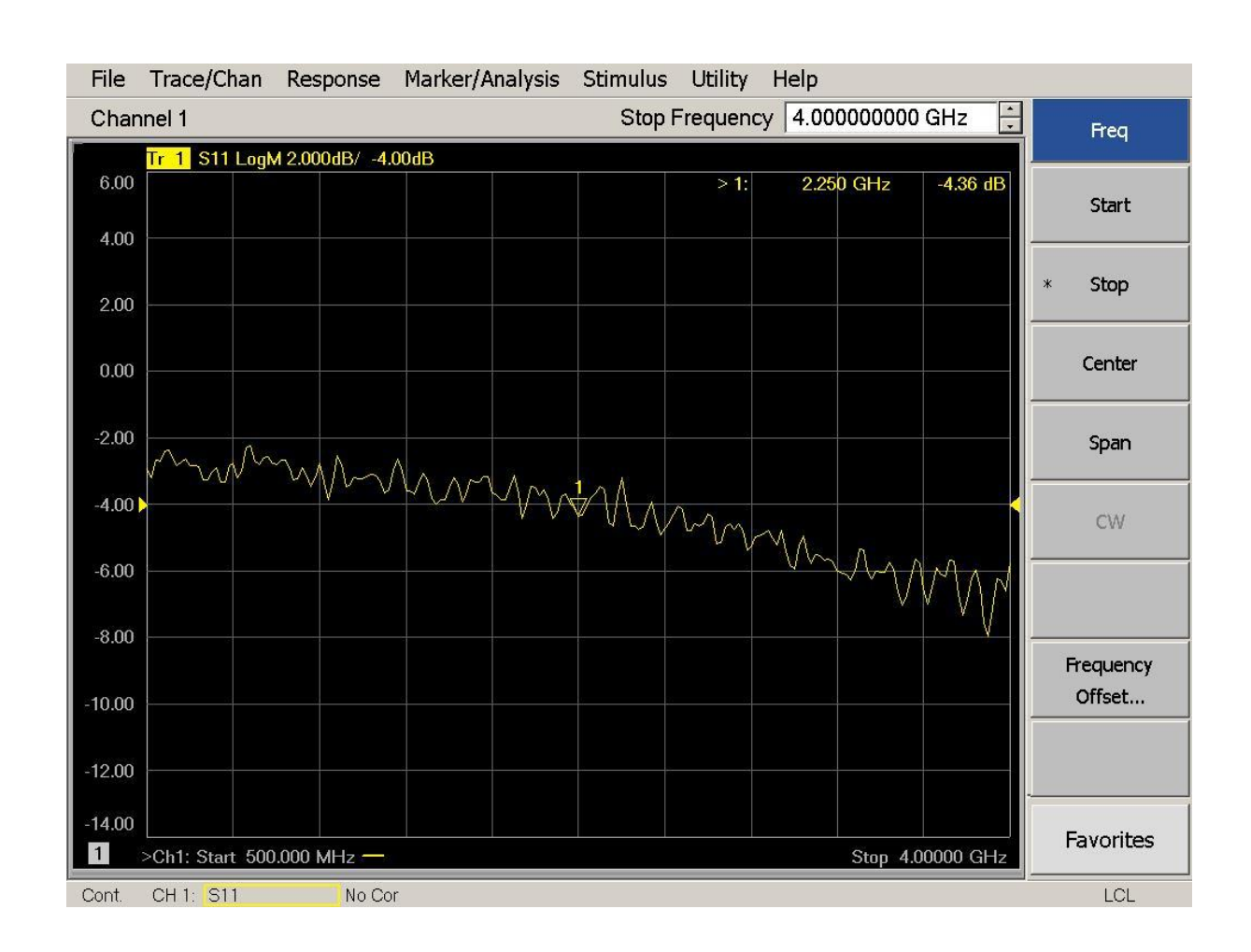


Figure.2.14. Uncalibrated  $S_{11}$  (dB) response.

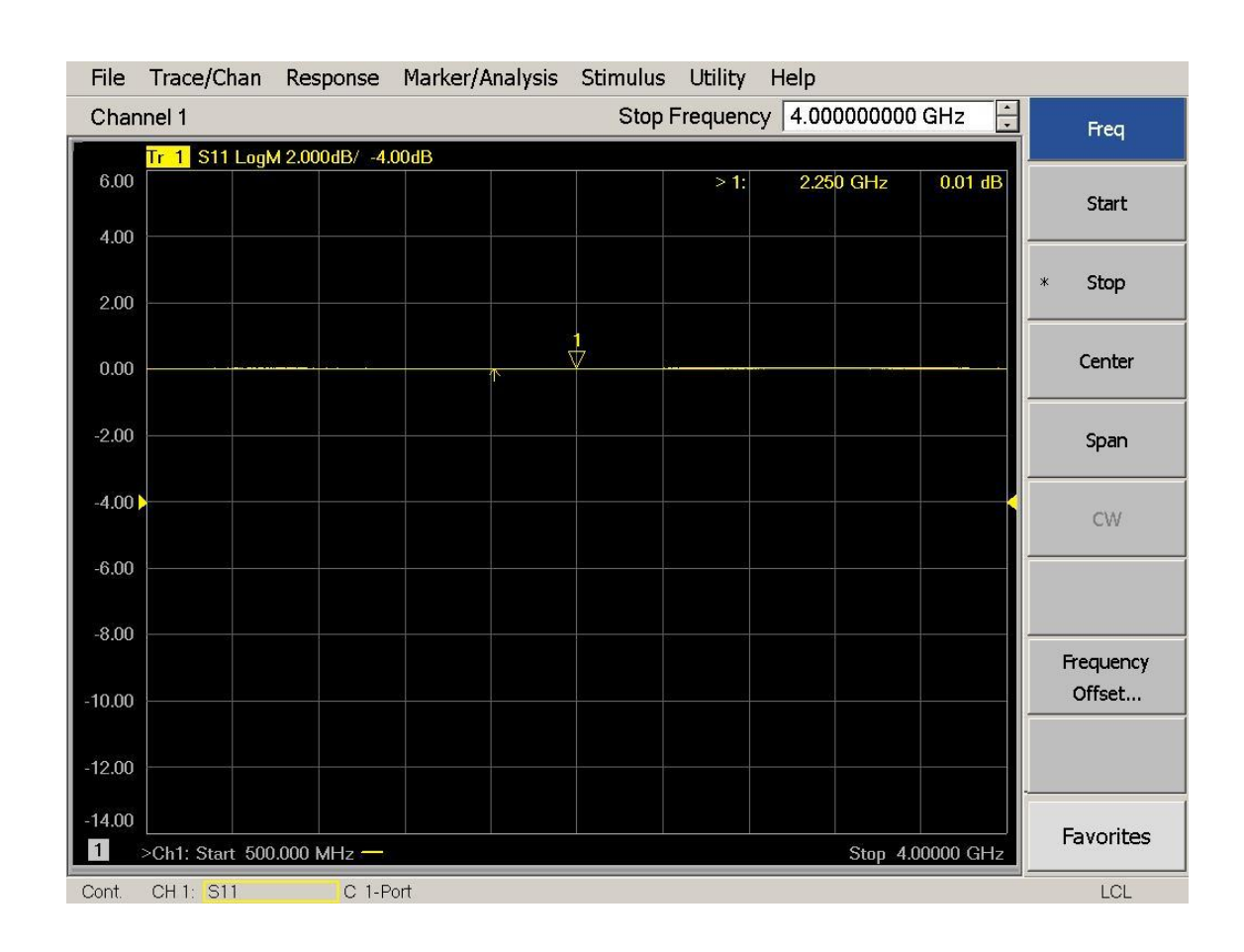


Figure.2.15. Calibrated  $S_{11}$  (dB) response.

# 2.6.4 De-embedding procedures

De-embedding can be broadly defined as any mathematical shifting of the electrical reference planes. Practically, the electrical characteristics of DUTs are not measurable at the reference plane of interest directly since they are mounted on a test fixture or the landing pads are further to the DUT itself. Hence, the ability to move the reference planes provides great assistance in microwave measurements, design and modelling. When the reference plane shifts closer to the DUT, it is de-embedding. And when the reference plane shifts away from the DUT, it is embedding. It is important to note that the calibration process is closely intertwined with the de-embedding concept [125].

By doing the calibration procedure on standard substrate as described in the previous Sec. 2.6.3, the electrical reference planes of the instrument ports can be shifted to the calibration planes, i.e., probes tip planes. In order to get the true behaviour of the DUT, the probe tip plane (after calibration) needs to be as close as possible to the ports of DUT. To better understand the de-embedding process, consider Fig. 2.16 which shows on-wafer measurement with the electrical reference planes specified.

To accurately measure the DUT in Fig. 2.16, two methods are described as follows [125]:

- Fabricate several on-wafer standards like open, short, load etc. embedded directly into the reference planes Y and Y'.
- 2) This has two steps: a) Calibration is performed till the probe tips (X and X') using calibration standards fabricated on other substrate (CS-5 substrate). This step is also called as "off-wafer calibration" (sec.2.6.3). b) Equivalent electrical models are used along with their dummy structure made on the wafer to remove effects of access transmission lines of the DUT. This second step in calibration is called the "deembedding procedure".

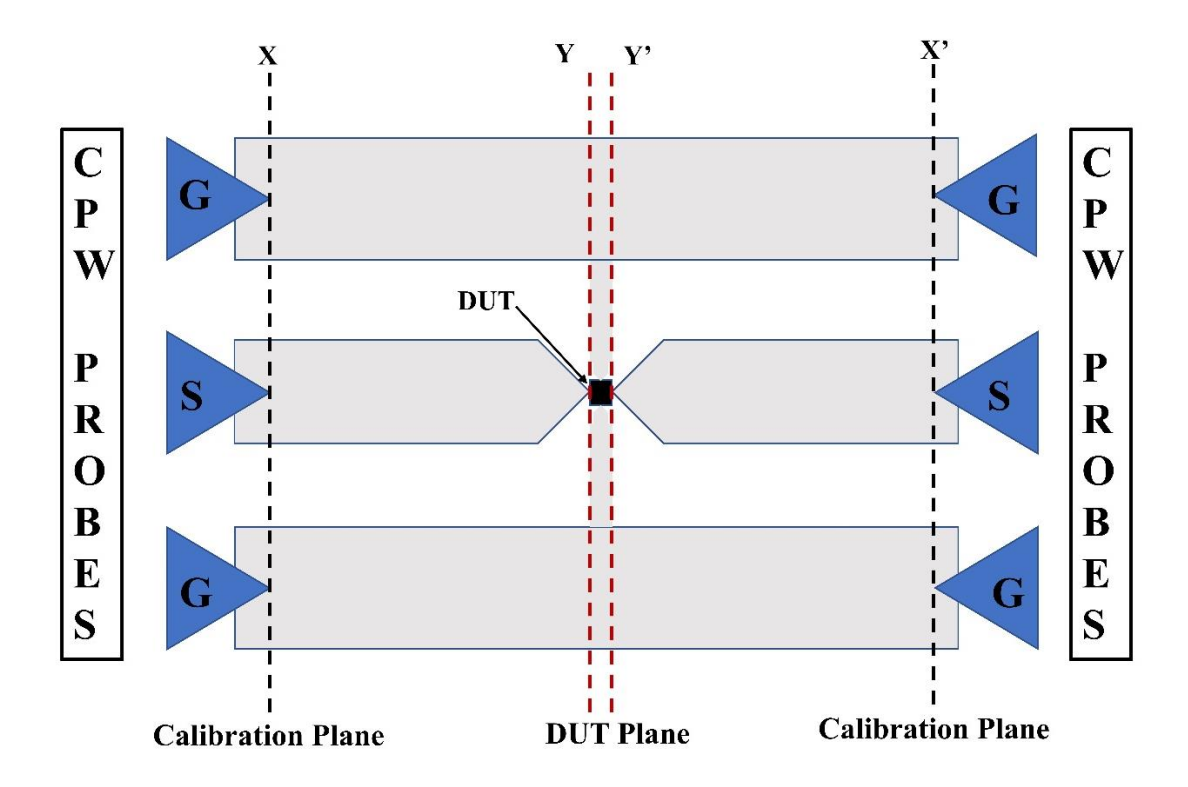


Figure 2.16. On-wafer probing of DUT showing the electrical reference planes.

Out of the two methods described, the second one is more widely used because the first method has various issues like difficulties in modelling if used in advanced silicon technologies in the millimetre wave frequency range.

As described in the fabrication steps, the design of the DUT, i.e., HBAR has been chosen such that it is easier during both fabrication and characterization. The HBARs discussed in this thesis are all 1-port devices and has the simple circular-patch-capacitor (CPC) structure. The basic advantage of this structure is that, the calibration plane (probe tip plane) coincides with the DUT port. Fig. 2.17 shows the On-wafer probing of the CPC structure. Because of this there is no need for the "de-embedding procedure" described above. Hence, the "off-wafer calibration" like SOLT calibration discussed in Sec. 2.6.3 is only required before the measurement of HBARs. Fig. 2.18 shows the response of an HBAR sample measured after calibration.

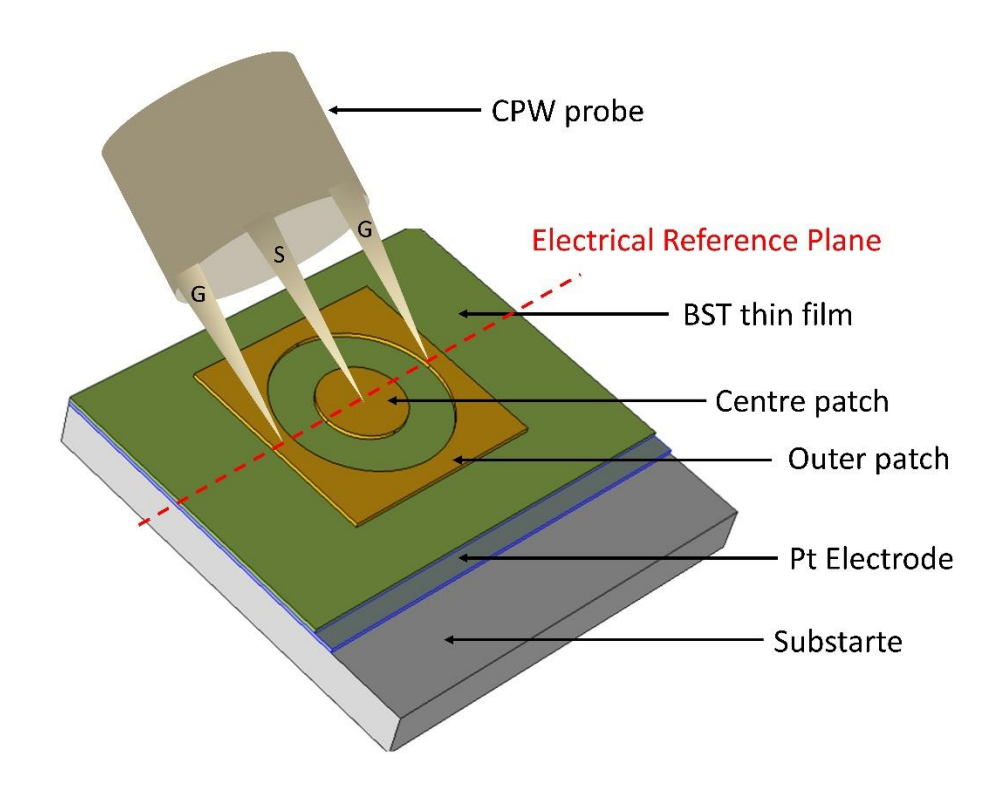


Figure 2.17 On-wafer probing of CPC structure of HBAR.

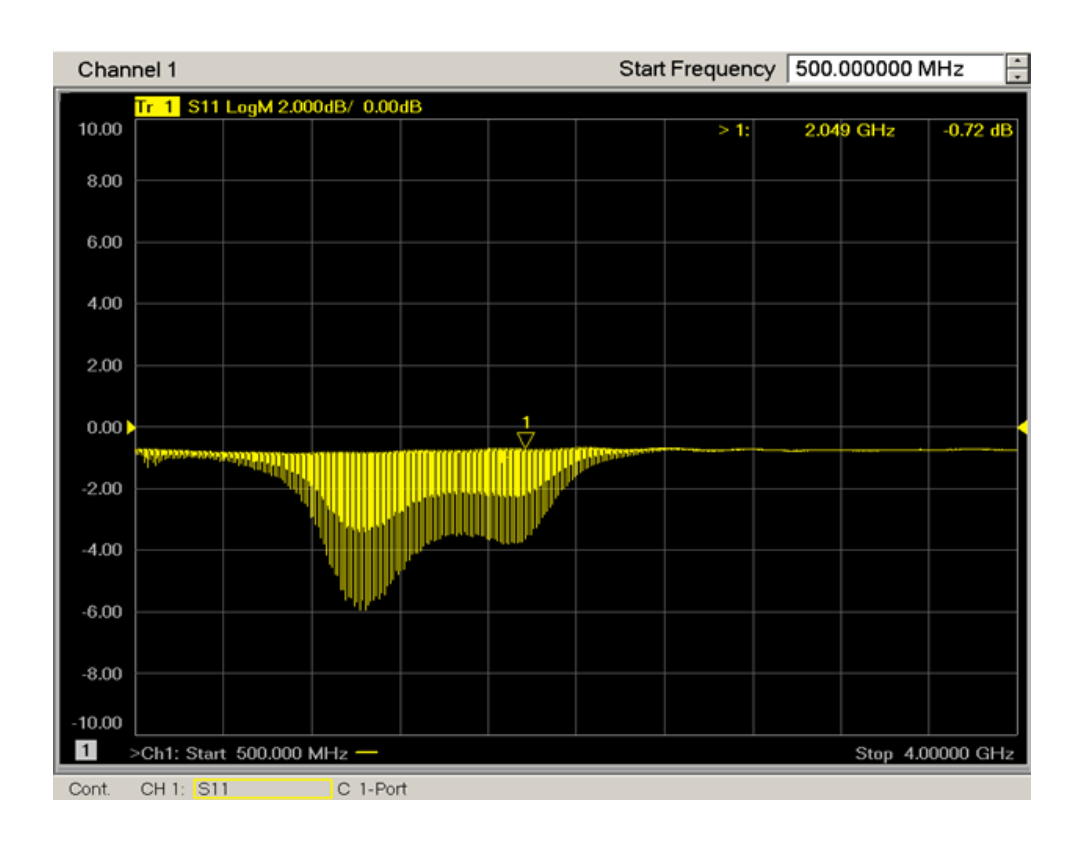


Figure.2.16. Measured DUT (HBAR) response after calibration.

#### 2.7 Software Used

This section discusses about the various software used in simulating various models of HBARs. Numerical simulations of HBAR models and experimental data processing of measured HBARs are done using MATLAB®, and both 2-D and 2-D axisymmetric HBAR models are simulated using COMSOL Multiphysics®.

#### **MATLAB®**

MATLAB® is a powerful tool used by many scientists and engineers all over the world for analyzing and designing systems and products which has wide applicability in automobiles, healthcare devices, communications, robotics, control systems, signal processing and more. MATLAB® is a dedicated platform for handling engineering and scientific problems. The code used in MATLAB® is a matrix-based language useful in expressing computational mathematics. The platform provides data visualization and tools for custom plots. Applications for various task such as data classification, curve fitting etc. are available. MATLAB® can be easily interfaced with various other software packages like C, C++, .NET, Java®, SQL, Python, Microsoft® Excel® etc. [126].

In this work, MATLAB® version R2018a is used for the numerical simulation of HBAR model which is discussed in the latter chapters. 1-D models of both HBAR and HBAR coated with additional layer are simulated using it. The equations which constitute the input impedance of the HBAR are written in MATLAB codes, and the responses are used for fitting with experimental results and for analysis. MATLAB® is not only used for numerical simulation but is also employed in analysis of experimental data. Extraction of series and parallel resonance frequencies from the frequency response is a major work carried out using MATALB®. The MATLAB® programs were used for numerical

simulation of HBAR models and extraction of experimental results from the measured data and are both given in Annexures.

# **COMSOL Multiphysics®**

COMSOL Multiphysics® is a powerful and versatile software package which provides an interactive platform used for modelling and solving numerous engineering and scientific issues or problems. This finite element analysis (FEA) based software helps in reducing the number of prototypes to be made and experiments to be performed in the designing, optimization or controlling stage of a device or process. Using an established FEA model which can predict the real-life behavior of a device or process, one can generate a significant understanding and intuition to improve a design and its working.

The basic working of such software is to express the laws of physics in terms of mathematical models. These laws are laws of classical mechanics, electromagnetism laws and different conservation laws. Partial differential equations (PDEs) are used to describe these physical laws and by solving the PDEs in a mathematical model, engineers and scientists can predict possible outcomes of an experiment. In such problems the PDEs of the models cannot be solved by analytical methods, instead numerical model equations are approximated from the PDEs by discretization. The solution to the model equations is again an approximation of the real solution to the PDEs. The finite element method (FEM) is used to handle and compute such kind of approximations [127].

COMSOL Multiphysics® offers various add-on modules such as electromagnetics, acoustics, heat transfer etc. which can be used individually or as coupled modules for simulating numerous engineering problems. For the 2-D and 2-D axisymmetric simulations of HBAR models reported in this thesis, the acoustic module of COMSOL Multiphysics® version 5.3 has been used.

# Chapter 3: Modelling of BST based High Overtone Bulk Acoustic Wave Resonators (HBAR)

#### 3.1 INTRODUCTION

This chapter deals with the design and modelling of the acoustic composite resonator also known as the High Overtone Bulk Acoustic Wave Resonator (HBAR) or the overmoded resonator. The HBAR discussed here is based on paraelectric phase ferroelectric thin film as the active layer in the transducer which is in a simple metal-insulator-metal (MIM) configuration. The high Q factor in the resonator is obtained by mounting the transducer onto a low acoustic loss (i.e., high mechanical Q) material like sapphire, YAG etc. This chapter discusses in details about the mechanism involved in exciting the Ba<sub>0.5</sub>Sr<sub>0.5</sub>TiO<sub>3</sub> films into acting like a piezoelectric material. The frequency spectra of the HBAR are extensively studied to derive various explicit formulae which comprise the resonant spectrum technique and is laid out such that it can be used in later chapters to extract the material parameter of the thin BST film. Numerical simulation is done from the formulae derived for the impedance of the HBAR which is further used to plot the spacing of parallel resonance frequency (SPRF) and effective coupling coefficient ( $k_{eff}^2$ ) which plays a major role in determining the material parameter extraction using the Resonant Spectrum Method (RSM).

#### 3.2 FIELD INDUCED PIEZOELECTRICITY MECHANISM IN BST

Ferroelectrics which maybe either in the ferroelectric (polar) or paraelectric phase are considered for applications in switchable and tunable resonators. In a dielectric material the electrostrictive strain,  $S = QP^2$  is a quadratic function of polarization, where Q is the electrostriction coefficient and P is polarization in the medium. For a ferroelectric phase material, the polarization includes spontaneous polarization ( $P_S$ ) along with polarization induced by the applied external DC and AC fields,  $P = P_S + P_{DC} + P_{AC}$ . Thus, the strain can be written as:

$$S = QP_{DC}^2 + QP_{AC}^2 + QP_S^2 + (2QP_{DC})P_{AC} + 2QP_SP_{DC} + 2QP_SP_{AC}$$
 (3.1)

The term  $QP_{DC}^2$  accounts for the constant strain due to an applied DC field or bias. The term  $QP_{AC}^2$  accounts for the alternating electrostrictive strain linked with the applied AC field. For cases where the spontaneous and the DC polarization is absent, this term accounts for the electrostrictive response in resonators.  $QP_S^2$  represents the spontaneous strain,  $2QP_SP_{DC}$  and  $2QP_SP_{AC}$  are the static and the alternating piezoelectric effects as linearized electrostriction, where  $g=2QP_S$ , is the piezoelectric voltage coefficient. When there is no applied DC field, the last term is linked to the generation of acoustic waves in polar phase ferroelectric resonators.  $(2QP_{DC})P_{AC}$  is the DC- induced piezoelectric effect specified by the DC- dependent piezoelectric coefficient,  $g_{DC}=2QP_{DC}$  and a linear dependence of the strain on AC polarization. Hence, from equation (3.1) it is clear that the applied AC field generates an oscillating strain (acoustic waves) and certain parameters like  $g_{DC}$  which are dependent on external DC field can be used for switching and tuning ferroelectric resonators [20].

# 3.2.1 Field dependence of material properties in ferroelectrics

The effect of external DC electric field on various piezoelectric and elastics properties of paraelectric phase ferroelectrics are considered and for simplicity of the model, only one component of each variable is considered and the system is regarded mechanically free. In order to get the full elucidation of the electrical switching and tuning of the electromechanical properties of ferroelectrics, the expansion of Landau free energy *P* incorporating nonlinear electrostriction is considered and generalized as below [128]:

$$F = \frac{\alpha_{ij}}{2} P_i P_j + \frac{\beta_{ijkl}}{4} P_i P_j P_k P_l + \frac{1}{2} c^0_{ijkl} S_{ij} S_{kl} - q_{ijkl} P_k P_l S_{ij} - \frac{1}{2} m_{ijklmn} P_m P_n S_{ij} S_{kl}$$
 (3.2)

where  $P_i$  is the ferroelectric part of the polarization,  $\beta_{ijkl}$  is the tensor of dielectric non-linearity,  $c^0_{ijkl}$  is the tensors of the elastic constant at constant P,  $S_{ij}$  is the tensor of strain,  $q_{ijkl}$  is tensor elements of linear electrostriction and  $m_{ijklpg}$  is the tensor elements of nonlinear electrostriction. The tensor component  $\alpha_{ij}$  is given below as:

$$\alpha_{ij} = \left(\chi_{ij}^{f0}\right)^{-1} \tag{3.3}$$

where  $\chi_{ij}^{f0}$  is the ferroelectric part of the susceptibility of the material at no DC bias field  $(E_{DC} = 0)$ .

The fundamental equations of the system can be derived using the following relations

$$\frac{\partial F}{\partial P_i} = E_i \tag{3.4}$$

$$\frac{\partial F}{\partial S_{ij}} = \sigma_{ij} \tag{3.5}$$

$$D_i = \varepsilon^b E_i + P_i \tag{3.6}$$

where  $E_i$  is the electric field,  $\sigma_{ij}$  is the stress tensor and  $\varepsilon^b$  is the background permittivity.

To see the electromecahnical nature of the system, the case of DC electric field  $E^{DC}$  superimposed with a comparatively smaller field  $E^{AC}$ , i.e.,  $E^{DC} >> E^{AC}$  is considered and hence all the variables are summed up to be of larger DC and small AC components written as below:

$$E^{tot} = E^{DC} + E^{AC} \tag{3.7}$$

$$P^{tot} = P^{DC} + P^{AC} \tag{3.8}$$

$$\sigma^{tot} = \sigma^{DC} + \sigma^{AC} \tag{3.9}$$

$$S^{tot} = S^{DC} + S^{AC} \tag{3.10}$$

The field dependent piezoelectric equations for  $E^{DC} = 0$  can be derived by linearization of equations (3.4) and (3.5) with respect to the AC components in equations (3.7) -(3.10) as:

$$E_{i} = \left(\chi_{ij}^{f}\right)^{-1} P_{j} - h_{ikl} S_{kl} \tag{3.11}$$

$$\sigma_{ij} = c_{ijkl}^P S_{kl} - h_{ijk} P_k \tag{3.12}$$

For the objective of simplifying the notation, the suffix "AC" is removed from the AC components. The piezoelectric tensor  $(h_{ijk},)$ , the ferroelectric contribution to susceptibility of the material  $(\chi_{ij}^f)$  and tensor of the elastic constant  $(c_{ijkl}^P)$  for constant P are given as a function of the polarization  $P^{DC}$  caused by the DC electric field as:

$$h_{ijk} = 2q_{iskl}P_S^{DC} (3.13)$$

$$c_{ijkl}^{P} = c_{ijkl}^{0} - m_{ijklmn} P_{m}^{DC} P_{n}^{DC}$$
 (3.14)

where,  $c_{ijkl}^0$  is the tensor of the elastic constant of the material without electric field. Only lower order terms of  $P^{DC}$  are used in equations (3.13) and (3.14). The induced polarization

due to  $P^{DC}$  and  $\chi_{ij}^f$  biased with this field is determined from (3.4) and (3.5) after eliminating the elastic variables. By keeping the lowest nonlinear term, the equation is given below:

$$E_i^{DC} = \alpha_{ij}^* P_i^{DC} + \beta_{ijkl}^* P_i^{DC} P_k^{DC} P_l^{DC}$$
 (3.15)

where the coefficients  $\alpha_{ij}^*$  and  $\beta_{ijkl}^*$  are dependent of the mechanical condition of the system. By considering the explicit expressions for the components of these tensors for thin film (in (100) and (111), orientation) on a substrate (clamped) [129],  $\chi_{ij}^f$  is given as:

$$\left(\chi_{ij}^{f}\right)^{-1} = \alpha_{ij}^{*} P_{j}^{DC} + 3\beta_{ijkl}^{*} P_{k}^{DC} P_{l}^{DC}$$
(3.16)

By changing the set of variables from "P,  $S \rightarrow E$ ,  $\sigma$ " to "E,  $S \rightarrow D$ ,  $\sigma$ ", the field dependent equations (3.11) and (3.12) are transformed to the standard form for use in thin film acoustic resonator (FBAR, SMR or HBAR) models as:

$$D_i = \varepsilon_{ij} E_j + e_{ijk} S_{jk} \tag{3.17}$$

$$\sigma_{ij} = c_{iikl}^E S_{kl} - e_{iik} E_k \tag{3.18}$$

where,  $\varepsilon_{ij}$  is the tensor of the clamped permittivity,  $c^E_{ijkl}$  is the tensor of the elastic constant for constant E and  $e_{ijk}$  is the tensor of the piezoelectric coefficients and are given by the relations below:

$$\varepsilon_{ij} = \varepsilon_{ij}^b + \chi_{ij}^f \tag{3.19}$$

$$c_{ijkl}^{E} = c_{ijkl}^{0} - m_{ijklmn} P_{m}^{DC} P_{n}^{DC} - h_{pij} \chi_{pq}^{f} h_{qkl}$$
 (3.20)

$$e_{ijk} = \chi_{is}^f h_{sjk} \tag{3.21}$$

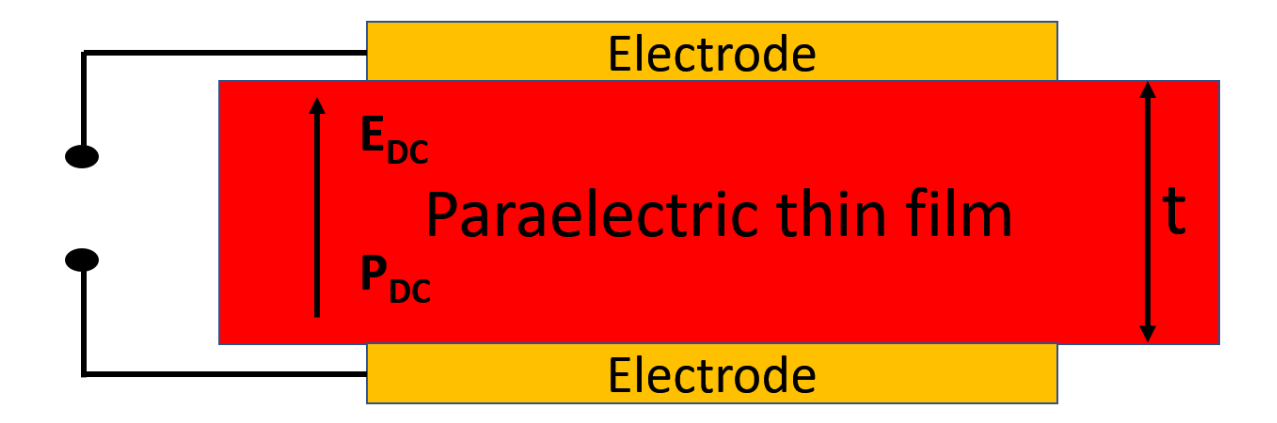


Figure. 3.1. Schematic of parallel plate transducer with TE mode.

Now in order to derive the field dependence on various parameters in a thickness extension (TE) mode resonator, a parallel plate capacitor structure comprising of the paraelectric thin film is taken into consideration and is shown in Fig. 3.1. Only the acoustic resonances linked to the thickness extension mode travelling in the thickness direction of cartesian (Z) axis is taken into consideration. This is possible only when a pure longitudinal acoustic wave is possible in this direction. In case of BST which is a paraelectric material, the condition is satisfied for epitaxial or textured films of (001), (111) and (110) orientations and polycrystalline films. So, for the schematic taken for this system, only z components of both the DC and AC fields are fitting. It is assumed that the film is clamped in the inplane and free to move in the out-of-plane direction. The electrodes in this case are considered as having zero mass.

Thus, the field dependent fundamental equations for the TE mode of the resonator can be laid out in Voigt notation as:

$$D_3 = \varepsilon_{33} E_3 + e_{33} S_3 \tag{3.22}$$

$$\sigma_{33} = c_{33}^E S_3 - e_{33} E_3 \tag{3.23}$$

where

$$e_{33} = \chi_{33}^f h_{33} \tag{3.24}$$

$$c_{33}^E = c_{33}^0 - m_{333} (P_3^{DC})^2 - h_{33} \chi_{33}^f h_{33}$$
 (3.25)

By using equations (3.22) - (3.25) and by taking into consideration the mechanical wave equation, mechanical boundary conditions and the Poisson equation, the admittance Y (or impedance Z) is derived as [130]:

$$Z(\omega) = \frac{1}{i\omega C_0} \left( 1 - k_t^2 \frac{\tan\left(\frac{kt}{2}\right)}{\left(\frac{kt}{2}\right)} \right)$$
(3.26)

where,  $\omega$  is the AC field angular frequency,  $C_0$  is the clamped or static capacitance, t is the thickness of the piezoelectric or ferroelectric thin film and k is the wave vector of the thickness extensional wave. The wave vector, the elastic constant  $c^D$  and the electromechanical coupling coefficient  $k_t^2$  are defined as:

$$k_t^2 = \frac{\omega}{\sqrt{c_{33}^D/\rho}} \tag{3.27}$$

$$c_{33}^D = c_{33}^E + \frac{e_{33}^2}{\varepsilon_{33}} \tag{3.28}$$

$$k_t^2 = \frac{e_{33}^2}{c_{33}^D \varepsilon_{33}} \tag{3.29}$$

By using equations (3.19) - (3.21) and (3.28),  $c^{D}$  at constant, D is expressed as:

$$c_{33}^{D} = c_{33}^{0} \left( 1 - \frac{m_{333}}{c_{33}^{0}} (P_{3}^{DC})^{2} - \frac{e_{33}^{2} \varepsilon_{33}^{b}}{\chi_{33}^{f} c_{33}^{0} \varepsilon_{33}^{3}} \right)$$
(3.30)

The relations for the parallel resonance ( $\omega_P$ ) and the series resonance frequency ( $\omega_S$ ) in Hz for the TE mode is given by [130]:

$$\omega_P = \frac{1}{2\pi t} \sqrt{c_{33}^D / \rho} \tag{3.31}$$

$$\omega_S = \frac{1}{2\pi t} \sqrt{(\pi^2 - 8k_t^2)c_{33}^D/\rho}$$
 (3.32)

The relation for the field dependence of the parallel and series resonance frequencies are derived by substituting equation (3.30) into equations (3.31) and (3.32). Simplification are done to get the realistic experimental situation and is given below:

$$\omega_P = \omega_0 \left[ 1 - k_t^2 \left( \gamma_t + \frac{\mu}{2} \right) \right] \tag{3.33}$$

$$\omega_{S} = \omega_{0} \left[ 1 - k_{t}^{2} \left( \gamma_{t} + \frac{\mu}{2} \right) - k_{t}^{2} \frac{4}{\pi^{2}} \right]$$
 (3.34)

where

$$\gamma_t \approx \frac{m_{333}}{8q_{33}^2 \varepsilon_{33}} \tag{3.35}$$

$$\mu \approx \frac{\varepsilon_{33}^b}{\varepsilon_{33}} \tag{3.36}$$

$$\omega_0 = \frac{1}{2t} \sqrt{\frac{c_{33}^0}{\rho}} \tag{3.37}$$

$$k_t^2 = \frac{4q_{33}^2 \varepsilon_{33}}{c_{33}^0} (P^{DC})^2 \tag{3.38}$$

From the above equations, the factor for switching and tuning DC field is included through two field dependent variables,  $\varepsilon_{33}(E^{DC})$  and  $P^{DC}(E^{DC})$ .  $\varepsilon_{33}(E^{DC})$  and  $P^{DC}(E^{DC})$  can be calculated by using an independent experiment or from (3.15) and (3.16) by neglecting the difference  $\varepsilon_{33}^f$  and  $\chi_{33}^f$  with the vectors  $E_i^{DC}$  and  $P_i^{DC}$  being set as (0.0  $E^{DC}$ ) and (0.0  $P^{DC}$ ) respectively.

# 3.2.2 The relation between relative tunability and the electromechanical coupling coefficient

The dependence of the electromechanical coupling coefficient to the DC electric field is one major attribute of a paraelectric based acoustic resonator like tunable FBARs or switchable HBARs. Within the limit of  $\varepsilon^b/\varepsilon << 1$ , the field dependence of  $k_t^2$  is related to the relative tunability of the dielectric permittivity  $T_r$  defined by [131]:

$$T_r = \frac{\varepsilon(0) - \varepsilon(E^{DC})}{\varepsilon(0)} \tag{3.39}$$

where  $\varepsilon(0)$  and  $\varepsilon(E^{DC})$  are the permittivity at zero bias field and under DC bias condition respectively. When non zero components of the field and polarization are taken for Z-axis and by using equations (3.3) and (3.16) and neglecting other background factors to the dielectric permittivity,  $\varepsilon(0)$  and  $\varepsilon(E^{DC})$  are given as:

$$\varepsilon_{33}(0) = \frac{1}{\alpha_{22}^*} \tag{3.40}$$

$$\varepsilon_{33}(E^{DC}) = \frac{1}{\alpha_{33}^* + 3\beta_{33}(P^{DC})^2}$$
 (3.41)

By using equations (3.39) -(3.41),  $T_r$  can be written as:

$$T_r = 3\beta_{33}\varepsilon_{33}(P^{DC})^2 (3.42)$$

So, by combining equations (3.38) and (3.42), the relation for relative tunability and coupling coefficient is given below:

$$k_t^2 = AT_r \tag{3.43}$$

$$A = \frac{4q_{33}^2}{3c_{23}^0\beta_{33}} \tag{3.44}$$

where *A* is the field dependent material parameter of the ferroelectric.

It is inferred from the above equations that the relative tunability of the permittivity of the ferroelectric film is proportional to the electromechanical coupling coefficient of the resonator, and hence better the tuning capability of permittivity the higher the coupling coefficient will be and hence more tuning of the resonance frequency. But there is another factor to the tuning of the resonant frequency which is the mechanical loading on the active layer. That is, with increase in mechanical load, the tunability of the resonant frequency decreases. Hence, in cases like HBAR, since the active BST layer is heavily loaded with the thick substrate, the tuning is negligible even though the coupling factor increases with increasing applied DC bias [128].

# 3.3 STUDY OF FREQUENCY SPECTRA OF HIGH OVERTONE BULK ACOUSTIC RESONATOR.

This section deals with the four- and five-layer model of an HBAR. These models lay the foundation for the characterization of the material properties of both the active layer or the coated layer (in case of five-layer model). This section describes the method to find out the impedance of the resonator and to study the parallel and the series resonances of the frequency spectra.

# 3.3.1 Resonant spectrum method

The resonant spectrum method is an indirect method to characterize the active thin film layer which is sandwiched between two electrodes forming a Metal-Insulator-Metal (MIM) capacitive structure mounted upon a low loss acoustic material [83,84,92]. By studying the frequency spectra of the composite resonator, three parameters of the active layer, i.e., the electromecahnical coupling coefficient, the elastic constant and the mass density can be extracted. Since a paraelectric material like BST is to be characterized, it is assumed that a DC electric field is applied across the capacitor along with the AC field as considered in the previous section, making the BST film to have induced piezoelectricity because of the electrostriction phenomenon and thus switching on the HBAR.

# 3.3.1.1 The impedance of a composite resonator (HBAR)

The HBAR structure has basically four layers, i.e., the two electrodes (bottom and top), the active transducer layer and the substrate. Fig. 3.2 shows the transfer matrix representation of a 4-layer composite resonator (HBAR). Transfer matrix approach is used for the derivation of the impedance of the HBAR [83]. Of the four layers, the top layer or the top electrode can be considered as having two acoustic port and its transfer matrix is given below:

$$\begin{bmatrix} F_0 \\ U_0 \end{bmatrix} = \begin{bmatrix} \cos \gamma_{e1} & j Z_{e1} \sin \gamma_{e1} \\ j \sin \gamma_{e1} / Z_{e1} & \cos \gamma_{e1} \end{bmatrix} \begin{bmatrix} F_1' \\ U_1' \end{bmatrix}$$
(3.45)

In the above equation F and U represent the force and displacement velocity respectively,  $Z_{el} = S\rho_{el}v_{el}$  is the acoustic impedance of the top electrode,  $\gamma_{el} = \omega l_{el}/v_{el}$  is the phase delay of the acoustic wave in the top electrode.  $\rho_{el}$ ,  $v_{el}$  and  $l_{el}$  are the density, acoustic velocity and thickness of the top electrode and S is the active area of the HBAR.

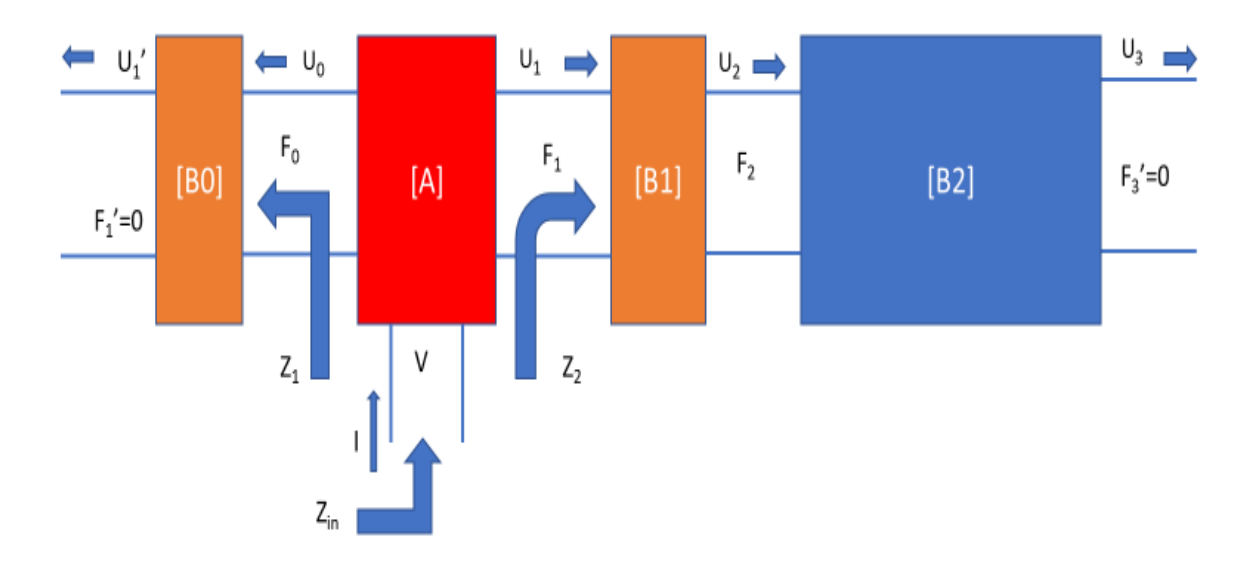


Figure 3.2. Transfer matrix representation of a composite resonator.

As seen from the Fig. 3.2, the left side of the top electrode is a free surface, i.e., it doesn't interact with any more layer and hence  $F_I$ '= 0. From this, the acoustic impedance of the top electrode which is attached to the left side of the active layer is derived by solving equation (3.45)

$$Z_1 = \frac{F_0}{U_0} = j \ Z_{e1} tan \gamma_{e1} \tag{3.46}$$

The bottom electrode has a similar form of transfer matrix as the top electrode as we have defined the direction of the displacement velocity U to be at opposite direction at each side of the active layer.

$$\begin{bmatrix} F_2 \\ U_2 \end{bmatrix} = \begin{bmatrix} \cos \gamma_{e2} & j \ Z_{e2} \sin \gamma_{e2} \\ j \sin \gamma_{e2} / \ Z_{e2} & \cos \gamma_{e2} \end{bmatrix} \begin{bmatrix} F_3 \\ U_3 \end{bmatrix}$$
(3.47)

Here,  $Z_{e2} = S\rho_{e2}v_{e2}$  is the acoustic impedance of the top electrode, and  $\gamma_{e2} = \omega l_{e2}/v_{e2}$  is the phase delay of the acoustic wave in the bottom electrode.  $\rho_{e2}$ ,  $\nu_{e2}$  and  $l_{e2}$  are the density, acoustic velocity and thickness of the bottom electrode. The transfer matrix of the substrate plate is the same as that of the top and the bottom electrode and is given as:

$$\begin{bmatrix} F_3 \\ U_3 \end{bmatrix} = \begin{bmatrix} \cos \gamma_{sb} & j Z_{sb} \sin \gamma_{sb} \\ j \sin \gamma_{sb} / Z_{sb} & \cos \gamma_{sb} \end{bmatrix} \begin{bmatrix} F_4 \\ U_4 \end{bmatrix}$$
(3.48)

where,  $Z_{sb} = S\rho_{sb}\nu_{sb}$  is the acoustic impedance of the top electrode,  $\gamma_{sb} = \omega l_{sb}/\nu_{sb}$  is the phase delay of the acoustic wave in the substrate plate.  $\rho_{sb}$ ,  $\nu_{sb}$  and  $l_{sb}$  are the density, acoustic velocity and thickness of the substrate.

From equations (3.47) and (3.48)

$$\begin{bmatrix} F_2 \\ U_2 \end{bmatrix} = \begin{bmatrix} \cos \gamma_{e2} & j Z_{e2} \sin \gamma_{e2} \\ j \sin \gamma_{e2} / Z_{e2} & \cos \gamma_{e2} \end{bmatrix} \cdot \begin{bmatrix} \cos \gamma_{sb} & j Z_{sb} \sin \gamma_{sb} \\ j \sin \gamma_{sb} / Z_{sb} & \cos \gamma_{sb} \end{bmatrix} \begin{bmatrix} F_3 \\ U_3 \end{bmatrix}$$
(3.49)

As seen from Fig. 3.2, it can be seen that the right side of the substrate is a free surface as there is no more layer underlaying the substrate and hence,  $F_4$ =0. The acoustic impedance of the middle electrode and the substrate involved in the right side of the active layer is given by solving equation (3.49)

$$Z_{2} = \frac{F_{2}}{U_{2}} = \frac{Z_{sb}tan\gamma_{sb} + Z_{e2}tan\gamma_{e2}}{1 - \left(\frac{Z_{sb}}{Z_{e2}}\right)tan\gamma_{e2}tan\gamma_{sb}}$$
(3.50)

Finally, the transfer matrix of the active layer is given by:

$$\begin{bmatrix} V \\ I \end{bmatrix} = [A] \cdot \begin{bmatrix} F_2 \\ U_2 \end{bmatrix} \tag{3.51}$$

The transfer function [A] of the piezoelectric thin film or that of ferroelectric thin film (induced piezoelectricity with applied dc bias) is obtained from the equivalent circuit analysis of Mason's in-line model,

$$[A] = \frac{1}{\emptyset H} \begin{bmatrix} 1 & j\emptyset^2/\omega C_0 \\ j\omega C_0 & 0 \end{bmatrix} \begin{bmatrix} \cos\gamma + jz_b\sin\gamma & Z_0(z_b\cos\gamma + jz_b\sin\gamma) \\ jz_b\sin\gamma/Z_0 & 2(\cos\gamma - 1) + jz_b\sin\gamma \end{bmatrix}$$
(3.52)

where  $\emptyset = k_t^2 C_0 Z_0 l/v$  is the transformer ratio in the Mason's equivalent circuit,

l is the thickness of the active ferroelectric layer,

v is the longitudinal acoustic wave velocity in the active ferroelectric layer along the direction normal to the resonator surface,

 $C_0 = \in S/l$  is the static/clamped capacitor of the resonator with area S,

 $Z_0 = S\rho v$  is the acoustic impedance of the active ferroelectric layer with density  $\rho$ ,

 $H=\cos \gamma -1 + j z_b \sin \gamma$ , where  $\gamma = \omega/lv$  is the phase delay of the acoustic wave in the ferroelectric film and  $\omega = 2\pi f$  is the angular frequency,

 $k_t^2$  is the coupling coefficient of the ferroelectric film at an applied bias voltage,

 $z_b=Z_b/Z_0$  is the normalized acoustic impedance of the backing material where  $Z_b$  is the acoustic impedance of the backing material.

By combining these equations, we get the electric input impedance of a composite resonator or the HBAR as given below:

$$Z_{in} = \frac{V}{I} = \frac{1}{j\omega C_0} \cdot \left[ 1 - \frac{k_t^2}{\gamma} \cdot \frac{(z_1 + z_2).sin\gamma + j.2(1 - cos\gamma)}{(z_1 + z_2).cos\gamma + j.(1 + z_1 z_2).sin\gamma} \right]$$
(3.53)

where  $z_1 = Z_1/Z_0$  and  $z_2 = Z_2/Z_0$  are normalized acoustic impedances of the top electrode layer and the bottom electrode substrate combination, normalized to the impedance of the ferroelectric layer.

By using the above equation (3.53), the magnitude of the impedance is plotted in Fig. 3.3. The parameter used for the numerical simulation is given in Table 3.1. The active area of the HBAR is defined by a circle of radius  $40 \, \mu m$ .

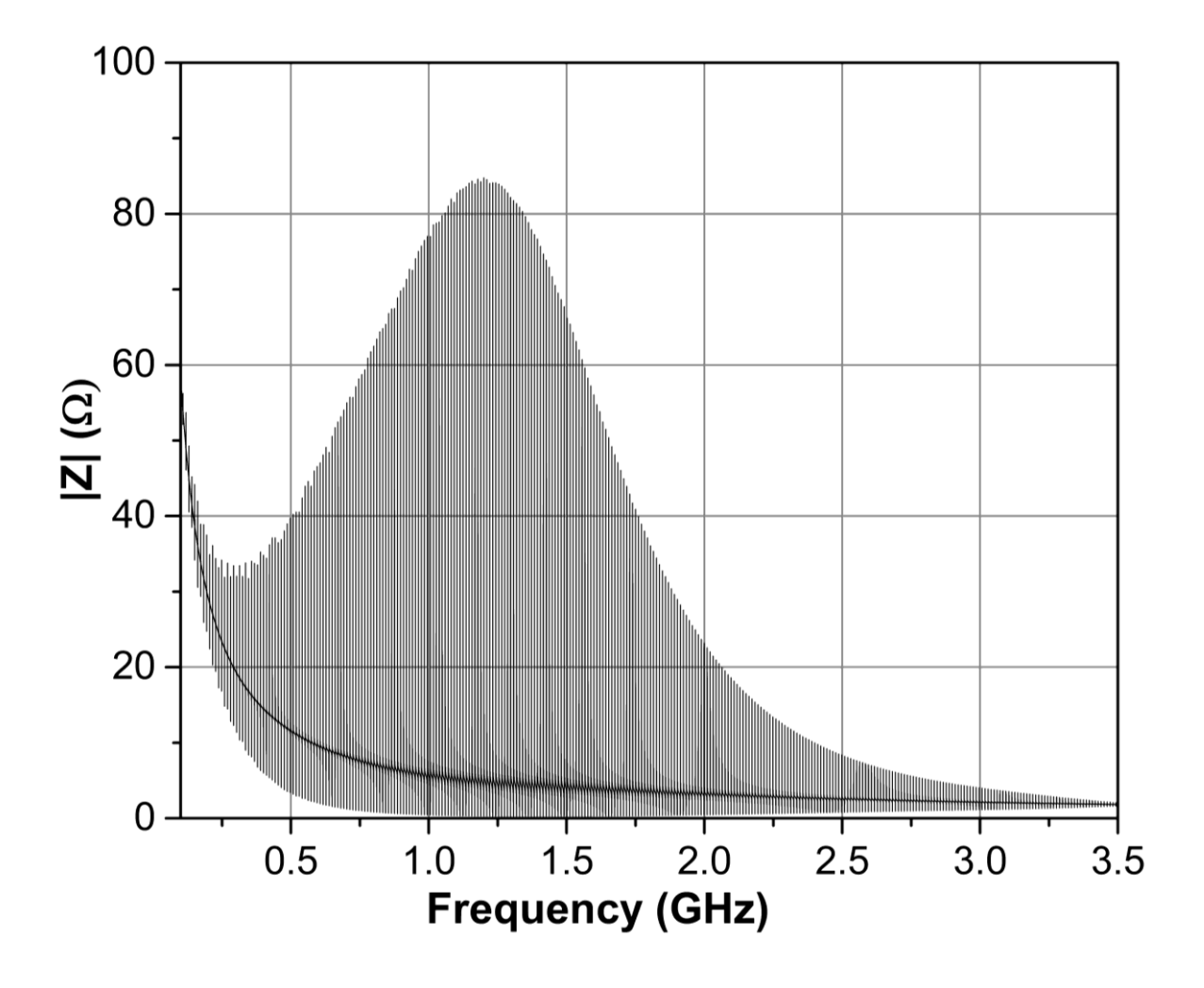


Figure 3.3. Frequency spectra of high overtone bulk acoustic resonator (HBAR)

It can be seen from Fig. 3.3 that the response has multiple resonances. These multiple resonances depend heavily on the acoustic properties of the materials and the thickness of the four layers. Due to the static capacitance ( $C_0 = \in S/l$ ) of the parallel plate MIM

capacitor structure, the impedance response has a hyperbolic decrease. And in region of the frequency response corresponding to the fundamental mode of the ferroelectric film, there are multiple resonant peaks present, each peak relates to a resonant mode of the HBAR. The static capacitance is related only with the hyperbolic decrease of the input impedance response and not with the resonant frequencies. On the other hand,  $k_t^2$  is related only with the resonant frequencies as in the case of a single piezoelectric plate.

Table 3.1: Material parameters used in simulation [84].

Material	ACOUSTIC VELOCITY (M/S)	Density (kg/m³)	Thickness (μm)	coupling coefficient $(k_t^2)$
BST	5088	5578	0.91	0.07
Platinum (Pt)	3300	21500	0.08	N. A
Gold (Au)	3200	19300	0.08	N. A
Sapphire (Al <sub>2</sub> O <sub>3</sub> )	8557 3993		450.59	N. A
Fused Silica	5973	2200	500	N. A
SU-8	2088	1100	2	N. A

# 3.3.1.2 Spacing of parallel resonant frequencies (SPRF) and effective coupling coefficient $k_{eff}^2(\mathbf{m})$

From the definition of IEEE standard, the parallel resonance frequency corresponds to the maximum of the real part of impedance. And the series resonance frequency corresponds to the maximum of the conductance [84]. So, by finding out the series and the parallel resonant frequency for every resonant peak present in the spectrum for the multimode composite resonator, the spacing of the parallel resonant frequencies (SPRF) is defined as:

$$\Delta f_p(m) = f_p(m+1) - f_p(m)$$
 (3.54)

The effective coupling coefficient of  $k_{eff}^2$  (m) for each resonant peak of the resonator is given as:

$$k_{eff}^{2}(m) = \frac{\pi^{2}}{4} \cdot \frac{f_{s}(m)}{f_{p}(m)} \cdot \left[1 - \frac{f_{s}(m)}{f_{p}(m)}\right]$$
(3.55)

where  $f_s$  (m) and  $f_p$  (m) are the m-order series and parallel resonance frequency respectively.

By using equations (3.54) and (3.55) the distribution of the SPRF and effective coupling coefficients ( $k_{eff}^2(m)$ ) are plotted in Figs. 3.4 and 3.5 respectively.

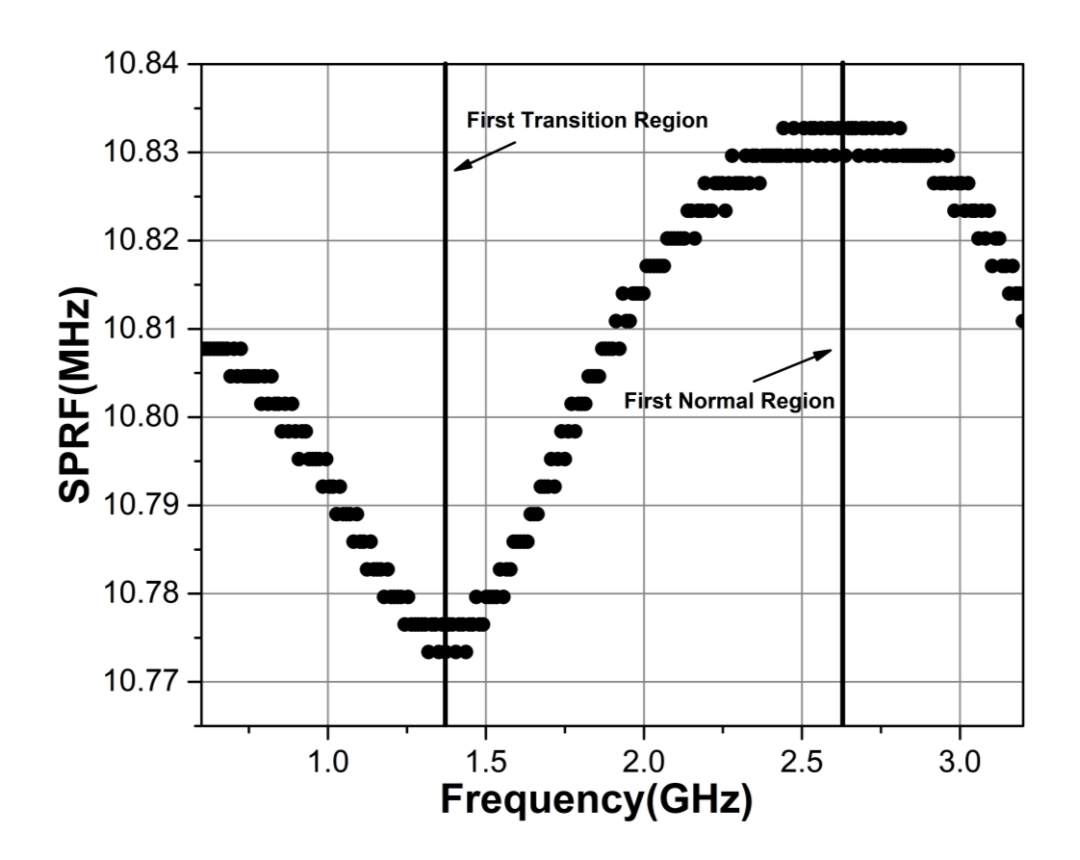


Figure 3.4. SPRF distribution of the high overtone bulk acoustic resonator (HBAR).

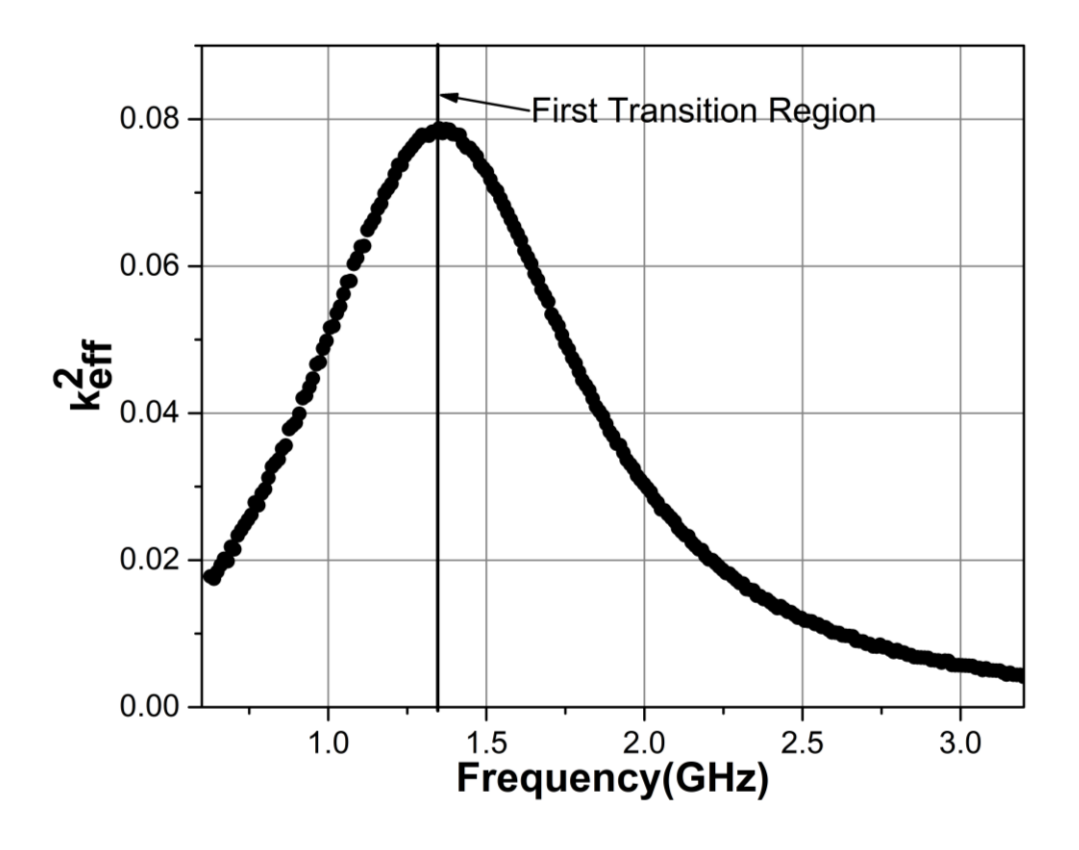


Figure 3.5.  $k_{eff}^2$  distribution of the high overtone bulk acoustic resonator (HBAR).

## 3.3.1.3 The first normal region, $\Delta f_N$ and coupling coefficient $k_t^2$

The normal regions are defined by the areas where  $\gamma$  is near to an integer multiple of  $\pi$  [83]. The SPRF, at the centre of the first normal region is given by:

$$\Delta f_N = f_p(m_N + 1) - f_p(m_N)$$

$$= \frac{1}{2} \frac{z_{sb}}{\left(\frac{z_{e1}l_{e1}}{v_{e1}} + \frac{z_{sb}l_{sb}}{v_{sb}} + \frac{z_{e2}l_{e2}}{v_{e2}} + \frac{l}{v}\right)}$$

$$= \frac{1}{2} \frac{\rho_{sb}v_{sb}}{\rho_{e1}l_{e1} + \rho_{sb}l_{sb} + \rho_{e2}l_{e2} + \rho l}$$

$$= \Delta f_0 \left(1 + \frac{\rho_{e1}l_{e1} + \rho_{e2}l_{e2} + \rho l}{\rho_{sb}l_{sb}}\right)^{-1}$$
(3.56)

From equation (3.56), the density of the active layer or the thin film ferroelectric in this case can be derived as:

$$\rho = \left(\frac{\rho_{sb}\nu_{sb}}{2\Delta f_N} - \rho_{sb}l_{sb} - \rho_{e1}l_{e1} - \rho_{e2}l_{e2}\right)/l \tag{3.57}$$

where  $\Delta f_0 = v_{sb}/2l_{sb}$  is the SPRF for the bare substrate layer which is a constant. This formula will be used in the following chapters to derive the mass density when all the other parameters are known.

Depending on the acoustic impedance of the substrate and the ferroelectric layer, substrates are categorised as

- 1) Soft substrate When  $Z_{sb} < Z_0$  (e.g., BST on fused silica),  $\Delta f_N$  relates to the first minimum of the SPRF.
- 2) Hard Substate When  $Z_{sb} > Z_0$  (e.g., BST on sapphire),  $\Delta f_N$  relates to the first maximum of the SPRF.

The coupling coefficient at the first normal region is given by:

$$k_t^2 = \frac{(1 + z_{sb} m_N)^2}{\left(1 + \frac{\rho_{e1} l_{e1} + \rho_{e2} l_{e2} + \rho_{sb} l_{sb}}{\rho l}\right)} k_{eff}^2(m_N + 1)$$
(3.58)

where  $z_{sb} = Z_{sb}/Z_0$ , the normalized acoustic impedance of the substrate.  $m_N$  is the mode order of the bare substrate layer, for most accurate calculation or extraction the mode with the maximum value of  $k_{eff}^2(m)$  is used. For the case of hard substrate, the maximum  $k_{eff}^2(m)$  lies in the first transition region and for soft substrate the maximum  $k_{eff}^2(m)$  lies in the first normal region. So, for half substrate the response corresponds to a quarter wavelength resonator and for soft substrate, the response corresponds to a half wavelength resonator.

To find the mode order  $m_N$ , a ratio R is defined as the ratio of the half wavelength resonant frequency of the top resonator  $(f_c)$  (only the transducer) to the half wavelength resonant frequency of the substrate  $(f_{sb})$  as:

$$R = \frac{f_c}{f_{sb}} = \frac{v(l_{sb} + 0.5\frac{\rho_{e2}l_{e2}}{\rho_{sb}})}{v_{sb}(l + \frac{\rho_{e1}l_{e1}}{\rho} + 0.5\frac{\rho_{e1}l_{e1}}{\rho})}$$
(3.59)

From the above equation, the mode order  $m_N$  at the centre of the first normal region is given by:

$$m_N$$
=the nearest integer of  $R$  (3.60)

If the value of R is near to an integer or is large enough that the fractional part can be ignored then, equation (3.58) can be written simply as:

$$k_t^2 = \frac{\rho l(\rho l + \rho_{e1} l_{e1} + \rho_{e2} l_{e2} + \rho_{sb} l_{sb})}{(\rho l + \rho_{e1} l_{e1} + 0.5 \rho_{e2} l_{e2})^2} \cdot k_{eff}^2(m_N + 1)$$
(3.61)

### 3.3.1.4 The first transition region, $\Delta f_T$ and coupling coefficient $k_t^2$

The transition regions are defined by the areas where  $\gamma$  is near to a half integer multiple of  $\pi$ . The SPRF, at the centre of the first transition region is given by [83]:

$$\Delta f_T = \Delta f_0 \left( 1 + z_{sb} \frac{v_{sb}l}{vl_{sb}} + \frac{z_{sb}v_{sb}l_{e2}}{z_{e2}v_{e2}l_{sb}} + z_{sb}z_{e1} \frac{v_{sb}l_{e1}}{v_{e1}l_{sb}} \right)^{-1}$$
(3.62)

From equation (3.62), the acoustic velocity of the ferroelectric thin film can be derived as:

$$v = \sqrt{\left(\frac{v_{sb}^2 \rho_{sb}l}{\rho l_{sb}} + \frac{v_{sb}^2 \rho_{sb} \rho_{e1} l_{e1}}{\rho^2 l_{sb}}\right) / \left(\frac{v_{sb}}{2 l_{sb} \Delta f_T} - 1 - \frac{v_{sb}^2 \rho_{sb} l_{e2}}{\rho_{e2} l_{sb} v_{e2}^2}\right)}$$
(3.63)

By using equations (3.57) and (3.63), the elastic constant is calculated as:

$$c_{33}^D = \rho v^2 (3.64)$$

The coupling coefficient at the first normal region is given by:

$$k_t^2 = \frac{\left[\frac{2m_T + 1}{z_{sb}} + 1\right]^2}{\left(1 + \frac{\rho v^2}{\rho_{sb} v_{sb}^2} \frac{l_{sb}}{l} + \frac{\rho v^2}{\rho_{e2} v_{e2}^2} \frac{l_{e2}}{l} + \frac{\rho}{\rho_{e1}} \frac{l_{e1}}{l}\right)} \frac{k_{eff}^2(m_T + 1)}{\Gamma}$$
(3.65)

where  $(m_T + 1)$  is the mode order at the centre of the first transition region,  $m_T$  is given as:

$$m_T$$
= the nearest integer of  $\left(\frac{R-1}{2}\right)$  (3.66)

When  $m_T$  is close to an integer or is very large such that the fractional part can be neglected, (3.65) is simply written as:

$$k_t^2 = \frac{1 + \frac{\rho_{e1} l_{e1}}{\rho l} + \frac{\rho v^2}{\rho_{sb} v_{sb}^2} \frac{l_{sb}}{l} + \frac{1}{2} \left( \frac{\rho^2 v^2}{\rho_{sb}^2 v_{sb}^2} + 1 \right) \frac{\rho_{e2} l_{e2}}{\rho l}}{\left( 1 + \frac{\rho_{e1} l_{e1}}{\rho l} + \frac{1\rho_{e2} l_{e2}}{2} \frac{\rho l}{\rho l} \right)^2} \frac{k_{eff}^2 (m_T + 1)}{\Gamma}$$
(3.67)

The correction factor  $(\Gamma)$  is introduced due to the difference between the first transition region centre and the  $(m_T+1)$  mode series resonance frequency and is given by:

$$\Gamma = 1 - 2 \frac{\rho v}{\rho_{sb} v_{sb}} \left( 1 + \frac{2\pi f_s l}{v} - \frac{\pi}{2} \right) \cdot \left( 2\pi f_s \left( \frac{l_{sb}}{v_{sb}} + \frac{\rho_{sb} v_{sb} l_{e2}}{\rho_{e2} v_{e2}^2} \right) - \left( m_T + \frac{1}{2} \right) \pi \right)$$
(3.68)

#### 3.3.2 The impedance of HBAR with a coated material

For modelling a five-layer HBAR by considering the additional material on the backside of the substrate, the four-layer case [83] is extended and the electrical input impedance of five-layer composite resonator is given in [132]. A schematic matrix model of the five-layer composite resonator is shown in Fig.3.6. The impedance,  $Z_a$  of the top electrode at the left side of the BST film and the impedance,  $Z_3$  of the SU-8 layer are given below:

$$Z_a = jZ_{Au} \tan \gamma_{Au} \tag{3.69}$$

$$Z_3 = j Z_{SU-8} \tan \gamma_{SU-8} \tag{3.70}$$

where  $Z_{Au} = A\rho_{Au}V_{Au}$  and  $Z_{SU-8} = A\rho_{SU-8}V_{SU-8}$  are the acoustic impedances of the top electrode and the SU-8 layer respectively.

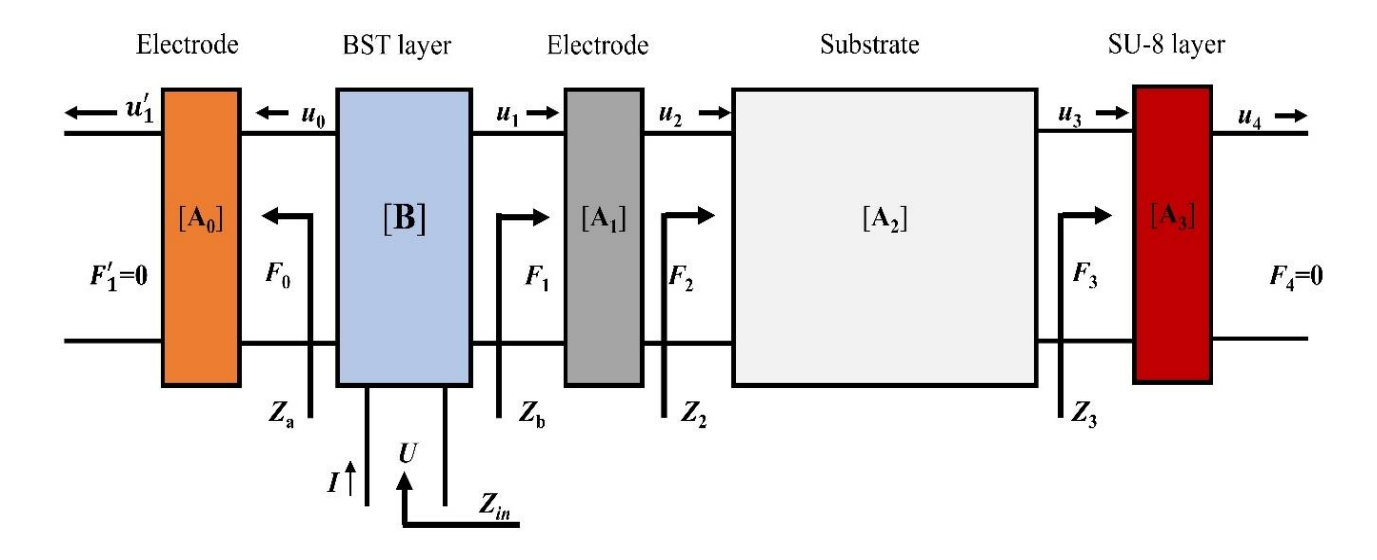


Figure 3.6: Schematic of five-layer composite resonator (HBAR).

The impedances  $Z_2$  and  $Z_b$  are given below:

$$Z_{2} = j \frac{Z_{SU-8} \tan \gamma_{SU-8} + Z_{S} \tan \gamma_{S}}{1 - \left(\frac{Z_{SU-8}}{Z_{S}}\right) \tan \gamma_{SU-8} \tan \gamma_{S}}$$
(3.71)

$$Z_b = j \frac{Z_2 + j Z_{Pt} \tan \gamma_{Pt}}{1 + j \left(\frac{Z_2}{Z_S}\right) \tan \gamma_{Pt}}$$
(3.72)

where  $Z_S = A\rho_S V_S$  and  $Z_{Pt} = A\rho_{Pt} V_{Pt}$  are the acoustic impedances of the substrate and the bottom electrode respectively. The electrical input impedance of the five-layer HBAR is thus given as:

$$Z_{in} = \frac{1}{j\omega C_0} \left[ 1 - \frac{k_t^2}{\gamma} \frac{(Z_x + Z_y)\sin\gamma + j2(1 - \cos\gamma)}{(Z_x + Z_y)\cos\gamma + j(1 + Z_x Z_y)\sin\gamma} \right]$$
(3.73)

where  $Z_x = Z_a/Z_0$  and  $Z_y = Z_b/Z_0$  are the normalized acoustic impedance of the top and bottom side of BST thin film layer and  $Z_0 = A\rho V$  is the acoustic impedance of the BST thin film layer;  $\gamma = \omega l/V$ ,  $\gamma_{Au} = \omega l_{Au}/V_{Au}$ ,  $\gamma_S = \omega l_S/V_S$ ,  $\gamma_{Pt} = \omega l_{Pt}/V_{Pt}$  and  $\gamma_{SU-8} = \omega l_{SU-8}/V_{SU-8}$  are the phase delay of the BST film, the top electrode, the substrate, the bottom electrode and the SU-8 layer respectively;  $\omega$  is the angular frequency;  $V_{Au}$ ,  $V_{Pt}$ ,  $V_{SU-8}$ ,  $V_{SU-8}$  are the acoustic wave velocity of the top electrode, the bottom electrode, the substrate and the SU-8 layer respectively;  $\rho_{Au}$ ,  $\rho_{Pt}$ ,  $\rho_S$ ,  $\rho_{SU-8}$  are mass density of the top electrode, the bottom electrode, the substrate and the SU-8 layer respectively;  $l_{Au}$ ,  $l_{Pt}$ ,  $l_{SU-8}$  are the thickness of the top electrode, the bottom electrode, the substrate and the SU-8 layer respectively;  $l_{Au}$ ,  $l_{Pt}$ ,  $l_{SU-8}$  are the thickness of the top electrode, the bottom electrode, the substrate and the SU-8 layer respectively;  $l_{Au}$ ,  $l_{Pt}$ ,  $l_{SU-8}$  are the thickness of the top electrode, the bottom electrode the BST film, the area of the top electrode and the static capacitance respectively.

By using the parameters from Table 3.1 in equation (3.73), and by numerical simulation of the model the input impedance of the HBAR with a coated material (SU-8) is plotted in Fig. 3.7. It can be seen from the figure that due to the introduction of a new layer in the system, the previous response has changed and there are perturbations in the frequency

response defined by the acoustic property and the thickness of the new material coated on the backside.

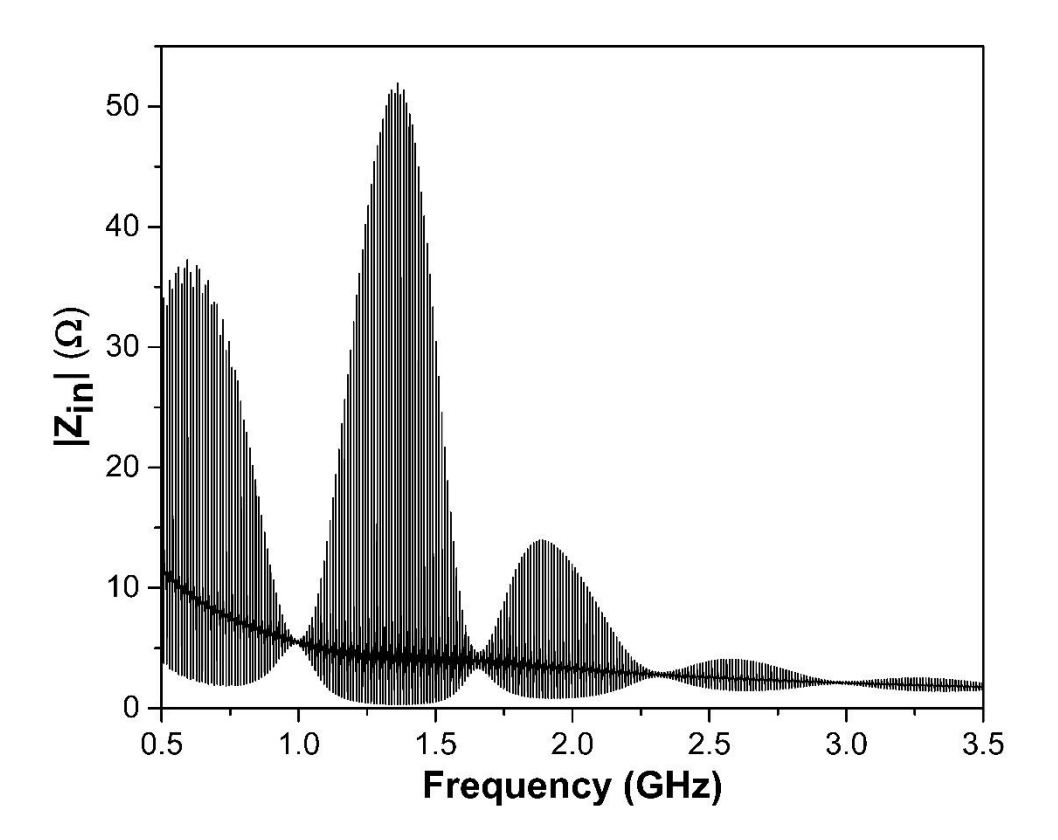


Figure 3.7. Frequency spectra of HBAR with SU-8 coated on backside.

By using equations (3.54) and (3.55), the SPRF and  $k_{eff}^2$  distributions for this case can be extracted for each and every mode of the HBAR with a coated polymer (SU-8) on the backside of the substrate and are plotted in Fig. 3.8 and 3.9 respectively.

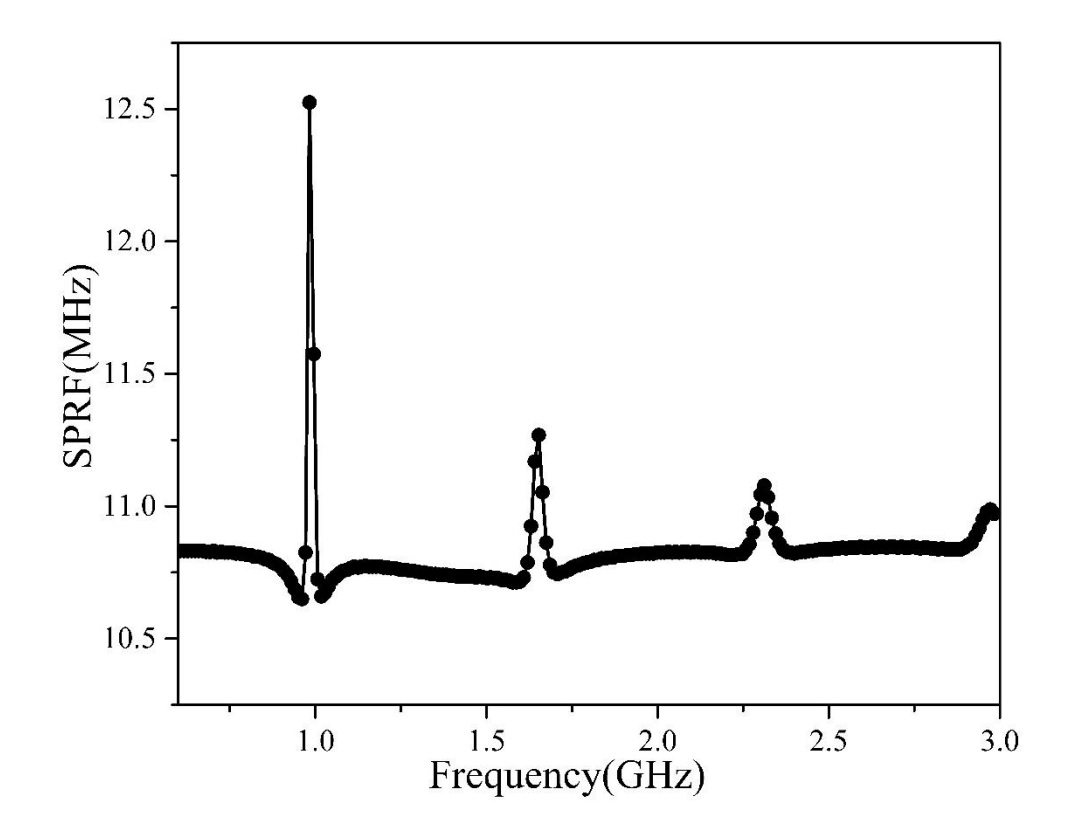


Figure 3.8. SPRF distribution of HBAR with coated material (SU-8).

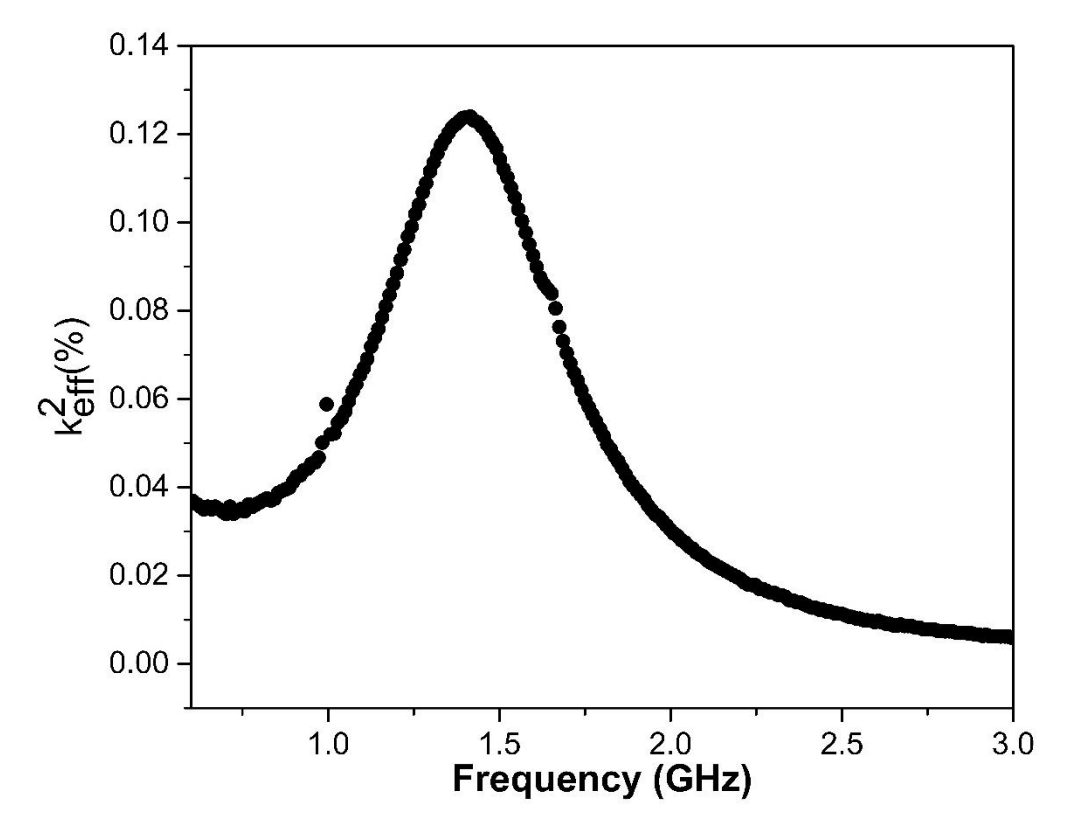


Figure 3.9.  $k_{eff}^2$  distribution of HBAR with coated material (SU-8).

Comparing the plots for the HBAR with and without a coating in the backside of the substrate, it is seen that there is significant change in the shape of the envelope of the impedance plot with and without the coating. Apart from the envelope due to the thin film BST, a new envelope is present in the spectra because of the deposition of an additional layer in the system. In the case of SU-8 coated HBAR, there appears to be certain specific areas in the spectrum wherein the intensity of the impedance has dropped considerably low as compared to the uncoated case. And they come across at a regular interval. There is also significant change in the SPRF distribution of the HBAR with SU-8 coating. From this observation, it can be inferred that just as the substrate of the HBAR determines the spacing between each adjacent resonant peak/mode, the thickness and the acoustic properties of the coated material determines the spacing between the modulated area in the spectrum. And this new interval can be calculated as:

$$\Delta f_c = \frac{v_c}{2.t_c} \tag{3.74}$$

This nature of response will be discussed in detail when considering the experimental results in the following chapters.

#### 3.4 Summary and Conclusions

In summary,

- The mechanism of how BST thin film exhibits induced piezoelectric behaviour due to
  electrostriction which occurs due to the external dc bias field applied across the
  ferroelectric thin film in its paraelectric phase is established.
- 2. The relation between the coupling coefficient of the thin film and the relative tunability of the thin film is established.
- 3. The model for the impedance of the HBAR which gives the frequency spectra of the resonator is derived and from this the SPRF and  $k_{eff}^2$  distribution of the composite resonator is obtained.
- 4. The resonant spectrum method which gives the formulae for deriving the acoustic velocity and coupling coefficient of the thin film is derived.
- Numerical simulation for the HBAR with a coated material on its backside is also performed.

From the above foundation laid out in this chapter, in the following chapters, these modelling and formulae will be used to correlate with the experimental results thereby giving a better understanding of the various mechanisms on how the HBAR works and how certain parameters are affected by conditions such as dc bias, mass loading or acoustic impedance change.

# Chapter 4: Characterization of BST based High Overtone Bulk Acoustic Wave Resonators (HBAR)

#### 4.1 INTRODUCTION

The use of piezoelectric thin films in fabrication of surface acoustic wave (SAW) and bulk acoustic wave (BAW) resonators has led to an advancement in RF filter designs and sensing applications. BAW resonators in particular have been prominent in the market due to its applicability in higher frequency range with improved performances as compared to SAW technology. The main category of BAW resonators, i.e., the thin film bulk acoustic wave resonator (FBAR) and the solidly mounted resonators (SMR) use piezoelectric films such as ZnO, AlN and PZT mainly due to the high coupling coefficients the thin film exhibits which is a key performance factor in RF filter design [133-137]. The properties of such conventional piezoelectric thin films could not be tuned either efficiently or significantly. Tuning the frequency of the resonators is becoming a very important factor in today's filter technology due to the constraints in device size and the ever-increasing demand for more frequency band specially in mobile communications and software defined radios (SDR). But with the introduction of new materials like BST, which is a ferroelectric material in the paraelectric phase, tuning has been made possible by application of DC bias [20,138-144]. One challenge is to characterize the thin film before application into FBAR or SMR. For example, in piezoelectric thin films, a composite resonator or HBAR that uses that film can be used to characterize the thin film by using a technique called the resonant spectrum method (RSM) (details in Chapter 3). In this chapter different types of HBAR are fabricated and characterized. Out of the different types of HBARs fabricated, two types in particular, i.e., the HBAR with sapphire and YAG (Yttrium Aluminium Garnet) substrate are characterized and studied by using both RSM and numerical simulation to extract material parameters of the active ferroelectric thin film. From the characterization, the material parameters of BST, i.e., mass density, acoustic velocity, elastic constant and coupling coefficient are extracted. Further, the effect of DC bias on the coupling coefficient and the Q factor of the resonators are studied and the relation between the relative tunability and the coupling coefficient is established. In the work reported in this chapter a very high  $Q \approx 30,000$  at a frequency around 2 GHz is observed in resonant modes of HBAR which can be used in designing oscillators and sensors or as phonon source in QAD systems. The work reported here is the first time where BST has been characterized using the RSM technique [84].

#### 4.2 Sample preparation and experimental set-up

The fabricated HBAR samples are based on ferroelectric film BST which are in the paraelectric phase. The basic structure of the device is a Metal-Insulator-Metal (MIM) structure mounted on a high Q double side polished substrate. The fabrication steps of the resonator have been given in detail in Chapter 2. In this chapter, to study the nature of the HBAR, different types of HBARs are fabricated on silicon, fused silica, sapphire and YAG. Using RF magnetron sputtering technique, metallization is done for both the top and the bottom electrodes and PLD technique is used to deposit the thin film of BST which is of thickness around 1 µm. The top electrode (40 µm radius – inner circle, and 300 µm diameter- outer circle) is patterned as a circular patch capacitor (CPC) in order to reduce the complexity in fabrication and is shown in Fig. 4.1. A simple measurement setup is shown in Fig. 4.2. In this type of device structure, the signal line of the CPW probe lands on the centre circular patch which will function as the top electrode of the capacitor while the ground lines of the CPW probe lands on the metal outside the patch which effectively functions as the ground plane. This technique, therefore, does not need any contact to be

made to the actual bottom electrode thereby making no requirement for the dielectric film to be patterned. The electrical pathway to the bottom platinum electrode of the MIM structure is established by the large capacitor formed in between the bottom metal electrode layer and the large outer top ground patch. When compared to this capacitance, the capacitance due to the capacitor formed by the top circular patch and the ground metal electrode is much smaller, hence, the response of the circuit is overall dominated by the smaller capacitor [145].

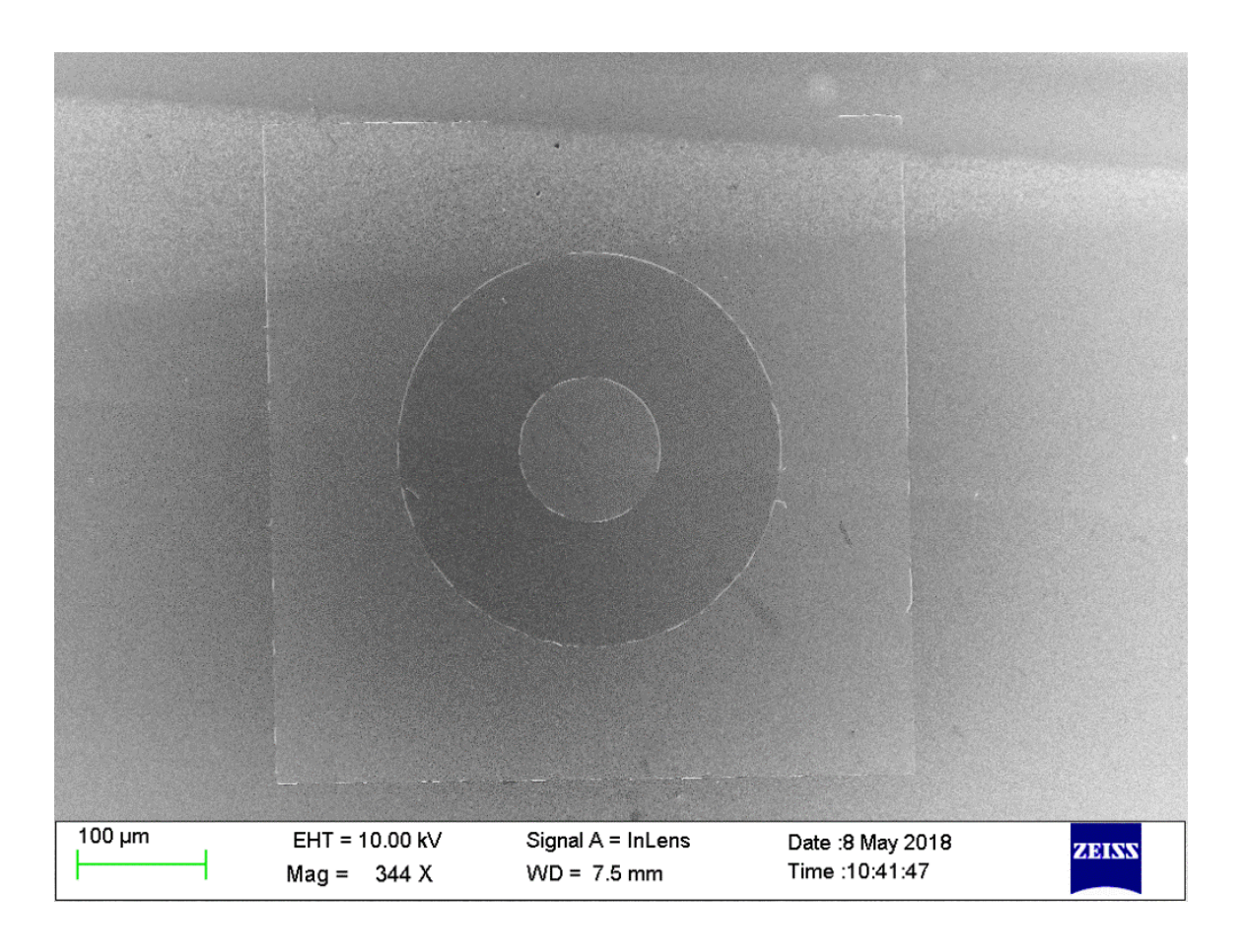


Figure 4.1. FESEM of Top electrode of fabricated HBAR.

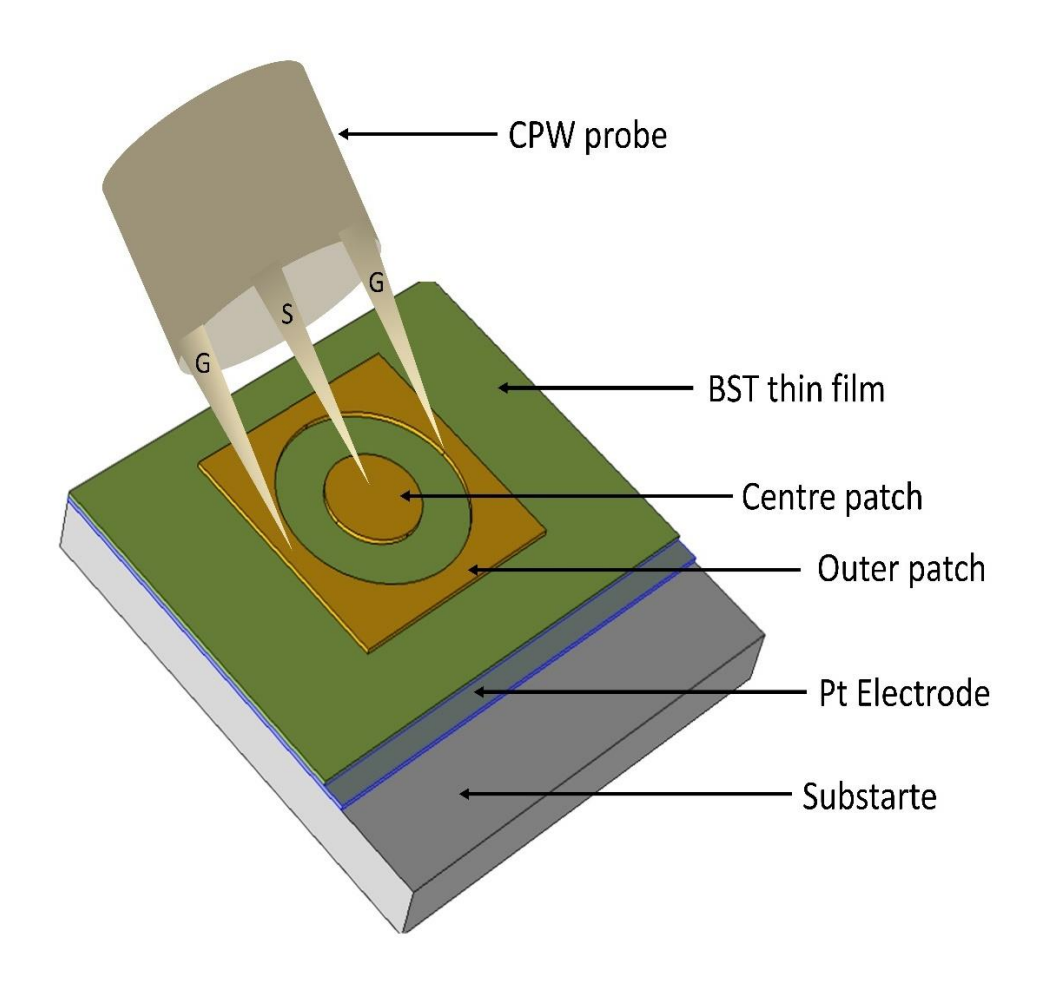


Figure 4.2. Probing set-up for the HBAR. Only the top electrode is patterned.

The HBARs are measured using on-wafer probing technique with a 250 µm pitched Ground-Signal-Ground probe (GGB Industries) and an Agilent E8361C Vector Network Analyzer (VNA). Calibration is done before the measurement using standard CS-5 substrate (GGB Industries) for the circuit elements short, open and load. One port S-parameter (S<sub>11</sub>) is measured for the calibrated frequency range for all the samples with and without DC bias voltages (using a DC bias tee) for further study. For all the cases of measurements, the number of data points taken for the span of frequency chosen is 32,000 which is the maximum the VNA can offer. For the calibrated range of frequency, in case of the RSM technique, the frequency range is broken down in steps of 100 MHz sub spans with 32,000 points so as to give maximum accuracy in the measurement. The intermediate

frequency (IF) is set for all the measurements to 700 Hz instead of the default 40 kHz in order to lower the noise floor during measurement which allows for detection of smaller signals [124] even though it is time consuming. A process flow diagram of the measurement set-up is shown in Fig. 4.3 to give a clearer picture of the processes involved. After measuring the  $S_{11}$  for the required frequency span, the experimental data is converted into impedance by using the following equation [145]:

$$Z_{in} = Z_o \frac{1 + S_{11}}{1 - S_{11}} \tag{4.1}$$

The capacitance if the device is given by

$$C = Re\left[\frac{1}{i\omega Z_{in}}\right] \tag{4.2}$$

where  $Z_o = 50\Omega$  is the characteristic impedance of the system.

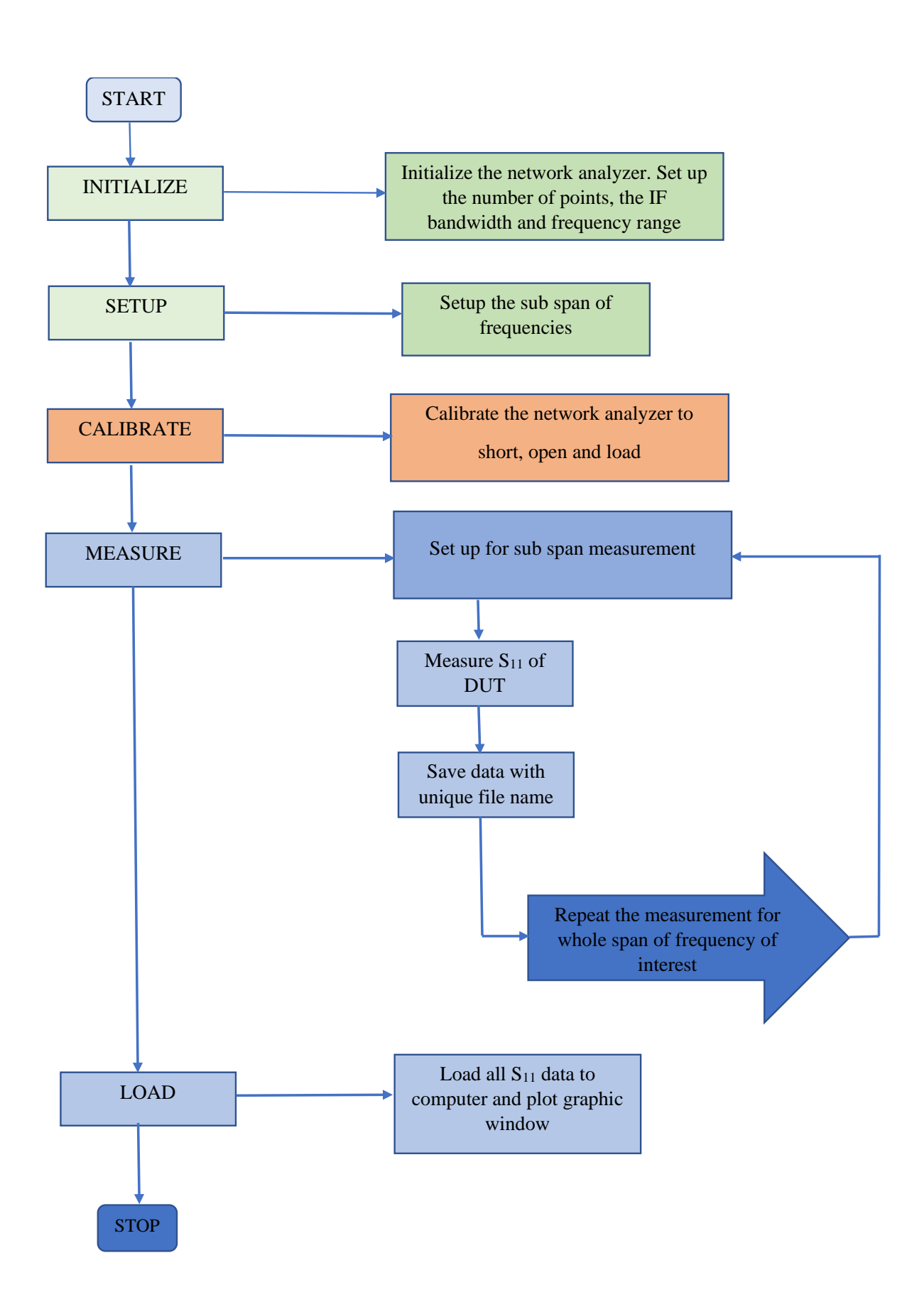


Figure 4.3. Process flow of measurement.

#### 4.3 Switchable HBAR based on ferroelectric thin film BST

The first high overtone bulk acoustic resonator based on ferroelectric thin film BST (70/30) was reported and characterized showing the voltage dependent nature of its coupling coefficient in [146]. We have also reported our work on switchable HBAR based on BST (50/50) [84, 147]. In this section, different types of HBARs on different substrates are measured using the technique as given in the previous section. The motivation behind the selection of different substrates is to demonstrate the dependence of spacing of the resonant peaks of the HBAR on the acoustic property and dimensions (thickness) of the substrate. HBARs with sapphire (0001), YAG (100), silicon (111) and fused silica as its substrate are considered for this study. Fig. 4.4 shows the extracted input impedance of all these types of HBAR in the frequency range 600 MHz- 4 GHz.

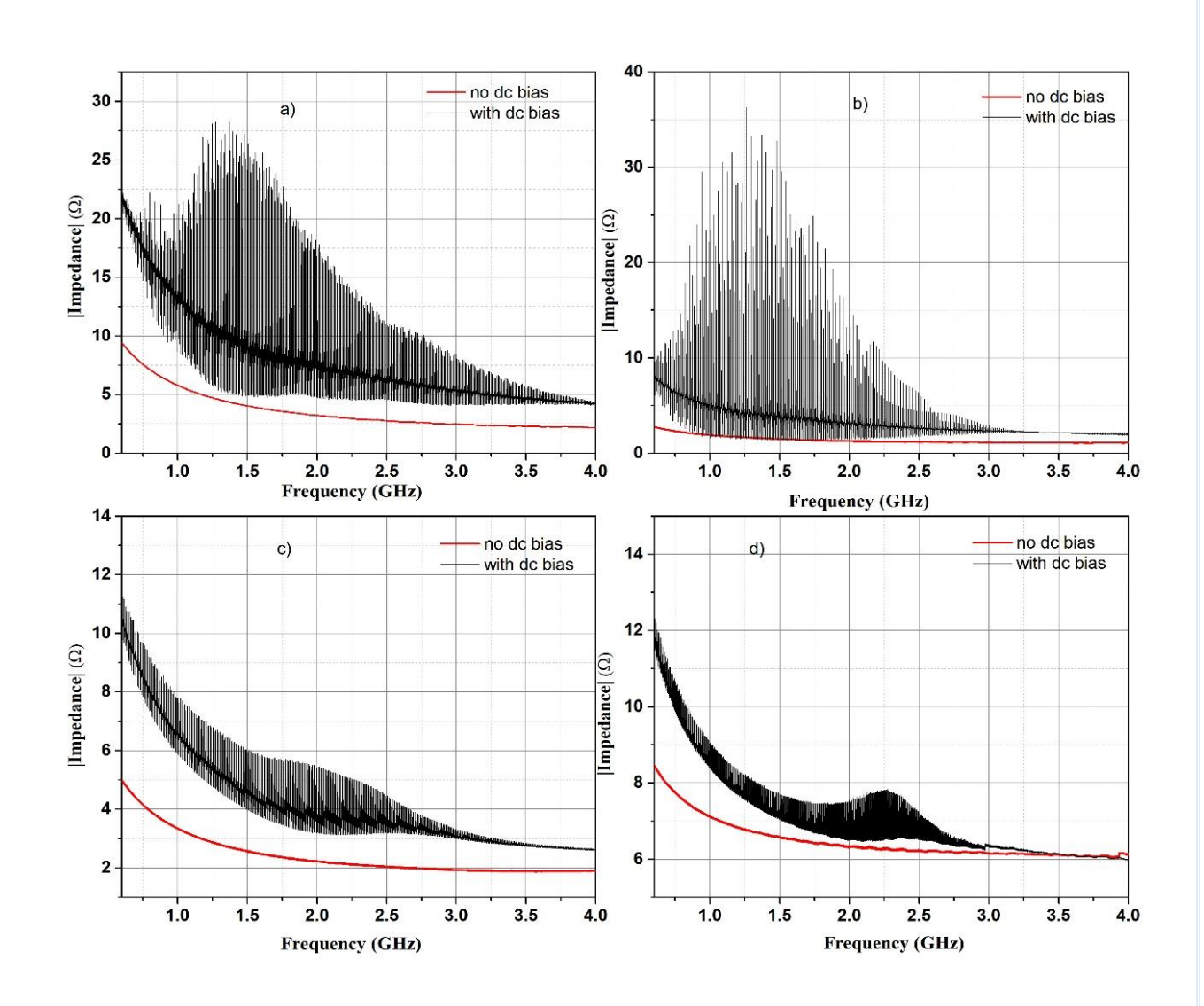


Figure 4.4. Frequency Spectra of HBAR with a) YAG b) Al<sub>2</sub>O<sub>3</sub> c) Si and d) Fused Silica as substrate

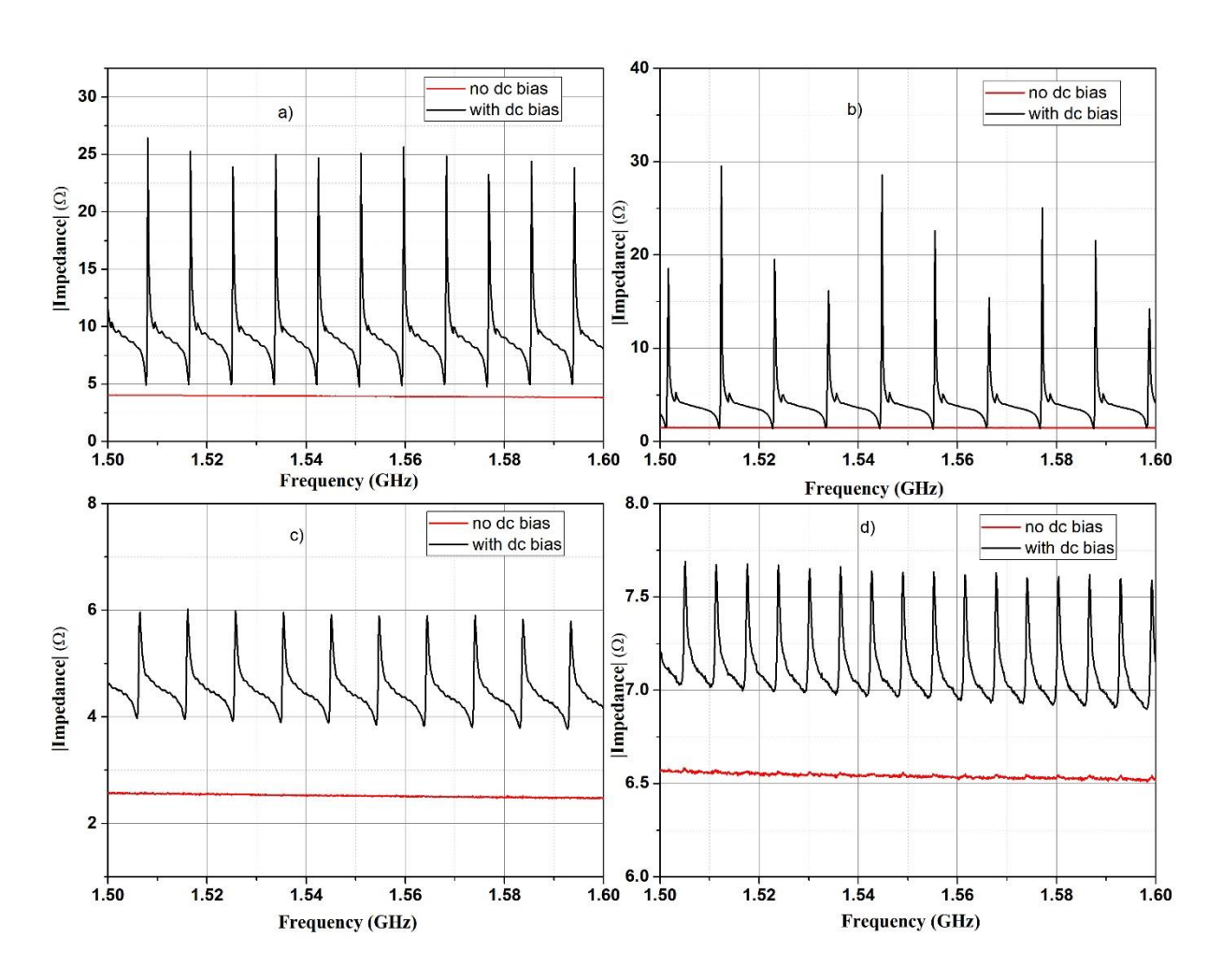


Figure 4.5. Multiple resonant peaks in a narrowband of HBAR with a) YAG b) Al<sub>2</sub>O<sub>3</sub> c) Si and d) Fused Silica as substrate.

As seen from Fig. 4.4, it is observed that for all the different types of HBARs, the multiple resonant peaks start appearing only after a DC bias is applied. This is due to electrostriction which induces piezoelectric effect in the paraelectric phase of ferroelectric thin film BST. The advantage this offers is that the resonator is switchable as compared to other HBAR which are based on non-ferroelectric type piezoelectric thin films like ZnO and AlN. Another interesting observation is the difference in the area where the peak of the spectra appears, in case of YAG and sapphire, the maxima points appear at a lower frequency range even though the thickness of the BST coated is similar for the cases. For the case of silicon and fused silica substrates, the maxima points appear at a higher frequency range. This nature of the HBARs happens because in case of YAG and sapphire as the substrate, the

ratio of the acoustic impedances of substrate to BST is greater than one and behaves as a 'quarter wavelength resonator' and for the case of silicon and fused silica, the ratio is less than one and behaves as a 'half wavelength resonator' [92]. And The responses of the HBARs in a narrowband frequency range of 1.5 GHz to 1.6 GHz is shown in Fig. 4.5. From these plots, it is evident that the spacing or gap for each case is different. This is due to the fact that the frequency spacing between adjacent peaks are governed by the acoustic wave velocity and the thickness of the substrate as given by the relation [97]:

$$\Delta f_S = \frac{v_S}{2.t_S} \tag{4.3}$$

where  $\Delta f_s$  is the frequency spacing,  $v_s$  is the acoustic velocity of the substrate and  $t_s$  is the thickness of the substrate. From this relation, the acoustic velocity or the thickness of the substrate can be approximately calculated when either one is a known value. The thickness of all the substrates is approximately 0.5 mm and from the spacing calculated from Fig. 4.5, the extracted acoustic velocities using equation (4.3) of the substrates YAG, sapphire, silicon and fused silica are given in Table 4.1. The acoustic velocities derived here are approximate values since the spacing changes due to various other factors from the active thin film and in relation to frequency. This will be studied in further sections. The analysis done here in this section is to just prove that the HBAR based on BST can be made. The dependence of the spacing of the resonant peaks due to change in thickness is shown in Fig. 4.6, where three different HBARs are made in the same condition but with different substrate thicknesses (0.3, 0.5 and 1 mm). It is clear from this figure that the thicker the substrate the more congested the spectrum is going to be. This also gives us a glimpse to why HBARs have multiple resonant peaks and FBAR with membrane does not. Because in case of the FBAR, the thickness of the substrate is negligible when compared to HBAR.

Table 4.1. Extracted acoustic velocities of substrates.

Substrates	$\Delta f_s$ (MHz)	Acoustic velocity (m/s)
YAG	8.6	8600
Sapphire	10.8	10800
Silicon	9.6	9600
Fused silica	6.9	6900

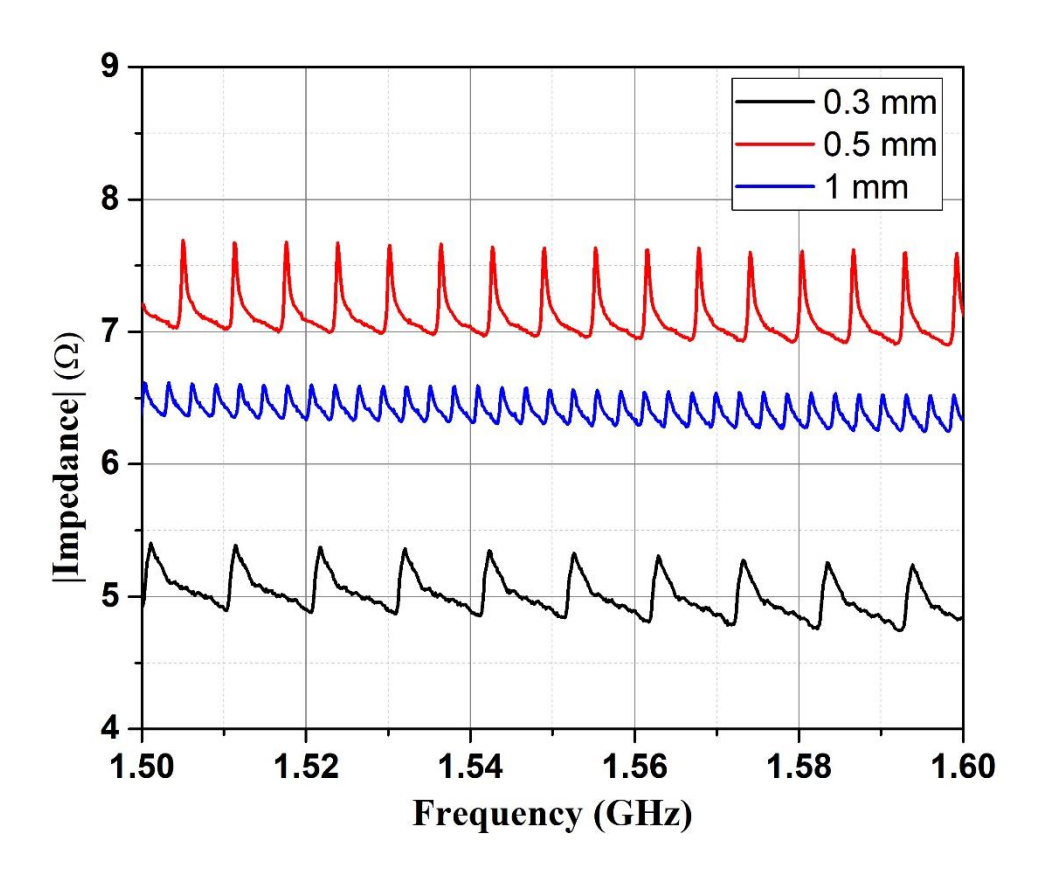


Figure 4.6. HBARs made on fused silica with different thicknesses.

#### 4.4 Material property extraction of BST using resonant spectrum method (RSM)

In this section, the properties of the thin BST film are extracted by using the resonant spectrum method. HBAR facilitates the extraction of properties such as acoustic wave velocity, mass density and coupling coefficient of the active thin film in the composite resonator [84]. Earlier works have characterized unpoled piezoelectric ceramic on a substrate with lamb waves and coating on a piezoelectric plate with bulk waves by using modal frequency spacing method [148,84]. Electromechanical coupling coefficient was extracted for ZnO employing an over-moded resonator structure and by using Butterworth Van Dyke (BVD) model in works of Ranjan Naik et.al [88]. The first reported use of distribution of effective coupling coefficient to extract electromechanical coupling coefficient of the thin films by using a composite resonator structure was reported by Z. Wang et.al wherein the effects of the electrodes were neglected and the calculation was based analysing the series and parallel resonant frequencies of the multiple modes in the frequency spectra [92]. Y. Zhang et.al. proposed the name RSM for the first time, laying down the foundation for characterization of piezoelectric thin films using a composite resonator where the effects of the electrodes were also included in the model [83]. From the past decades many groups have done both numerical simulations and experimental analysis to extract the material properties of thin films like ZnO and AlN using the methods based on the spectrum of the HBAR or the composite resonator [46,92,101,149,150]. In this section, the characterization of BST thin film using RSM technique is presented. It is for the first time a switchable paraelectric phase thin ferroelectric film was characterized and reported by this method [84]. The work from our previous publication [84] has been extended by incorporating numerical simulations. The effects of DC bias on various aspects of the BST based HBAR is discussed in detail.

#### 4.4.1 HBAR on sapphire substrate

A BST based HBAR made on sapphire substrate is used for the extraction of the material properties of the BST thin film. DC bias of 40 V is given across the 1  $\mu$ m thick thin film (BST) transducer and measurements are carried out as discussed in the previous section. First of all, the distribution of spacing of the parallel resonance frequencies (SPRF) and the effective coupling coefficient ( $k_{eff}^2$ ) are calculated from the multiple resonant peaks or modes in the spectra using equations (3.54) and (3.55) respectively. Fig. 4.7 and Fig. 4.8 show the SPRF and the  $k_{eff}^2$  distribution of both the experimental result and the numerical simulation results. The parameters used in the simulation is given in Table 4.2.

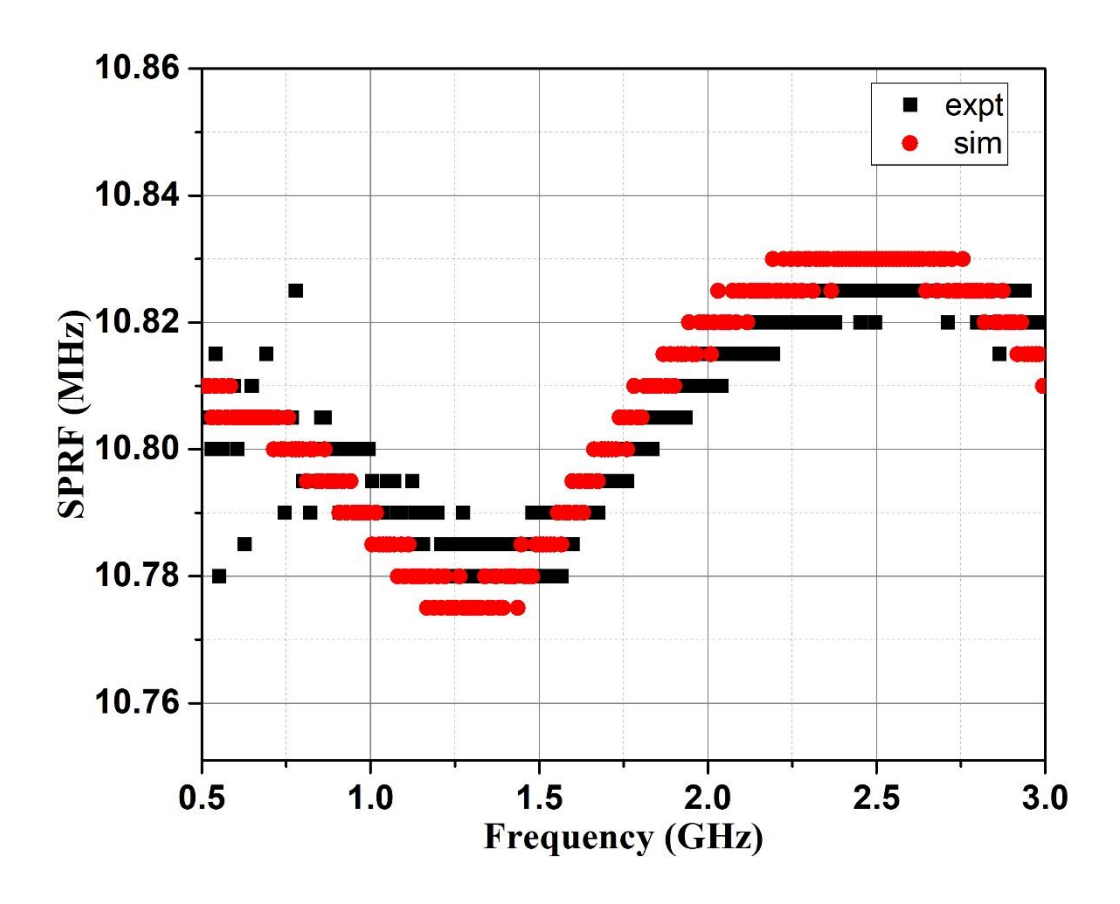


Figure 4.7. SPRF distribution for HBAR with sapphire as substrate.

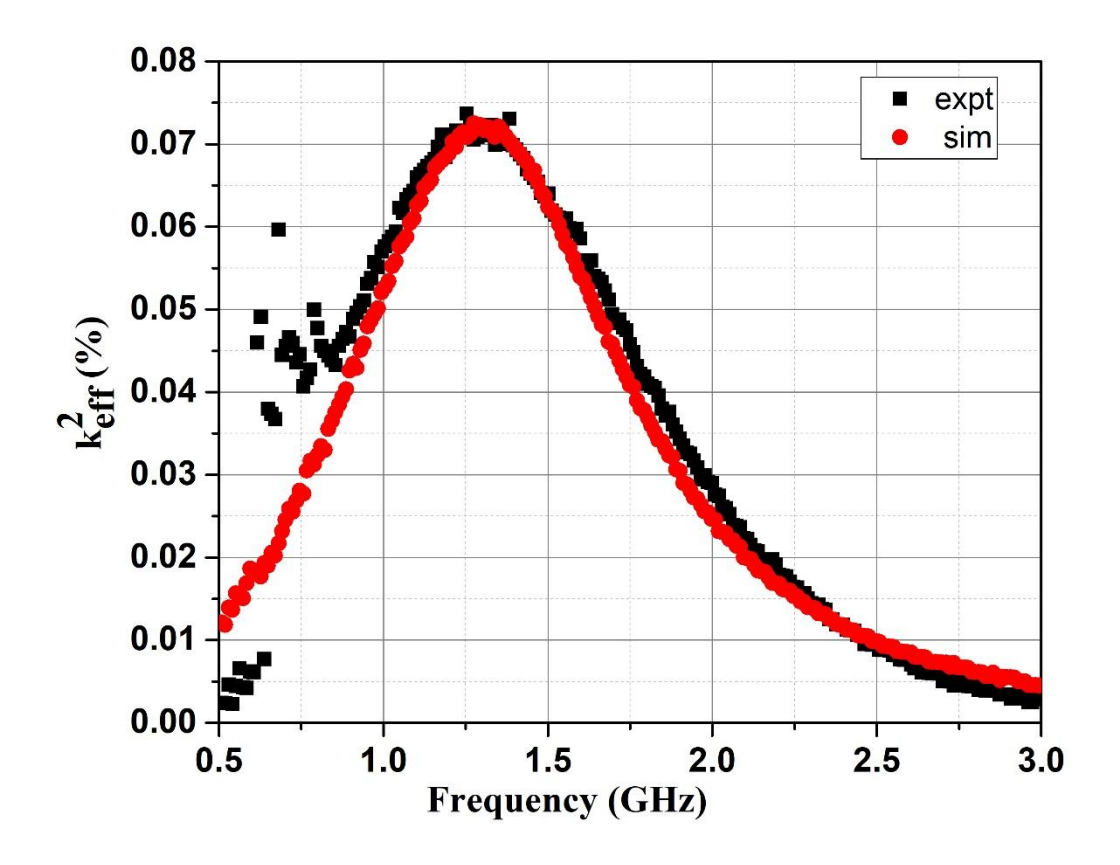


Figure 4.8.  $k_{eff}^2$  distribution for HBAR with sapphire as substrate.

Table 4.2. Parameters used in simulation for HBAR with sapphire as substrate.

Material	ACOUSTIC VELOCITY (M/S)	Density (kg/m³)	Thickness (μm)	coupling coefficient $(k_t^2)$ (%)
BST	5200	5678	1	6.4
Platinum (Pt)	3300	21500	0.08	
Gold (Au)	3200	19300	0.08	
Sapphire (Al <sub>2</sub> O <sub>3</sub> )	10500	3993	450	

As discussed earlier in this chapter and in chapter 3, since this particular HBAR with sapphire substrate is a hard substrate case, the maximum of the  $k_{eff}^2$  occurs in the first transition region and hence, the explicit formulae for the transition region case will be applied for extracting the material properties. By using equations (3.57) and (3.63), the mass density and the acoustic wave velocity of the BST thin film is extracted. Equations (3.65) and (3.67) are applied to extract the elastic constant and the coupling coefficient of the thin film. The details of the result are tabulated in Table 4.3.

Table 4.3. Experimental results for HBAR with sapphire as substrate.

Experimental results			Extracted material parameters			
$\Delta f_N$	$\Delta f_N$ $\Delta f_T$ $k_{eff}^2(m+1)$		ρ	$c_{33}^D$	v	$k_t^2$
(MHz)	(MHz)	(%)	(kg/m <sup>3</sup> )	$(10^{10} \text{N/m}^2)$	(m/s)	(%)
10.83	10.78	0.0722	5760	15	5099	6.62

#### 4.4.2 HBAR on YAG substrate

In this case, a BST based HBAR made on YAG substrate is used for the extraction of the material properties of the BST thin film. DC bias of 30 V is given across the 0.8  $\mu$ m thick thin film (BST) transducer and measurements are carried out as discussed in the previous section. First of all, the distribution of spacing of the parallel resonance frequencies (SPRF) and the effective coupling coefficient ( $k_{eff}^2$ ) are calculated from the multiple resonant peaks or modes in the spectra using equations (3.54) and (3.55) respectively. Fig. 4.9 and Fig. 4.10 show the SPRF and the  $k_{eff}^2$  distribution of both the experimental result and the numerical simulation results. The parameters used in the simulation is given in Table 4.4.

Table 4.4. Parameters used in simulation for HBAR with YAG as substrate.

Material	ACOUSTIC VELOCITY (M/S)	Density (kg/m³)	Thickness (μm)	coupling coefficient $(k_t^2)$ (%)
BST	5100	5700	0.8	5
Platinum (Pt)	3300	21500	0.08	
Gold (Au)	3200	19300	0.08	
YAG	8557	4500	495	

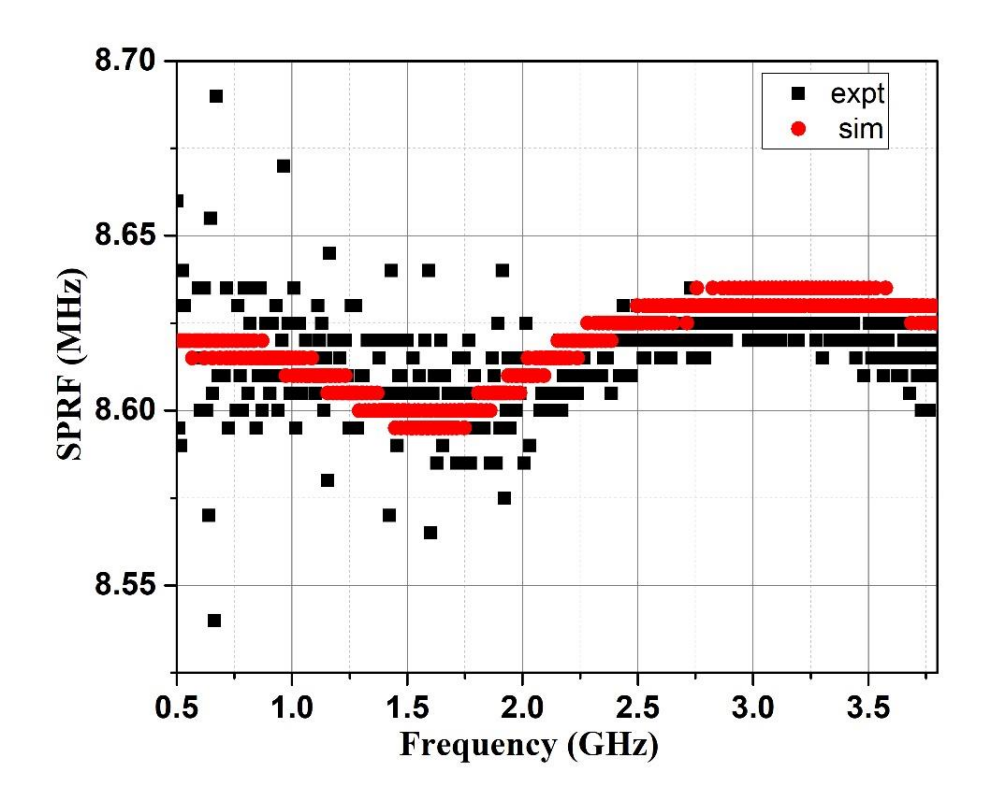


Figure 4.9. SPRF distribution for HBAR with YAG as substrate.

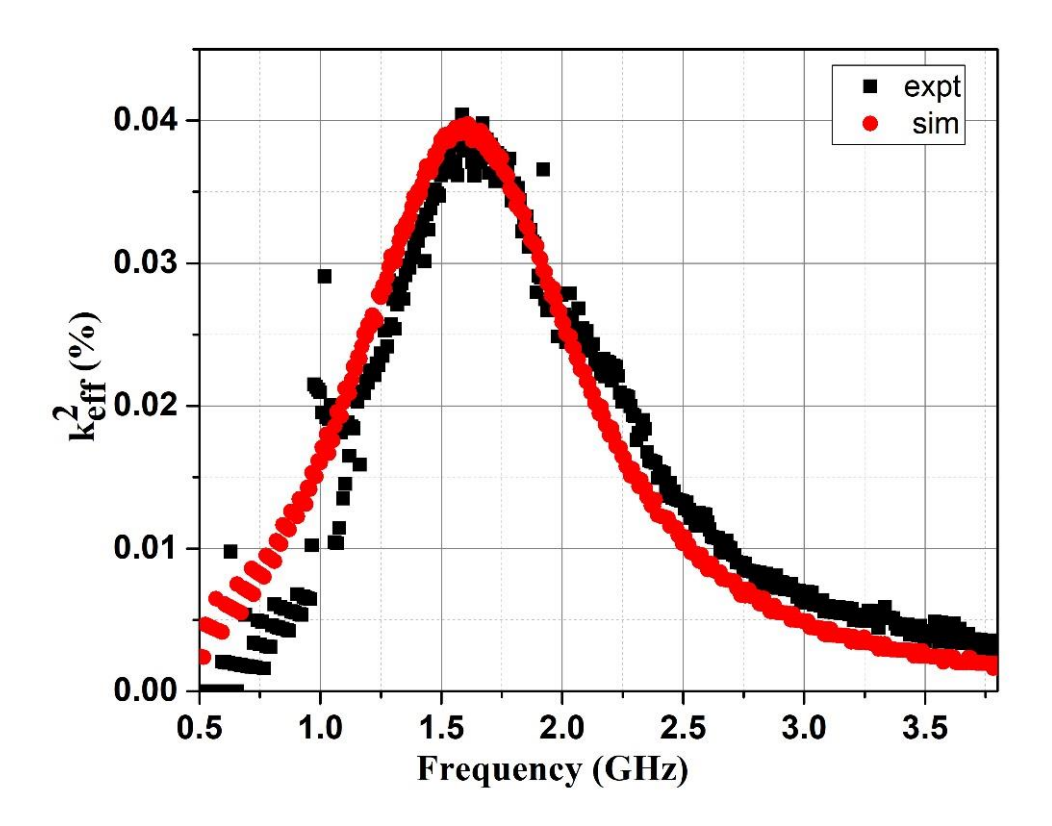


Figure 4.10.  $k_{eff}^2$  distribution for HBAR with YAG as substrate.

Similar to the case of HBAR with sapphire substrate, the HBAR with YAG substrate is also a hard substrate case and hence, the maximum of the  $k_{eff}^2$  occurs in the first transition region and hence, the explicit formulae for the transition region case will be applied for extracting the material properties. By using equations (3.57) and (3.63), the mass density and the acoustic wave velocity of the BST thin film is extracted. Equations (3.65) and (3.67) are applied to extract the elastic constant and the coupling coefficient of the thin film. The details of the result are tabulated in Table 4.5.

Table 4.5. Experimental results for HBAR with YAG as substrate.

Experimental results			Extracted material parameters			
$\Delta f_N$	$\Delta f_T$	$k_{eff}^2(m_T+1)$	ρ	$c_{33}^{D}$	v	$k_t^2$
(MHz)	(MHz)	(%)	(kg/m <sup>3</sup> )	$(10^{10} \text{N/m}^2)$	(m/s)	(%)
8.625	8.6	0.04	5280	13.67	5088	5

#### 4.5 Effect of DC bias on BST based HBAR

In the previous sections, the BST based HBARs are characterized using the RSM method, and the major factor involved in this ferroelectric based HBAR is that certain parameters of the resonator are wholly dependent on the DC bias applied. So, in this section the effect of a varying DC bias is discussed for both the samples of HBAR, i.e., sapphire and YAG as the substrates. The impedance plot of both the sapphire HBAR and YAG HBAR are plotted in Figs. 4.11 and 4.12. In these plots it can be seen that the intensity of the resonant peaks increases with an increase in the DC bias. This shows the switchable and tunable nature of the BST based HBAR. Further studies are presented in detail in the following sections.

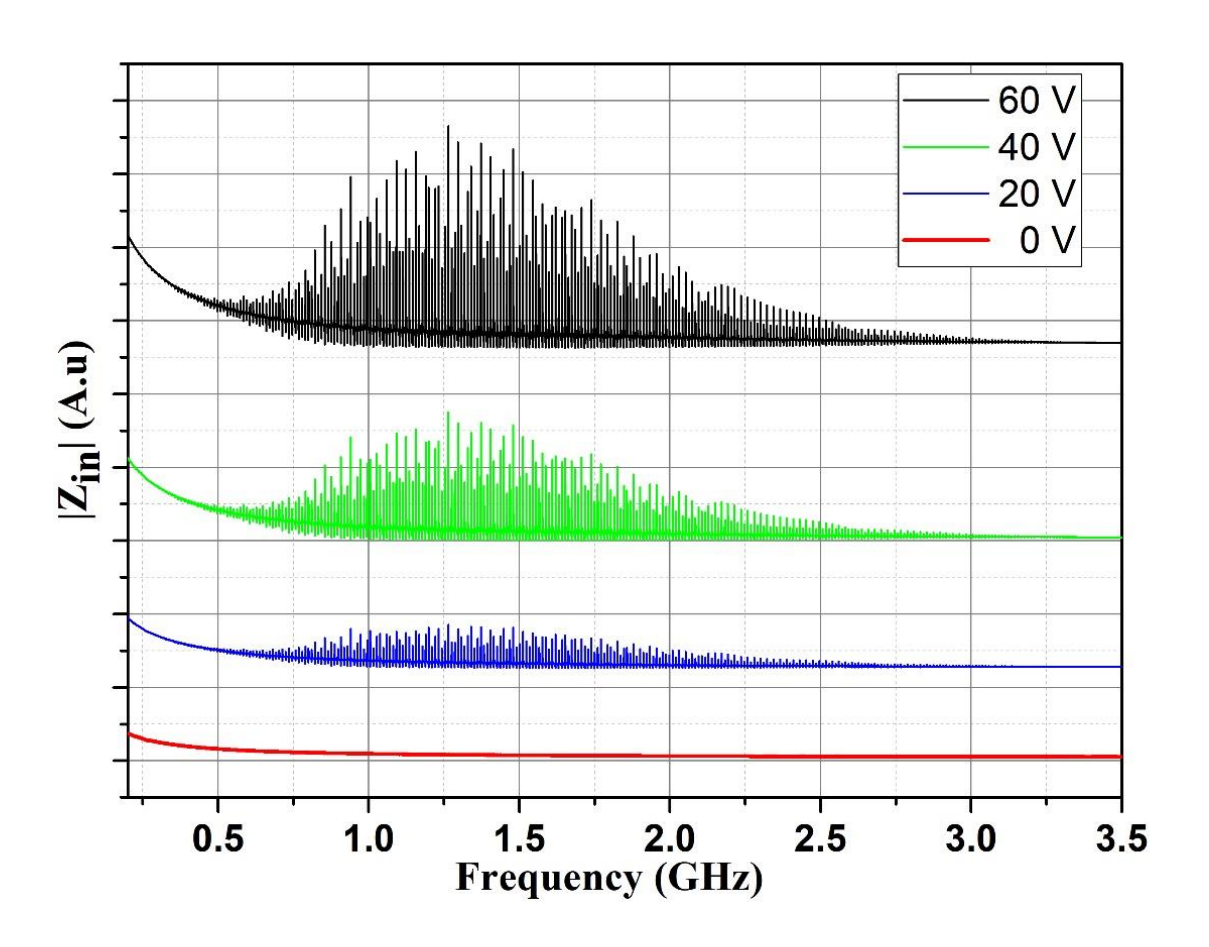


Figure 4.11. Frequency spectra of HBAR (sapphire) with varying DC bias.

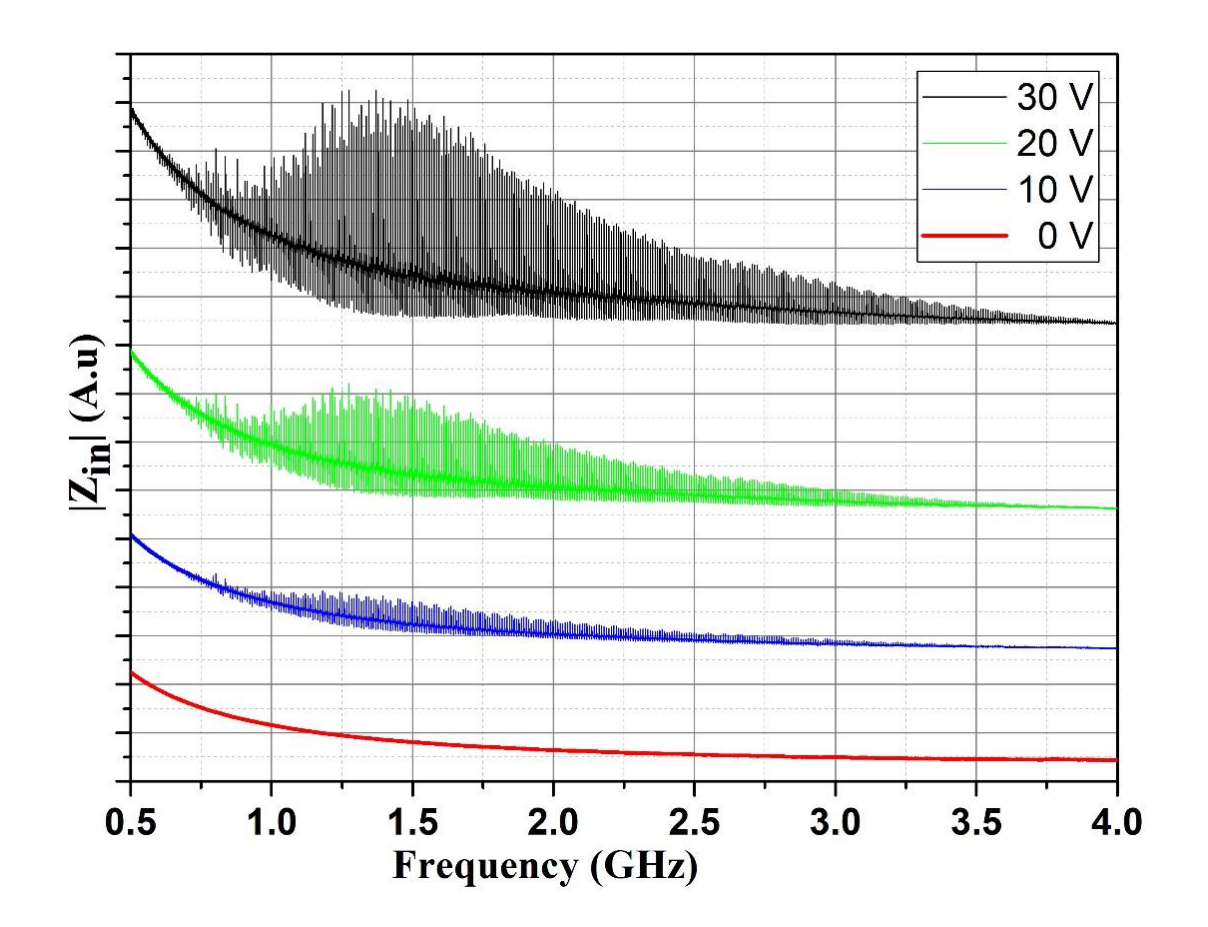


Figure 4.12. Frequency spectra of HBAR (YAG) with varying DC bias.

In this section the Q factor of the resonators are studied as well and the Q factor is derived from the slope of the phase  $(\phi)$  response given by [88]:

$$Q = \frac{f}{2} \frac{\delta \phi}{\delta f} \tag{4.4}$$

#### 4.5.1 HBAR on sapphire substrate

Similar to section 4.4.1, the SPRF and the  $k_{eff}^2$  distributions of the HBAR made with sapphire as the substrate are calculated by applying DC bias of 20V, 40V and 60V across the active transducer. Figs. 4.13, 4.14 and 4.15 show the plots for the SPRF, the  $k_{eff}^2$  and the Q factor distribution for all the different DC bias applied.

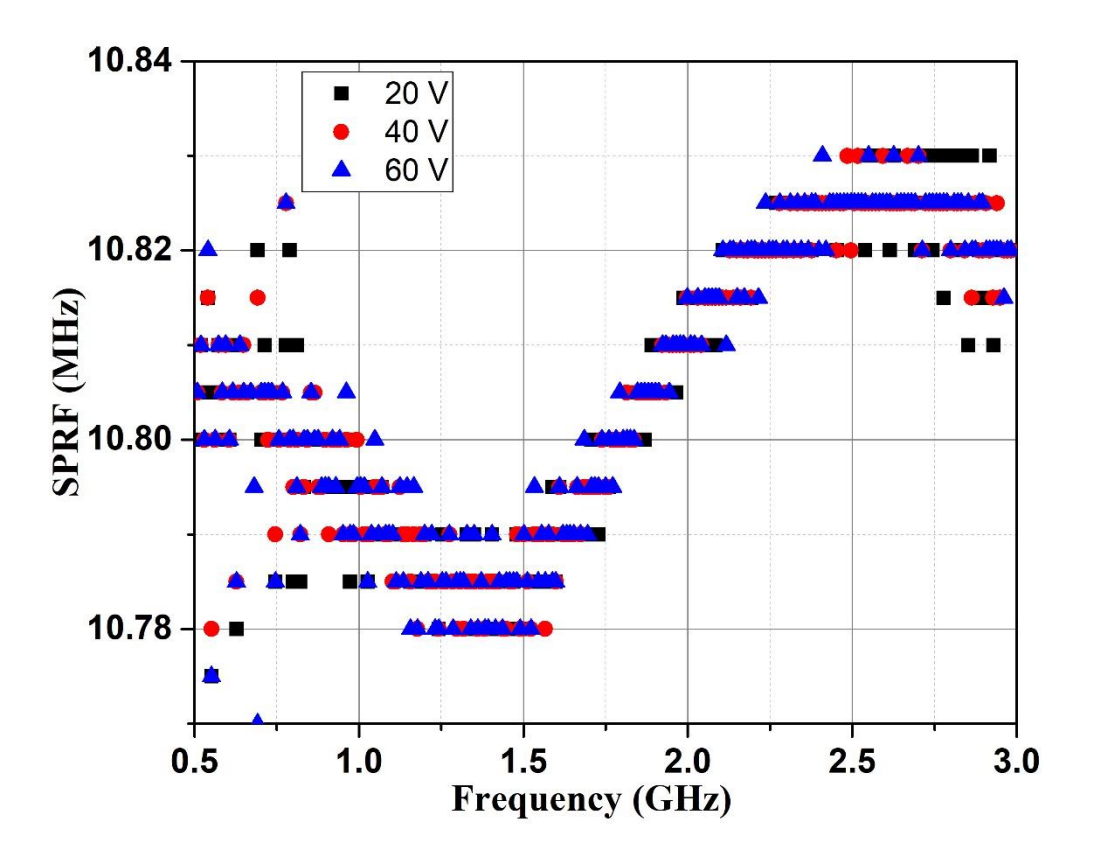


Figure 4.13. SPRF distribution (Expt.) of the HBAR (sapphire) with different DC bias of 20V, 40V and 60V.

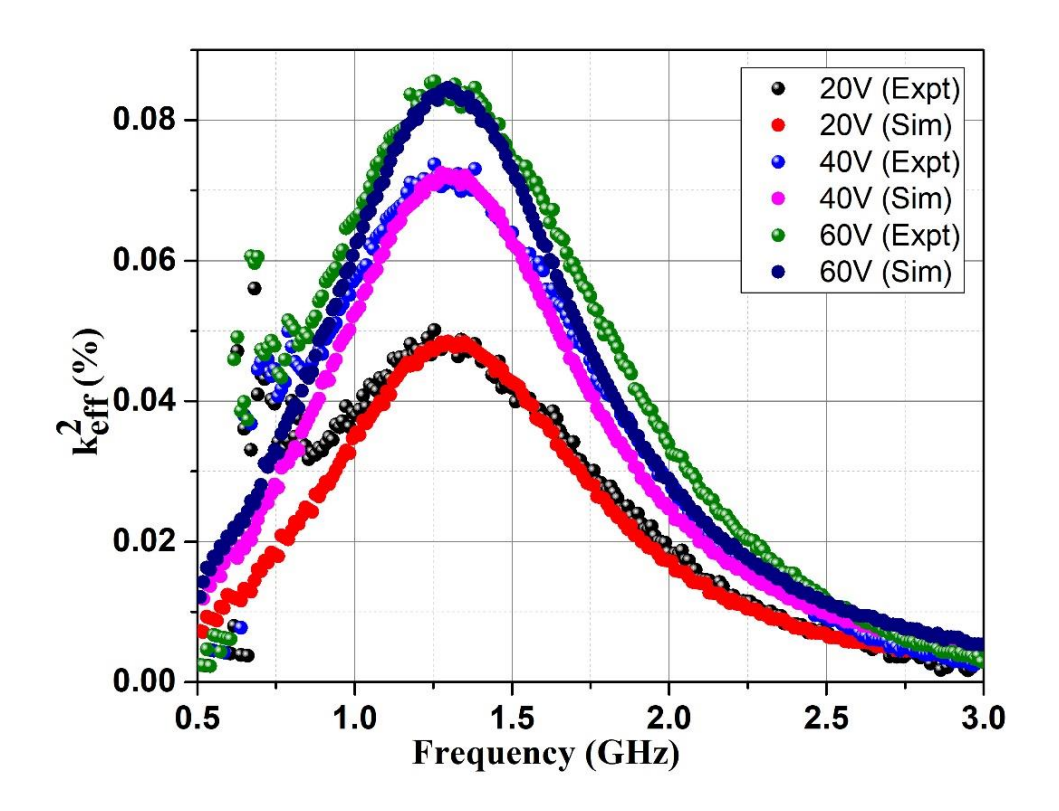


Figure 4.14.  $k_{eff}^2$  distribution of the HBAR (sapphire) with different DC bias of 20V, 40V and 60V.

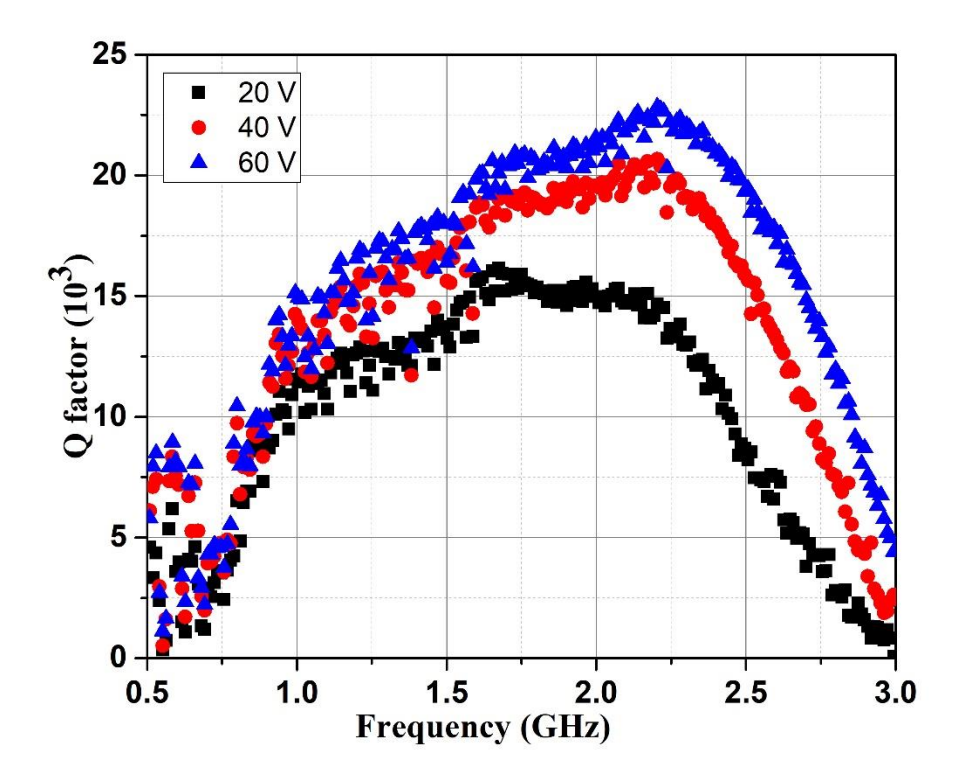


Figure 4.15. Q-factor distribution (Expt.) of the HBAR (sapphire) with different DC bias of 20V, 40V and 60V.

As the SPRF of the HBAR is dependent mostly on the acoustic properties and the thickness of the substrate, it is clearly seen from Fig. 4.13 that with change in the DC bias, there is no significant change in the SPRF distribution of the HBAR. From this observation it can be inferred that the mass density and the acoustic wave velocity of the thin BST film doesn't change by changing the DC bias once the HBAR is switched on. Further, from the RSM technique, the most important factor in determining the acoustic properties of the thin active film i.e., the  $\Delta f_N$  and  $\Delta f_T$  has not changed as seen in the figure.

However, for the case of the  $k_{eff}^2$  and the Q-factor, it is evident from Figs. 4.14 and 4.15 that there is significant change in the values and both the  $k_{eff}^2$  and the Q-factor tend to increase with an increase in the DC bias voltage. The increase in the  $k_{eff}^2$  can be explained by using equation (3.43) which relates the coupling coefficient to the relative tunability and the field dependent material properties of the ferroelectric thin film. As for the case of the increase of Q-factor, similar responses are observed for SMR based on BST [151,152]. With increased DC bias, the ferroelectric is in a clamped state where the soft lattice mode got reduced degree of freedom resulting in reduced anharmonicity encountered by it, leading to lower losses and hence, higher Q value. The fabricated HBAR shows extremely high Q factor even at higher frequencies over the broad range of frequencies. This high Q nature which is DC bias dependent shows huge potential in consideration for the design of oscillators and sensors.

# 4.5.2 HBAR on YAG substrate

The SPRF and the  $k_{eff}^2$  distributions of the HBAR made with YAG as the substrate are calculated by applying DC bias of 10, 20 and 30 Volts across the active transducer. Figs. 4.16, 4.17 and 4.18 show the plots for the SPRF,  $k_{eff}^2$  and the Q factor distribution for all the different DC bias applied. Similar observations are made for this case to that of the HBAR in section 4.5.1.

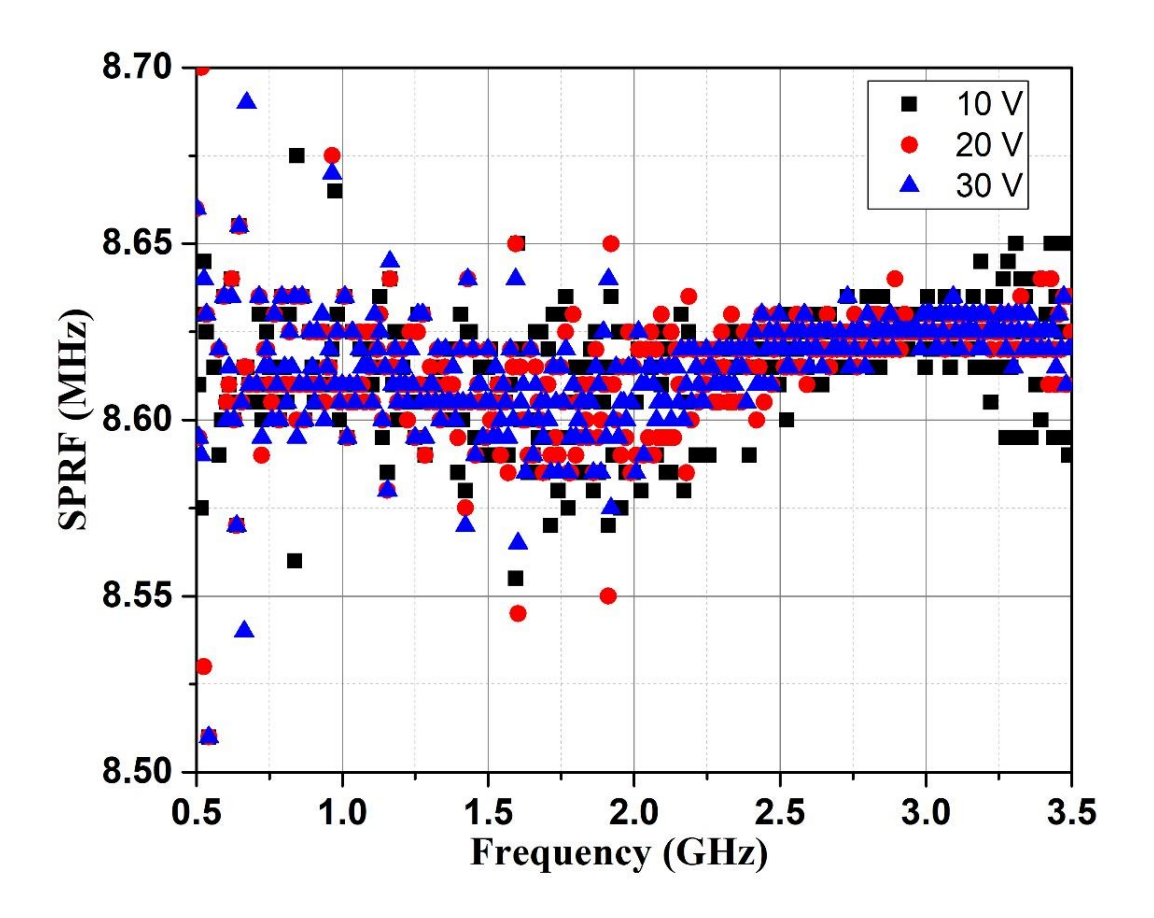


Figure 4.16. SPRF distribution (Expt.) of the HBAR (YAG) with different DC bias of 10 V,20 V and 30 V.

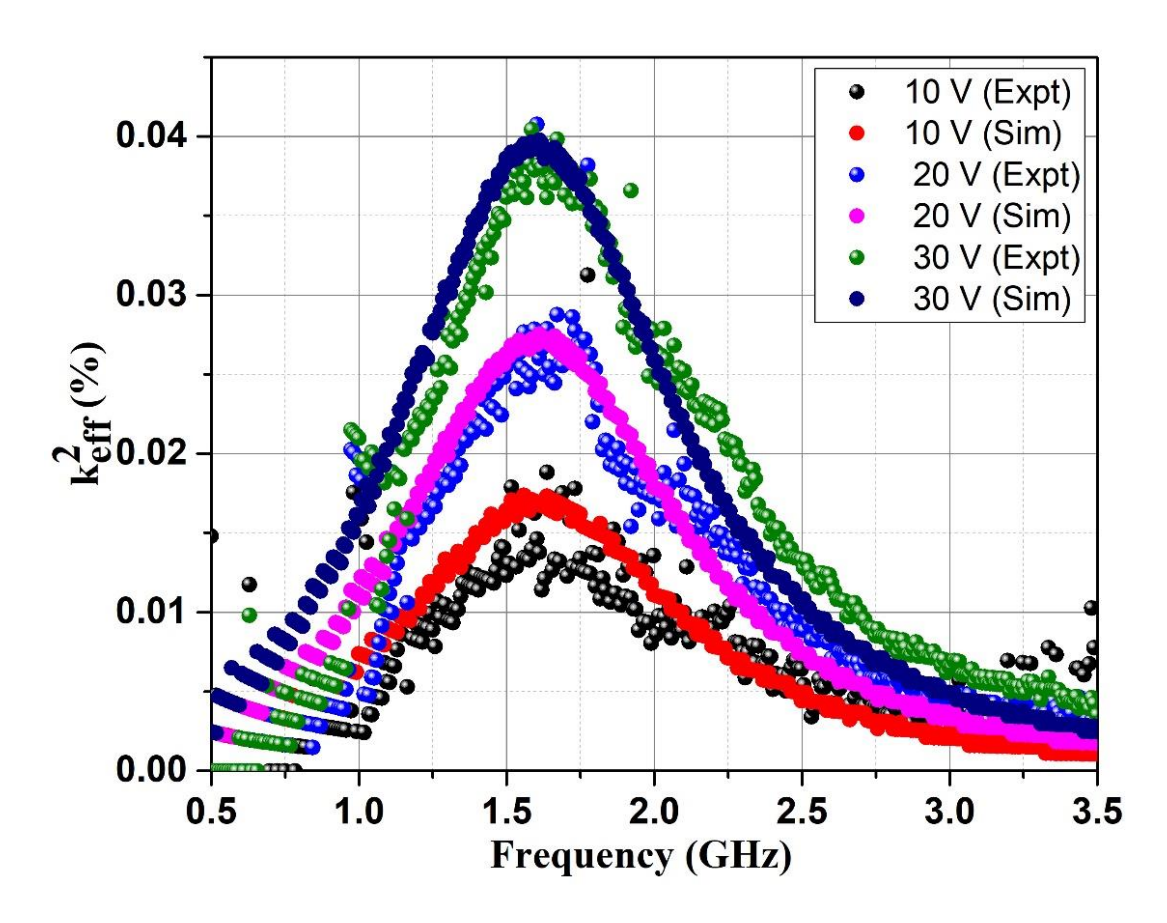


Figure 4.17.  $k_{eff}^2$  distribution of the HBAR (YAG) with different DC bias of 10 V,20 V and 30 V.

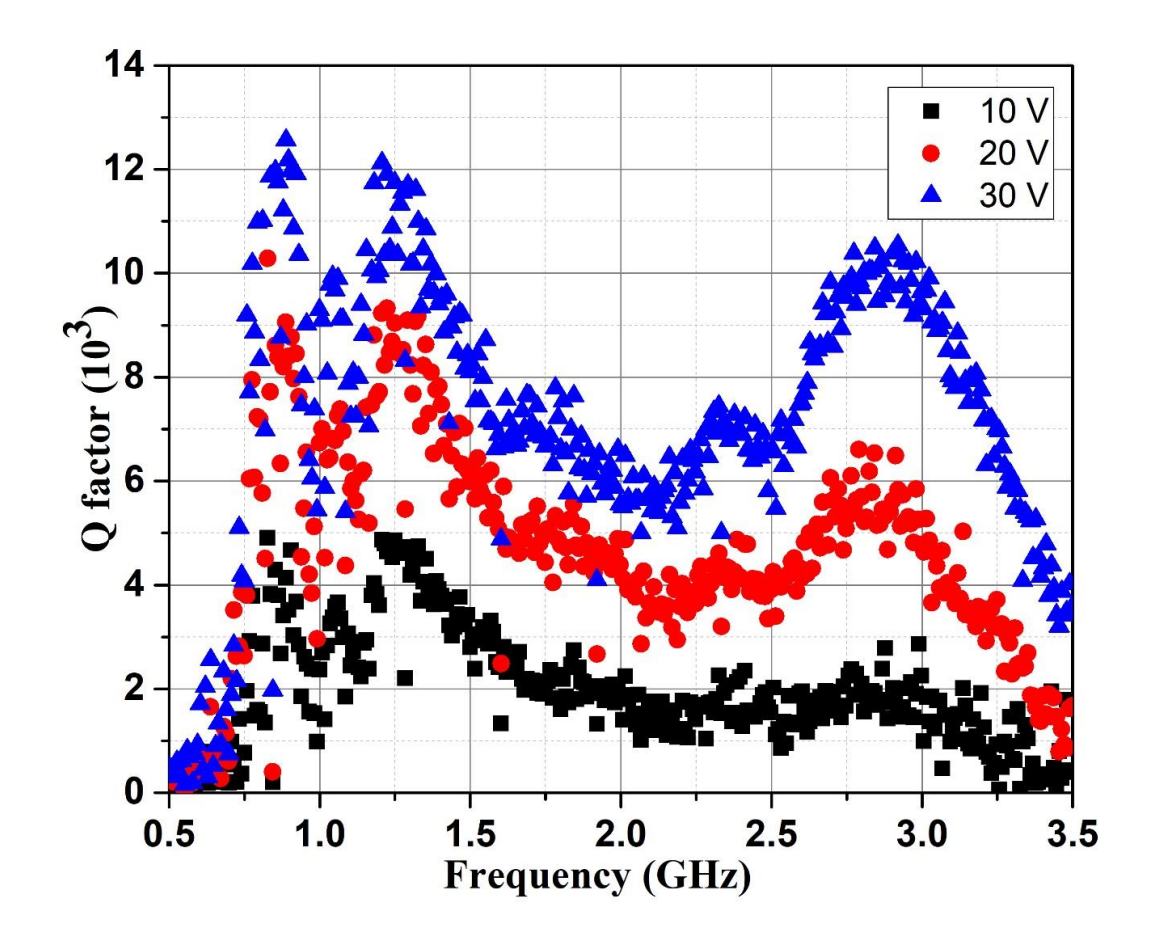


Figure 4.18. Q-factor distribution (Expt.) of the HBAR (YAG) with different DC bias of  $10\ V, 2\ V$  and  $30\ V.$ 

#### 4.5.3 Relationship between the relative tunability and the coupling coefficient

In Secs. 4.5.1 and 4.5.2, it is observed that the  $k_{eff}^2$  distribution for both the samples of HBAR with sapphire and YAG as substrates increases with an increase in the DC bias voltage. This phenomenon can be explained by the relation between the relative tunability of the thin film and the coupling coefficient  $(k_t^2)$  of the BST thin film. Equation (3.43) establishes that the coupling coefficient  $(k_t^2)$  of the BST thin film is proportional to the relative tunability  $(T_r)$  of the thin film upon application of DC bias with a proportionality factor (A) which is the field dependent material parameter of the ferroelectric. The  $k_t^2$  of the thin films are calculated from the  $k_{eff}^2$  distribution of HBAR for each of the DC bias condition for both the sapphire and YAG HBARs using the RSM method. The results of the  $k_t^2$  and  $T_r$  for both the resonators are given in Table 4.6.

Table 4.6.  $k_t^2$  and  $T_r$  for different DC bias voltages.

HBAR with Sapphire substrate			HBAR with YAG substrate		
DC bias	$T_r$ (%) at 1	$k_t^2$	DC bias	$T_r$ (%) at 1	$k_t^2$
<b>(V)</b>	GHZ	(%)	<b>(V)</b>	GHz	(%)
20	44	4.6	10	21	2.2
40	62	6.6	20	40	3.5
60	73	7.8	30	50	5.0

Ferroelectrics thin film (like BST) which are in their paraelectric phase exhibits high dielectric permittivity which are dependent on factors like temperature, mechanical stress and external electric field. The effect of applied electric field on the dielectric permittivity

of BST can be explained using the *Phenomenological (Thermodynamic) Theory* by Tagantsev et al. [153]. The relation is given below:

$$\varepsilon(E) = \frac{\varepsilon(0)}{1 + 3\beta \varepsilon_0^3 E^2 \varepsilon^3(0)} \tag{4.5}$$

where  $\beta$  is the nonlinearity coefficient,  $\varepsilon_0$  is the dielectric constant of vacuum, E is the externally applied electric field and  $\varepsilon(0)$  is the relative permittivity when no external electric field is applied. The relative tunability as defined in equation (3.39) gives a measure of how the permittivity changes with different bias field applied.

The  $k_t^2$  as defined for paraelectric thin film like BST is given in equation (3.38) [141] as

$$k_t^2 = \frac{4q_{33}^2 \varepsilon_{33}(E)}{c_{33}^0} (P^{DC}(E))^2$$
 (4.6)

where,  $c_{33}^0$  is the tensor of the elastic constant of the material without electric field and  $q_{33}$  is the tensor of the linear electrostriction. The two variables  $\varepsilon_{33}(E)$  and  $P^{DC}(E)$  are field dependent relative permittivity (as defined in equation (4.5)) and field dependent polarization of the BST film. From equation (4.6) it is clear that the electromechanical coupling coefficient is proportional to both  $\varepsilon_{33}(E)$  and  $P^{DC}(E)$  for the case of paraelectric thin film BST. The electromechanical coupling coefficient which is a measure for conversion efficiency between electrical and mechanical (or acoustic) energy is fixed in case of piezoelectric thin films. But in case of BST thin film, due to the bias dependent nature of its permittivity,  $k_t^2$  becomes tunable with DC bias. In case of FBAR and SMR, where there is less mass loading compared to HBAR (HBAR is heavily loaded by its thick substrate), from equation (3.33) and (3.34), it can be seen that with an increase in  $k_t^2$ , the frequency tunability of the resonator increases. Thus, paraelectric films like BST with field dependent  $k_t^2$  is extremely useful for designing high performance tunable FBAR and SMR which has applications in tunable filters, oscillators, switches etc [154].

#### 4.6 Summary and conclusion

In summary,

- The fabrication and experimental procedure for measuring the HBAR for characterization is explained.
- 2. Experimental results demonstrating high overtone response for the BST based HBAR fabricated on various substrate materials and substrates with different thicknesses are given. All the different HBAR samples studied show switchable nature. The approximate acoustic velocities of the substrates are also extracted from the spacing of adjacent resonant peaks.
- 3. By using the resonant spectrum method and by fitting numerical simulation results, the material properties of BST thin films are extracted for two different types of HBAR, i.e., with: a) sapphire and b) YAG substrates.
- 4. The effect of DC bias on the BST based HBARs is studied by applying varying dc voltages to the resonators. High Q factor for both the HBARs are achieved at high frequency. The SPRF of the resonator is not affected by the change in DC bias voltage once it is switched on.
- 5. The relationship between the coupling coefficient of the BST thin film and the relative tunability of the film is established.

In this chapter, the switchable nature of the BST based HBAR is established and it is concluded that by using low acoustic loss or high mechanical Q substrates like sapphire and YAG, the HBAR exhibits very high Q factor which is important in designing oscillators and sensors. Another added advantage for such kind of ferroelectric based HBAR is the switchable nature of the resonator and the tunable capability of the coupling coefficient and

the Q factor using DC bias. Similar to FBAR and SMR which are based on ferroelectric thin films, an HBAR based on BST thin film also follows the same trend that the coupling coefficient of the thin BST film is directly proportional to the relative tunability of the thin film.

# Chapter 5: Effects of a coated material layer on HBAR and its possible applications

#### 5.1 INTRODUCTION

The use of high overtone bulk acoustic wave resonator (HBAR) or the composite resonator in applications such as oscillators and material properties characterization is well known. This is possible because of the high Q factor it exhibits in high frequencies in the GHz range. In Chapter 3 and 4, the characterization of BST thin film using the RSM technique is demonstrated. Apart from this application, HBAR has been employed for characterizing acoustic wave velocities and acoustical attenuation with measurements done in the time domain at 1 GHz to design acoustic matching layers using SU-8 based nanocomposites for lab-on-chip applications [98]. HBAR has also found applications in non-destructive evaluation (NDE) of thickness variation of elastic plates from the resonant spectra, i.e., change in spacing of parallel resonance frequencies (SPRF) of the resonator. However, this was done using numerical simulation on model of the HBAR [100,155,156]. Key research has been done in the past two decades in the field of characterizing thin piezoelectric and ferroelectric films using the RSM technique.

Effects of different electrode materials and the variation of its thicknesses and also the variation in the substrate materials on the HBAR's coupling coefficient, Q factor, and SPRF responses have been extensively studied and reported [83,104,149,150,157]. The characterization performed in these previous reported works concentrate basically on the HBAR being considered as a four layered configuration of an acoustic transducer upon a low acoustic loss substrate. But, the effect of introducing an additional layer on the HBAR configuration has not been studied well. In this chapter, the effect of an additional layer

coating on the backside of the substrate of the resonator is discussed. By using both experimental results and numerical simulation results (from model), the HBAR with and without coating is studied and the effects in terms of the effective coupling coefficient, the SPRF and the Q factor are analysed. From the analysis, the acoustic velocity of SU-8 is calculated. It is also found out that the mechanical loss or Q factor of the layer coated has significant effect on the parameters of the resonator. This technique is also found to be suited for extracting acoustic velocity and the mechanical Q of the additional layer which in this case is a polymer (SU-8). Possible applications of this technique are in characterization of the polymer composites and in mass loading or gravimetric detection.

# **5.2** Experimental setup and measurement results

#### 5.2.1 Experimental setup

The HBAR samples fabricated are based on ferroelectric film BST which are in the paraelectric phase. The basic structure of the device is a Metal-Insulator-Metal (MIM) structure mounted on a high Q double side polished sapphire substrate. The fabrication steps of the resonator have been given in details in Chapter 2. Using RF magnetron, sputtering metallization is done with thicknesses of 150 nm for both the top and the bottom electrodes and the PLD technique is used to deposit the thin film of BST which is of thickness around 1 µm. The top electrode (80 µm radius – inner circle and 300 µm diameter – outer circle) is patterned as a circular patch capacitor (CPC) in order to reduce the complexity in fabrication and is shown in Fig. 5.1. The fabricated HBAR is characterised without any polymer coating at first. Similar to what has been described in Chapter 4, onwafer probing is carried out using an Agilent E8361C vector network analyser (VNA) and a 250 µm pitch GSG (ground-Signal-Ground) probe. The S<sub>11</sub> parameter of the 1-port HBAR is measured after doing calibration with open, short and load of the standard CS-5 substrate

(GGB Industries). A DC bias is given using a DC bias tee to excite the induced piezoelectric effect in the BST based HBAR.

For studying the effect of the coating on HBAR, SU-8 (Microchem) which is a polymer is taken into consideration as it can be easily coated using spin coating. Besides, removing it from the HBAR is easy, which is very important as the same resonator is to be used for characterizing different coating thicknesses as well in order to get a bigger picture of the effects. Three different thickness of around 2.1  $\mu$ m, 3.2  $\mu$ m and 6.1  $\mu$ m of SU-8 are coated on the backside of the substrate (Fig. 5.1) and measured one by one.

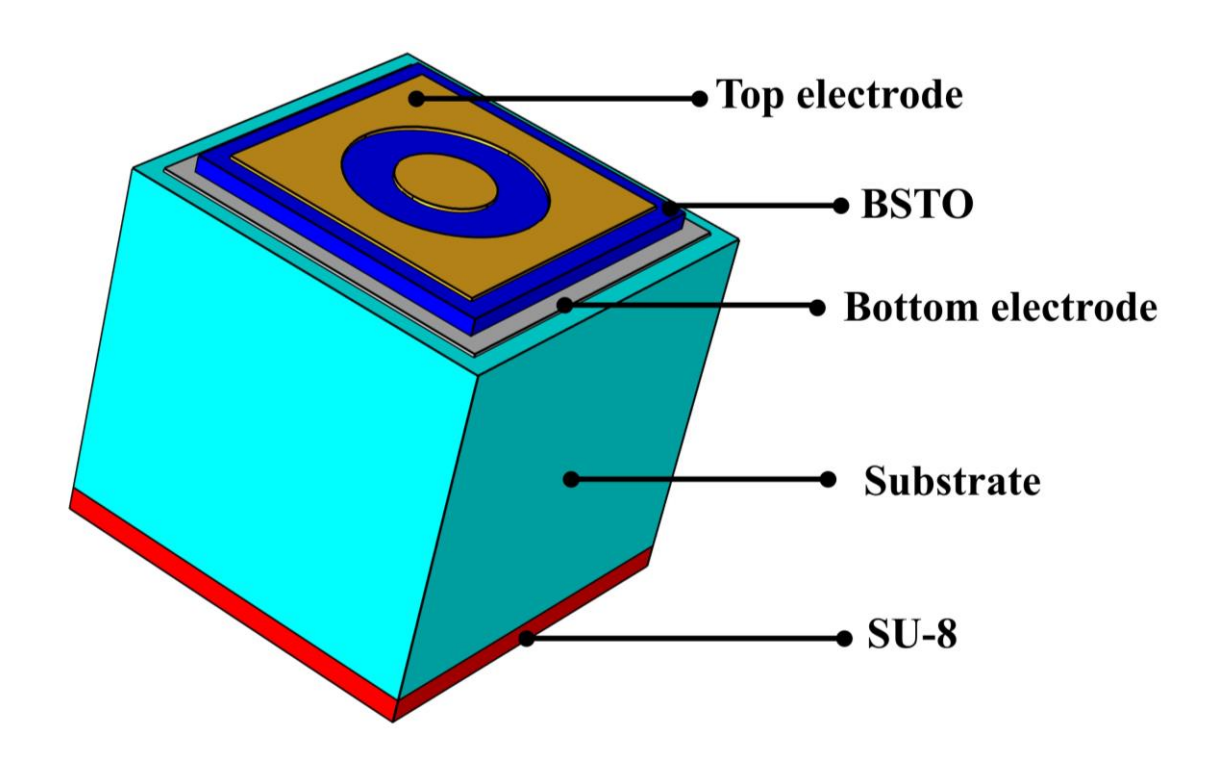


Figure 5.1. Schematic of HBAR with SU-8 coating

# **5.2.2** Experimental Results

The input impedance of the HBAR without the coating is extracted from the  $S_{11}$  from the measurement in the frequency range of 600 MHz to 3.5 GHz and is plotted in Fig. 5.2. A DC bias of 60 V is applied across the BST transducer during the measurement to get the induced piezoelectric effect in the resonator. Fig. 5.3 shows the plot of the frequency spectra of the HBAR with SU-8 of thickness 2.1  $\mu$ m coated on the backside of the substrate.

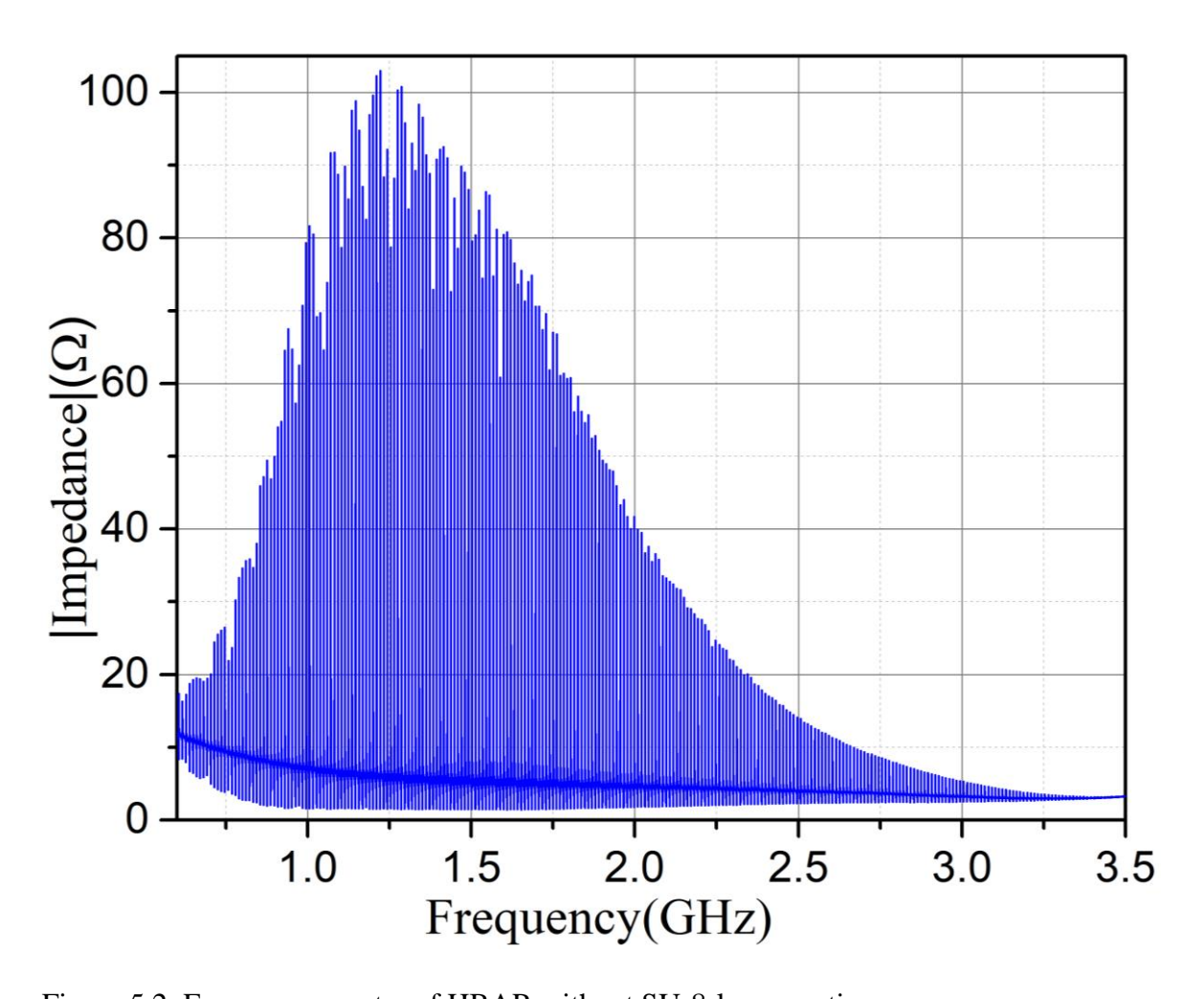


Figure 5.2. Frequency spectra of HBAR without SU-8-layer coating.

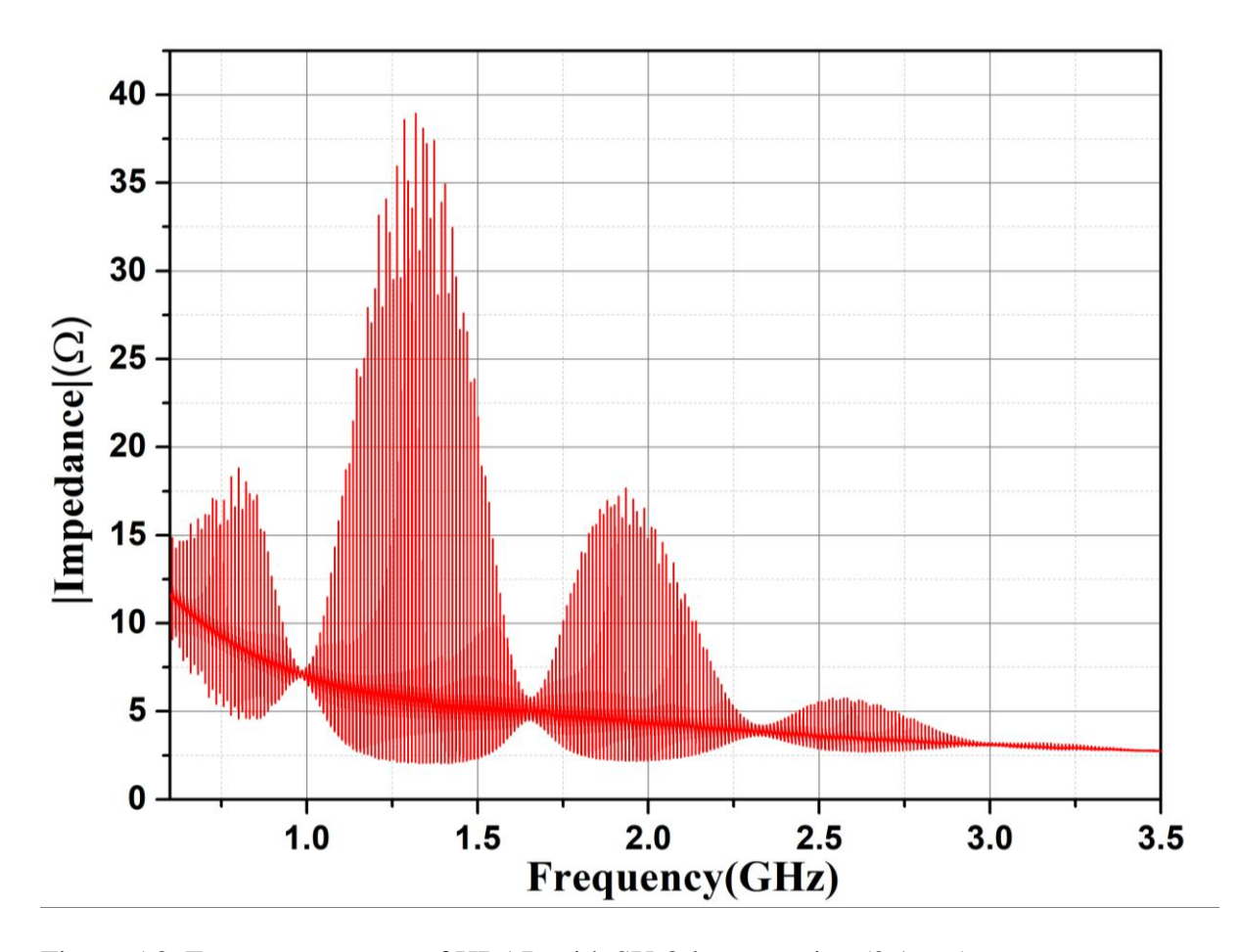


Figure 5.3. Frequency spectra of HBAR with SU-8-layer coating (2.1 μm).

As observed from Figs. 5.2 and 5.3, there is a significant change in the response of the HBAR with and without an SU-8 coating. The shape of the envelope of the frequency spectra for the HBAR has changed after the introduction of a new layer on the acoustic pathway i.e., the SU-8 layer coated on the backside of the substrate. For the case of the SU-8 coated HBAR, at certain specific areas in the spectra, the impedance has dropped considerably low as compared to the case without the SU-8 coating. It is also observed that these regions where the intensity drop happens appear to occur at a regular interval in the frequency spectra. From this, it can be inferred that similar to the spacing created between the adjacent resonant peaks in the response because of the acoustic property and the thickness of the substrate as discussed in chapter 4, the thickness and the acoustic properties of the material coated onto the substrate influence the spacing between the perturbed area

in the spectrum. The influence of the thickness of the SU-8 layer coated on the response of the HBAR is shown in Fig. 5.4.

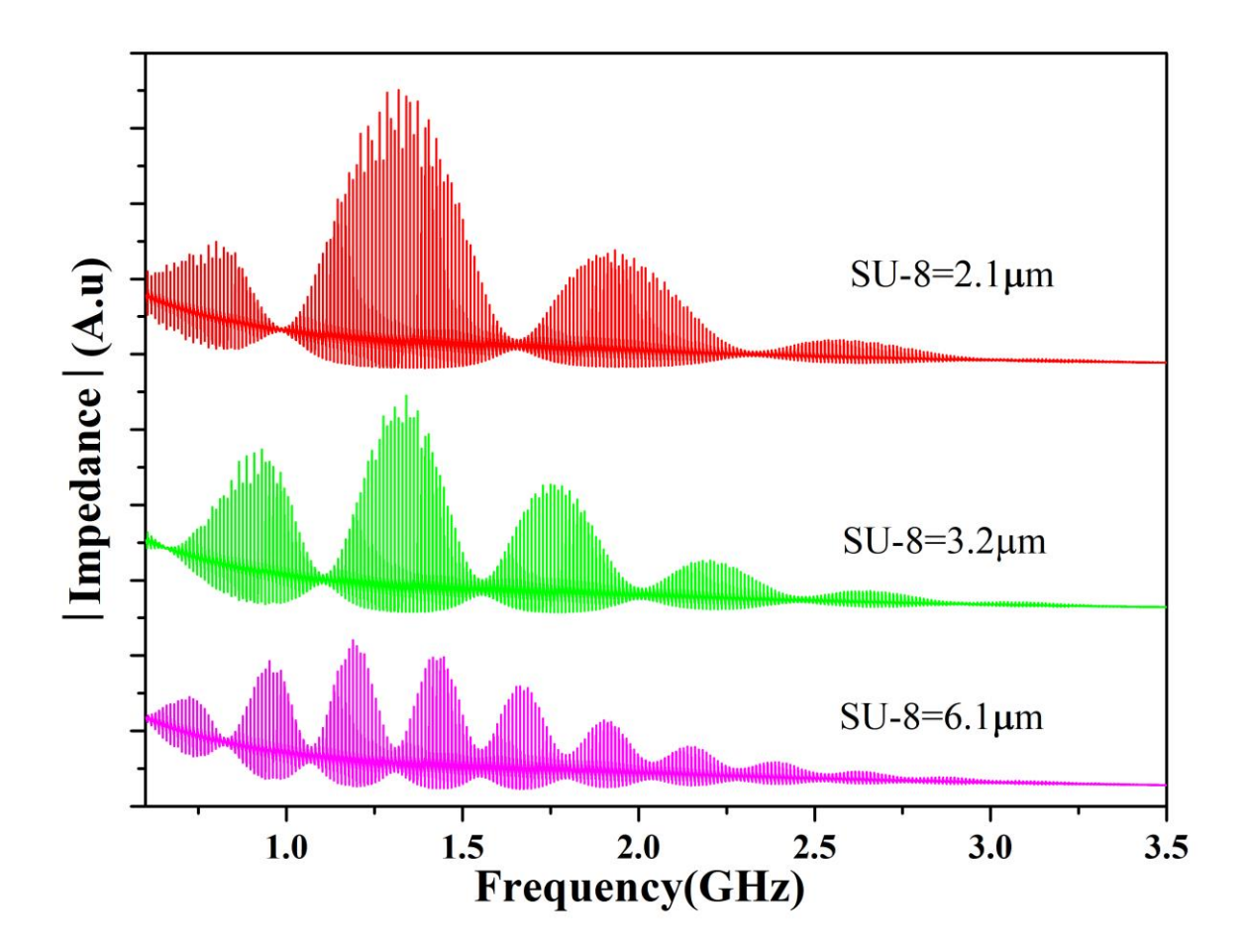


Figure 5.4. Frequency spectra of HBAR for different thickness of SU8 coating.

The new interval between the perturbed regions may be thus calculated using:

$$\Delta f_c = \frac{v_c}{2.t_c} \tag{5.1}$$

where,  $v_c$  and  $t_c$  are the acoustic velocity and thickness of the coated material.

From equation (5.1), it is notable that by extracting the interval and from the value of any of the known parameters i.e., either the velocity or the thickness, the other can be calculated. The dependence of this periodicity on the acoustic velocity and the thickness of the coating set a limitation to the type of the material and the thickness which can be used for characterization. It is evident from equation (5.1) that if the acoustic velocity is high and

the thickness is comparatively low for the material (the coating on the backside of HBAR) to be analyzed, then the frequency interval of the perturbation regions will be large and thereby, does not confine within the resonance spectra where the resonant peaks are of high amplitudes. On the other hand, if the acoustic velocity is low and the thickness is high, the interval of perturbation regions will appear too close to each other making it difficult to distinguish from the intervals caused by the substrate. In this chapter, the thickness and the material to be coated on the backside of the substrate has been carefully chosen such that at least two or more perturbations (peak burning) appear within the frequency range where the resonant peaks of bare BST thin film occur. Since there are multiple peaks in the resonant spectra of the HBAR, it is easier to study the effects in terms of derived parameters like the effective coupling coefficient, the spacing of parallel resonance frequencies and the Q factor of the resonator. The next section gives the experimental results for all these derived quantities for both the bare HBAR without SU-8 coating and with SU-8 coating.

# 5.2.3 Effect of coating on SPRF, $k_{eff}^2$ and Q factor of HBAR

The distributions of SPRF,  $k_{eff}^2$  and Q factor for all the cases to be discussed in this section are derived using equations (3.54), (3.55) and (4.4) respectively. First of all, the parameters for the HBAR without the SU-8 are extracted (as in chapter 4) and plotted in Figs. 5.5 and 5.6. Similar plots for the distributions of SPRF,  $k_{eff}^2$  and Q factor for HBAR with coating of SU-8 with different thicknesses of approximately 2.1  $\mu$ m, 3.2  $\mu$ m and 6.1  $\mu$ m are shown in Figs. 5.7-5.9.

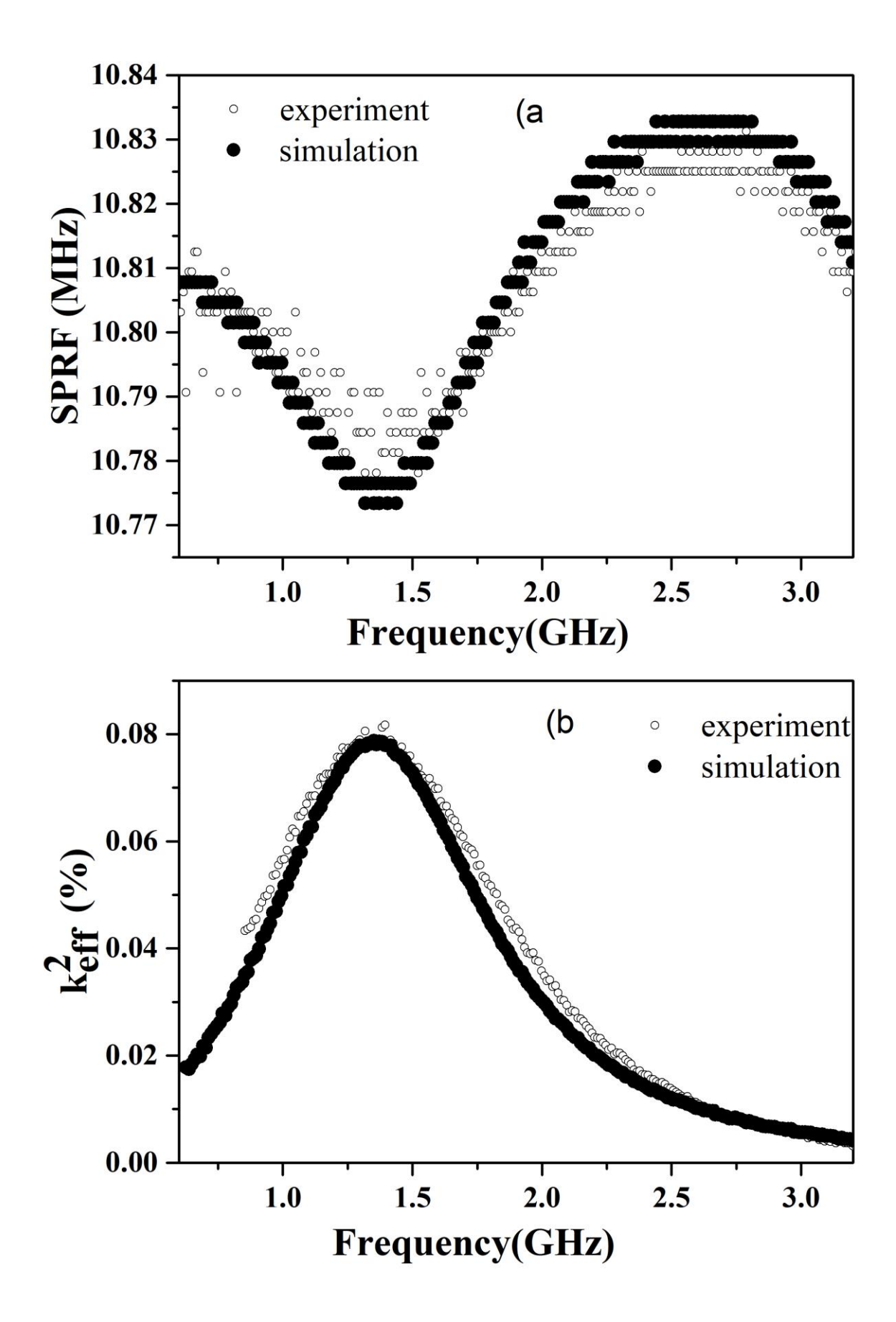


Figure 5.5. (a) SPRF and (b)  $k_{eff}^2$  distributions of the uncoated HBAR.

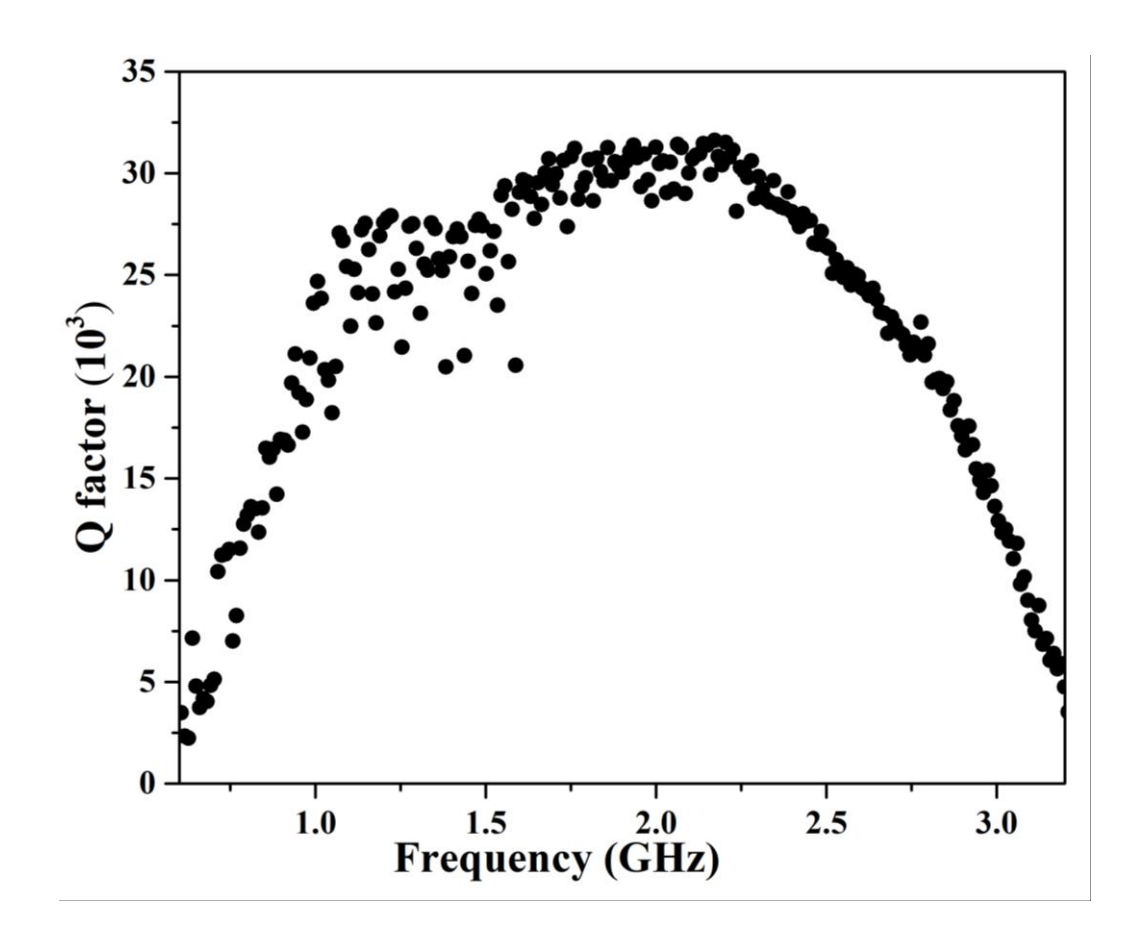


Figure 5.6. Q factor distributions of the uncoated HBAR.

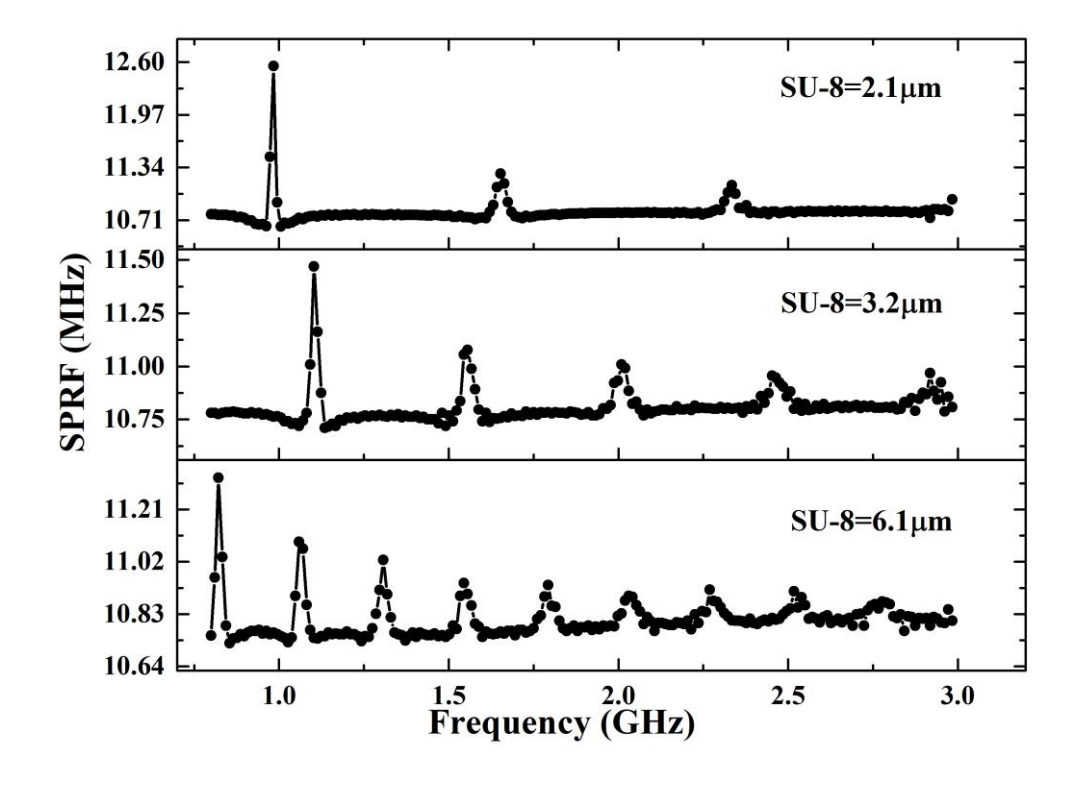


Figure 5.7. SPRF distributions of the SU-8 coated HBAR.

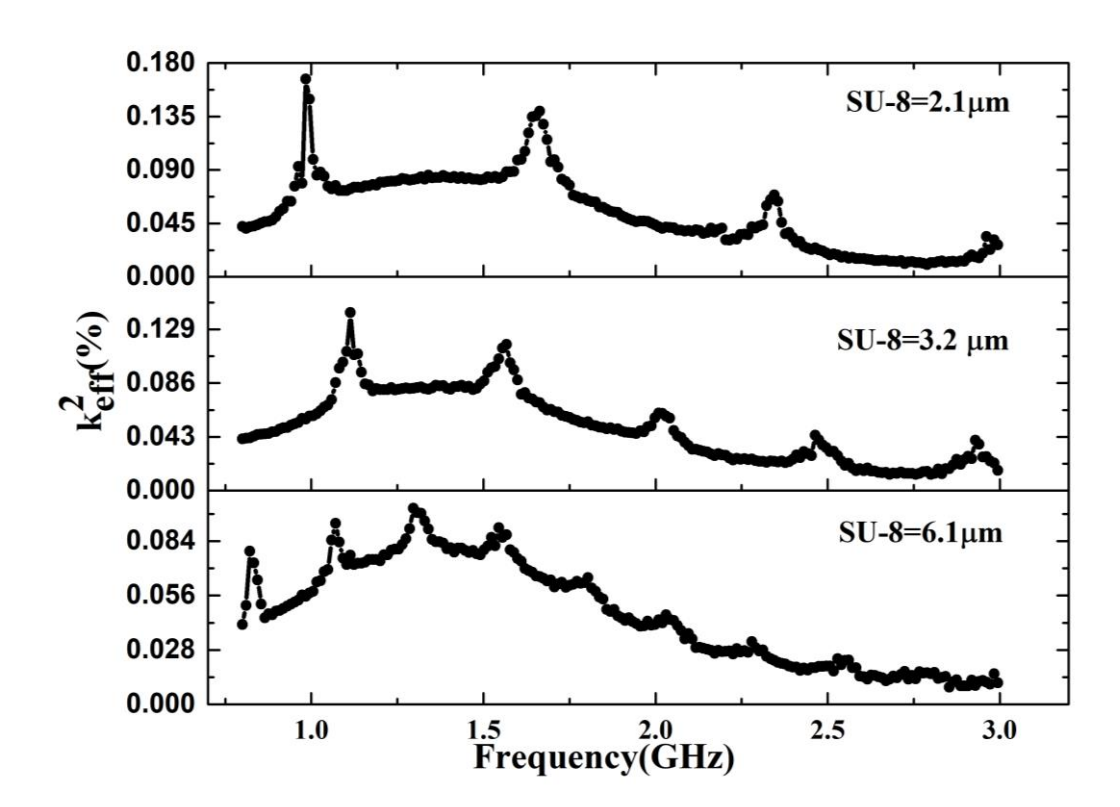


Figure 5.8.  $k_{eff}^2$  distributions of the SU-8 coated HBAR.

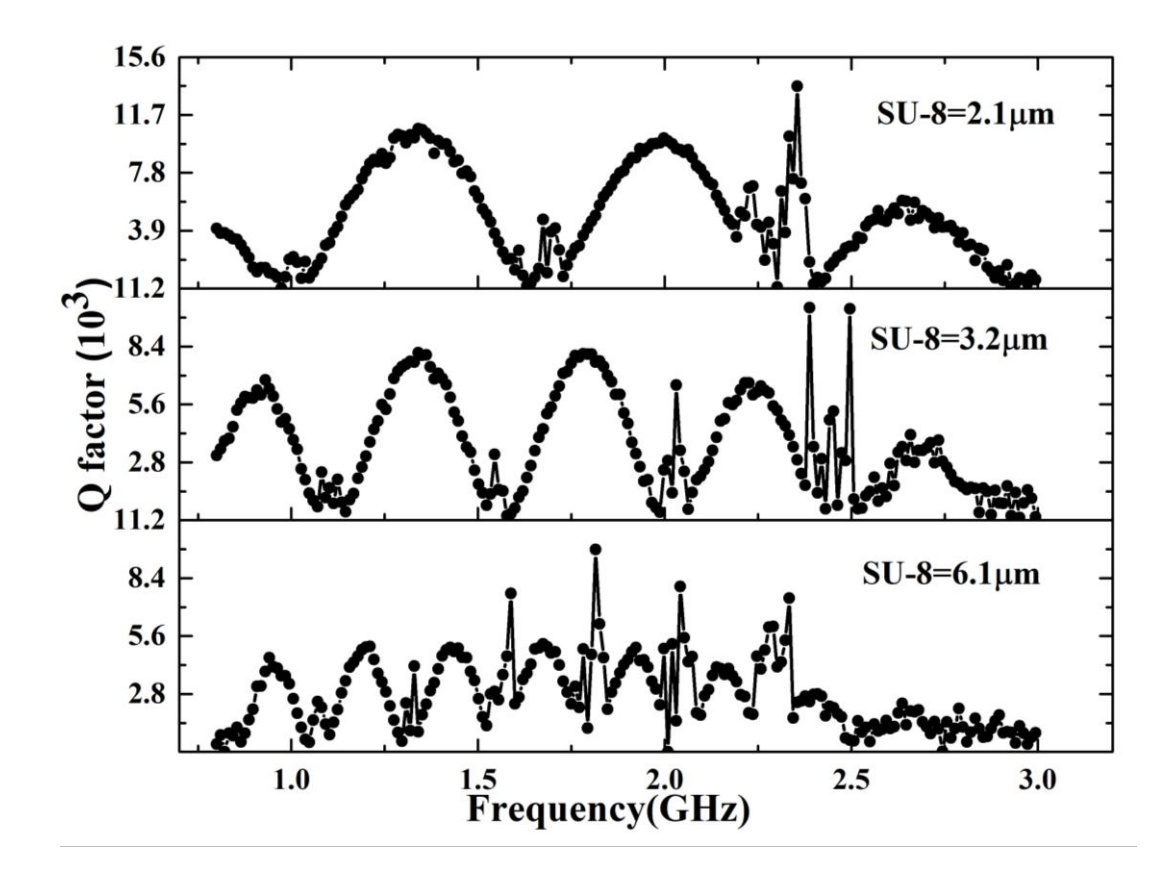


Figure 5.9. Q factor distributions of the SU-8 coated HBAR.

Comparing the plots for the uncoated and the coated HBAR, it can be clearly seen that the SPRF, the  $k_{eff}^2$  and the Q factor have been changed significantly with the coating. There is similarity with the impedance plots as discussed in the previous section. In the regions of the perturbation in the impedance plot, there is significant change in the HBAR parameters i.e., the SPRF, the  $k_{eff}^2$  and the Q factor. To picture the change in the parameters better, a comparative plot for the case with HBAR coated with 6.1  $\mu$ m thick SU-8 and HBAR without any coating is shown in Figs. 5.10 and 5.11.

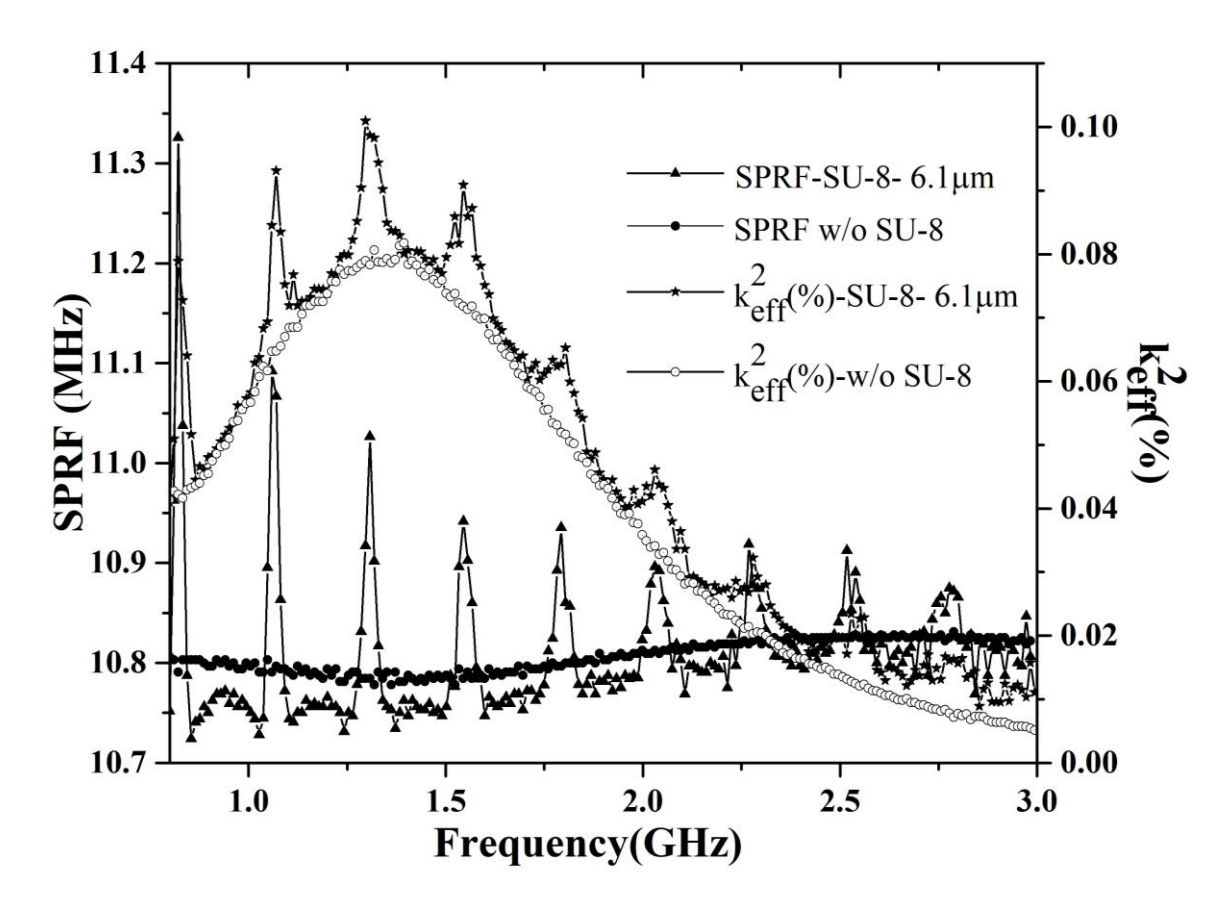


Figure 5.10. SPRF and  $k_{eff}^2$  distribution for both coated and uncoated HBAR.

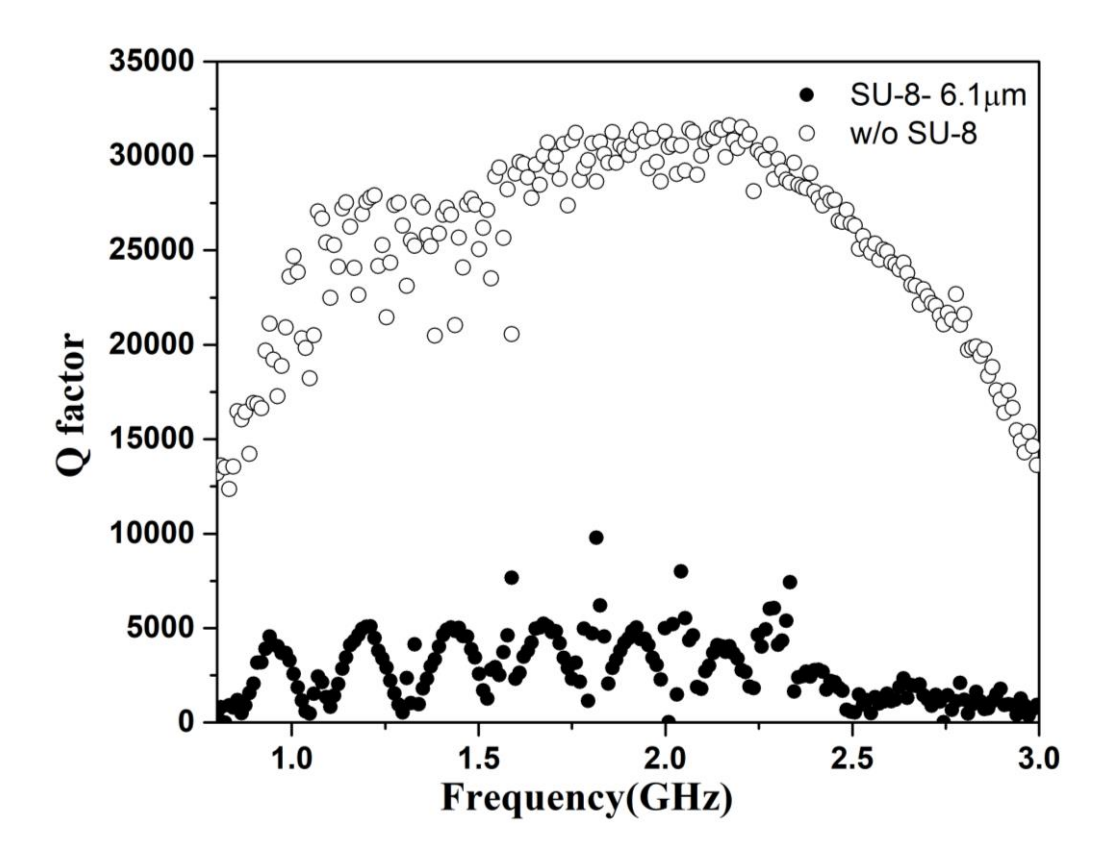


Figure 5.11. Q factor distribution of coated and uncoated HBAR.

The acoustic velocity of SU-8 as reported in [98] is 2886 m/s. From equation (5.1) and by using the thickness and the acoustic velocity of the SU-8, it seems that the maxima in the spacing of the SPRF and the  $k_{eff}^2$  and the minima in the case of Q factor occur around the regions where the coated layer thickness match with half wavelength of the acoustic wave travelling in the medium (SU-8 in this case). Another interesting observation made from the plots is that for the case of the SPRF, even though there is a drastic change in the distribution, as seen from Fig. 5.10, the overall SPRF of the coated HBAR decreases which is due to the addition of the layer in the substrate increasing the effective thickness of the substrate. This observation is in accordance with the work reported in [100,155,156]. As for the case of the  $k_{eff}^2$ , in the work discussed in [83], the mechanical loss or the Q of the substrate and the thin film has little effect on the  $k_{eff}^2$  distribution which is explained as due to the storage of energy confined mostly in the low loss substrate. But in contrast to

their observation, here, with the introduction of a high loss and low Q material in the acoustic path, the energy is shared by both the high Q substrate and the lossy SU-8 material. In the regions where the integral multiple of the half wavelength of acoustic wave is satisfied by the SU-8 layer, the lossy extended layer significantly increases the effective coupling coefficients. The Q factor distribution, as shown in Fig. 5.11, is drastically reduced overall due to the mass loading effect on the HBAR due to the SU-8 coating and this is more significant in the regions where the integral multiple of the half wavelength of acoustic wave is satisfied by the SU-8 layer. The work reported here is the first time this effect of the additional layer coating on the HBAR is studied experimentally [104]. Even though the experimental results give a comprehensive idea on the effect of the coating on HBAR, numerical simulations based on the model discussed in Chapter 3 and the finite element method (FEM) are necessary to properly extract the acoustic velocity and the Q factor of the SU-8 layer.

# 5.3 Simulation to extract the acoustic property of SU-8

In this section, numerical simulations are done using the model discussed in Chapter 3 for the HBAR coated with an additional layer. The SPRF and the  $k_{eff}^2$  distribution are extracted using this model. The SPRF of the numerical simulation is compared and fitted to the experimental results and the acoustic velocity and Q factor of the SU-8 layer are determined. Finite element method (FEM) is also used to demonstrate the effect of the SU-8 coating on the response of the HBAR.

#### **5.3.1** Numerical simulation

For numerical simulation, first of all the input impedance of the HBAR is derived from the model using equation (3.73), the parameters used in the simulation are given in Table 5.1. Using equations (3.54) and (3.55), the SPRF and the  $k_{eff}^2$  for the multiple resonant peaks in the frequency spectra are calculated. The SPRF distribution extracted from the numerical simulation along with the experimental results are potted in Fig. 5.12.

Table 5.1. Material parameters used in simulation

Material	Acoustic velocity (m/s)	Density (kg/m³)	Thickness (μm)	coupling coefficient $(k_t^2)$
BST	5088	5578	0.91	0.07
Platinum (Pt)	3300	21500	0.08	
Gold (Au)	3200	19300	0.08	
Sapphire (Al <sub>2</sub> O <sub>3</sub> )	10500	3993	450.59	
SU-8	2886 [1]	1100	2.18,3.26,6.07	

In the simulation of the coated HBARs, the acoustic velocities of SU-8 [98] are added with an imaginary part which is a function of the Q factor of the SU-8 or the material that is being coated. In the work reported in [100,155,156], instead of coating an additional layer, the thickness of the substrate is extended and hence the SPRF has reduced from the original case due to the increase in the overall increase of the acoustic cavity (the substrate). But these works are based on simulations of models and no experiments were conducted, moreover, for such case there is no change in the Q factor or the acoustic properties in the boundary as there is no introduction of a new material in the acoustic pathway. As seen

from Fig. 5.12, it is clear that the simulation result is very close to the experimental result. The reported Q factor of SU-8 is around 25 [157], and in the simulation performed here, the Q used is around 21-23 which is very close to the reported value. Only when the Q factor is properly chosen, the SPRF value approaches the experimental value. Thus, by fitting the numerical model results to experimental result, the Q factor is found out. Apart from the Q factor, the acoustic velocity of the SU-8 is found to be around 2886 m/s. The distribution of  $k_{eff}^2$  doesn't fit properly to the experimental result, but there is sudden increase in the  $k_{eff}^2$  value which is observed in the simulation result as well (Fig. 5.13).

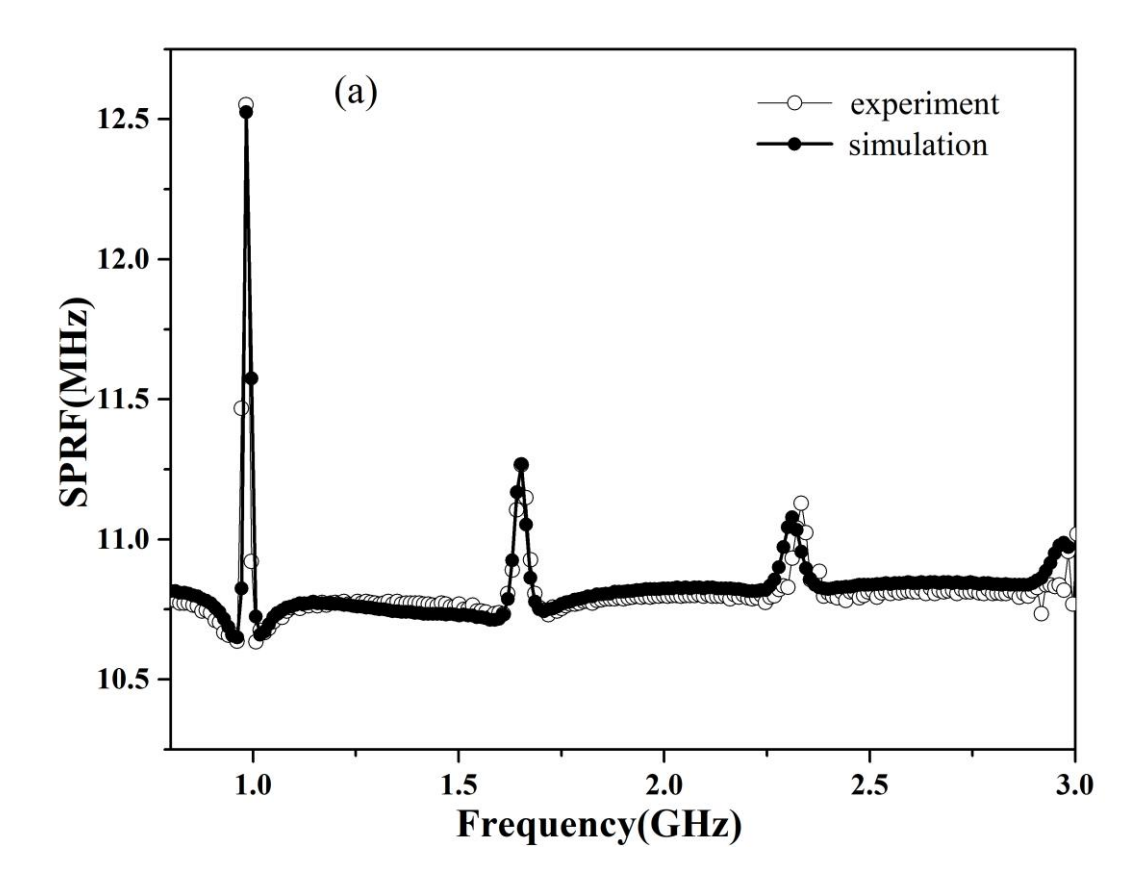


Figure 5.12(a). SPRF distribution for both simulation and experimental results where thickness of SU-8 coated is  $2.1 \,\mu m$ .

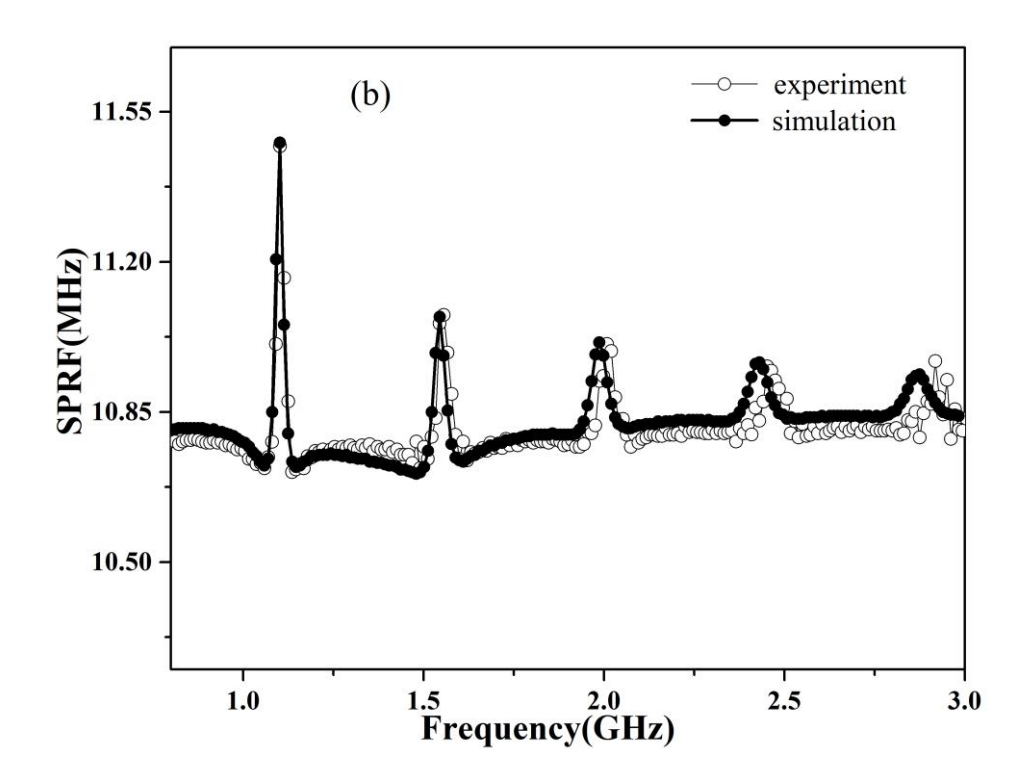


Figure 5.12(b). SPRF distribution for both simulation and experimental results where thickness of SU-8 coated is  $3.2 \, \mu m$ .

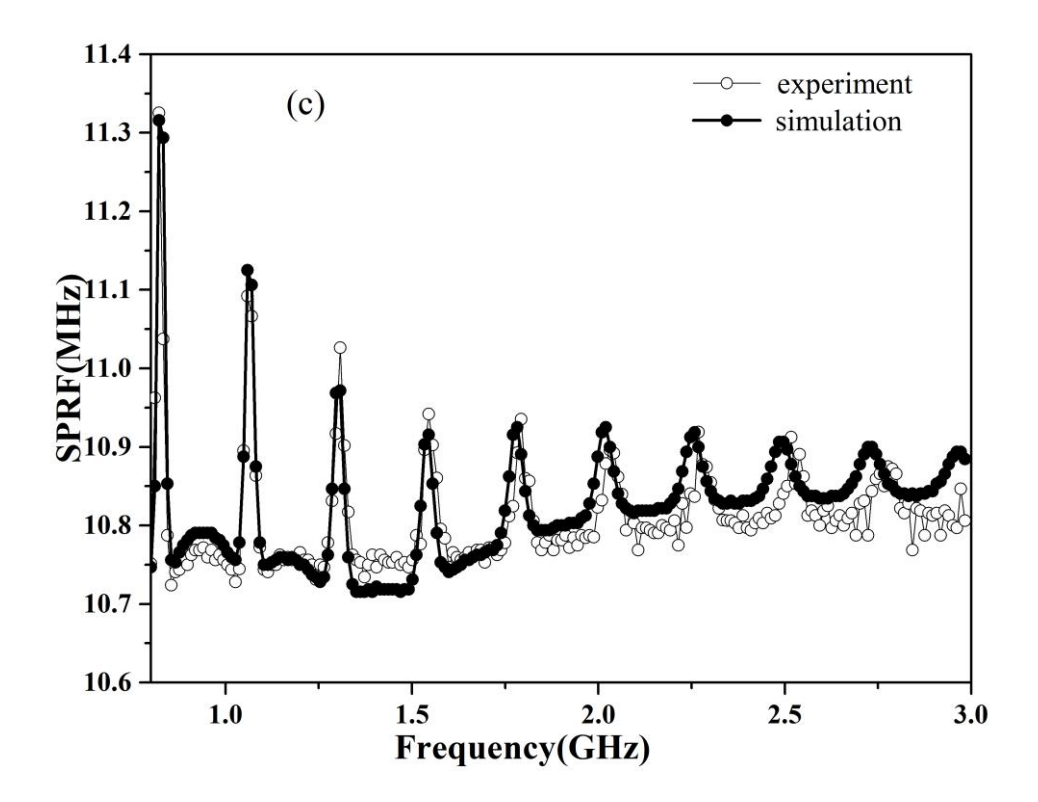


Figure 5.12(c). SPRF distribution for both simulation and experimental results where thickness of SU-8 coated is 6.1  $\mu$ m.

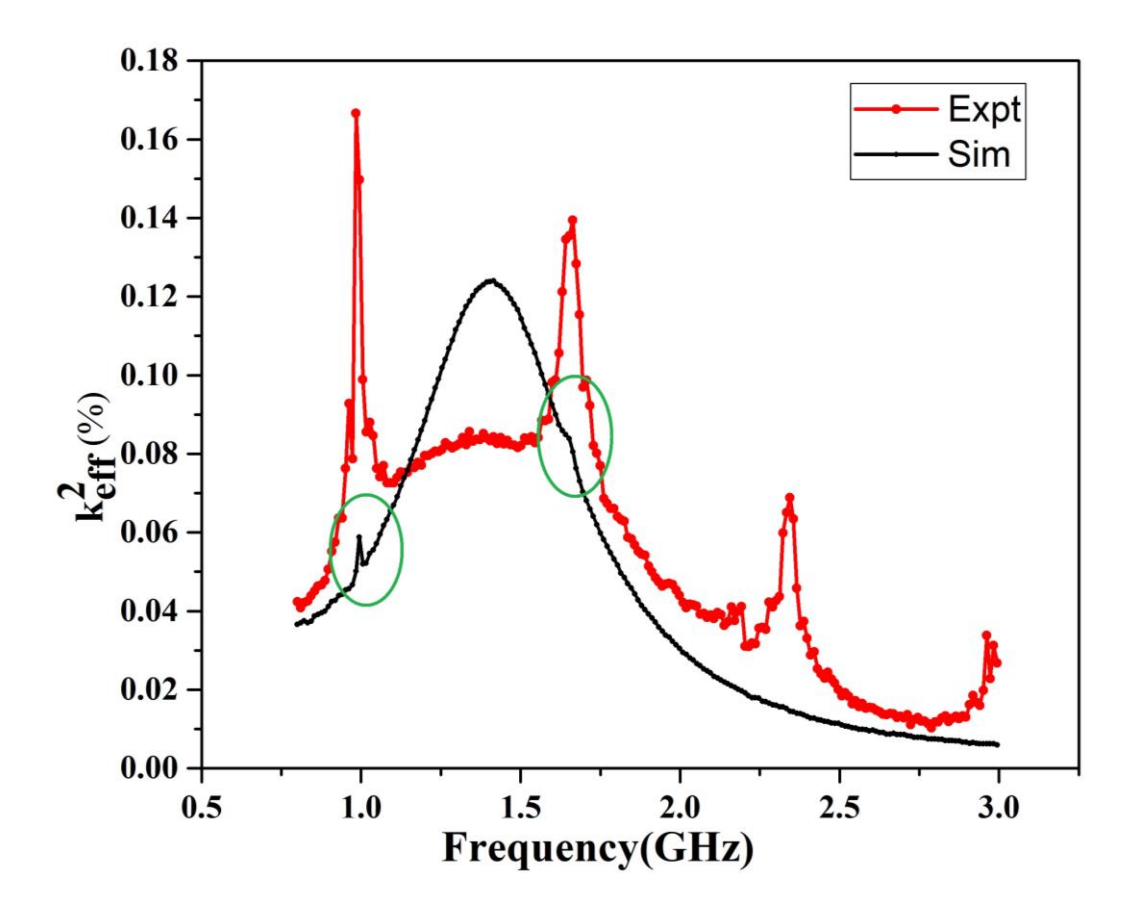


Figure 5.13.  $k_{eff}^2$  for HBAR with 2.18 µm thick SU-8 coating (Simulation).

As seen in Fig. 5.13, the experimental and the simulation results for the  $k_{eff}^2$  distribution does not fit well as in the case of the SPRF distributions (Fig. 5.12). But, the values of the  $k_{eff}^2$  for both the experimental and the simulation are in the same order and in some regions (encircled in green in Fig. 5.13), the  $k_{eff}^2$  value from the simulation shows a sudden increase in its value similar to the case of experimental distribution. This difference in the plot for the experimental and the simulation results for the  $k_{eff}^2$  may be due to the fact that the mechanical loss or the Q factor has little effect on the  $k_{eff}^2$  based on the model. This was also observed for cases in works reported in [83]. To further elaborate, the effect of the Q factor of the SU-8 on the SPRF and the  $k_{eff}^2$  of the HBAR, numerical simulation is done

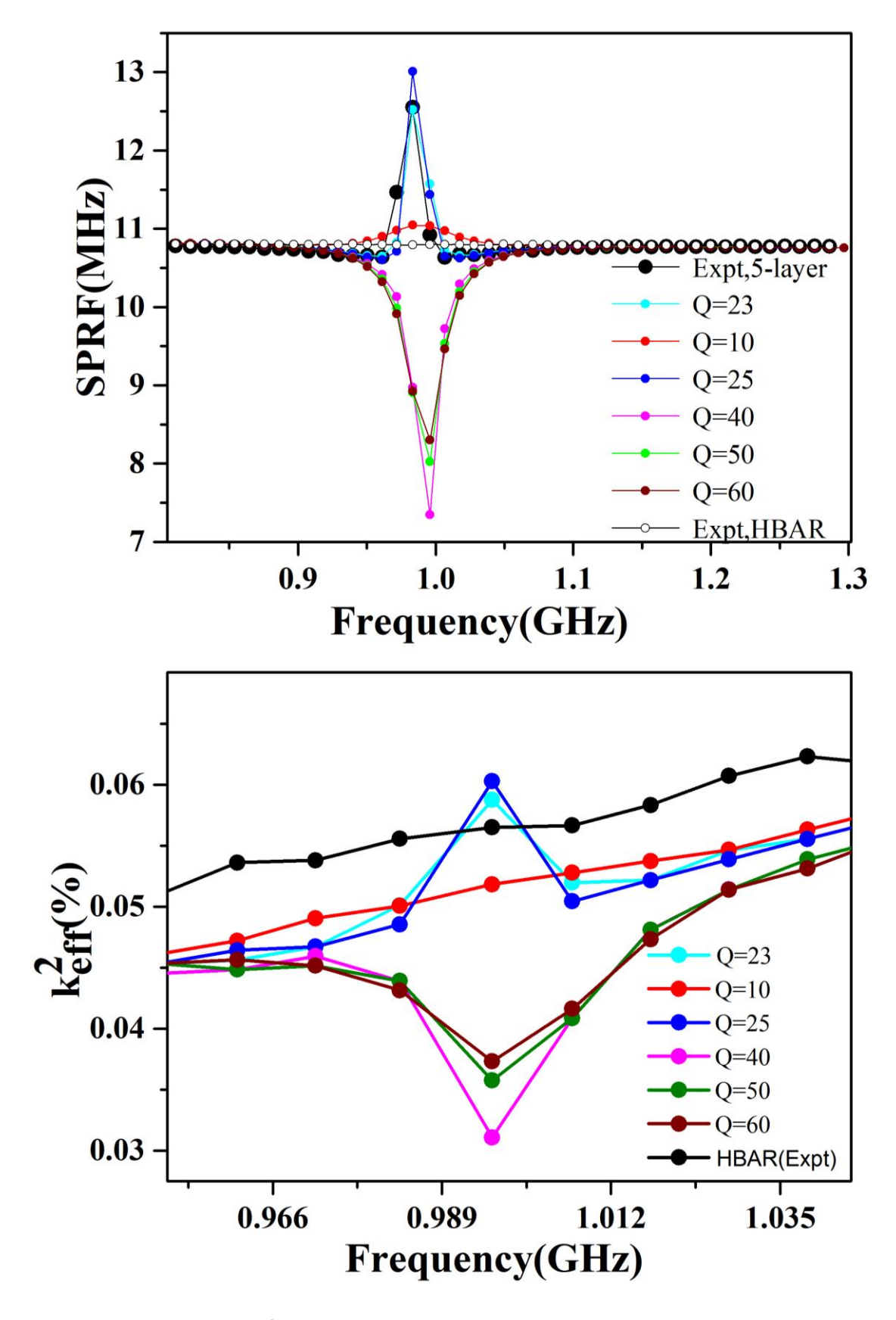


Figure 5.14. SPRF and  $k_{eff}^2$  distribution for different cases of Q factor of SU-8 given during simulation.

for a narrow band frequency (around the perturbation region) for different values of the Q factor of the SU-8 with a thickness of 2.18 µm and is shown in Fig. 5.14.

As shown in the distribution of the SPRF in Fig. 5.14, it is clearly seen that the experimental and the simulation results fit well only when the value of Q is chosen to be 23. This is not the case for the  $k_{eff}^2$  distribution (it deviates from the experimental result as shown in Fig. 5.13). The frequency range considered in Fig. 5.14 is the region where perturbation due to the additional SU-8 layer occurs. As discussed before in the experimental section, the acoustic energy is now distributed between the lossy SU-8 layer and the sapphire substrate. The sharp contrast in acoustic impedance and the Q factor when the acoustic wave passes from sapphire to SU-8 might be the reason why there is a drastic change in the values of the SPRF and the  $k_{eff}^2$ . The SPRF and the  $k_{eff}^2$  around this region seem to heavily depend on the value of Q of the coated layer. It is to be noted that Fig. 5.14 is mainly to show how the fitting of data is done (specifically for SPRF). The change in the SPRF and the  $k_{eff}^2$  with the change in Q factor of SU-8 in the simulation results can be attributed to the mechanical losses introduced in the complex acoustic wave propagation in the 1-D model [149,150] as:

$$V_c = V_r \left( 1 + j \frac{V_i}{V_r} \right) \tag{5.2}$$

$$\frac{v_r}{v_i} = 2Q \tag{5.3}$$

where  $V_c$  is the complex acoustic velocity,  $V_r$  and  $V_i$  are the real and imaginary part of the acoustic velocity respectively, and Q is the material Q-factor.

Comparing the simulation result and the experimental values, the acoustic velocity and the Q factor is found to be 2886 m/s and 23 respectively which is close to the values reported in [98,157].

#### **5.3.2** Finite element method (FEM) simulation

Apart from the numerical simulation done using the 1-D model, FEM simulation is done for the HBAR with and without coating. The FEM simulation is done to get a clearer picture of the acoustic wave transmission in the resonator and its response. Since the HBAR is fairly large, modeling the whole structure for a broad range of frequency is difficult due to the amount of time and resources it consumes. So, a narrowband of frequency window is selected where the minima occur in the spectra of the response. For FEM simulation, COMSOL Multiphysics ® is used, and the model is chosen to be 2D-axisymmetric. The acoustic bundle of the software is used and the materials are chosen from the material library. The properties and the dimensions of each layer is modified according to the parameters given in Table 5.1. For the simulation, SU-8 of thickness 2 µm is chosen. The active area of the resonator is given to be the area defined by an 80 µm in diameter circle. Since the properties of BST is not available in the software, BTO (Barium titanate) is used instead. This selection does not have any significant implication since the interest is to see the response of the effect of the coating on the HBAR. The acoustic velocity, the thickness and the density of the material are modified with the values of BST. A perfectly matched layer (PML) is used during simulation to take care of the effect of propagation and absorption of elastic waves in the surrounding regions which are not considered in their true geometric scale [158].

The impedance plots for both the experimental and the simulation results are plotted in Fig. 5.15, for a frequency window of 0.97 GHz to 1.025 GHz for both HBAR with and without SU-8 coating. From Fig. 5.15, it is clearly seen that the spacing between the parallel resonant peaks are increasing in both the experimental as well as the FEM simulation results. It is quite evident in the plots that the intensity and the bandwidth of the resonant peaks have significantly decreased and increased respectively for both the experimental

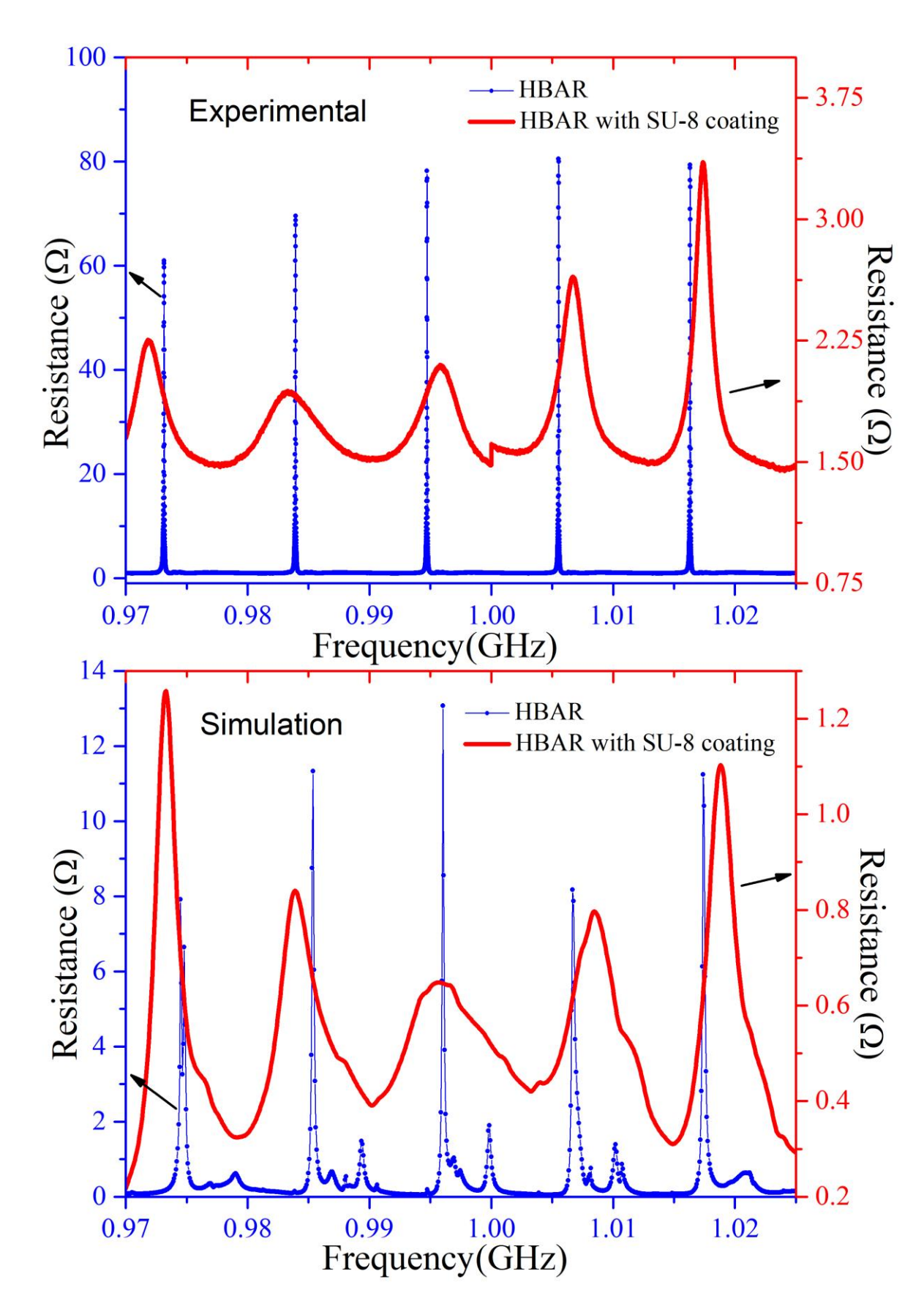


Figure 5.15. Real part of impedance of HBAR with and without SU-8 layer for experimental (top) and FEM model (bottom).

freq=1.0067E9 Hz Surface: Displacement field, Z component (nm)

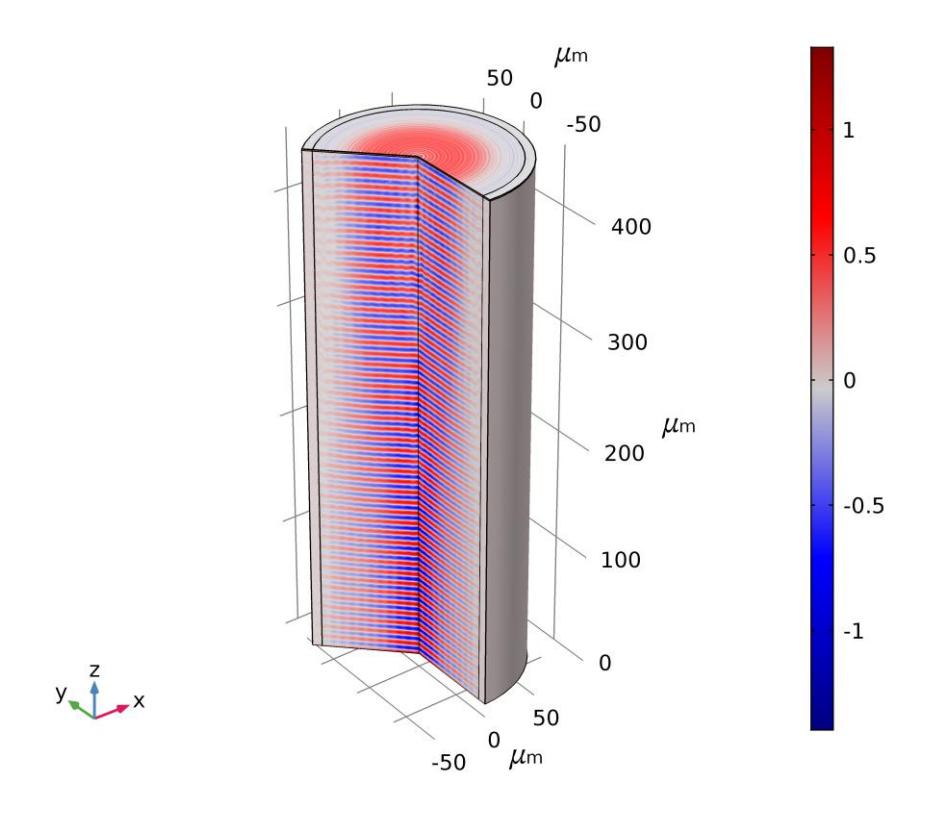


Figure 5.16. Thickness extensional mode of the HBAR without SU-8 layer.



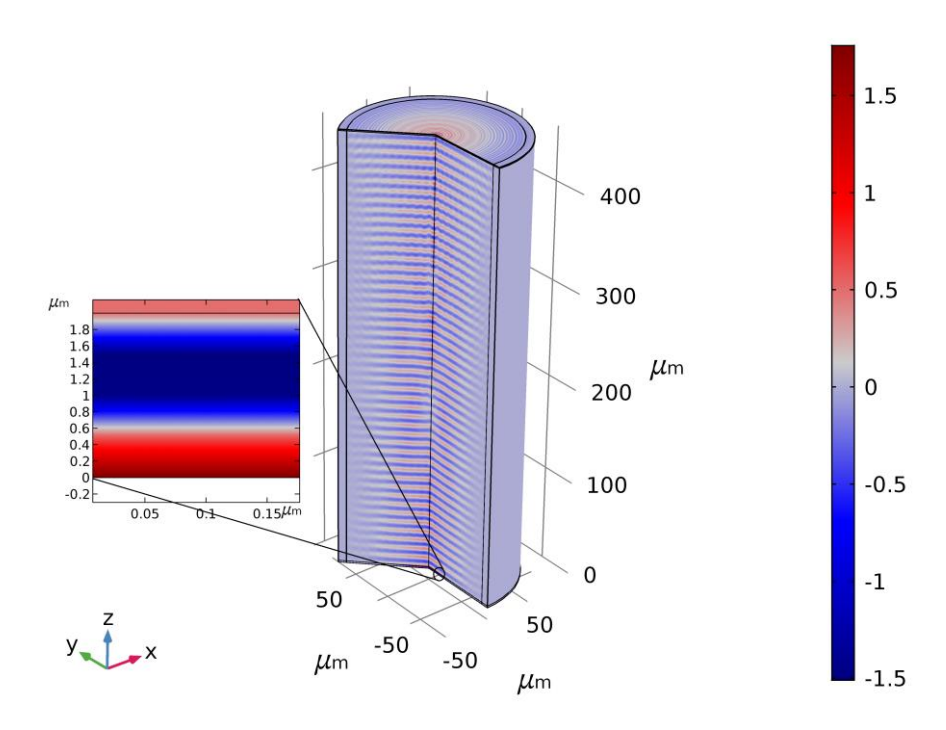


Figure 5.17. Thickness extensional mode of the HBAR with SU-8 layer.

and the FEM cases. Fig. 5.16 shows the thickness extensional nature of the HBAR without the SU-8. In Fig. 5.17, the HBAR with the SU-8 layer, exhibits the thickness extensional nature with maximum displacement occurring in the SU-8 layer.

# 5.4 Summary and Conclusion

In summary,

- The effect of coating an additional SU-8 layer on the backside of the substrate in an HBAR is studied. Disturbance or perturbation in the frequency spectra of the coated HBAR is observed. This perturbation is found to be dependent on the thickness and the acoustic wave velocity of the material that is coated.
- 2. The effect of the SU-8 coating on the various parameter of the resonator i.e., the SPRF, the  $k_{eff}^2$  and the Quality factor are studied. Significant changes are observed for all the parameters when compared to the response of the HBAR without any coating.
- 3. Numerical simulations are done from which the acoustic velocity and the Q factor of the SU-8 are extracted. FEM simulation confirms the decrease of intensity of the resonant peaks thereby reducing the Q factor of the resonant peaks. The sudden increase in the spacing of parallel resonance frequency is also observed in the results of both numerical and FEM simulation and the Q factor of the material is found to be a major factor in this phenomenon.

In this chapter, the effect of an additional coating on the HBAR is studied and is found that the responses of the resonator changes drastically. From this, it is inferred that the HBAR is highly sensitive to the mass loaded onto it. This effect due to mass can be further developed for applications in gravimetric sensing. Apart from mass loading, it is evident that the acoustic property and the thickness of the coated layer can be characterized, which

will be useful in determining either the Q factor or the acoustic velocity of the unknown polymer composites. The acoustic velocity of the SU-8 material is extracted to be around 2886 m/s and the Q factor is around 23. Limitation to this technique for characterization is that, the layer thickness and the acoustic velocity when chosen should not make the spacing of the perturbations regions to be too large or too small. Advantage of this technique is that this provides a direct method in characterizing unknown or composite polymers which has low Q, and it is not necessarily required to know the initial response of the HBAR.

# CHAPTER 6: Effect of electrode on the parameters of High Overtone Bulk Acoustic Resonators (HBAR)

# 6.1 INTRODUCTION

This chapter deals with the effect that the electrode material, its area and geometry have on the various parameters of HBAR like the SPRF, the  $k_{eff}^2$  and the Q factor. The effect of the electrode on the HBAR response has been studied in works reported by [150,159-161], and all of them have arrived at a conclusion that the parameters of the HBAR are affected by the choice of the electrode material, its thickness as well as its area. Except for the work reported in [161], other works in [150,159,160] are all based on numerical simulations of the models. Simulations do give us an idea of the nature of the responses but they may differ from experimental results due to various factors. The experimental work reported in [161] deals with only a few selected resonant modes; it is not a broadband study. In this chapter, the effects of the electrodes are studied for a broad range of frequencies and hence, the nature of how the distribution of the SPRF, the  $k_{eff}^2$  and the Q factor are affected by the electrodes can be understood.

#### **6.2** The electrode material

In order to study the effect of the electrode material, four different BST based HBARs are fabricated with different combinations of the top and the bottom electrodes. The different HBARs are assigned a name as given in Table 6.1. Table 6.2 gives the material properties of the HBARs.

Table 6.1. Name of Samples fabricated

Name of HBAR	<b>Bottom The electrode</b>	Top the electrode	
PP	Platinum (Pt)	Platinum (Pt)	
PG	Platinum (Pt)	Gold (Au)	
GG	Gold (Au)	Gold (Au)	
GP	Gold (Au)	Platinum (Pt)	

Table 6.2. Acoustic properties of materials [150,84].

Material	Acoustic Velocity (m/s)	Density (kg/m³)	Acoustic impedance (10 <sup>6</sup> kg/m <sup>2</sup> · s)	Thickness (μm)
BSTO	5088	5280	26.86	1
Platinum (Pt)	4017	21500	86.36	0.130
Gold (Au)	3361	19490	65.50	0.130
Sapphire	10500	3993	41.62	450

The thickness of the BST thin film for all cases is around 1  $\mu$ m with sapphire as the substrate (thickness ~ 0.5 mm). The CPC structure used for measurement in all the HBARs has a centre circular conductor of radius 80  $\mu$ m. During measurements for all the HBAR samples, a DC bias of 40 Volts is given across the thickness of the BST film. Similar to the

case in Chapter 4, the distribution of spacing of the parallel resonance frequencies (SPRF) and the effective coupling coefficient  $(k_{eff}^2)$  are calculated from the multiple resonant peaks or modes in the spectra (for different HBARs) using equation (3.54) and (3.55) respectively. The Q factor distributions can be calculated using equation (4.4).

#### **6.2.1** Effect of the electrode material on SPRF

Fig. 6.1 shows the SPRF distributions for the HBARs – GG, GP, PP and PG as defined in Table 6.1. Equation (3.54) is used for calculating the SPRF for resonant modes in the spectra of the HBARs.

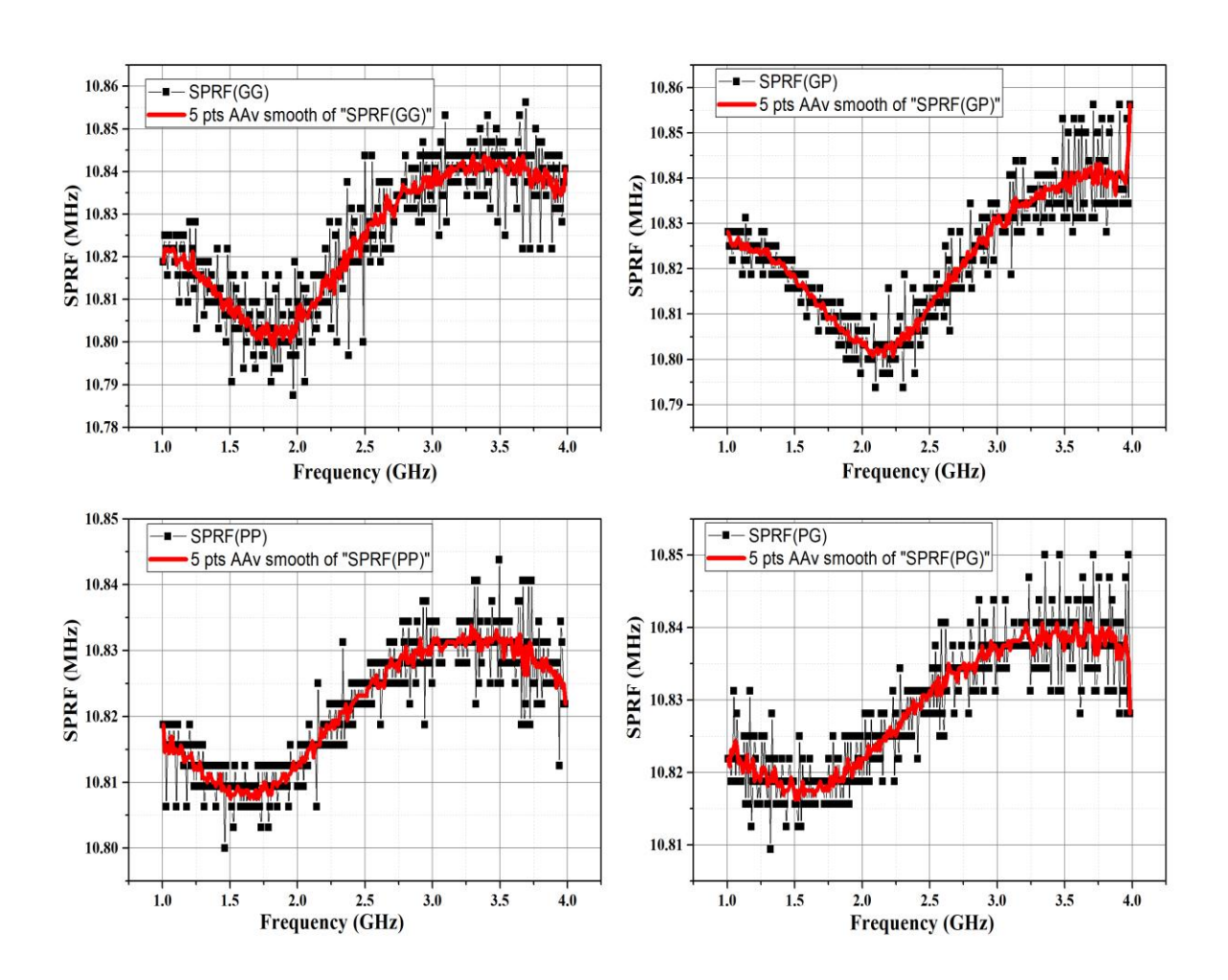


Figure 6.1. SPRF distributions for HBARs: - GG, GP, PP and PG.

In Fig. 6.1., the minima of the SPRF i.e., the first transition region seems to depend on the bottom electrode. In sample GG and GP, the bottom electrode is Au and for PP and PG, the bottom electrode is Pt. For sample GG and GP, the transition region is around 2 GHz and that of sample PP and PG is around 1.5 GHz. Another difference between these two sets is that the SPRFs values around the transition region are less for the case of GG and GP when compared to the samples with Pt as the bottom electrodes. The minima of the SPRF for both GG and GP are around 10.8 MHz, while that of PP and PG are 10.81 MHz and 10.82 MHz respectively.

Comparing GG and GP in Fig. 6.1, it is seen that the transition region for GG is around 1.8 GHz and that of GP is 2.1 GHz. The higher the acoustic impedance of the Pt the electrode seems to make the hard substrate (sapphire) softer [159], thereby shifting the transition region to higher frequency. This trend follows for the HBARs PP and PG, wherein the transition region of PP is around 1.64 GHz which is higher than that of PG which is around 1.51 GHz.

# 6.2.2 Effect of the electrode material on Effective Coupling Coefficient $(k_{eff}^2)$

Fig. 6.2. shows the SPRF distributions for HBARs – GG, GP, PP and PG. Equation (3.55) is used for calculating the  $k_{eff}^2$  for resonant modes in the spectra of the HBARs.

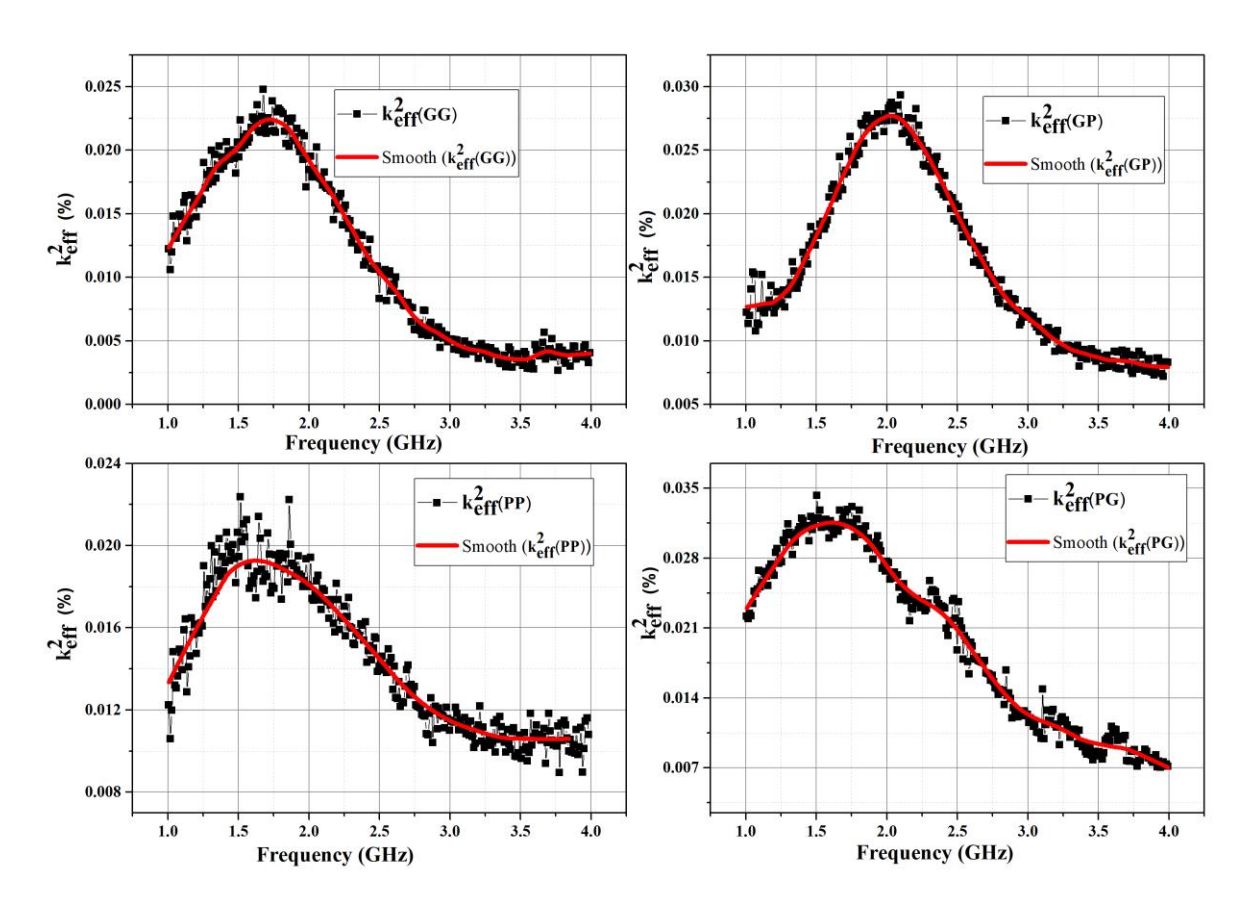


Figure 6.2.  $k_{eff}^2$  distributions for HBARs: - GG, GP, PP and PG.

From Fig. 6.2, it is observed that the HBAR PG exhibits the highest  $k_{eff}^2$  when compared to other HBARs with a value of around 0.031%. Likewise, in the case of the SPRF discussed in section 6.2.1, it is seen that the frequency (mode) of maximum  $k_{eff}^2$  for GG is around 1.8 GHz and that of GP is 2.1 GHz. Higher the acoustic impedance of the top electrode, apparently it seems to make the hard substrate (sapphire) softer [159], thereby shifting the transition region to higher frequency and hence, the shift in the mode with maximum  $k_{eff}^2$  towards a higher frequency. This trend follows for the HBARs PP and PG also, where the mode with the maximum  $k_{eff}^2$  for PP is at around 1.64 GHz which is higher

than that of PG which is around 1.56 GHz. The variation of  $k_{eff}^2$  are observed for FBARs and SMRs when different electrode materials are chosen. In the works reported in [162-164], they found that the highest obtainable  $k_{eff}^2$  is satisfied at an optimal thickness of the electrode used. A small variation of thickness of the electrode had considerable effect on the  $k_{eff}^2$  of the resonator.

## 6.2.3 Effect of the electrode material on Q factor of HBAR

Fig. 6.3. shows the Q factor distributions for the HBARs – GG, GP, PP and PG. Equation (4.4) is used for calculating the Q factor for the resonant modes in the spectra of the HBARs.

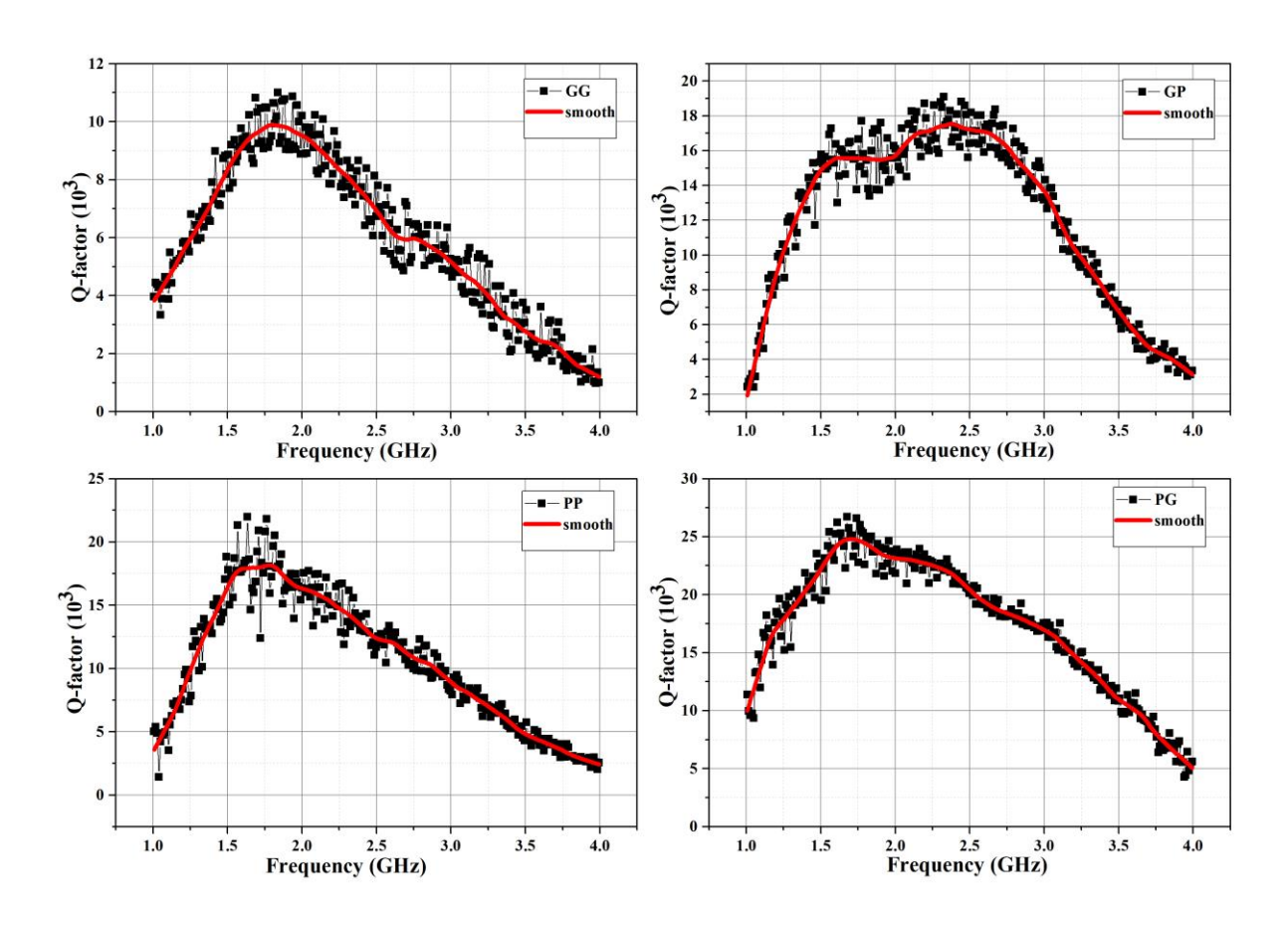


Figure 6.3. Q factor distributions for HBARs of electrode combination: - GG, GP, PP and PG.

It is clear from Fig. 6.3 that the Q factor of HBAR is dependent on the choice of the electrodes. The HBAR PG with Pt as the bottom electrode and Au as the top electrode exhibits the highest Q factor of around 25,000 in the frequency range of 1.5 GHz to 2 GHz. The HBAR GG, with Au as both the top and the bottom electrode exhibits the lowest value of Q factor of around 10,000 in the frequency range of 1.5 GHz to 2 GHz. Except for GG, the other HBARs also exhibit Q factor of around 20,000 in the frequency range of 1.5 GHz to 2 GHz. Ideally in numerical simulation as reported in [160], the Q factors of all the HBARs should be more or less the same or shouldn't vary significantly. The drastic variation in the Q factor of GG when compared to the other HBARs might be due to short comings in fabrication processes, especially when it comes to BST films grown over gold electrodes.

#### 6.3 Effect of the electrode shape and area

In order to study the effect of the top electrode area on various parameters of the HBAR, HBARs are fabricated with the top electrode design having various geometry and areas of the electrodes as shown in Fig. 6.4. The top electrode is made of Au and the bottom electrode is Pt deposited using RF sputtering. Sapphire substrate is chosen and BST thin film of thickness 1 µm is coated using PLD technique. Table 6.3 specifies the various names given to the HBARs with different top electrode geometry and areas. Eight different HBARs are measured and studied. The smallest square could not be studied as it shorted. DC bias of 40 V (400 kV/cm) is given during measurement for all the samples.

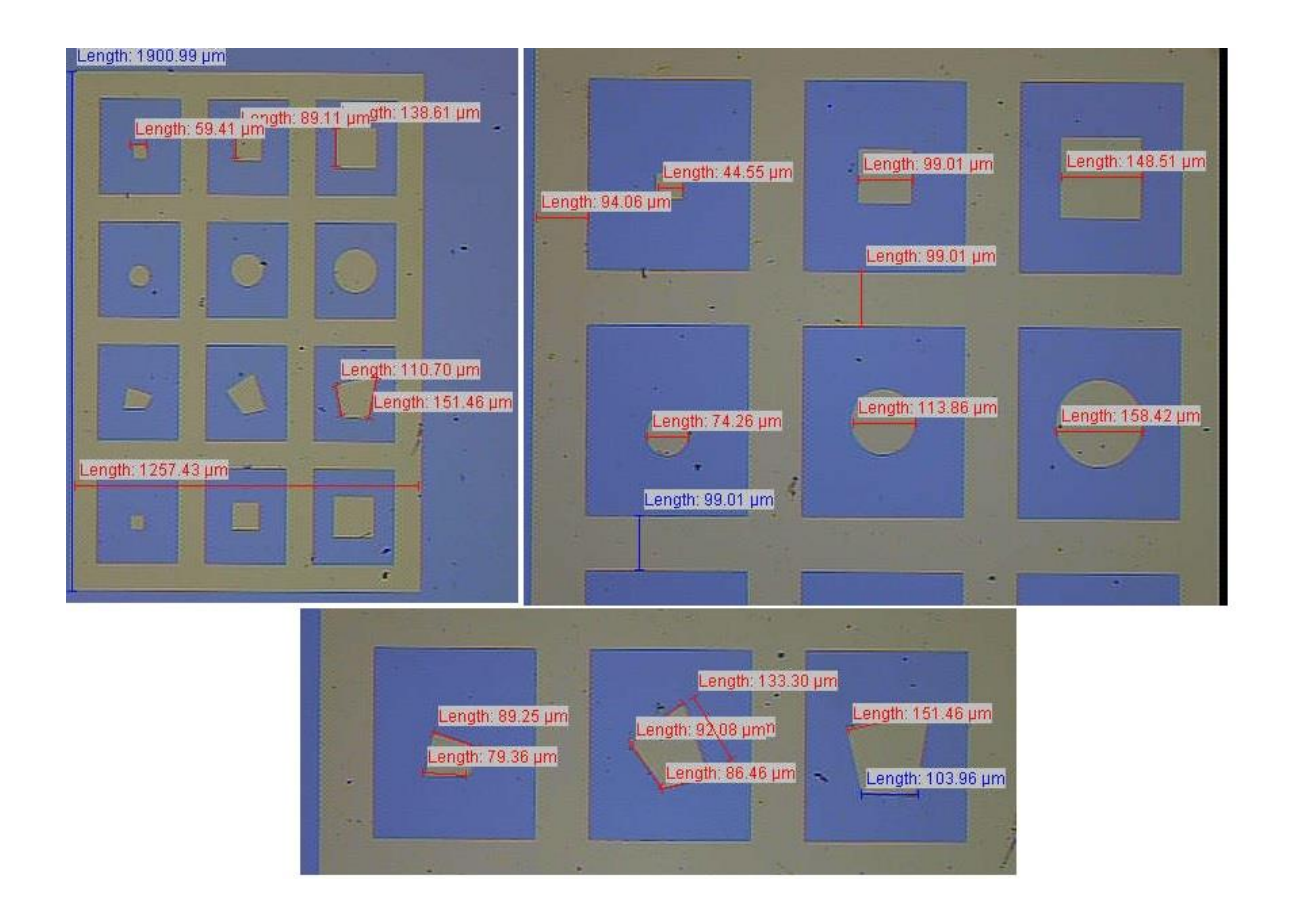


Figure 6.4. Various geometry and sizes of top electrodes.

Table 6.3. Name of HBARs with different top electrode geometry and areas.

Name	Geometry	Area
		$(10^{-3} \ \mu m^2)$
ВС	Circular	20
MC	Circular	11
SC	Circular	5
BS	Square	22.5
MS	Square	10
BA	Apodized	17
MA	Apodized	11
SA	Apodized	4.5

(The first letter of the name specifies the comparative size, B as in big, M as in medium and S as in small; the second letter specifies the shape of the top electrode).

#### **6.3.1** Circular electrodes

As shown in Fig. 6.4, there are three circular patterns with three different radii i.e.,  $40 \,\mu\text{m}$ ,  $60 \,\mu\text{m}$  and  $80 \,\mu\text{m}$ . These three circular electrodes are categorized as three different HBARs i.e., SC, MC and BC based on their areas. The design of the patterns is similar to that of the CPC which is discussed in Chapter 4. Figs. 6.5, 6.6 and 6.7 show the SPRF, the  $k_{eff}^2$  and the Q factor distributions of SC, MC and BC. The values of the SPRF, the  $k_{eff}^2$  and the Q factor are derived using equation (3.54), (3.55) and (4.4) respectively.

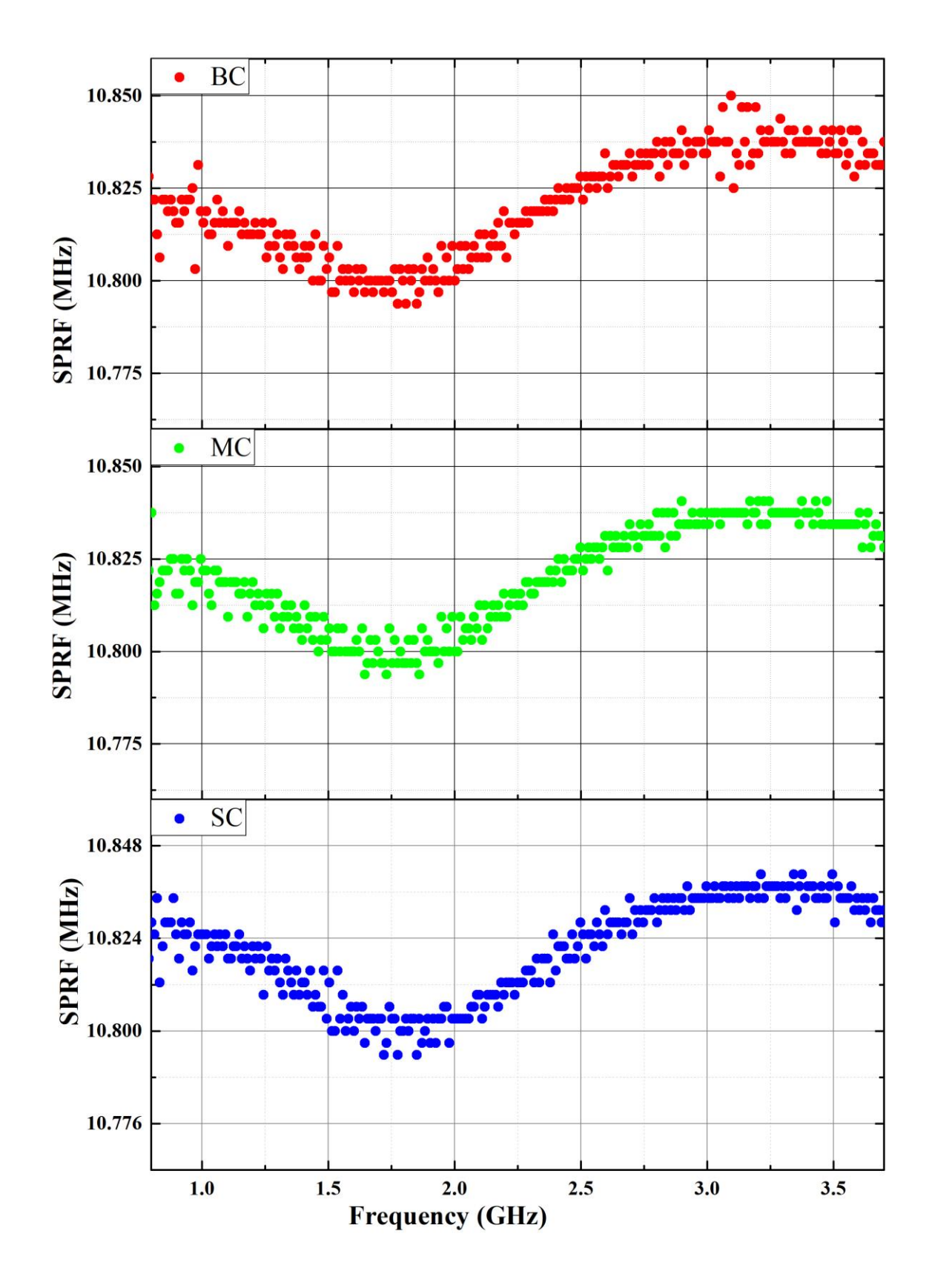


Figure 6.5. SPRF distributions for HBARs: - SC, MC and BC.

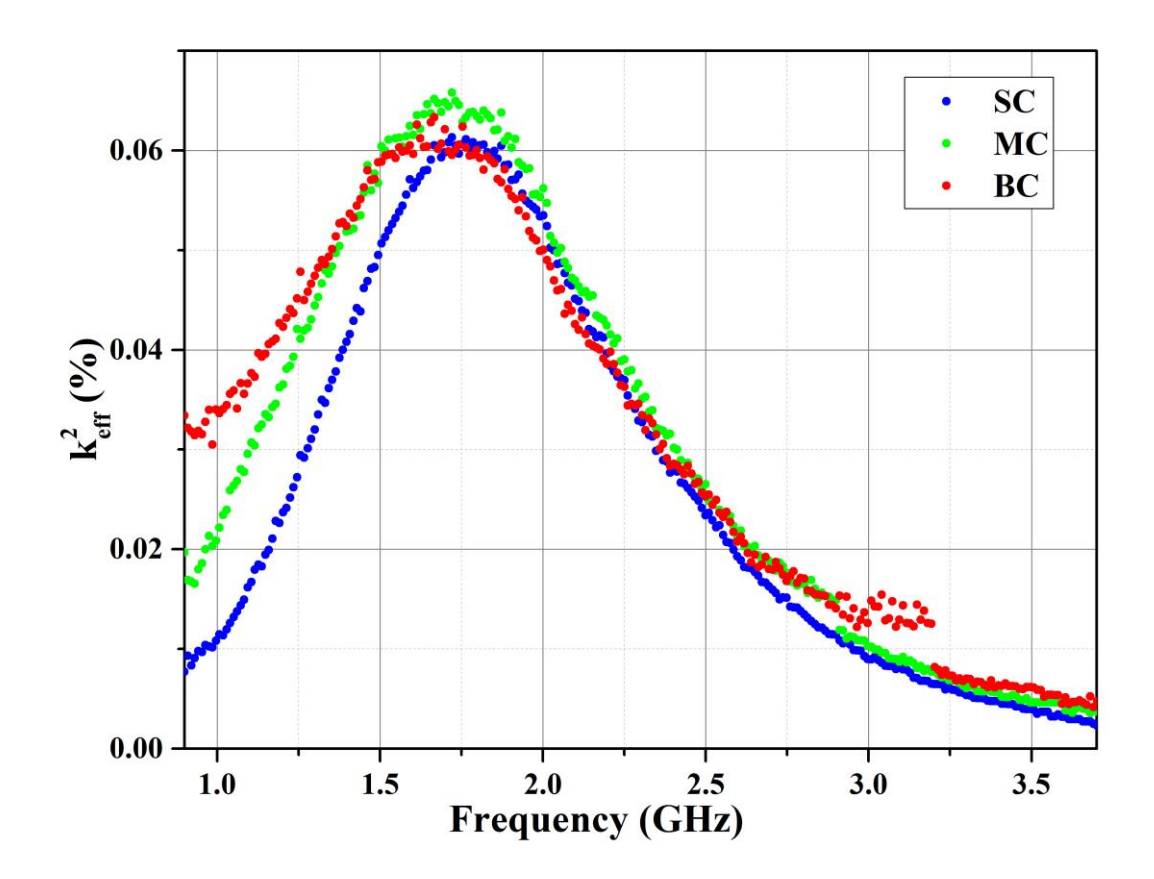


Figure 6.6.  $k_{eff}^2$  distributions for HBARs: - SC, MC and BC.

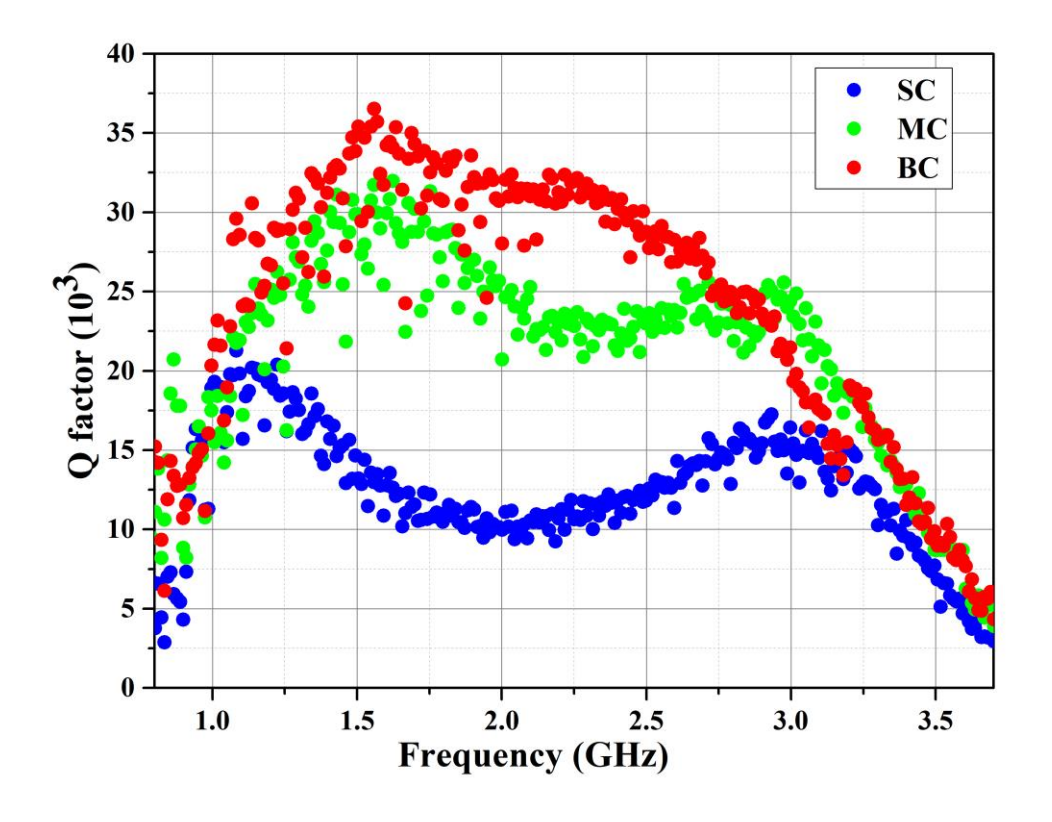


Figure 6.7. Q factor distributions for HBARs: - SC, MC and BC.

From Fig. 6.5, it is observed that the SPRF values for SC, MC and BC are almost the same. The transition region (or minima) is around 1.75 GHz and the value of the SPRF is around 1.80 MHz. The normal region is around 3.25 GHz and the value of the SPRF for all circular HBARs is around 10.84 MHz. Hence, the area of the top circular electrode does not affect the SPRF distribution of the HBAR. In Fig. 6.6, the resonant frequency or mode with the highest effective coupling coefficient  $(k_{eff}^2)$  occurs around 1.75 GHz (transition region) and the values of the  $k_{eff}^2$  is around 0.06 % for all the cases. Hence, the area of the top circular electrode seems to have little effect on the  $k_{eff}^2$  distribution of the HBAR. However, from Fig. 6.7, it is evident that the Q factor is affected by the change in area of top electrode i.e., BC which has the largest electrode area amongst the three different HBARs exhibits the highest Q factor. A Q factor of over 30,000 in the frequency range of 1.25 GHz to 2.5 GHz is exhibited by BC. Another observation made from the figure is that, the change in the Q factor from SC to MC is much more compared to the change from MC to BS. There may be a threshold value of area after which the Q does not increase even after increasing the area. A larger active area incorporates more crystal defects in the transducing thin film (BST) and the variation of the thickness of the thin film (BST) increases. These are some parameters which can affect the Q factor of the resonator. Another major factor is that when the active area is large, the capacitance increases and hence, for a supplied electrical energy, the transducer stores more energy and less acoustic energy to resonate in the low loss substrate (sapphire) [161]. Due to the limited pattern (different area) present in the mask, this could not be tested.

## 6.3.2 Apodized electrode

Apodized electrodes are the electrodes with non-parallel sides. These three apodized electrodes are categorized as three different HBARs, i.e., SA, MA and BA based on their area. The design of the patterns is similar to that of the CPC which is discussed in Chapter 4. Figs. 6.8, 6.9 and 6.10 show the SPRF, the  $k_{eff}^2$  and the Q factor distributions of SC, MC and BC. The values of the SPRF, the  $k_{eff}^2$  and the Q factor are derived using equations (3.54), (3.55) and (4.4) respectively.

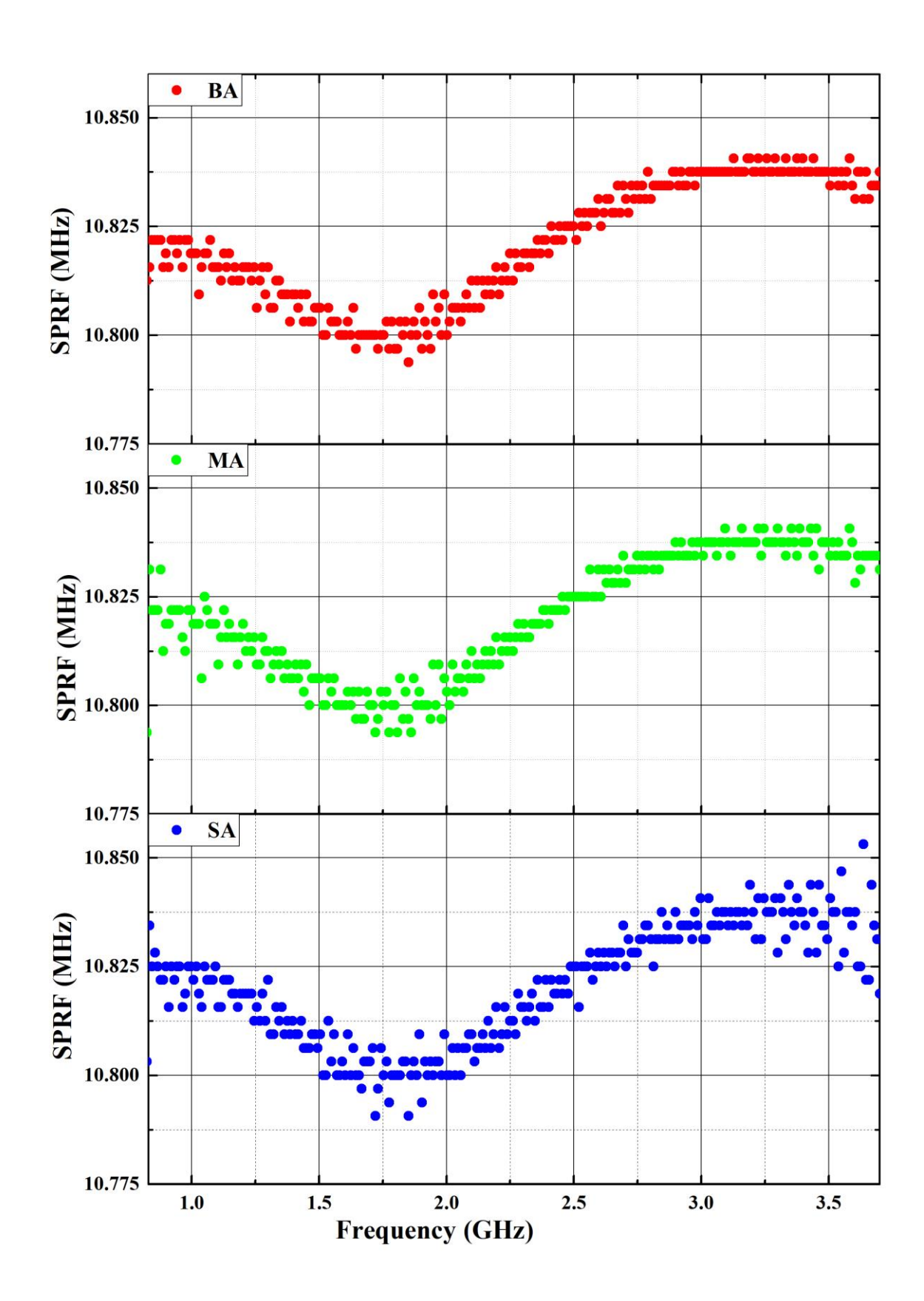


Figure 6.8. SPRF distributions for HBARs: - SA, MA and BA.

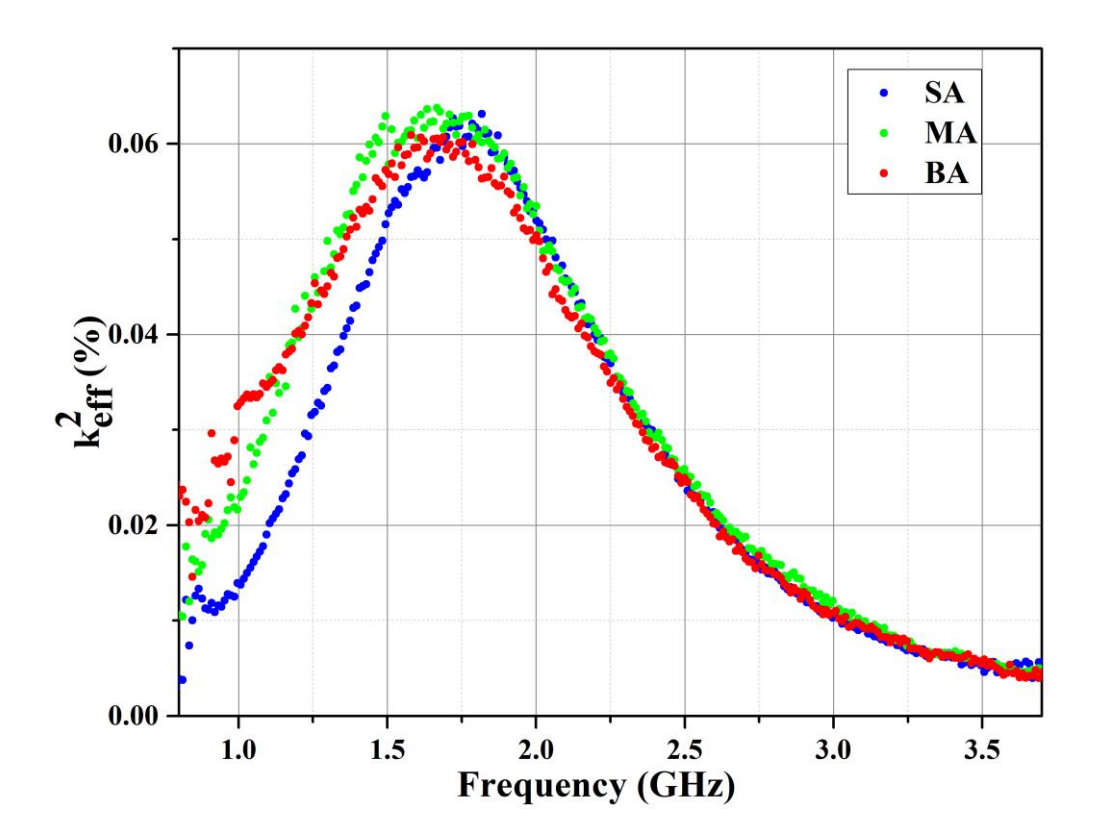


Figure 6.9.  $k_{eff}^2$  distributions for HBARs: - SA, MA and BA.

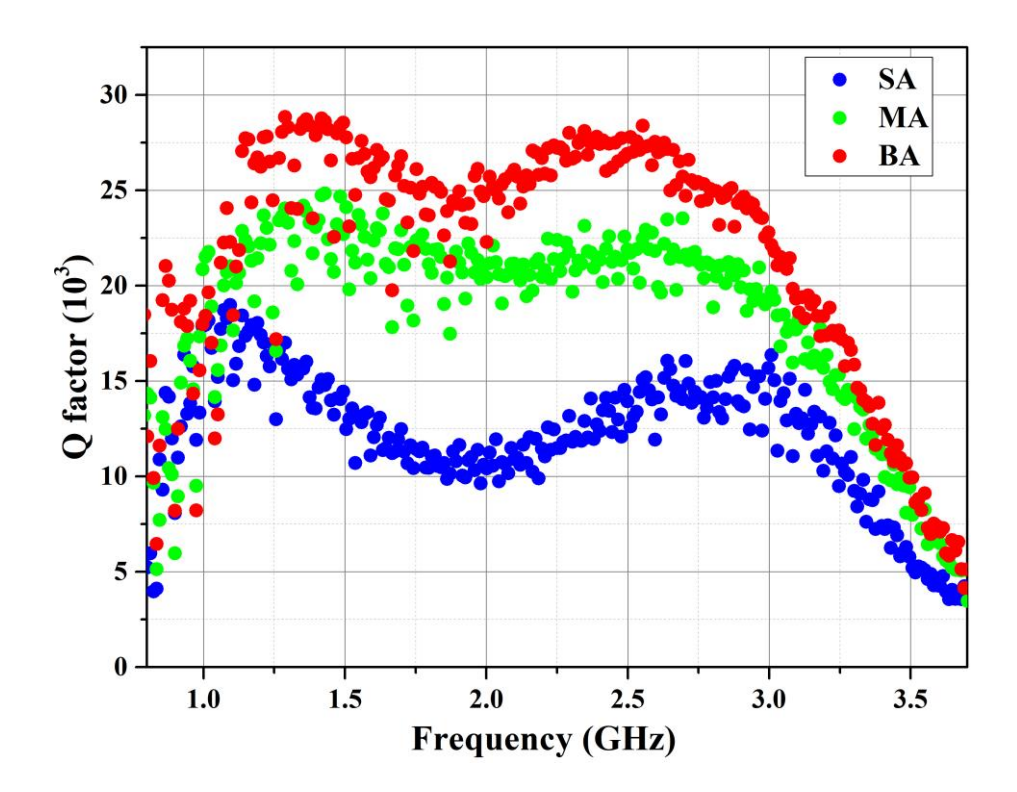


Figure 6.10. Q factor distributions for HBARs: - SA, MA and BA.

From Fig. 6.8, it is observed that the SPRF values for SA, MA and BA are almost the same. The transition region (or minima) is around 1.75 GHz and the value of the SPRF there is around 1.80 MHz. The normal region is around 3.25 GHz and the value of the SPRF there for all apodized HBARs are around 10.84 MHz. It can be noticed that, the area of the top apodized electrode does not affect the SPRF distribution of the HBAR similar to the observations made with the circular electrodes. In Fig. 6.9, the resonant frequency or mode with the highest effective coupling coefficient  $(k_{eff}^2)$  occur at around 1.75 GHz (transition region) and the values of the  $k_{eff}^2$  is around 0.06 % for all the cases of the apodized electrode areas. Hence, the area of the top apodized electrode seems to have little effect on the  $k_{eff}^2$  distribution of the HBAR. However, from Fig. 6.10, it is evident that the Q factor is affected by the change in area i.e., BA which has the largest area amongst the three different HBARs with the apodized electrodes exhibits the highest Q factor, as observed in the case of other electrode geometries. A Q factor of over 25,000 in the frequency range of 1.25 GHz to 2.5 GHz is exhibited by BA. Another observation made from the figure is that, the change in the Q factor from SA to MA is much more compared to the change from MA to BA. There may be a threshold value of area after which the Q does not increase even after increasing the area. Due to the limited patterns (of different area) present in the mask, this could not be tested.

#### 6.3.3 Square electrode

As shown in Fig. 6.4, there are three square patterns with three different sides i.e., 50  $\mu$ m, 100  $\mu$ m and 150  $\mu$ m. These three square electrodes are categorized as three different HBARs i.e., SS, MS and BS based on their area. The smallest square could not be studied as it got shorted. The design of the patterns is similar to that of the CPC which is discussed in Chapter 4. Fig. 6.11, 6.12 and 6.13 show the SPRF, the  $k_{eff}^2$  and the Q factor distributions

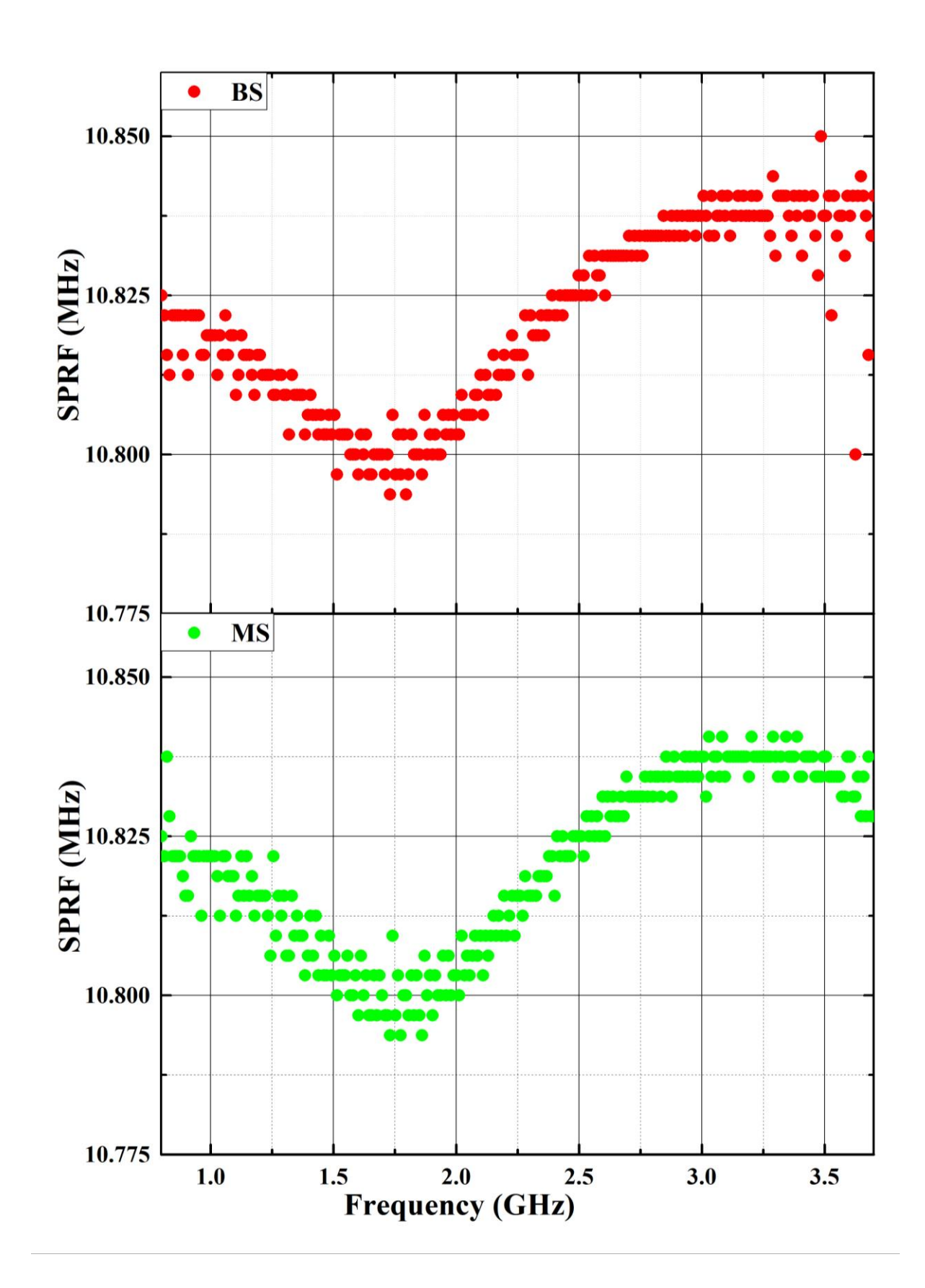


Figure 6.11. SPRF distributions for HBARs: - MS and BS.

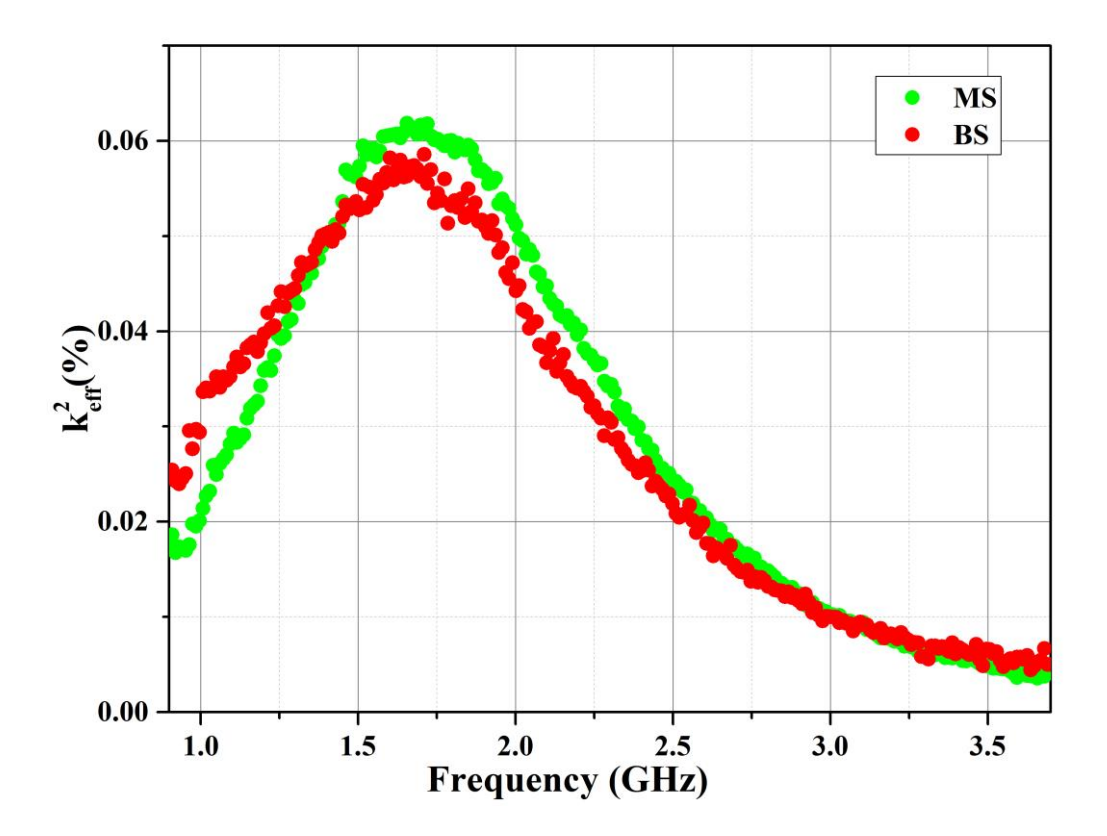


Figure 6.12.  $k_{eff}^2$  distributions for HBARs: - MS and BS.

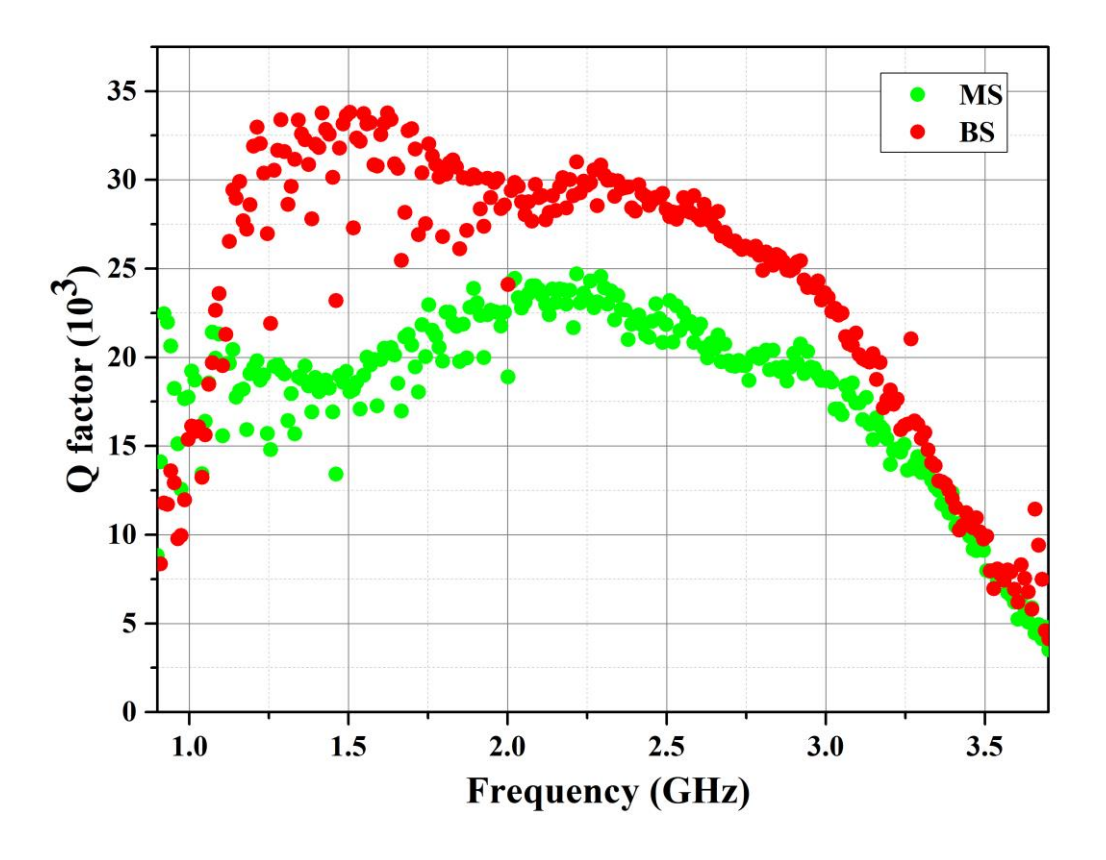


Figure 6.13. Q factor distributions for HBARs: - MS and BS.

of SC, MC and BC. The values of the SPRF, the  $k_{eff}^2$  and the Q factor are derived using equations (3.54), (3.55) and (4.4) respectively.

From Fig. 6.11, it is observed that the SPRF values for MS and BS are almost the same. The transition region (or minima) is around 1.75 GHz and the value of the SPRF there is around 1.80 MHz. The normal region is around 3.23 GHz and the value of the SPRF for both the square HBARs are around 10.84 MHz. Hence, the area of the top square electrode does not affect the SPRF distribution of the HBAR similar to the observations made with the circular electrodes and the apodized electrodes. In Fig. 6.12, the resonant frequency or mode with the highest effective coupling coefficient ( $k_{eff}^2$ ) occurs at around 1.75 GHz (transition region) and the values of the  $k_{eff}^2$  is around 0.06 % for both the cases. Hence, the area of the top square electrode seems to have little effect on the  $k_{eff}^2$  distribution of the HBAR. However, the Q factor of BS is higher than MS, a trend which is similar to the observation made in both circular and apodized electrode. A Q factor of over around 30,000 is exhibited by BS over a frequency range of 1.25 GHz to 2.5 GHz.

For all the eight HBARs discussed above, the SPRF and the  $k_{eff}^2$  distribution are not significantly affected by the area of the electrode. BC exhibits the highest Q factor compared to other HBARs. In order to better understand the increase of the Q factor with an increase of active area of the HBAR, the finite element method (FEM) is used to see how the acoustic waves in the resonator travels. A 2D FEM model of HBAR is created using COMSOL®. The model is not for the exact dimension as the practical HBARs fabricated so that the computing time and complexity of the model is reduced. Sapphire of thickness 10  $\mu$ m is considered instead of 450  $\mu$ m. The width of the model is 100  $\mu$ m and the top electrode's width is chosen in the range of 10  $\mu$ m to 35  $\mu$ m in steps of 5  $\mu$ m. Fig. 6.14 shows the displacement in the resonator in one of the resonant modes of this HBAR.

It can be seen from the figure that with an increase of the width of the top electrode, acoustic waves are mostly confined under the active area of the resonator. The total displacement of the resonator increases with an increase of the width of the top electrode. Loss of acoustic energy in the lateral direction (shear waves) seems to be the reason for the low Q in HBAR with lower top electrode area [9,10].

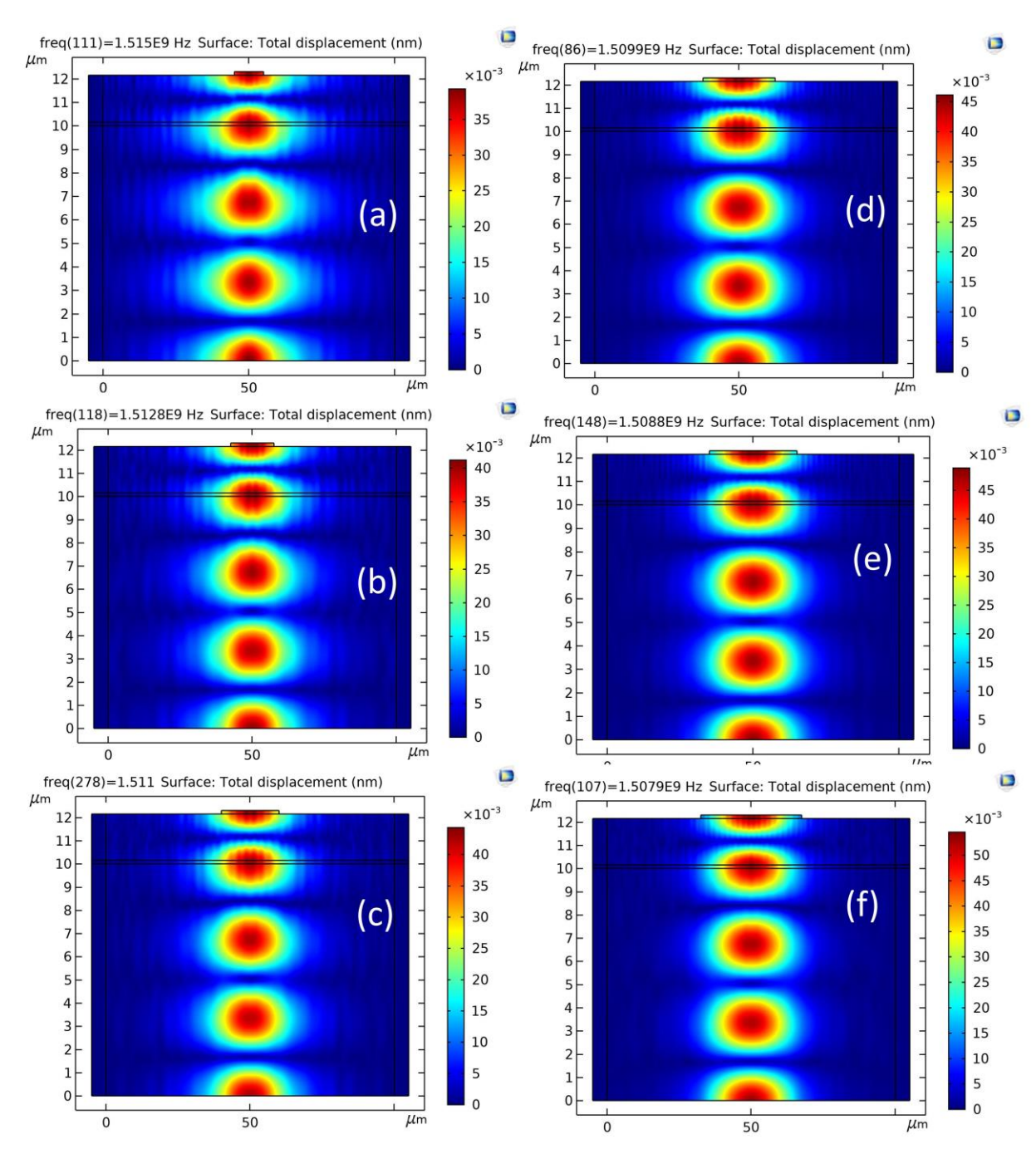


Figure 6.14. Displacement in the resonator with different top electrodes with widths of;(a) 10  $\mu$ m, (b)15  $\mu$ m, (c)20  $\mu$ m, (d)25  $\mu$ m, (e) 30  $\mu$ m and (f) 35  $\mu$ m.

#### **6.4 Summary and Conclusions**

In summary,

- Four HBARs with different combinations of the top and the bottom electrode materials
  are fabricated and studied.
- 2. Among the four HBARs, the combination of Pt as the bottom electrode and Au as the top electrode exhibited the highest effective coupling coefficient and Q factor.
- 3. Eight HBARs are fabricated on the same substrate (sapphire) with different electrode shapes and areas. Their characteristics are studied.
- 4. The SPRF and the  $k_{eff}^2$  distribution do not change significantly with the change in the electrode area but the Q factor of the HBAR increases with an increase in the active area of the resonator.
- 5. The geometry of the top electrode does not have significant effect on the SPRF and the  $k_{eff}^2$  distribution, but the HBAR with the top circular electrode with an area of  $20*10^{-3}$   $\mu$ m<sup>2</sup> exhibits the highest Q factor of over 35,000 around 1.5 GHz.
- 6. FEM is used to simulate 2D models of HBAR with varying width of the electrode. The results from simulation indicate that acoustic energy is more confined in the active area of the resonator when the electrode area is large.

In this chapter, the effect of the choice of the electrode materials on the parameters of an HBAR is studied and is concluded that the HBAR responses depend not only on the substrate and the BST thin films used but also on the electrode materials chosen. The effect of the electrode area is also studied and is found that HBAR with larger area of the top electrode exhibits a higher Q factor. The SPRF and the  $k_{eff}^2$  is not affected significantly by the change in the active area of the resonator. The 2D FEM gives a clearer picture as to

why the Q factor increases with electrode area. From the simulations, it is observed that the acoustic energy is confined in the active area of the resonator when the top electrode area is sufficiently large. To thoroughly understand the effects of the electrode materials, it's thicknesses and the geometry on the parameters of the resonators, an elaborate 3D FEM simulation is necessary. Due to the lack of computing resources and time, a full fledge broad spectrum simulation of HBAR has gone beyond the scope of this thesis. In order to design HBAR for oscillators or other applications like sensing, optimization of the resonator is required by using both simulation as well as experiments.

# CHAPTER 7: Conclusions and Future Work

#### 7.1 Conclusions

After an elaborate discussion in the introductory part of this thesis, it can be stated that the high overtone bulk acoustic resonator (HBAR) has promising prospects in high end applications such as microwave sources, acoustic spectroscopy, sensing and quantum acoustodynamics (QAD) systems. The high Q factor coupled with its capability to operate at very high frequency utilizing its overtone responses and its inherent quality of being compact in size for easy integrations due to the fact that it uses acoustic waves are some of the attributes that make HBAR and interesting area to study and develop new applications with it.

Much effort has been put forth in developing HBARs which utilize piezoelectric thin films. However, there are more features to be explored in HBARs which use electrostrictive transduction, for pushing forward the applications to achieve better performances. Another lesser explored area is the frequency domain analysis of HBARs coated with a material layer on HBARs. The thesis is, therefore, focused primarily on characterizing the high Q switchable HBAR based on BST thin film and HBAR as a means of acoustic spectroscopy. The various studies and analysis done in this thesis can be concluded as follows:

Chapter 1 provides the necessary discussions and literature review which shows the direction towards which the work of this thesis is to be focused on. It is identified that the application of HBAR is concentrated in microwave sources, quantum acoustics and acoustic spectroscopy. From the unique properties presented by ferroelectric thin film in the paraelectric phase, Ba<sub>0.5</sub>Sr<sub>0.5</sub>TiO<sub>3</sub> (BST) is the material of choice considered as the

transducing agent for all the HBARs fabricated for the purpose of the experiment presented in the thesis.

Chapter 2 brings forward the methodologies and techniques used for fabrication, characterization and analysis of the various aspects of HBAR such as thin film deposition, high frequency measurement, FEM simulations etc.

Chapter 3 serves as the theoretical foundation of the intricate working and mechanisms involved in the BST thin film which makes the HBAR DC bias dependent. The relationship between the coupling coefficient of the induced piezoelectric BST film under DC bias condition and the relative tunability of the thin film is discussed. The frequency spectra of both HBAR (i.e., without coated layer) and HBAR with coated layer are simulated and studied using the one-dimensional numerical models.

Chapter 4 reports the successful fabrication and characterization of various HBARs with different substrates with special focus on the low acoustic loss substrates, i.e., YAG and sapphire. The HBAR realized on YAG and sapphire substrates are capable of exhibiting multiple resonant modes which have high Q and are controllable by DC bias. Through acoustic spectroscopy, the material properties of the BST thin films are extracted. The Q factor and the electromechanical coupling coefficient are significantly influenced by the external DC bias applied. From the results presented in this chapter, it is clear that the tunable nature of both the coupling coefficient and the Q factor of the HBAR have huge potential in further developments of applications like microwave source, QAD, acoustic spectroscopy and sensors.

Chapter 5 investigates the effect of an additional layer coating on the backside of the substrate of the resonator. By using both the experimental results and the numerical simulation results (from model), the HBAR with and without coating is studied and the

effects in terms of the effective coupling coefficient, the SPRF and the Q factor are analyzed. From the analysis, the acoustic velocity of SU-8 is calculated. It is also found out that the mechanical loss or Q factor of the layer coated has significant effect on the parameters of the resonator. This technique is also found to be suited for extracting acoustic velocity and the mechanical Q of the additional layer which in this case is a polymer (SU-8). Possible applications of this technique are in characterization of polymer composites and in mass loading or gravimetric detection.

Chapter 6 studies the effect of the choice of the electrode materials on various parameters of the HBAR. The HBAR responses depend not only on the substrate and the BST thin films used but also on the electrode materials chosen. HBARs with larger area of the top electrode exhibits a higher Q factor. The SPRF and the  $k_{eff}^2$  is not affected significantly by the change in the active area of the resonator. From the FEM simulations, it is observed that the acoustic energy is confined in the active area of the resonator when the top electrode area is sufficiently large. Designing HBAR for oscillators or other applications like sensing requires optimization using both simulation and experiments.

#### 7.2 Potential for future work

The work presented in this thesis is an attempt to gather as much information on the newly developed BST thin film based high overtone bulk acoustic resonator (HBAR). The entirety of the work is focused on the inceptive idea that switchable and tunable HBARs have lots to offer for further developments in the field of microwave sources or QAD systems. The HBARs fabricated and characterized in this work do exhibit high Q factor and high coupling coefficients at higher frequencies, but certain areas need further probing in order to achieve better performances. The focus for future work is identified as below:

- Further optimization of thin films to get higher coupling coefficient at higher frequency
  range (lowering thickness) to get highly intense frequency response for achieving high
  Q coupling between the transducer and substrate material. Both the top and the bottom
  electrode design needs to be done further using 3D simulation tools to reduce the energy
  loss in lateral direction and supressing spurious modes in the HBAR.
- 2. For HBARs which are targeted for use in QAD systems, extremely high Q materials like diamond needs to be investigated and the amount of Q factor of the resonator achievable with DC biasing is worth analysing.
- 3. The integration of the switchable HBAR discussed for on-chip applications in oscillators, phonon generators in QAD systems, time standards or sensors is where the future scope of the study awaits.

## **REFERENCES**

- ANSI/ASA S1.1 & S3.20 Standard Acoustical & Bioacoustical Terminology Database, Acoustical Society of America (online site).
- 2. R. B.Lindsay, J. Acoust. Soc. Am. 36:2242 (1964)
- 3. Pierce, Allan D. *Acoustics: an introduction to its physical principles and applications*. New York McGraw-Hill Book Co, 1981.
- 4. Ensminger D, Bond LJ. *Ultrasonics: fundamentals, technologies, and applications*. CRC press; 2011 Sep 19.
- 5. Graff, Karl. "Historical highlights in ultrasonics-2." In *Proceedings of the 2004 IEEE International Frequency Control Symposium and Exposition*, 2004., pp. 5-10. IEEE, 2004.
- 6. Naor, Omer, Steve Krupa, and Shy Shoham. "Ultrasonic neuromodulation." *Journal of neural engineering* 13, no. 3 (2016): 031003.
- 7. Planès, Thomas, and Eric Larose. "A review of ultrasonic Coda Wave Interferometry in concrete." *Cement and Concrete Research* 53 (2013): 248-255.
- 8. Newman, Paul G., and Grace S. Rozycki. "The history of ultrasound." *Surgical clinics of north America* 78, no. 2 (1998): 179-195.
- 9. Harput, Sevan, and Ayhan Bozkurt. "Ultrasonic phased array device for acoustic imaging in air." *IEEE sensors journal* 8, no. 11 (2008): 1755-1762.
- E. A. Kraut, "Applications of Elastic Waves to Electronic Devices, Nondestructive Evaluation, and Seismology," 1976 Ultrasonics Symposium, Annapolis, MD, USA, 1976, pp. 1-7, doi: 10.1109/ULTSYM.1976.196618.
- 11. Graff, Karl F. "Ultrasonics: historical aspects." In 1977 Ultrasonics Symposium, pp. 1-10. IEEE, 1977.
- 12. Graff, Karl F. "A history of ultrasonics." In Physical acoustics, vol. 15, pp. 1-97. Academic Press, 1981.
- 13. Lindsay, R. Bruce. "The story of acoustics." *The Journal of the Acoustical Society of America* 39, no. 4 (1966): 629-644.
- 14. Rayleigh, John William Strutt Baron. The theory of sound. Vol. 2. Macmillan, 1896.
- 15. Mason, Warren P. "Applications of acoustical phenomena." *The Journal of the Acoustical Society of America* 68, no. 1 (1980): 53-63.
- 16. Campanella, Humberto. Acoustic wave and electromechanical resonators: concept to key applications. Artech House, 2010.
- 17. Weigel, Robert, David P. Morgan, John M. Owens, Arthur Ballato, Kenneth M. Lakin, Ken-Ya Hashimoto, and Clemens CW Ruppel. "Microwave acoustic materials, devices, and applications." *IEEE Transactions on microwave theory and techniques* 50, no. 3 (2002): 738-749.
- 18. Feynman, Richard P., Robert B. Leighton, and Matthew Sands. *The Feynman lectures on physics, Vol. I: The new millennium edition: mainly mechanics, radiation, and heat.* Vol. 1. Basic books, 2011.
- 19. Cheeke, J. David N. Fundamentals and applications of ultrasonic waves. CRC press, 2017.
- 20. Gevorgian, Spartak, Alexander Tagantsev, and Andrei K. Vorobiev. *Tuneable film bulk acoustic wave resonators*. Springer Science & Business Media, 2013.

- 21. Tirado, Jordi Verdú. "Bulk acoustic wave resonators and their application to microwave devices." *PhD*, *Universitat Antonoma de Barcelona* (2010).
- 22. Newell, W. E. "Face-mounted piezoelectric resonators." *Proceedings of the IEEE* 53, no. 6 (1965): 575-581.
- Grudkowski, T. W., J. F. Black, T. M. Reeder, D. E. Cullen, and R. A. Wagner. "Fundamental-mode VHF/UHF minature acoustic resonators and filters on silicon." *Applied Physics Letters* 37, no. 11 (1980): 993-995.
- 24. Lakin, K. M., and J. S. Wang. "Acoustic bulk wave composite resonators." *Applied Physics Letters* 38, no. 3 (1981): 125-127.
- 25. Nakamura, K., H. Sasaki, and H. Shimizu. "ZnO/SiO2-diaphragm composite resonator on a silicon wafer." *Electronics Letters* 17, no. 14 (1981): 507-509.
- 26. K.M. Lakin, J. Wang, G. Kline, A. Landin, Y. Chen, J. Hunt, "Thin Film Resonators and Filters", *Ultrasonics Symp.*, 1982, pp. 466-475.
- 27. Ruby, Rich. "11E-2 review and comparison of bulk acoustic wave FBAR, SMR technology." In 2007 *IEEE Ultrasonics Symposium Proceedings*, pp. 1029-1040. IEEE, 2007.
- 28. Ruby, R. et al. "Acoustic FBAR for filters, duplexers and front-end modules". *IEEE MTT-S Int. Microwave Symp.* Dig. 2, 931–934 (2004).
- 29. Kumar, P. & Tripathi, C. C. "Design of a New Step-like Frame FBAR for Suppression of Spurious Resonances". *Radioeng*. 22, 687–693 (2013).
- 30. He, X. L., L. Garcia-Gancedo, P. C. Jin, J. Zhou, W. B. Wang, S. R. Dong, J. K. Luo, A. J. Flewitt, and W. I. Milne. "Film bulk acoustic resonator pressure sensor with self temperature reference." *Journal of Micromechanics and Microengineering* 22, no. 12 (2012): 125005.
- 31. Qiu, Xiaotun, Jon Oiler, Jie Zhu, Ziyu Wang, Rui Tang, Cunjiang Yu, and Hongyu Yu. "Film bulk acoustic-wave resonator based relative humidity sensor using ZnO films." *Electrochemical and Solid State Letters* 13, no. 5 (2010): J65.
- 32. Qiu, Xiaotun, Rui Tang, Jie Zhu, Jon Oiler, Cunjiang Yu, Ziyu Wang, and Hongyu Yu. "The effects of temperature, relative humidity and reducing gases on the ultraviolet response of ZnO based film bulk acoustic-wave resonator." *Sensors and Actuators B: Chemical* 151, no. 2 (2011): 360-364.
- 33. Chiu, Kuan-Hsun, Hong-Ren Chen, and Star Ruey-Shing Huang. "High-performance film bulk acoustic wave pressure and temperature sensors." *Japanese journal of applied physics* 46, no. 4R (2007): 1392.
- 34. Xuan, Weipeng, Jin Chen, Ting Wu, Jinkai Chen, Xiwei Huang, Shurong Dong, Xiaozhi Wang, Hao Jin, and Jikui Luo. "Bulk acoustic wave resonator based wireless and passive pressure sensor." *Vacuum* (2020): 109433.
- 35. Lin, Anderson, Hongyu Yu, Michael S. Waters, Eun Sok Kim, and Steven D. Goodman. "Explosive trace detection with FBAR-based sensor." In 2008 IEEE 21st International Conference on Micro Electro Mechanical Systems, pp. 208-211. IEEE, 2008.
- 36. Pang, Wei, Hongyuan Zhao, Eun Sok Kim, Hao Zhang, Hongyu Yu, and Xiaotang Hu. "Piezoelectric microelectromechanical resonant sensors for chemical and biological detection." *Lab on a Chip* 12, no. 1 (2012): 29-44.

- Johnston, Matthew L., Hassan Edrees, Ioannis Kymissis, and Kenneth L. Shepard. "Integrated VOC vapor sensing on FBAR-CMOS array." In 2012 IEEE 25th International Conference on Micro Electro Mechanical Systems (MEMS), pp. 846-849. IEEE, 2012.
- 38. Zhao, Xiubo, Fang Pan, Gregory M. Ashley, Luis Garcia-Gancedo, Jikui Luo, Andrew J. Flewitt, William I. Milne, and Jian R. Lu. "Label-free detection of human prostate-specific antigen (hPSA) using film bulk acoustic resonators (FBARs)." *Sensors and Actuators B: Chemical* 190 (2014): 946-953.
- 39. García-Gancedo, Luis, Z. Zhu, Enrique Iborra, M. Clement, J. Olivares, A. J. Flewitt, W. I. Milne et al. "AlN-based BAW resonators with CNT electrodes for gravimetric biosensing." *Sensors and Actuators B: Chemical* 160, no. 1 (2011): 1386-1393.
- 40. Zhao, Xiubo, Gregory M. Ashley, Luis Garcia-Gancedo, Hao Jin, Jikui Luo, Andrew J. Flewitt, and Jian R. Lu. "Protein functionalized ZnO thin film bulk acoustic resonator as an odorant biosensor." *Sensors and Actuators B: Chemical* 163, no. 1 (2012): 242-246.
- 41. Fu, Yong Qing, J. K. Luo, Nam-Trung Nguyen, A. J. Walton, Andrew John Flewitt, Xiao-Tao Zu, Yifan Li et al. "Advances in piezoelectric thin films for acoustic biosensors, acoustofluidics and lab-on-chip applications." *Progress in Materials Science* 89 (2017): 31-91.
- 42. Zhang, Yi, Jikui Luo, Andrew J. Flewitt, Zhiqiang Cai, and Xiubo Zhao. "Film bulk acoustic resonators (FBARs) as biosensors: A review." *Biosensors and Bioelectronics* 116 (2018): 1-15.
- 43. Mujahid, Adnan, Adeel Afzal, and Franz L. Dickert. "An overview of high frequency acoustic sensors—QCMs, SAWs and FBARs—chemical and biochemical applications." *Sensors* 19, no. 20 (2019): 4395.
- 44. García-Gancedo, L., J. Pedrós, E. Iborra, M. Clement, X. B. Zhao, J. Olivares, J. Capilla et al. "Direct comparison of the gravimetric responsivities of ZnO-based FBARs and SMRs." *Sensors and Actuators B: Chemical* 183 (2013): 136-143.
- 45. Chen, Guohao, Xinru Zhao, Xiaozhi Wang, Hao Jin, Shijian Li, Shurong Dong, A. J. Flewitt, W. I. Milne, and J. K. Luo. "Film bulk acoustic resonators integrated on arbitrary substrates using a polymer support layer." *Scientific reports* 5 (2015): 9510.
- 46. Cornez, D., S. Lapp, S. Cochran, and K. J. Kirk. "P1I-1 Acoustical Parameters Characterisation of Aluminium Nitride Thin Film BAW Resonators Using Resonant Spectrum Approach." In 2007 IEEE Ultrasonics Symposium Proceedings, pp. 1437-1440. IEEE, 2007.
- 47. Lee, Tae Yong, and Joon Tae Song. "Detection of carcinoembryonic antigen using AlN FBAR." *Thin Solid Films* 518, no. 22 (2010): 6630-6633.
- 48. Kim, Eungkwon, Young-Kwan Choi, Juntae Song, and Jaehyoeng Lee. "Detection of various self-assembled monolayers by AlN-based film bulk acoustic resonator." *Materials Research Bulletin* 48, no. 12 (2013): 5076-5079.
- 49. Quimby, Shirley Leon. "On the experimental determination of the viscosity of vibrating solids." *Physical Review* 25, no. 4 (1925): 558.
- 50. Sliker, T. R., and D. A. Roberts. "A thin-film CdS-quartz composite resonator." *Journal of Applied Physics* 38, no. 5 (1967): 2350-2358.
- 51. Page, D. J. "A cadmium sulfide-silicon composite resonator." *Proceedings of the IEEE* 56, no. 10 (1968): 1748-1749.

- 52. Gerber, E. A., T. Lukaszek, and A. Ballato. "Advances in microwave acoustic frequency sources." *IEEE transactions on microwave theory and techniques* 34, no. 10 (1986): 1002-1016.
- 53. Moore, R. A., F. W. Hopwood, T. Haynes, and B. R. McAvoy. "Bulk acoustic resonators for microwave frequencies." In *33rd Annual Symposium on Frequency Control*, pp. 444-448. IEEE, 1979.
- 54. Moore, R. A., J. Goodell, A. Zahorchak, R. A. Sundelin, W. Hopwood, T. Haynes, B. R. McAvoy, and J. Murphy. "High Q bulk acoustic resonators for direct microwave oscillator stabilization." *afc* (1980): 243-251.
- 55. Haynes, J. T., H. Salvo, R. A. Moore, and B. R. McAvoy. *Low phase noise multiple frequency microwave source*. Westinghouse Defence and Electronic Systems Centre Baltimore Md Systems Development Div., 1983.
- 56. Haynes, J. T., M. S. Buchalter, R. A. Moore, H. L. Salvo, S. G. Shepherd, and B. R. McAvoy. "Stable microwave source using high overtone bulk resonators." In *1985 IEEE MTT-S International Microwave Symposium Digest*, pp. 243-246. IEEE, 1985.
- 57. Moore, R. A., J. T. Haynes, and B. R. McAvoy. "High overtone bulk resonator stabilized microwave sources." In *1981 Ultrasonics Symposium*, pp. 414-424. IEEE, 1981.
- 58. Lakin, Kenneth M., Gerald R. Kline, and Kevin T. McCarron. "High-Q microwave acoustic resonators and filters." *IEEE transactions on microwave theory and techniques* 41, no. 12 (1993): 2139-2146.
- 59. Kervinen, Mikael, Ilkka Rissanen, and Mika Sillanpää. "Interfacing planar superconducting qubits with high overtone bulk acoustic phonons." *Physical Review B* 97, no. 20 (2018): 205443.
- 60. Baumgartel, Lukas, and Eun Sok Kim. "Experimental optimization of electrodes for high Q, high frequency HBAR." In 2009 IEEE International Ultrasonics Symposium, pp. 2107-2110. IEEE, 2009.
- 61. Rosenbaum, Joel Frederick. *Bulk acoustic wave theory and devices*. Artech House Acoustics Library, 1988.
- 62. Driscoll, M. M., Robert A. Jelen, and N. Matthews. "Extremely low phase noise UHF oscillators utilizing high-overtone, bulk-acoustic resonators." *IEEE transactions on ultrasonics, ferroelectrics, and frequency control* 39, no. 6 (1992): 774-779.
- 63. Ferre-Pikal, Eva S., MC Delgado Aramburo, Fred L. Walls, and Kenneth M. Lakin. "1/f frequency noise of 2-GHz high-Q thin-film sapphire resonators." *IEEE transactions on ultrasonics, ferroelectrics, and frequency control* 48, no. 2 (2001): 506-510.
- 64. Yu, Hongyu, C-Y. Lee, Wei Pang, Hao Zhang, Alan Brannon, John Kitching, and ES Sok Kim. "HBAR-Based 3.6 GHz oscillator with low power consumption and low phase noise." *IEEE transactions on ultrasonics, ferroelectrics, and frequency control* 56, no. 2 (2009): 400-403.
- 65. Daugey, Thomas, Jean-Michel Friedt, Gilles Martin, and Rodolphe Boudot. "A high-overtone bulk acoustic wave resonator-oscillator-based 4.596 GHz frequency source: Application to a coherent population trapping Cs vapor cell atomic clock." *Review of Scientific Instruments* 86, no. 11 (2015): 114703.
- 66. Torunbalci, Mustafa Mert, Tanay Arun Gosavi, Kerem Yunus Camsari, and Sunil Ashok Bhave. "Magneto acoustic spin hall oscillators." *Scientific reports* 8, no. 1 (2018): 1-10.
- 67. Schoelkopf, R. J., and S. M. Girvin. "Wiring up quantum systems." *Nature* 451, no. 7179 (2008): 664-669.

- 68. Kharel, Prashanta, Yiwen Chu, Michael Power, William H. Renninger, Robert J. Schoelkopf, and Peter T. Rakich. "Ultra-high-Q phononic resonators on-chip at cryogenic temperatures." *APL Photonics* 3, no. 6 (2018): 066101.
- 69. Manenti, Riccardo, Anton F. Kockum, Andrew Patterson, Tanja Behrle, Joseph Rahamim, Giovanna Tancredi, Franco Nori, and Peter J. Leek. "Circuit quantum acoustodynamics with surface acoustic waves." *Nature communications* 8, no. 1 (2017): 1-6.
- 70. Bienfait, Audrey, Kevin J. Satzinger, Y. P. Zhong, H-S. Chang, M-H. Chou, Chris R. Conner, É. Dumur et al. "Phonon-mediated quantum state transfer and remote qubit entanglement." *Science* 364, no. 6438 (2019): 368-371.
- 71. Chu, Yiwen, Prashanta Kharel, William H. Renninger, Luke D. Burkhart, Luigi Frunzio, Peter T. Rakich, and Robert J. Schoelkopf. "Quantum acoustics with superconducting qubits." *Science* 358, no. 6360 (2017): 199-202.
- 72. Arrangoiz-Arriola, Patricio, E. Alex Wollack, Marek Pechal, Wentao Jiang, Zhaoyou Wang, Timothy P. McKenna, Jeremy Witmer et al. "Microwave Quantum Acoustic Processor." In 2019 IEEE MTT-S International Microwave Symposium (IMS), pp. 255-258. IEEE, 2019.
- 73. MacQuarrie, E. R., T. A. Gosavi, N. R. Jungwirth, S. A. Bhave, and G. D. Fuchs. "Mechanical spin control of nitrogen-vacancy centers in diamond." *Physical review letters* 111, no. 22 (2013): 227602.
- 74. MacQuarrie, E. R., T. A. Gosavi, A. M. Moehle, N. R. Jungwirth, S. A. Bhave, and G. D. Fuchs. "Coherent control of a nitrogen-vacancy center spin ensemble with a diamond mechanical resonator." *Optica* 2, no. 3 (2015): 233-238.
- 75. Chen, Huiyao Y., E. R. MacQuarrie, and Gregory David Fuchs. "Orbital state manipulation of a diamond nitrogen-vacancy center using a mechanical resonator." *Physical review letters* 120, no. 16 (2018): 167401.
- 76. Gokhale, Vikrant J., Brian P. Downey, D. Scott Katzer, Neeraj Nepal, Andrew C. Lang, Rhonda M. Stroud, and David J. Meyer. "Epitaxial bulk acoustic wave resonators as highly coherent multi-phonon sources for quantum acoustodynamics." Nature communications 11, no. 1 (2020): 1-9.
- 77. Zhang, Hao, Wei Pang, and Eun Sok Kim. "Miniature high-frequency longitudinal wave mass sensors in liquid." *IEEE transactions on ultrasonics, ferroelectrics, and frequency control* 58, no. 1 (2011): 255-258.
- 78. He, Yanbo, Bichoy Bahr, Mengwei Si, Peide Ye, and Dana Weinstein. "A tunable ferroelectric based unreleased RF resonator." *Microsystems & Nanoengineering* 6, no. 1 (2020): 1-7.
- 79. Khudiyev, Tural, Jefferson Clayton, Etgar Levy, Noémie Chocat, Alexander Gumennik, Alexander M. Stolyarov, John Joannopoulos, and Yoel Fink. "Electrostrictive microelectromechanical fibres and textiles." *Nature communications* 8, no. 1 (2017): 1-7.
- 80. Martin, Lane W., and Andrew M. Rappe. "Thin-film ferroelectric materials and their applications." *Nature Reviews Materials* 2, no. 2 (2016): 1-14.
- 81. A. Noeth, T. Yamada, P. Muralt, A. K. Tagantsev and N. Setter, "Tunable thin film bulk acoustic wave resonator based on BaxSr1-xTiO3 thin film," in *IEEE Transactions on Ultrasonics, Ferroelectrics, and Frequency Control*, vol. 57, no. 2, pp. 379-385, February 2010, doi: 10.1109/TUFFC.2010.1417.

- 82. Liu, J-M., B. Pan, H. L. W. Chan, S. N. Zhu, Y. Y. Zhu, and Z. G. Liu. "Piezoelectric coefficient measurement of piezoelectric thin films: an overview." *Materials Chemistry and Physics* 75, no. 1-3 (2002): 12-18.
- 83. Zhang, Yuxing, Zuoqing Wang, and J. David N. Cheeke. "Resonant spectrum method to characterize piezoelectric films in composite resonators." *IEEE Transactions on Ultrasonics, Ferroelectrics, and Frequency Control* 50, no. 3 (2003): 321-333.
- 84. Sandeep, Kongbrailatpam, J. Pundareekam Goud, and K. C. James Raju. "Resonant spectrum method for characterizing Ba0. 5Sr0. 5TiO3 based high overtone bulk acoustic wave resonators." *Applied Physics Letters* 111, no. 1 (2017): 012901.
- 85. Kushibiki, J., T. Sannomiya, and N. Chubachi. "Performance of sputtered SiO2 film as acoustic antireflection coating at sapphire/water interface." *Electronics Letters* 16, no. 19 (1980): 737-738.
- 86. Kushibiki, Jun-ichi, Hiroyuki Maehara, and Noriyoshi Chubachi. "Measurements of acoustic properties for thin films." *Journal of Applied Physics* 53, no. 8 (1982): 5509-5513.
- 87. Mansfeld, G. D. "BAW composite resonator spectroscopy." In 1994 Proceedings of IEEE Ultrasonics Symposium, vol. 2, pp. 655-658. IEEE, 1994.
- 88. Naik, Rajan S., Joseph J. Lutsky, Rafael Reif, and Charles G. Sodini. "Electromechanical coupling constant extraction of thin-film piezoelectric materials using a bulk acoustic wave resonator." *IEEE transactions on ultrasonics, ferroelectrics, and frequency control* 45, no. 1 (1998): 257.
- 89. Wang, Z., X. Li, and J. David N. Cheeke. "A modified modal frequency spacing method for coating characterization." *The Journal of the Acoustical Society of America* 104, no. 5 (1998): 3119-3122.
- 90. Cheeke, J. D. N., Y. Zhang, Z. Wang, M. Lukacs, and M. Sayer. "Characterization for piezoelectric films using composite resonators." In 1998 IEEE Ultrasonics Symposium. Proceedings (Cat. No. 98CH36102), vol. 2, pp. 1125-1128. IEEE, 1998.
- 91. Zhang, Y., Z. Wang, J. D. N. Cheeke, and F. S. Hickernell. "Direct characterization of ZnO films in composite resonators by the resonance spectrum method." In 1999 IEEE Ultrasonics Symposium. Proceedings. International Symposium (Cat. No. 99CH37027), vol. 2, pp. 991-994. IEEE, 1999.
- 92. Wang, Zuoging, Yuxing Zhang, and J. David N. Cheeke. "Characterization of electromechanical coupling coefficients of piezoelectric films using composite resonators." *IEEE transactions on ultrasonics, ferroelectrics, and frequency control* 46, no. 5 (1999): 1327-1330.
- 93. Nakamura, Kiyoshi, Hideaki Kobayashi, and Hirofumi Kanbara. "Evaluation of acoustic properties of thin films using piezoelectric overtone thickness-mode resonators." In 2000 IEEE Ultrasonics Symposium. Proceedings. An International Symposium (Cat. No. 00CH37121), vol. 1, pp. 593-597. IEEE, 2000.
- 94. Zhang, Y., Z. Wang, and J. D. N. Cheeke. "Simulation of electromechanical coupling coefficient by modified modal frequency spectrum method including the electrode effect." *Ultrasonics* 38, no. 1-8 (2000): 114-117.
- 95. Zhou, Qing-Biao, Yue-kai Lu, and Shu-Yi Zhang. "Extraction of electromechanical coupling coefficient of piezoelectric thin films deposited on substrates." *Ultrasonics* 39, no. 5 (2001): 377-382.

- 96. Zhang, Hui, Zuoqing Wang, and Shu-Yi Zhang. "Electrode effects on frequency spectra and electromechanical coupling factors of HBAR." *IEEE transactions on ultrasonics, ferroelectrics, and frequency control* 52, no. 6 (2005): 1020-1025.
- 97. Zhang, Hao, Wei Pang, Hongyu Yu, and Eun Sok Kim. "High-tone bulk acoustic resonators on sapphire, crystal quartz, fused silica, and silicon substrates." *Journal of applied physics* 99, no. 12 (2006): 124911.
- 98. Wang, Shengxiang, Pierre Campistron, Julien Carlier, Dorothée Callens-Debavelaere, Bertrand Nongaillard, Assane NDieguene, Georges Nassar, Caroline Soyer, and Xingzhong Zhao. "SU-8-based nanocomposites for acoustical matching layer." *IEEE transactions on ultrasonics, ferroelectrics, and frequency control* 56, no. 7 (2009): 1483-1489.
- 99. Zhou, Chong, Wei Pang, Qiang Li, Hongyu Yu, Xiaotang Hu, and Hao Zhang. "Extracting the electromechanical coupling constant of piezoelectric thin film by the high-tone bulk acoustic resonator technique." *IEEE transactions on ultrasonics, ferroelectrics, and frequency control* 59, no. 5 (2012): 958-962.
- 100.Zhang, Hui, Yu-ran Wang, Shu-yi Zhang, and Li Fan. "Nondestructive evaluation of thickness variations for elastic plates by high-overtone bulk acoustic resonance." *IEEE transactions on ultrasonics, ferroelectrics, and frequency control* 59, no. 12 (2012): 2709-2715.
- 101.Liu, Mengwei, Jian Li, Chenghao Wang, Junhong Li, and Jun Ma. "Influence of electrodes on the effective electromechanical coupling coefficient distributions of high-overtone bulk acoustic resonator." *Ultrasonics* 56 (2015): 566-574.
- 102. Soutome, Takumi, and Takahiko Yanagitani. "A method to estimate k t 2 of piezoelectric films from the change of lattice strain by XRD without removing substrate." In 2019 IEEE International Ultrasonics Symposium (IUS), pp. 301-304. IEEE, 2019.
- 103. Kinoshita, Sarina, and Takahiko Yanagitani. "A Method for Extracting Mechanical Q Factor of the Piezoelectric Film without Etching Substrate." In 2019 IEEE International Ultrasonics Symposium (IUS), pp. 299-300. IEEE, 2019.
- 104. Kongbrailatpam, Sandeep, J. Pundareekam Goud, and KC James Raju. "Effects of a Coated Material Layer on High Overtone Bulk Acoustic Resonator and its Possible Applications." *IEEE Transactions on Ultrasonics, Ferroelectrics, and Frequency Control* (2020).
- 105. Uchino, Kenji. Ferroelectric devices. CRC press, 2018.
- 106. Gevorgian, Spartak. Ferroelectrics in microwave devices, circuits and systems: physics, modeling, fabrication and measurements. Springer Science & Business Media, 2009.
- 107. Koohi, Milad Zolfagharloo, and Amir Mortazawi. "Reconfigurable Radios Employing Ferroelectrics: Recent Progress on Reconfigurable RF Acoustic Devices Based on Thin-Film Ferroelectric Barium Strontium Titanate." *IEEE Microwave Magazine* 21, no. 5 (2020): 120-135.
- 108. Fardin, E. "Barium strontium titanate thin films for tunable microwave applications." (2007).
- 109. Shaw, T. M., Z. Suo, M. Huang, E. Liniger, R. B. Laibowitz, and J. D. Baniecki. "The effect of stress on the dielectric properties of barium strontium titanate thin films." *Applied physics letters* 75, no. 14 (1999): 2129-2131.
- 110. Vorobiev, Andrei, Pär Rundqvist, K. Khamchane, and S. Gevorgian. "Microwave loss mechanisms in Ba 0.25 Sr 0.75 TiO 3 thin film varactors." *Journal of Applied Physics* 96, no. 8 (2004): 4642-4649.

- 111. Suryanarayana, Cury. "Mechanical alloying and milling." *Progress in materials science* 46, no. 1-2 (2001): 1-184.
- 112. Kang, Suk-Joong L. Sintering: densification, grain growth and microstructure. Elsevier, 2004.
- 113.Agrawal, Dinesh. "Microwave sintering of ceramics, composites, metals, and transparent materials." *Journal of Materials Education* 19 (1997): 49-58.
- 114. Ohring, Milton. Materials science of thin films. Elsevier, 2001.
- 115. Chopra, Kasturi L. "Thin film phenomena." Mcgraw-Hill Book Company, USA, 1969.
- 116. Eason, Robert, ed. *Pulsed laser deposition of thin films: applications-led growth of functional materials.*John Wiley & Sons, 2007.
- 117. Geohegan, D. B., D. B. Chrisey, and G. K. Hubler. "Pulsed laser deposition of thin films." *Chrisey and GK Hubler (eds), Wiely, New York* (1994): 59-69.
- 118.Nöth, Andreas. *Micromachined tunable devices based on silicon integrated BaxSr1-xTiO3 thin films*. THESIS. EPFL, 2009.
- 119.Lee, Victor Chia. "Switchable and Tunable Ferroelectric Devices for Adaptive and Reconfigurable RF Circuits." PhD diss., 2014.
- 120. Campbell, Stephen A. *The science and engineering of microelectronic fabrication*. Oxford university press, 2001.
- 121.Flewitt, Peter EJ, and Robert K. Wild. *Physical methods for materials characterisation*. CRC Press, 2017.
- 122.Leng, Yang. *Materials characterization: introduction to microscopic and spectroscopic methods*. John Wiley & Sons, 2009.
- 123.https://www.keysight.com/upload/cmc\_upload/All/NetworkAnalysisBacktoBasics.pdf.
- 124. Wartenberg, Scott A. RF measurements of die and packages. Artech house, 2002.
- 125. Crupi, Giovanni, and Dominique Schreurs, eds. *Microwave de-embedding: from theory to applications*. Academic Press, 2013.
- 126.https://in.mathworks.com/help/pdf\_doc/matlab/learn\_matlab.pdf
- 127.https://www.comsol.co.in/multiphysics
- 128.Noeth, Andreas, Tomoaki Yamada, Alexander K. Tagantsev, and Nava Setter. "Electrical tuning of dc bias induced acoustic resonances in paraelectric thin films." *Journal of Applied Physics* 104, no. 9 (2008): 094102.
- 129. Tagantsev, A. K., N. A. Pertsev, P. Muralt, and N. Setter. "Strain-induced diffuse dielectric anomaly and critical point in perovskite ferroelectric thin films." *Physical Review B* 65, no. 1 (2001): 012104.
- 130.Lakin, Kenneth M. "Modeling of thin film resonators and filters." In 1992 IEEE MTT-S Microwave Symposium Digest, pp. 149-152. IEEE, 1992.
- 131. Tagantsev, A. K., V. O. Sherman, K. F. Astafiev, J. Venkatesh, and N. Setter. "Ferroelectric materials for microwave tunable applications." *Journal of electroceramics* 11, no. 1-2 (2003): 5-66.
- 132.Tian, Hao, Junqiu Liu, Bin Dong, J. Connor Skehan, Michael Zervas, Tobias J. Kippenberg, and Sunil A. Bhave. "Hybrid integrated photonics using bulk acoustic resonators." arXiv preprint arXiv:1907.10177 (2019).

- 133.Lakin, Ki M., G. R. Kline, and K. T. McCarron. "Thin film bulk acoustic wave filters for GPS." In *IEEE 1992 Ultrasonics Symposium Proceedings*, pp. 471-476. IEEE, 1992.
- 134.Lakin, Kenneth M., Gerald R. Kline, and Kevin T. McCarron. "High-Q microwave acoustic resonators and filters." *IEEE transactions on microwave theory and techniques* 41, no. 12 (1993): 2139-2146.
- 135.K. M. Lakin, G. R. Kline and K. T. McCarron, "Development of miniature filters for wireless applications," *Proceedings of 1995 IEEE MTT-S International Microwave Symposium*, Orlando, FL, USA, 1995, pp. 883-886 vol.2.
- 136.Qiu, Xiaotun, Jie Zhu, Jon Oiler, Cunjiang Yu, Ziyu Wang, and Hongyu Yu. "Film bulk acoustic-wave resonator based ultraviolet sensor." *Applied physics letters* 94, no. 15 (2009): 151917.
- 137.Bi, Frank Z., and Bradley P. Barber. "Bulk acoustic wave RF technology." *IEEE microwave magazine* 9, no. 5 (2008): 65-80.
- 138.Sbrockey, N. M., T. S. Kalkur, A. Mansour, H. Khassaf, H. Yu, M. Aindow, S. P. Alpay, and G. S. Tompa. "Switchable and tunable film bulk acoustic resonator fabricated using barium strontium titanate active layer and Ta2O5/SiO2 acoustic reflector." *Applied Physics Letters* 109, no. 5 (2016): 052902.
- 139. Vorobiev, Andrei, and Spartak Gevorgian. "Intrinsically switchable thin film bulk acoustic wave resonators." *Applied Physics Letters* 104, no. 22 (2014): 222905.
- 140.Saddik, G. N., D. S. Boesch, S. Stemmer, and R. A. York. "dc electric field tunable bulk acoustic wave solidly mounted resonator using Sr Ti O 3." *Applied Physics Letters* 91, no. 4 (2007): 043501.
- 141.Noeth, Andreas, Tomoaki Yamada, Vladimir O. Sherman, Paul Muralt, Alexander K. Tagantsev, and Nava Setter. "Tuning of direct current bias-induced resonances in micromachined Ba 0.3 Sr 0.7 TiO 3 thin-film capacitors." *Journal of Applied Physics* 102, no. 11 (2007): 114110.
- 142. Noeth, Andreas, Tomoaki Yamada, Vladimir O. Sherman, Paul Muralt, Alexander K. Tagantsev, and Nava Setter. "DC bias-dependent shift of the resonance frequencies in BST thin film membranes." *IEEE transactions on ultrasonics, ferroelectrics, and frequency control* 54, no. 12 (2007): 2487-2492.
- 143.Gevorgian, Spartak, Andrei Vorobiev, and T. Lewin. "dc field and temperature dependent acoustic resonances in parallel-plate capacitors based on Sr Ti O 3 and Ba 0.25 Sr 0.75 Ti O 3 films: Experiment and modeling." *Journal of Applied Physics* 99, no. 12 (2006): 124112.
- 144.Tappe, S., U. Böttger, and R. Waser. "Electrostrictive resonances in (Ba 0.7 Sr 0.3) TiO 3 thin filmsat microwave frequencies." *Applied physics letters* 85, no. 4 (2004): 624-626.
- 145.Ma, Zhengxiang, Andrew J. Becker, P. Polakos, Harold Huggins, John Pastalan, Hui Wu, K. Watts, Y. H. Wong, and P. Mankiewich. "RF measurement technique for characterizing thin dielectric films." *IEEE Transactions on electron devices* 45, no. 8 (1998): 1811-1816.
- 146. Sanchez, Sylvia, G. Le Rhun, Aurélien Suhm, and Emmanuel Defaÿ. "High coupling high overtone bulk acoustic wave resonator using (Ba, Sr) TiO 3." In *The 40th European Microwave Conference*, pp. 799-802. IEEE, 2010.
- 147. Sandeep, K., J. Pundareekam Goud, and KC James Raju. "Switchable high overtone resonances in BST film with MIM structure on sapphire substrate." In 2016 Joint IEEE International Symposium on the Applications of Ferroelectrics, European Conference on Application of Polar Dielectrics, and Piezoelectric Force Microscopy Workshop (ISAF/ECAPD/PFM), pp. 1-3. IEEE, 2016.

- 148. Wang, Z., and J. David N. Cheeke. "Characterizing unpoled piezoelectric ceramic film by Lambwaves." *IEEE transactions on ultrasonics, ferroelectrics, and frequency control* 46, no. 5 (1999): 1094-1100.
- 149.Pao, Shih-Yung, Zuoqing Wang, Zi-Neng Huang, Min-Chiang Chao, C. S. Lam, and Pei-Zen Chang. "Characteristics of the unique modes in HBARs." In *IEEE International Frequency Control Symposium and PDA Exhibition Jointly with the 17th European Frequency and Time Forum, 2003. Proceedings of the 2003*, pp. 785-793. IEEE, 2003.
- 150.Zhang, Hui, Shu-Yi Zhang, and Kai Zheng. "Parameter characterization of high-overtone bulk acoustic resonators by resonant spectrum method." *Ultrasonics* 43, no. 8 (2005): 635-642.
- 151.Tian-Ying, Yang, Jiang Shu-Wen, Li Ru-Guan, and Jiang Bin. "Tunable Ba0. 5Sr0. 5TiO3 film bulk acoustic resonators using SiO2/Mo Bragg reflectors." *Chinese Physics B* 21, no. 10 (2012): 106801.
- 152. Vorobiev, Andrei, and Spartak Gevorgian. "Tunable Ba x Sr 1– x TiO 3 FBARs based on SiO 2/W Bragg reflectors." In *2010 IEEE MTT-S International Microwave Symposium*, pp. 1444-1447. IEEE, 2010.
- 153. Tagantsev, A. K., V. O. Sherman, K. F. Astafiev, J. Venkatesh, and N. Setter. "Permittivity, tunability and loss in ferroelectrics for reconfigurable high frequency electronics." In *Electroceramic-Based MEMS*, pp. 235-324. Springer, Boston, MA, 2005.
- 154.Berge, John, and Spartak Gevorgian. "Tunable bulk acoustic wave resonators based on Ba 0.25 Sr 0.75 TiO 3 thin films and a HfO 2/SiO 2 Bragg reflector." *IEEE transactions on ultrasonics, ferroelectrics, and frequency control* 58, no. 12 (2011): 2768-2771.
- 155.Deblock, Yves, Pierre Campistron, Marc Lippert, and Christian Bruneel. "Electrical characterization of plate piezoelectric transducers bonded to a finite substrate." *The Journal of the Acoustical Society of America* 111, no. 6 (2002): 2681-2685.
- 156.Hui, Zhang, Zhang Shu-Yi, and Fan Li. "Effects of thickness deviation of elastic plates in multi-layered resonance systems on frequency spectra." *Chinese Physics Letters* 26, no. 8 (2009): 084301.
- 157.Ghannam, Ayad, Christophe Viallon, David Bourrier, and Thierry Parra. "Dielectric microwave characterization of the SU-8 thick resin used in an above IC process." In 2009 European Microwave Conference (EuMC), pp. 1041-1044. IEEE, 2009.
- 158. Thin-Film BAW Composite Resonator, Comsol Models, COMSOL multiphysics®.
- 159.Zhang, Hui, Zuoqing Wang, and Shu-Yi Zhang. "Electrode effects on frequency spectra and electromechanical coupling factors of HBAR." *IEEE transactions on ultrasonics, ferroelectrics, and frequency control* 52, no. 6 (2005): 1020-1025.
- 160.Zhang, Hui, Shu-yi Zhang, and Kai Zheng. "Electrode effects on general modes in high-overtone bulk acoustic resonators." *Ultrasonics* 44 (2006): e737-e740.
- 161.Baumgartel, Lukas, and Eun Sok Kim. "Experimental optimization of electrodes for high Q, high frequency HBAR." In 2009 IEEE International Ultrasonics Symposium, pp. 2107-2110. IEEE, 2009.
- 162. Vorobiev, Andrei, and Spartak Gevorgian. "Impact of the electrode material and shape on performance of intrinsically tunable ferroelectric FBARs." *IEEE transactions on ultrasonics, ferroelectrics, and frequency control* 61, no. 5 (2014): 840-848.

- 163.Lakin, K. M., J. Belsick, J. F. McDonald, and K. T. McCarron. "Improved bulk wave resonator coupling coefficient for wide bandwidth filters." In 2001 IEEE Ultrasonics Symposium. Proceedings. An International Symposium (Cat. No. 01CH37263), vol. 1, pp. 827-831. IEEE, 2001.
- 164.Chen, Qingming, and Qing-Ming Wang. "The effective electromechanical coupling coefficient of piezoelectric thin-film resonators." *Applied Physics Letters* 86, no. 2 (2005): 022904.
- 165. Thalhammer, Robert, and Robert Aigner. "Energy loss mechanisms in SMR-type BAW devices." *mirror* 40, no. 30 (2005): 20.

# LIST OF FIGURES

Fig. 1.1	Lindsay's Wheel of Acoustics	3
Fig. 1.2	Schematic of an acoustic (a) longitudinal wave b) shear wave, in	6
	infinite solid material.	
Fig. 1.3	Longitudinal velocity of sound in various solid materials.	7
Fig. 1.4	Shear/transverse velocity of sound in various solid materials	8
Fig. 1.5	Excitations of thickness longitudinal and shear modes in	9
	piezoelectric thin film. Arrows indicate the direction of	
	propagation of the particle (oscillations).	
Fig. 1.6	Configurations of thin film BAW.	13
Fig. 1.7	2D simulation showing the total displacement (thickness	14
	extensional mode) in FBAR (top) and SMR (bottom).	
Fig. 1.8	Q values of various resonators in the frequency range of 10 MHz to	17
	10 GHz.	
Fig. 1.9	Q and attenuation of different material.	18
Fig. 1.10	Schematic of HBAR; not to scale (practically the thickness of	20
	substrates is hundreds of microns and that of PE/FE just few	
	microns).	
Fig. 1.11	Thickness extensional mode of HBAR.	22
Fig. 1.12	Frequency response of HBAR in measured S <sub>11</sub> of the device.	22
Fig. 1.13	Schematic of HBAR implemented in a) 1.2 GHz Colpitts oscillator	24
	and b) 3.6 GHz Pierce oscillator.	
Fig. 1.14	MASH oscillators with a) strain b) current and c) magnetic field	26
	feedback.	

Fig. 1.15	Device schematic to achieve direct coupling of phonons and	29
	diamond NV centre spins.	
Fig. 1.16	Schematic of on-chip realization of HBAR, a split Josephson	29
	junction transmon qubit and microwave CPW cavity.	
Fig. 1.17	Relation between input and output in a material system.	38
Fig. 1.18	1-D rigid-ion spring models of a) piezoelectric and b) field induced	39
	strain.	
Fig. 1.19	The multifunctionality of ferroelectric materials.	41
Fig. 1.20	BST is in ferro or paraelectric phase depending on the temperature	43
	relative to $T_c$ .	
Fig. 1.21	Permittivity vs temperature for different concentrations of BST.	43
Fig. 1.22	Unit cell of BST in paraelectric phase (left) and ferroelectric phase	44
	(right).	
Fig. 1.23	Dielectric constant as a function of temperature for Ba <sub>0.7</sub> Sr <sub>0.3</sub> TiO <sub>3</sub> .	45
Fig. 1.24	Mechanisms contributing to dielectric loss in BST.	46
Fig. 1.25	Various techniques available for BST thin film deposition/growth	48
Fig. 2.1	X-ray diffraction of Ba <sub>0.5</sub> Sr <sub>0.5</sub> TiO <sub>3</sub> target.	55
Fig. 2.2	FESEM and EDAX of Ba <sub>0.5</sub> Sr <sub>0.5</sub> TiO <sub>3</sub> target	55
Fig. 2.3	Schematic drawing of a Pulse Laser Deposition (PLD) system.	57
Fig. 2.4	PLD used in this work	58
Fig. 2.5	X-Ray diffraction patterns of BST thin films on Pt coated sapphire	59
	substrate.	
Fig. 2.6	FESEM image of thin film BST on Pt coated sapphire substrate.	60

Fig. 2.7	Schematic Diagram of a RF magnetron sputtering system.	61
Fig. 2.8	The RF magnetron sputtering system used in this study.	61
Fig. 2.9	Process flow for the fabrication of High Overtone Bulk Acoustic	64
	Resonator (HBAR).	
Fig. 2.10	Diffraction of X-ray from atoms in a crystal.	67
Fig. 2.11	On-wafer probing setup for measuring HBAR characteristics.	71
Fig. 2.12	Block diagram of Vector Network Analyzer.	71
Fig. 2.13	Short, Open, and 50 $\Omega$ load standards of CS-5 used for calibration.	75
Fig. 2.14	Uncalibrated S <sub>11</sub> (dB) response.	<b>7</b> 6
Fig. 2.15	Calibrated S <sub>11</sub> (dB) response.	77
Fig. 2.16	On-wafer probing of DUT showing the electrical reference planes.	79
Fig. 2.17	On-wafer probing of CPC structure of HBAR.	80
Fig. 2.18	Measured DUT (HBAR) response after calibration.	80
Fig. 3.1	Schematic of parallel plate transducer with TE mode.	88
Fig. 3.2	Transfer matrix representation of a composite resonator.	94
Fig. 3.3	Frequency spectra of high overtone bulk acoustic resonator (HBAR)	97
Fig. 3.4	SPRF distribution of the high overtone bulk acoustic resonator (HBAR).	100
Fig. 3.5	$k_{eff}^2$ distribution of the high overtone bulk acoustic resonator (HBAR).	100
Fig. 3.6	Schematic of five-layer composite resonator (HBAR).	104
Fig. 3.7	Frequency spectra of HBAR with SU-8 coated on backside.	106

Fig. 3.8	SPRF distribution of HBAR with coated material (SU-8).	107
Fig. 3.9	$k_{eff}^2$ distribution of the HBAR with coated material (SU-8).	107
Fig. 4.1	FESEM of Top electrode of fabricated HBAR.	112
Fig. 4.2	Probing set-up for the HBAR. Only the top electrode is patterned.	113
Fig. 4.3	Process flow of measurement.	115
Fig. 4.4	Frequency Spectra of HBAR with a) YAG b) Al <sub>2</sub> O <sub>3</sub> c) Si and d)	117
	Fused Silica as substrate.	
Fig. 4.5	Multiple resonant peaks in a narrowband of HBAR with a) YAG	118
	b) Al <sub>2</sub> O <sub>3</sub> c) Si and d) Fused Silica as substrate	
Fig. 4.6	HBARs made on fused silica with different thicknesses.	120
Fig. 4.7	SPRF distribution for HBAR with sapphire as substrate	122
Fig. 4.8	$k_{eff}^2$ distribution for HBAR with sapphire as substrate.	123
Fig. 4.9	SPRF distribution for HBAR with YAG as substrate.	126
Fig. 4.10	$k_{eff}^2$ distribution for HBAR with YAG as substrate.	126
Fig. 4.11	Frequency spectra of HBAR (sapphire) with varying DC bias.	128
Fig. 4.12	Frequency spectra of HBAR (YAG) with varying DC bias.	129
Fig. 4.13	SPRF distribution (Expt.) of the HBAR (sapphire) with different	130
	DC bias of 20V, 40V and 60V	
Fig. 4.14	$k_{eff}^2$ distribution of the HBAR (sapphire) with different DC bias of	131
	20V, 40V and 60V.	
Fig. 4.15	Q-factor distribution (Expt.) of the HBAR (sapphire) with different	131
	DC bias of 20V, 40V and 60V.	

Fig. 4.16	SPRF distribution (Expt.) of the HBAR (YAG) with different DC	133
	bias of 10 V,20 V and 30 V.	
Fig. 4.17	$k_{eff}^2$ distribution of the HBAR (YAG) with different DC bias of 10	134
	V,20 V and 30 V.	
Fig. 4.18	Q-factor distribution (Expt.) of the HBAR (YAG) with different	135
	DC bias of 10 V, 2 V and 30 V.	
Fig. 5.1	Schematic of HBAR with SU-8 coating.	142
Fig. 5.2	Frequency spectra of HBAR without SU-8-layer coating.	143
Fig. 5.3	Frequency spectra of HBAR with SU-8-layer coating (2.1 μm).	144
Fig. 5.4	Frequency spectra of HBAR for different thickness of SU8 coating.	145
Fig. 5.5	(a) SPRF and (b) $k_{eff}^2$ distributions of the uncoated HBAR.	147
Fig. 5.6	Q factor distributions of the uncoated HBAR.	148
Fig. 5.7	SPRF distributions of the SU-8 coated HBAR.	148
Fig. 5.8	$k_{eff}^2$ distributions of the SU-8 coated HBAR.	149
Fig. 5.9	Q factor distributions of the SU-8 coated HBAR.	149
Fig. 5.10	SPRF and $k_{eff}^2$ distribution for both coated and uncoated HBAR.	150
Fig. 5.11	Q factor distribution of coated and uncoated HBAR.	151
Fig. 5.12	SPRF distributions for both simulation and experimental results	154,
	where thicknesses of SU-8 coated are a) 2.1 $\mu$ m b) 3.2 $\mu$ m and c) 6.1	155
	μm	
Fig. 5.13	$k_{eff}^2$ for HBAR with 2.18 $\mu$ m thick SU-8 coating (Simulation).	156
Fig. 5.14	SPRF and $k_{eff}^2$ distribution for different cases of Q factor of SU-8	157
	given during simulation.	

Fig. 5.15	Real part of impedance of HBAR with and without SU-8 layer for	160
	experimental (top) and FEM model (bottom).	
Fig. 5.16	Thickness extensional mode of the HBAR without SU-8 layer.	161
Fig. 5.17	Thickness extensional mode of the HBAR with SU-8 layer.	161
Fig. 6.1	SPRF distributions for HBARs: - GG, GP, PP and PG.	166
Fig. 6.2	$k_{eff}^2$ distributions for HBARs: - GG, GP, PP and PG.	168
Fig. 6.3	Figure 6.3. Q factor distributions for HBARs of electrode combination: - GG, GP, PP and PG.	169
Fig. 6.4	Various geometry and sizes of top electrodes.	171
Fig. 6.5	SPRF distributions for HBARs: - SC, MC and BC.	173
Fig. 6.6	$k_{eff}^2$ distributions for HBARs: - SC, MC and BC.	174
Fig. 6.7	Q factor distributions for HBARs: - SC, MC and BC.	174
Fig. 6.8	SPRF distributions for HBARs: - SA, MA and BA.	177
Fig. 6.9	$k_{eff}^2$ distributions for HBARs: - SA, MA and BA.	178
Fig. 6.10	Q factor distributions for HBARs: - SA, MA and BA.	178
Fig. 6.11	SPRF distributions for HBARs: - MS and BS.	180
Fig. 6.12	$k_{eff}^2$ distributions for HBARs: - MS and BS.	181
Fig. 6.13	Q factor distributions for HBARs: - MS and BS.	181
Fig. 6.14	Displacement in the resonator with different top electrodes with	183
	widths of;(a) 10 $\mu m,$ (b)15 $\mu m,$ (c)20 $\mu m,$ (d)25 $\mu m,$ (e) 30 $\mu m$ and (f) 35 $\mu m.$	

### LIST OF FIGURES

Table 1.1	Literature review of material characterization using composite	32-
	resonator/HBAR.	37
Table 2.1	Atomic percentages of elements in the BST target.	56
Table 3.1	Material parameters used in simulation.	98
Table 4.1	Extracted acoustic velocities of substrates.	120
Table 4.2	Parameters used in simulation for HBAR with sapphire as	123
	substrate.	
Table 4.3	Experimental results for HBAR with sapphire as substrate.	124
Table 4.4	Parameters used in simulation for HBAR with YAG as substrate.	125
Table 4.5	Experimental results for HBAR with YAG as substrate.	127
Table 4.6	$k_t^2$ and $T_r$ for different DC bias voltages.	136
Table 5.1	Material parameters used in simulation.	153
Table 6.1	Name of Samples fabricated.	165
Table 6.2	Acoustic properties of materials.	165
Table 6.2	Name of HBARs with different top electrode geometry and areas.	171

### **Abbreviations**

RF	Radio frequency
MEMS	Microelectromechanical Systems
SAW	Surface acoustic wave
BAW	Bulk acoustic wave
HBAR	High overtone bulk acoustic resonator
FBAR	Film bulk acoustic wave resonator
SMR	Solidly mounted resonator
Q	Quality factor
NDE	Non-Destructive evaluation
SONAR	Sound navigation and ranging
SoC	System on Chip
EM	Electromagnetic
IC	Integrated circuit
PE	Piezoelectric
DRIE	Deep reactive-ion etching
QED	Quantum electrodynamics
QAD	Quantum acoustodynamics
CPW	Circular patch waveguide
QCM	Quartz crystal microbalance
BST	Barium strontium titanate (Ba 0.5 Sr 0.5 TiO3)
STO	Strontium titanate
MUT	Material under test
RSM	Resonant spectrum method
L	

$k_{eff}^2$	Effective coupling coefficient
$k_t^2$	Electromechanical coupling coefficient
SPRF	Spacing of parallel resonance frequency
PLD	Pulsed laser deposition
FEM	Finite element method
MIM	Metal-insulator-metal
GSG	Ground signal ground

#### LIST OF PUBLICATIONS:

### As Part of the thesis:

- Kongbrailatpam Sandeep, J. Pundareekam Goud, and K. C. James Raju, "Effects of a Coated Material Layer on High Overtone Bulk Acoustic Resonator and its Possible Applications", IEEE Transactions on Ultrasonics, Ferroelectrics, and Frequency Control, Sept-21, (2020). DOI: 10.1109/TUFFC.2020.3025618.
- 2. **Kongbrailatpam Sandeep**, J. Pundareekam Goud, and K. C. James Raju, Resonant spectrum method for characterizing Ba<sub>0.5</sub>Sr<sub>0.5</sub>TiO<sub>3</sub> based high overtone bulk acoustic wave resonators, **Applied Physics Letters 111, 012901 (2017).**

#### Other Publications:

- 3. J. Pundareekam Goud, **Kongbrailatpam Sandeep**, Sivanagi Reddy Emani, Mahmoud. S. Alkathy, Kuna Lakshun Naidu and K C James Raju "Zr-substituted Ba<sub>0.6</sub>Sr<sub>0.4</sub>TiO<sub>3</sub> ferroelectric thin films grown by pulsed laser deposition (PLD) at different laser fluence". **Ferroelectrics**, **VOL. 516**, **28–35**, **(2017)**.
- 4. J. Pundareekam Goud, S Ramakanth, Andrews Joseph, Kongbrailatpam Sandeep, G L N Rao, and K C James Raju, "Effect of crystallinity on microwave tunability of Pulsed laser deposited Ba<sub>0.5</sub>Sr<sub>0.5</sub>TiO<sub>3</sub> Thin Films" Thin Solid Films, 626, 126–130 (2017).
- 5. J. Pundareekam Goud, Mahmoud S. Alkathy, **Kongbrailatpam Sandeep**, S Ramakanth and K. C. James Raju "Influence of laser fluence on structural, optical and microwave dielectric properties of pulsed laser deposited Ba<sub>0.6</sub>Sr<sub>0.4</sub>TiO<sub>3</sub> thin films". **Journal of Materials Science: Materials in Electronics**, **29**, **15973–15982** (**2018**).
- 6. J. Pundareekam Goud, Ajeet Kumar, S Ramakanth, **Kongbrailatpam Sandeep**, Partha Ghoshal and K.C. James Raju, "Tunable microwave device fabrication on low-temperature

- crystallized **Ba<sub>0.5</sub>Sr<sub>0.5</sub>TiO<sub>3</sub>** thin films by an alternating deposition and laser annealing process", **Manuscript being reviewed**.
- 7. J. Pundareekam Goud, Ajeet Kumar, Kongbrailatpam Sandeep, Deepak Kumar, S. Ramakanth, A.R. James, Partha Ghoshal and K. C. James Raju "Reducing the leakage current in BST by a low temperature crystallization process", Manuscript under preparation.

### **Conference Proceedings**

 Kongbrailatpam Sandeep, J. Pundareekam Goud, K.C. James Raju, "Switchable High Overtone Resonance in BST film with MIM structure on Sapphire Substrate", 978-1-5090-1871-2016 IEEE Workshop (ISAF/ECAPD/PFM IEEE International Symposium) (2016).

#### **Patent**

1. J. Pundareekam Goud, S Ramakanth, Kongbrailatpam Sandeep, Ajeet Kumar and K.C. James Raju "Laser based method to crystallize ferroelectric thin film at 300°C temperatures for tunable microwave devices", Filed for an Indian patent. Application no. 201941007633 dated February 27, 2019.

### Conferences/Symposium/ Workshops attended

- International Microwave and RF Conference (IMaRC 2015), Hyderabad Novotel, Hyderabad, India. (Participated in the Ph. D Students' Program)
- IEEE Workshop (ISAF/ECAPD/PFM IEEE International Symposium) (2016), Darmstadt, Germany. (Oral Presentation with proceeding)
- 3. 6<sup>th</sup> International symposium on Integrated Functionalities (ISIF-2017), New Delhi, India. (Oral Presentation)

- Oxford Instruments Nanotechnology Workshop, University of Hyderabad, 2017,
   Hyderabad, India.
- Symposium on Emerging Trends in Electronics (SETE-2019) University of Hyderabad,
   Hyderabad, India. (Oral Presentation).
- 6. 5th International Conference on Emerging Electronics (IEEE-ICEE 2020), Indian Institute of Technology Delhi, India. (E-poster presentation)

### **Appendix**

denpzo=5280;% APL

### A. Example of a 1-D model for simulating frequency spectra of HBAR

```
clc
clear all
% FOUR LAYER TRANSMISSION LINE MODEL%%
%composite with electrode impedance
%d1-thickness of top electrode, d2-thickness of bottom
% electrode, lp-thickness of piezo electrode, ls-thickness of substrate electrode
% A-surface area ,den1,den2-densities of topand bottom electrode
% densb-density of substrate, denpzo-density of piezolayer
%V1, V2, Vsb, Vpzo- extensional velocities of top, bottom
%electrodes, substrate, piezo layer
%kt2-electromechanical coupling coeff of pzo
% perm33-permitivity of the piezo film(thickness mode)
%BST YAG with Al electrode
%datas provided%
d1=100e-9;% Au
d2=100e-9;% Pt
lp=850e-9;%BST
%ls=493e-6;%YAG %big effect on the response
%ls=430e-6;%YAG %big effect on the response
ls=526.2e-6;
A=pi*(75e-6)^2;
den1=19490;
den2=21500;
densb=3990;
```

```
%Giving imaginary value that accounts for quality factor of the material
Qp=4000;
Vpz=5100;
Vi=0.5*(Vpz/Qp)
Qsub=40000;
Vsub=11350;
Vsubi=0.5*(Vsub/Qsub)
V1=3361;
V2=4020;
Vsb=11350+ 0.4539j;% actual_fixed
Vpzo=5100 + 1.6375j;%random_fixed
kt2=0.08;
perm33=(70*8.85e-12);
Zo=A*denpzo*Vpzo;
Zsb=A*densb*Vsb;
Z1=A*den1*V1;
Z2=A*den2*V2;
Co=(perm 33*A)/lp;
fr = 600e6:32000:3.5e9;% frequency sweep
Zot = zeros(size(fr));
for i = 1:length(fr)
w=2*pi*fr(i);
R1=((w*d1)/V1);
R2=((w*d2)/V2);
Rsb=((w*ls)/Vsb);
Rpzo=(w*lp)/Vpzo;
Za=j*(Z1*tan(R1));
a1=(Zsb*tan(Rsb))+(Z2*tan(R2));
a2=1-((Zsb/Z2)*tan(R2)*tan(Rsb));
Zb=j*(a1/a2);
```

```
Z3=Za/Zo;
Z4=Zb/Zo;
b1=kt2*(((Z3+Z4)*sin(Rpzo))+(j*2*(1-cos(Rpzo))));
b2=Rpzo*(((Z3+Z4)*cos(Rpzo))+(j*((1+(Z3*Z4))*sin(Rpzo))));
Zin=(1/(j*w*Co))*(1-(b1/b2)); % absolute value of impedance
Zot(i)=abs(Zin);
Y(i)= abs(1/Zin);
Zot1(i)=real(Zin); % impedance
Zot2(i)=real(1/Zin); % admittance
end
plot(fr,Zot,'r')
```

### B. Example for Matlab® program to extract parallel, series, and Q factor of HBAR.

```
clc
clear all
format long
filename='2600.csv';
k = csvread(filename);
% new = k(15:25,:)
columnA0 = k(1:2300,1);
columnB0 = k(1:2300,2);
columnC0 = k(1:2300,3);
% columnA0 = k(23001:20001,1);
% columnB0 = k(23001:20001,2);
% columnC0 = k(23001:20001,3);
Z0=50;
%plot(columnA,columnB,'r')
%hold on
%plot(columnA,columnC,'b')
```

```
% magnitude= 20 * log(sqrt(Re^2 + Im^2))
[f0]=size(columnA0);
[B0]=size(columnB0);
[C0]=size(columnC0);
for i0=1:[f0]
freq0(i0) = columnA0(i0);
real0(i0)=columnB0(i0);
imag0(i0)=columnC0(i0);
magnitude0(i0) = 10 * log(sqrt(real0(i0).^2 + imag0(i0).^2));
S110(i0) = complex(real0(i0), imag0(i0));
Z=((1+(real+((imag))/(1-(real+imag)))*Z0
ZT(i0)=Z0*((1+S110(i0))/(1-S110(i0)));
YT(i0)=1/ZT(i0);
P0(i0) = angle(ZT(i0));
Y0_{real}(i0)=real(YT(i0));
Y0_{imag}(i0)=imag(YT(i0));
Z0_{real}(i0)=real(ZT(i0));
Z0_{imag}(i0)=imag(ZT(i0));
Cap0(i0) = -(1/(2*pi*freq0(i0)*Z0_imag(i0)));
perm0(i0) = (Cap0(i0)*(931e-9))/((pi*(45e-6)^2)*(8.85e-12));
tand 0 (i0) = -(Z0\_real (i0)/Z0\_imag (i0));
Za0(i0)=abs(ZT(i0));
end
[maxi01,ind01]=max(Z0_real);%parallel resonance
fp0=columnA0(ind01)
%%calculation of Q factor dP/dFp
```

```
dp0 = diff(P0(:))./diff(freq0(:));
dpp0 = (dp0(ind01)*(fp0))/2;
Qp0=abs(dpp0)
[maxi02,ind02]=max(Y0_real);% series resonance
fs0=columnA0(ind02)
%% calculation of Q factor dP/dFs
ds0 = diff(P0(:))./diff(freq0(:));
dss0=(ds0(ind01)*(fs0))/2;
Qs0=abs(dss0)
filename='2600.csv';
k = csvread(filename);
% new = k(15:25,:)
columnA1 = k(2300:4400,1);
columnB1 = k(2300:4400,2);
columnC1 = k(2300:4400,3);
Z0=50;
%plot(columnA,columnB,'r')
%hold on
%plot(columnA,columnC,'b')
[f1]=size(columnA1);
[B1]=size(columnB1);
```

```
[C1]=size(columnC1);
for i1=1:[f1]
freq1(i1)=columnA1(i1);
real1(i1)=columnB1(i1);
imag1(i1)=columnC1(i1);
magnitude1(i1) = 10 * log(sqrt(real1(i1).^2 + imag1(i1).^2));
S111(i1) = complex(real1(i1), imag1(i1));
%Z = ((1 + (real + ((imag))/(1 - (real + imag)))*Z0)
ZT(i1)=Z0*((1+S111(i1))/(1-S111(i1)));
YT(i1)=1/ZT(i1);
P1(i1) = angle(ZT(i1));
Y1_real(i1)=real(YT(i1));
Z1_{real(i1)=real(ZT(i1))};
Z1_{imag(i1)=imag(ZT(i1))};
Cap1(i1) = -(1/(2*pi*freq1(i1)*Z1_imag(i1)));
perm1(i1) = (Cap1(i1)*(1150e-9))/((pi*(80e-6)^2)*(8.85e-12));
tand1(i1) = -(Z1\_real(i1)/Z1\_imag(i1));
Za1(i1)=abs(ZT(i1));
end
[maxi11,ind11]=max(Z1_real);%parallel resonance
fp1=columnA1(ind11)
%% calculation of Q factor dP/dFp
dp1 = diff(P1(:))./diff(freq1(:));
dpp1 = (dp1(ind11)*(fp1))/2;
Qp1=abs(dpp1)
[maxi12,ind12]=max(Y1_real);% series resonance
fs1=columnA1(ind12)
```

```
%% calculation of Q factor dP/dFs
ds1 = diff(P1(:))./diff(freq1(:));
dss1=(ds1(ind11)*(fs1))/2;
Qs1=abs(dss1)
filename='2600.csv';
k = csvread(filename);
% new = k(15:25,:)
columnA2 = k(4400:6700,1);
columnB2 = k(4400:6700,2);
columnC2 = k(4400:6700,3);
Z0=50;
%plot(columnA,columnB,'r')
%hold on
%plot(columnA,columnC,'b')
[f2]=size(columnA2);
[B2]=size(columnB2);
[C2]=size(columnC2);
for i2=1:[f2]
freq2(i2)=columnA2(i2);
real2(i2)=columnB2(i2);
imag2(i2)=columnC2(i2);
magnitude2(i2) = 10 * log(sqrt(real2(i2).^2 + imag2(i2).^2));
S112(i2)=complex(real2(i2),imag2(i2));
Z=((1+(real+((imag))/(1-(real+imag)))*Z0
ZT(i2)=Z0*((1+S112(i2))/(1-S112(i2)));
YT(i2)=1/ZT(i2);
P2(i2) = angle(ZT(i2));
```

```
Y2_real(i2)=real(YT(i2));
Z2_real(i2)=real(ZT(i2));
Z2_imag(i2)=imag(ZT(i2));
Cap2(i2) = -(1/(2*pi*freq2(i2)*Z2\_imag(i2)));
perm2(i2) = (Cap2(i2)*(1150e-9))/((pi*(45e-6)^2)*(8.85e-12));
tand2(i2) = -(Z2\_real(i2)/Z2\_imag(i2));
Za2(i2)=abs(ZT(i2));
end
[maxi21,ind21]=max(Z2_real);% parallel resonance
fp2=columnA2(ind21)
%% calculation of Q factor dP/dFp
dp2 = diff(P2(:))./diff(freq2(:));
dpp2 = (dp2(ind21)*(fp2))/2;
Qp2=abs(dpp2)
[maxi22,ind22]=max(Y2_real);% series resonance
fs2=columnA2(ind22)
%%calculation of Q factor dP/dFs
ds2 = diff(P2(:))./diff(freq2(:));
dss2=(ds2(ind21)*(fs2))/2;
Qs2=abs(dss2)
filename='2600.csv';
k = csvread(filename);
% new = k(15:25,:)
```

```
columnA3 = k(6700:8800,1);
columnB3 = k(6700:8800,2);
columnC3 = k(6700:8800,3);
Z0=50;
%plot(columnA,columnB,'r')
%hold on
%plot(columnA,columnC,'b')
[f3]=size(columnA3);
[B3]=size(columnB3);
[C3]=size(columnC3);
for i3=1:[f3]
freq3(i3)=columnA3(i3);
real3(i3)=columnB3(i3);
imag3(i3)=columnC3(i3);
magnitude3(i3) = 10 * log(sqrt(real3(i3).^2 + imag3(i3).^2));
S113(i3)=complex(real3(i3),imag3(i3));
%Z = ((1 + (real + ((imag))/(1 - (real + imag)))*Z0)
ZT(i3)=Z0*((1+S113(i3))/(1-S113(i3)));
YT(i3)=1/ZT(i3);
P3(i3) = angle(ZT(i3));
Y3_real(i3)=real(YT(i3));
Z3_real(i3)=real(ZT(i3));
Z3_{imag}(i3)=imag(ZT(i3));
Cap3(i3) = -(1/(2*pi*freq3(i3)*Z3_imag(i3)));
perm3(i3) = (Cap3(i3)*(1150e-9))/((pi*(45e-6)^2)*(8.85e-12));
tand3(i3) = -(Z3\_real(i3)/Z3\_imag(i3));
Za3(i3)=abs(ZT(i3));
end
[maxi31,ind31]=max(Z3_real);%parallel resonance
fp3=columnA3(ind31)
```

```
%% calculation of Q factor dP/dFp
dp3 = diff(P3(:))./diff(freq3(:));
dpp3 = (dp3(ind31)*(fp3))/2;
Qp3=abs(dpp3)
[maxi32,ind32]=max(Y3_real);% series resonance
fs3=columnA3(ind32)
%% calculation of Q factor dP/dFs
ds3 = diff(P3(:))./diff(freq3(:));
dss3 = (ds3(ind31)*(fs3))/2;
Qs3=abs(dss3)
filename='2600.csv';
k = csvread(filename);
% new = k(15:25,:)
columnA4 = k(8800:10940,1);
columnB4 = k(8800:10940,2);
columnC4 = k(8800:10940,3);
Z0=50;
%plot(columnA,columnB,'r')
%hold on
%plot(columnA,columnC,'b')
[f4]=size(columnA4);
[B4]=size(columnB4);
[C4]=size(columnC4);
```

```
for i4=1:[f4]
freq4(i4)=columnA4(i4);
real4(i4)=columnB4(i4);
imag4(i4)=columnC4(i4);
magnitude4(i4) = 10 * log(sqrt(real4(i4).^2 + imag4(i4).^2));
S114(i4)=complex(real4(i4),imag4(i4));
%Z = ((1 + (real + ((imag))/(1 - (real + imag)))*Z0)
ZT(i4)=Z0*((1+S114(i4))/(1-S114(i4)));
YT(i4)=1/ZT(i4);
P4(i4) = angle(ZT(i4));
Y4_real(i4)=real(YT(i4));
Z4_real(i4)=real(ZT(i4));
Z4_{imag}(i4)=imag(ZT(i4));
Cap4(i4) = -(1/(2*pi*freq4(i4)*Z4_imag(i4)));
perm4(i4) = (Cap4(i4)*(1150e-9))/((pi*(45e-6)^2)*(8.85e-12));
tand4(i4) = -(Z4\_real(i4)/Z4\_imag(i4));
Za4(i4)=abs(ZT(i4));
end
[maxi41,ind41]=max(Z4_real);%parallel resonance
fp4=columnA4(ind41)
%% calculation of Q factor dP/dFp
dp4 = diff(P4(:))./diff(freq4(:));
dpp4 = (dp4(ind41)*(fp4))/2;
Qp4=abs(dpp4)
[maxi42,ind42]=max(Y4_real);% series resonance
fs4=columnA4(ind42)
%%calculation of Q factor dP/dFs
```

```
ds4 = diff(P4(:))./diff(freq4(:));
dss4 = (ds4(ind41)*(fs4))/2;
Qs4=abs(dss4)
filename='2600.csv';
k = csvread(filename);
% new = k(15:25,:)
columnA5 = k(10940:13150,1);
columnB5 = k(10940:13150,2);
columnC5 = k(10940:13150,3);
Z0=50;
%plot(columnA,columnB,'r')
%hold on
%plot(columnA,columnC,'b')
[f5]=size(columnA5);
[B5]=size(columnB5);
[C5]=size(columnC5);
for i5=1:[f5]
freq5(i5)=columnA5(i5);
real5(i5)=columnB5(i5);
imag5(i5)=columnC5(i5);
magnitude5(i5) = 10 * log(sqrt(real5(i5).^2 + imag5(i5).^2));
S115(i5)=complex(real5(i5),imag5(i5));
Z=((1+(real+((imag))/(1-(real+imag)))*Z0
ZT(i5)=Z0*((1+S115(i5))/(1-S115(i5)));
YT(i5)=1/ZT(i5);
P5(i5) = angle(ZT(i5));
```

```
Y5_real(i5)=real(YT(i5));
Z5_real(i5)=real(ZT(i5));
Z5_{imag}(i5)=imag(ZT(i5));
Cap5(i5) = -(1/(2*pi*freq5(i5)*Z5_imag(i5)));
perm5(i5) = (Cap5(i5)*(1150e-9))/((pi*(80e-6)^2)*(8.85e-12));
tand5(i5) = -(Z5\_real(i5)/Z5\_imag(i5));
Za5(i5)=abs(ZT(i5));
end
[maxi51,ind51]=max(Z5_real);% parallel resonance
fp5=columnA5(ind51)
%% calculation of Q factor dP/dFp
dp5 = diff(P5(:))./diff(freq5(:));
dpp5 = (dp5(ind51)*(fp5))/2;
Qp5=abs(dpp5)
[maxi52,ind52]=max(Y5_real);% series resonance
fs5=columnA5(ind52)
%%calculation of Q factor dP/dFs
ds5 = diff(P5(:))./diff(freq5(:));
dss5 = (ds5(ind51)*(fs5))/2;
Qs5=abs(dss5)
filename='2600.csv';
k = csvread(filename);
% new = k(15:25,:)
```

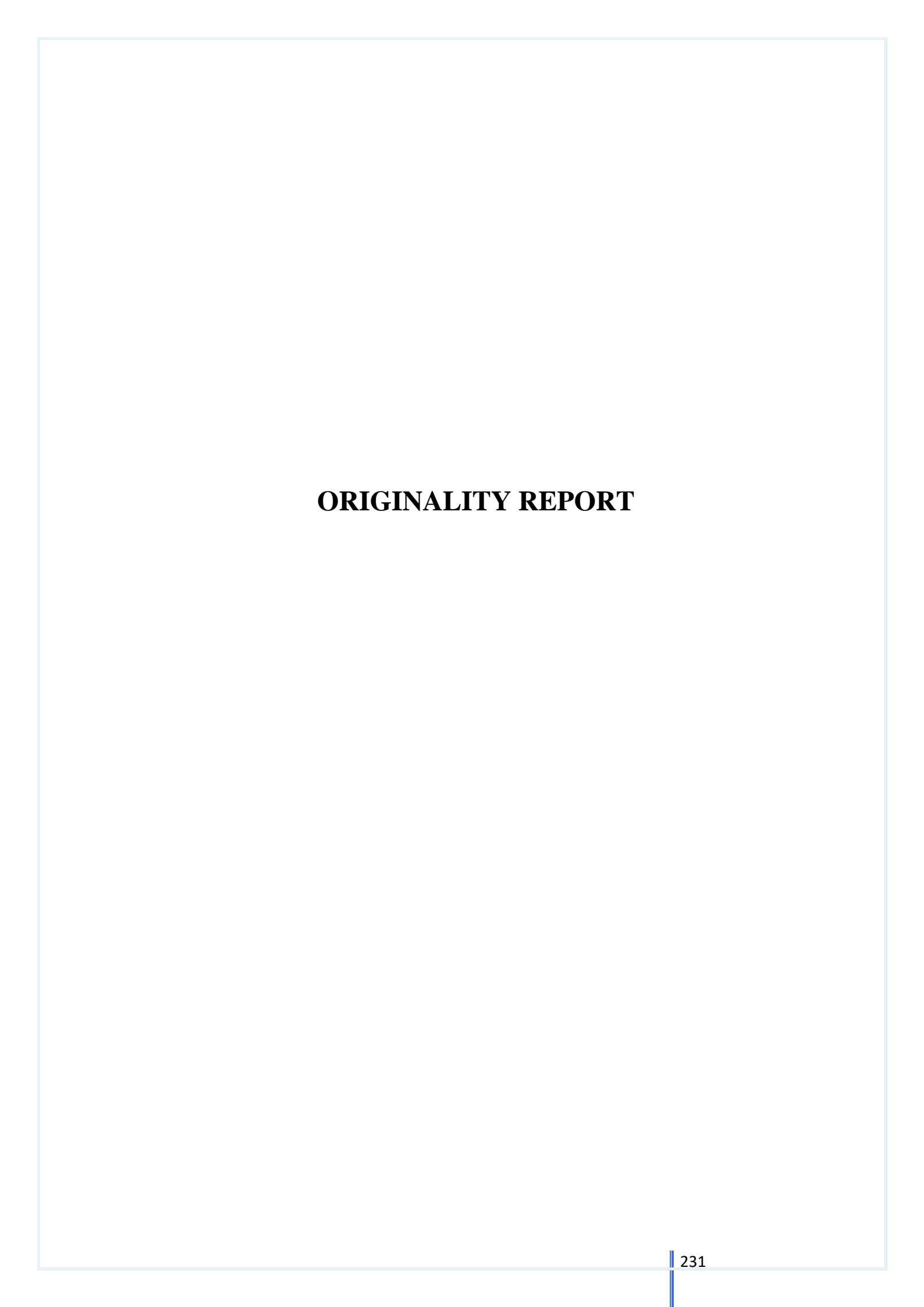
```
columnA6 = k(13150:15200,1);
columnB6 = k(13150:15200,2);
columnC6 = k(13150:15200,3);
Z0=50;
%plot(columnA,columnB,'r')
%hold on
%plot(columnA,columnC,'b')
[f6]=size(columnA6);
[B6]=size(columnB6);
[C6]=size(columnC6);
for i6=1:[f6]
freq6(i6)=columnA6(i6);
real6(i6)=columnB6(i6);
imag6(i6)=columnC6(i6);
magnitude6(i6) = 10 * log(sqrt(real6(i6).^2 + imag6(i6).^2));
S116(i6)=complex(real6(i6),imag6(i6));
%Z = ((1 + (real + ((imag))/(1 - (real + imag)))*Z0)
ZT(i6)=Z0*((1+S116(i6))/(1-S116(i6)));
YT(i6)=1/ZT(i6);
P6(i6) = angle(ZT(i6));
Y6_real(i6)=real(YT(i6));
Z6_{real}(i6)=real(ZT(i6));
Z6_{imag}(i6)=imag(ZT(i6));
Cap6(i6) = -(1/(2*pi*freq6(i6)*Z6_imag(i6)));
perm6(i6) = (Cap6(i6)*(1150e-9))/((pi*(66e-6)^2)*(8.85e-12));
tand6(i6) = -(Z6\_real(i6)/Z6\_imag(i6));
Za6(i6)=abs(ZT(i6));
end
[maxi61,ind61]=max(Z6_real);%parallel resonance
```

```
fp6=columnA6(ind61)
%% calculation of Q factor dP/dFp
dp6 = diff(P6(:))./diff(freq6(:));
dpp6=(dp6(ind61)*(fp6))/2;
Qp6=abs(dpp6)
[maxi62,ind62]=max(Y6_real);% series resonance
fs6=columnA6(ind62)
%% calculation of Q factor dP/dFs
ds6 = diff(P6(:))./diff(freq6(:));
dss6 = (ds6(ind61)*(fs6))/2;
Qs6=abs(dss6)
filename='2600.csv';
k = csvread(filename);
% new = k(15:25,:)
columnA7 = k(15200:17520,1);
columnB7 = k(15200:17520,2);
columnC7 = k(15200:17520,3);
Z0=50;
[f7]=size(columnA7);
[B7]=size(columnB7);
[C7]=size(columnC7);
for i7=1:[f7]
```

```
freq7(i7)=columnA7(i7);
real7(i7)=columnB7(i7);
imag7(i7)=columnC7(i7);
magnitude7(i7)= 10 * log(sqrt(real7(i7).^2 + imag7(i7).^2));
S117(i7)=complex(real7(i7),imag7(i7));
Z=((1+(real+((imag))/(1-(real+imag)))*Z0
ZT(i7)=Z0*((1+S117(i7))/(1-S117(i7)));
YT(i7)=1/ZT(i7);
P7(i7) = angle(ZT(i7));
Y7_real(i7)=real(YT(i7));
Z7_real(i7)=real(ZT(i7));
Z7_{imag}(i7)=imag(ZT(i7));
Cap7(i7) = -(1/(2*pi*freq7(i7)*Z7_imag(i7)));
perm7(i7) = (Cap7(i7)*(1150e-9))/((pi*(66e-6)^2)*(8.85e-12));
tand7(i7) = -(Z7\_real(i7)/Z7\_imag(i7));
Za7(i7)=abs(ZT(i7));
end
[maxi71,ind71]=max(Z7_real);%parallel resonance
fp7=columnA7(ind71)
%%calculation of Q factor dP/dFp
dp7 = diff(P7(:))./diff(freq7(:));
dpp7 = (dp7(ind71)*(fp7))/2;
Qp7=abs(dpp7)
[maxi72,ind72]=max(Y7_real);% series resonance
fs7=columnA7(ind72)
%%calculation of Q factor dP/dFs
```

```
ds7 = diff(P7(:))./diff(freq7(:));
dss7 = (ds7(ind71)*(fs7))/2;
Qs7=abs(dss7)
filename='2600.csv';
k = csvread(filename);
% new = k(15:25,:)
columnA8 = k(17520:20001,1);
columnB8 = k(17520:20001,2);
columnC8 = k(17520:20001,3);
Z0=50;
[f8]=size(columnA8);
[B8]=size(columnB8);
[C8]=size(columnC8);
for i8=1:[f8]
freq8(i8)=columnA8(i8);
real8(i8)=columnB8(i8);
imag8(i8)=columnC8(i8);
magnitude8(i8) = 10 * log(sqrt(real8(i8).^2 + imag8(i8).^2));
S118(i8)=complex(real8(i8),imag8(i8));
Z=((1+(real+((imag))/(1-(real+imag)))*Z0
ZT(i8)=Z0*((1+S118(i8))/(1-S118(i8)));
YT(i8)=1/ZT(i8);
P8(i8) = angle(ZT(i8));
Y8_real(i8)=real(YT(i8));
Z8_real(i8)=real(ZT(i8));
Z8_imag(i8)=imag(ZT(i8));
Cap8(i8) = -(1/(2*pi*freq8(i8)*Z8\_imag(i8)));
```

```
perm8(i8) = (Cap8(i8)*(1150e-9))/((pi*(66e-6)^2)*(8.85e-12));
tand8(i8) = -(Z8\_real(i8)/Z8\_imag(i8));
Za8(i8)=abs(ZT(i8));
end
[maxi81,ind81]=max(Z8_real);% parallel resonance
fp8=columnA8(ind81)
%%calculation of Q factor dP/dFp
dp8 = diff(P8(:))./diff(freq8(:));
dpp8 = (dp8(ind81)*(fp8))/2;
Qp8=abs(dpp8)
[maxi82,ind82]=max(Y8_real);% series resonance
fs8=columnA8(ind82)
%%calculation of Q factor dP/dFs
ds8 = diff(P8(:))./diff(freq8(:));
dss8 = (ds8(ind81)*(fs8))/2;
Qs8=abs(dss8)
```



# Novel Switchable and DC Bias Controllable High-Quality Factor High-Overtone Bulk Acoustic Resonators (HBAR)

by Kongbrailatpam Sandeep Sharma

Submission date: 08-Jan-2021 02:51PM (UTC+0530)

Submission ID: 1484490321

File name: Thesis\_14PHPE04\_Kongbrailatpam\_Sandeep\_S.pdf (14.94M)

Word count: 34035 Character count: 169334

# Novel Switchable and DC Bias Controllable High-Quality Factor High-Overtone Bulk Acoustic Resonators (HBAR)

ORIGIN	IALITY REPORT			
SIMIL	% ARITY INDEX	3% INTERNET SOURCES	6% PUBLICATIONS	1% STUDENT PAPERS
PRIMA	RY SOURCES			
1	with low noise", Il	Yu. "HBAR-Base power consumpt EEE Transactions ctrics and Freque	ion and low ph s on Ultrasonio	nase cs
2	Kerem Y "Magnet	Mert Torunbalci, unus Camsari, S o Acoustic Spin F c Reports, 2018	unil Ashok Bh	ave.
3	Katzer, M. Strou acoustic multi-pho	J. Gokhale, Brian Neeraj Nepal, And d, David J. Meye wave resonators onon sources for dynamics", Nature	drew C. Lang, r. "Epitaxial bu as highly coh quantum	Rhonda ılk erent
4	www.nck	oi.nlm.nih.gov e		1%

5	aip.scitation.org Internet Source	1%
6	www.coursehero.com Internet Source	<1%
7	Anil K. Maini, Varsha Agrawal. "Satellite Technology", Wiley, 2006 Publication	<1%
8	Submitted to Cornell University Student Paper	<1%
9	R. Weigel, D.P. Morgan, J.M. Owens, A. Ballato, K.M. Lakin, K. Hashimoto, C.C.W. Ruppel. "Microwave acoustic materials, devices, and applications", IEEE Transactions on Microwave Theory and Techniques, 2002	<1%
10	cwww.intechopen.com Internet Source	<1%
11	worldwidescience.org Internet Source	<1%
12	Eun Sok Kim. "High-frequency bulk acoustic resonant microbalances in liquid", Proceedings of the 2005 IEEE International Frequency Control Symposium and Exposition 2005, 2005 Publication	<1%
13	M.M. Driscoll. "Low noise, microwave signal	

generation using bulk and surface acoustic wave resonators", Proceedings of the 42nd Annual Frequency Control Symposium 1988, 1988

<1%

Publication

Lukas Baumgartel, Eun Sok Kim. "Experimental optimization of electrodes for high Q, high frequency HBAR", 2009 IEEE International Ultrasonics Symposium, 2009

<1%

Publication

Exclude quotes

Exclude bibliography

On On Exclude matches

< 14 words

# Novel Switchable and DC Bias Controllable High-Quality Factor High-Overtone Bulk Acoustic Resonators (HBAR)

by Kongbrailatpam Sandeep Sharma

Submission date: 08-Jan-2021 02:51PM (UTC+0530)

Submission ID: 1484490321

File name: Thesis\_14PHPE04\_Kongbrailatpam\_Sandeep\_S.pdf (14.94M)

Word count: 34035 Character count: 169334

# Novel Switchable and DC Bias Controllable High-Quality Factor High-Overtone Bulk Acoustic Resonators (HBAR)

13%	5%	12%	1%
SIMILARITY INDEX	INTERNET SOURCES	PUBLICATIONS	STUDENT PAPERS
PRIMARY SOURCES			
Sandee	p Kongbrailatpam	, J. Pundareek	sam 5%
	(. C. James Raju.		oated
	Layer on High O		
	tor and its Possibl		
	tions on Ultrasoni	cs, Ferroelecti	rics, and School of Ph University of Hy Hyderabad-500 0
Publication	ncy Control, 2020		Hyderdoda-500 o
	ccorp.com		1
Internet Sour	ce		1 %
aip.scita	ition.org		1
Internet Sour	ce		7 %
lc.epfl.c	h		1
Internet Sour	ce		1 %
5 Spartak	Sh Gevorgian, Al	exander K Tag	gantsev, 1
0	Vorobiev. "Tune		0/
Acoustic	Wave Resonator	s", Springer S	cience
	iness Media LLC,	And the second s	
Publication			

# "Magneto Acoustic Spin Hall Oscillators", Scientific Reports, 2018

Publication

P Bao. "Barium strontium titanate thin film varactors for room-temperature microwave device applications", Journal of Physics D Applied Physics, 03/21/2008

<1%

- Publication
- Vikrant J. Gokhale, Brian P. Downey, D. Scott Katzer, Neeraj Nepal, Andrew C. Lang, Rhonda M. Stroud, David J. Meyer. "Epitaxial bulk acoustic wave resonators as highly coherent multi-phonon sources for quantum acoustodynamics", Nature Communications, 2020

<1%

- Publication
- Zhang, H.. "Parameter characterization of highovertone bulk acoustic resonators by resonant spectrum method", Ultrasonics, 200508

<1%

K. Sandeep, J. Pundareekam Goud, K. C
James Raju. "Switchable high overtone
resonances in BST film with MIM structure on
sapphire substrate", 2016 Joint IEEE
International Symposium on the Applications of
Ferroelectrics, European Conference on

Application of Polar Dielectrics, and

<1%

Dr. K.C. James Raju Professor School of Physics University of Hyderabad Hyderabad-500 046, INDIA

### Microengineering, 01/01/2012 Publication "Nanostructured Metal Oxides and Devices", <1% 64 Springer Science and Business Media LLC, 2020 Publication M.M. Driscoll. "Low noise, microwave signal <1% 65 generation using bulk and surface acoustic wave resonators", Proceedings of the 42nd Annual Frequency Control Symposium, 1988., 1988 Publication Anil K. Maini, Varsha Agrawal. "Satellite <1% 66 Technology", Wiley, 2006 Publication Submitted to University of Sheffield 67 Student Paper Lukas Baumgartel, Eun Sok Kim. "Experimental 68 optimization of electrodes for high Q, high frequency HBAR", 2009 IEEE International Ultrasonics Symposium, 2009

Exclude quotes On Exclude matches < 14 words
Exclude bibliography Off

Publication

### UNIVERSITY OF HYDERABAD

## CENTRE FOR ADVANCED STUDIES IN ELECTRONICS SCIENCE AND TECHNOLOGY (CASEST)

### SCHOOL OF PHYSICS

HYDERABD 500046, INDIA

Dr. K. C. James Raju

11-01-2021

Professor

This is to certify that the thesis titled "Novel Switchable and DC Bias Controllable High-Quality factor High-Overtone Bulk Acoustic Resonators (HBAR)" submitted by Mr. Kongbrailatpam Sandeep Sharma (Reg.no. 14PHPE04), has been screened by the Turnitin software at Indira Gandhi memorial library (IGML), University of Hyderabad. This software shows 14% similarity index out of which more than 5% came from the candidates own publications (where he is the first author) directly related to this thesis.

From the detailed similarity index report, it is obvious that the remaining 9% (or less) of the similarity index, is due to the resemblance caused by the frequent use of well-known standard terms such as High-quality, High overtone bulk acoustic resonator (HBAR), external electric fields, acoustic wave velocity, coupling coefficient, elastic constant, thin film, film bulk acoustic resonator (FBAR), Bragg reflector, surface acoustic wave (SAW), standing acoustic wave, Butterworth Van Dyke (BVD) model, Q factor, high tunability, low dielectric loss, BST thin films, electrostriction coefficient, effective coupling coefficient, ferroelectric film, spacing of parallel resonance frequency (SPRF), relative tunability, Pulse laser deposition, X-Ray diffraction, Scanning electron microscope (SEM), Barium strontium titanate (BST) thin films, Vector network analyzer, SOLT, SOLR, TRL, LRRM, half wavelength resonator, thickness, SU-8 coating and frequency range. The use of terms is rampant in the literature, and hence it is not surprising that the similarity index is artificially inflated. It should be noted that the use of such standard terms cannot be avoided.

Prof. K. C. James Rajusessor

School of Physics (Supervisor) iversity of Hyderabad Hyderabad-500 046, INDIA

kcjrsp@uohyd.emet.in

Ph: 040-23134305 Mob: 9441917858 Fax: 040-23010227